The dynamics of realistic field theory solitons

Daniel Jiménez Aguilar

eman ta zabal zazu

Universidad del País Vasco
Euskal Herriko Unibertsitatea

Under the supervision of

Prof. José Juan Blanco-Pillado and Prof. Jon Urrestilla

Department of Physics
2023

Contents

Agradecimientos

En esta tesis se recoge el trabajo que he llevado a cabo durante los últimos casi cinco años. Ha sido un camino largo y exigente en el que no han faltado cuestas, callejones sin salida y espejismos. Aun así, el doctorado ha sido sin duda una experiencia muy enriquecedora a muchos niveles. He conseguido sacar adelante esta tesis después de incontables horas de aprendizaje, organización y de reflexión, y hay mucha gente a la que debo agradecérselo.

En primer lugar, tengo que darles las gracias a mis directores de tesis, Jon Urrestilla y José Juan Blanco-Pillado. Muchas gracias por vuestra implicación, por vuestra cercanía y por tener la paciencia de explicarme las cosas todas las veces que hicieran falta. Gracias por echarme un cable cuando no me salía nada, por la infinidad de correos que hemos intercambiado y por todas las veces que os habéis sentado a mi lado en el despacho a pensar. Sé que no todo el mundo ha tenido esa suerte con sus directores. He aprendido de vuestra forma de pensar y de hacer las cosas, y siento que he crecido mucho como físico y que he ganado confianza. Ojalá se me haya pegado lo mejor de cada uno, y espero seguir en contacto con los dos durante mucho tiempo. Podéis contar conmigo para lo que sea.

Lo anterior es también extensivo a José Queiruga, con el que he tenido el placer de colaborar durante casi todo este tiempo. Gracias por toda tu ayuda, por compartir tus anécdotas y tu conocimiento, y por todos los momentos divertidos fuera y dentro del trabajo.

También quiero darle las gracias a toda la gente del departamento por haber hecho que el ambiente de trabajo sea excelente. Joanes, gracias de nuevo por presentar mis papeles en el registro el verano de 2018, y Asier, gracias por ofrecerme tu ayuda y consejo para lo que necesite en mi futura etapa en Boston. También estoy muy agradecido a Mariam y Ruth, con las que he tenido la oportunidad de dar clases en la universidad por primera vez. Es algo que he disfrutado mucho, y a ambas les guardo un cariño especial. I Raül, gràcies per solucionar sempre qualsevol problema que tingués amb harria i wilmore, però sobre tot per fer-me sentir més a prop de casa.

El doctorado me ha dado la oportunidad de conocer a físicos a los que nunca me habría imaginado conocer, de dar seminarios y participar en congresos, de viajar, y de colaborar e incluso entablar amistad con investigadores de distintos países. Algunas de las personas que he conocido y con las que he podido interaccionar gracias a estas colaboraciones, viajes y charlas han sido José Ricardo Correia, Albert Escrivà, Andrew Long, Carlos Martins, Levon Pogosian, Javier Redondo y Andrzej Wereszczynski. Otros investigadores que me acogieron en persona en sus respectivas universidades y a los que quiero agradecer particularmente su hospitalidad son Alberto Izquierdo, Ken Olum, Teerthal Patel, Oriol Pujolàs, Tanmay Vachaspati y Alex Vilenkin.

Algo fundamental que también me ha brindado el doctorado y que me llevo para siempre son los amigos que he hecho en la universidad. Hemos trabajado codo con codo, nos hemos entendido, nos hemos apoyado y nos hemos divertido juntos: salidas en bares, comidas, cenas, paseos por el monte y por la ciudad, tardes y noches de juegos, partidos de pádel... E incluso sobrevivimos a un tiroteo. Por todo ello, mil gracias a Adrián, Aitor, Álvaro, Ander, Araceli, Asier, Eneko, Marco, Sara y Unai, y en especial, a Fran, María y Mikel. Sois geniales. También quiero acordarme de otros compañeros que conocí durante mis primeros meses de doctorado (Iker, Jeremy y João) y desearle suerte a las nuevas incorporaciones (Carlos, Paloma y Samuel).

Fuera de la universidad también he podido conocer a otras personas con las que tengo buenos recuerdos: Aitziber, Clara, Clàudia, Miri, Nastassja, Raúl, Santi y Simón. Tampoco puedo olvidarme de Claudia y Cris, que tienen un lugar muy especial en mi cabeza, y tampoco de Taida, que es sin duda de lo mejor que me llevo de esta etapa. Quiero darles las gracias a todos ellos, así como a Vladimir y a mis amigos de Menorca, especialmente a Alba, Alejandro, Elena, Júlia, Laura, Mare y Ramiro.

Gracias también a Diego Pavón, con el que he tenido la suerte de mantener el contacto después del grado, por escuchar siempre mis ideas, por enseñarme tantas cosas interesantes y por su sabio consejo.

A la familia le debo esencialmente su constante apoyo incondicional, así como el darme fuerzas para continuar cada vez que se aproximaba el momento de verles. Quiero agradecérselo especialmente a mis padres y a Rafa, y también a Lucía. Rafa y yo hemos vivido esta experiencia simultáneamente (aunque en lugares distintos), así que ha podido lidiar con las fluctuaciones de mi estado de ánimo con conocimiento de causa. Él me conoce mejor que nadie, y ha sido clave en esta etapa y en todas las anteriores.

También quiero dedicarle unas líneas a mi tío Fernando. Estuvo presente en uno de los momentos que marcaron mis inicios en la física, y me emociona recordar lo orgulloso que estuvo de mí entonces y saber que también lo estaría ahora. Gracias por formar parte de aquello. Te recordaremos todos siempre.

Finalmente, quiero darle las gracias a la persona que ha hecho que esta etapa de mi vida sea increíble: Leire. Gracias por animarme constantemente, por escucharme e incluso hacerme preguntas cuando te hablo de física, por cuidarme y por hacerme sentir tantas cosas nuevas. Podría llenar hojas y hojas de agradecimientos solo hacia ti, pero esta tesis ya es suficientemente larga. Gracias por todo.

Resumen

Las cuerdas cósmicas son defectos topológicos que podrían haberse creado durante una transición de fase cosmológica en el universo primigenio. También podrían tratarse de supercuerdas amplificadas a escalas cosmológicas por la expansión del universo. Estos objetos son estables y podrían perdurar a día de hoy como si de fósiles se trataran. Dado que su formación ocurre a escalas de energía mucho mayores a la que puede alcanzarse en cualquier experimento en la Tierra, su detección puede constituir una fuente muy valiosa de información acerca de teorías más allá del Modelo Estándar y cosmología.

El objetivo principal del trabajo de investigación llevado a cabo es entender las discrepancias que existen actualmente entre las simulaciones de redes de cuerdas cósmicas en teoría de campos y las simulaciones tipo Nambu-Goto. Por una parte, en las simulaciones de teoría de campos, la evolución de las redes se obtiene resolviendo numéricamente las ecuaciones no-lineales que se derivan de la acción de la teoría. Por otra parte, en las simulaciones Nambu-Goto, se asume que la cuerda es infinitamente delgada, por lo que su dinámica viene descrita por la llamada acción de Nambu-Goto. El primer grupo de simulaciones captura toda la dinámica de la red de cuerdas, por lo que es la forma estrictamente correcta de evolucionarla. Sin embargo, a nivel de computación, cuenta con ciertas limitaciones debidas a la gran diferencia existente entre las escalas relevantes del sistema de estudio. Lo idóneo sería simular las redes en volúmenes lo más grandes posible (varios órdenes de magnitud por encima del grosor de las cuerdas), pero al mismo tiempo debe tenerse suficiente resolución en el núcleo de las cuerdas para poder evolucionarlas correctamente. Esto requiere un número muy elevado de puntos, y por tanto, tiempos de simulación extremadamente largos. Además, existe un problema añadido si las simulaciones se llevan a cabo en un universo que se expande: el grosor de la cuerda se va reduciendo en coordenadas comóviles, por lo que se necesita un número total de puntos todavía mayor para poder confiar en los resultados de la simulación a tiempos largos. Como las cuerdas no tienen grosor en el caso de Nambu-Goto, este problema no existe y las simulaciones pueden llevarse a cabo en volúmenes mucho mayores. Sin embargo, debe tenerse en cuenta que la aproximación de Nambu-Goto ignora los

efectos de los campos en la dinámica de las cuerdas (en particular, la posibilidad de que las cuerdas emitan radiación o la estructura interna de las mismas). Por tanto, es importante determinar si estos efectos juegan un papel relevante en la dinámica de las cuerdas en un contexto cosmológico.

Las predicciones de ambos tipos de simulaciones son similares en cuanto a las cuerdas infinitas de la red, pero son radicalmente distintas respecto a los *loops* que se forman a partir de sus intersecciones. Por una parte, en las simulaciones de teoría de campos, los *loops* emiten radiación en forma de partículas y van perdiendo longitud hasta evaporarse por completo. Por otra parte, en las simulaciones Nambu-Goto, este canal de decaimineto no existe y los *loops* solo pueden evaporarse por la emisión de ondas gravitacionales. A diferencia del caso anterior, en las simulaciones Nambu-Goto se encuentran *loops* que no experimentan auto-intersecciones (*non-self-intersecting loops*). Esto conduce a una discrepancia importante en la densidad de *non-self-intersecting loops*, y, por tanto, en la potencia emitida en ondas gravitacionales por las redes de cuerdas.

La hipótesis en la que se basa este trabajo es que las discrepancias entre los dos grupos de simulaciones son debidas a que las cuerdas se excitan sustancialmente durante su formación y a lo largo de la evolución cosmológica como parte de la red. Esta energía extra puede permanecer almacenada en el núcleo de las cuerdas durante periodos de tiempo muy largos en comparación a cualquier otra escala de tiempo naturalmente determinada por los parámetros de la teoría, y, por tanto, podría alterar significativamente la dinámica de las cuerdas durante el tiempo de simulación. Por todo ello, esta tesis se centra fundamentalmente en el estudio de la dinámica de solitones en teoría de campos y en su comparación con la aproximación de Nambu-Goto. Más concretamente, se ha investigado en profundidad el papel que pueden jugar las excitaciones internas de solitones de distinta dimensionalidad en la dinámica de los mismos.

El primer paso ha sido el estudio de las excitaciones internas de *kinks* en $1+1$ dimensiones en la teoría $\lambda\phi^4$. Este estudio se detalla en el capítulo 2. Las autofunciones de la ecuación de Schrödinger para perturbaciones lineales alrededor de la solución estática del *kink* pueden clasificarse en los tres siguientes grupos: el modo cero, el modo *shape* y los modos de *scattering*. El modo cero corresponde a pequeñas traslaciones rígidas del *kink*, con lo cual no aporta energía extra. Los modos de *scattering* corresponden a radiación, y tienen la forma de ondas viajeras en el límite asintótico. Por último, el modo *shape* puede asociarse a fluctuaciones en el grosor del *kink*. Esta perturbación está localizada en el espacio y puede almacenar una cantidad sustancial de energía extra durante escalas de tiempo enormes en comparación al tiempo que tarda la luz en recorrer la anchura del *kink*. Por tanto, este es el modo que puede ser responsable de una alteración de la dinámica esperada del *kink* a tiempos largos.

La energía almacenada en el modo *shape* puede determinarse a partir de su amplitud, que decae lentamente debido a un acoplo no-lineal a los modos de *scattering*. La escala de tiempo asociada a este decaimiento puede estimarse analíticamente mediante el método de la función de Green, y sigue la llamada ley de Manton-Merabet. Numéricamente, la amplitud del modo *shape* se halla proyectando la perturbación sobre la autofunción correspondiente a todo tiempo. Lo que se observa es que el tiempo de decaimiento es varios órdenes de magnitud mayor al grosor del *kink*, incluso para amplitudes cercanas al régimen no-lineal. Por otra parte, se demuestra que el modo *shape* puede almacenar una energía hasta dos veces mayor que la propia masa del *kink*.

Se ha cuantificado la excitación del modo *shape* en el proceso de formación de *kinks* en una transición de fase cosmológica, así como en la interacción de estos objetos con un baño térmico. En el primer escenario, se encuentra que los *kinks* se excitan con una energía extra del 20 %, cantidad que se presume suficiente como para alterar su dinámica de forma significativa. En el segundo, se distinguen dos regímenes: a temperaturas bajas, la energía en el modo *shape* aumenta linealmente con la temperatura, mientras que satura a un valor constante (también cercano al 20 % de la masa del *kink*) en el límite de altas temperaturas.

Los resultados de este análisis se detallan en el artículo

J.J. Blanco-Pillado, D. Jiménez-Aguilar, J. Urrestilla. *Exciting the domain wall soliton.* *J*CAP 01 (2021) 027. https://arxiv.org/abs/2006.13255

En el capítulo 3 se estudia la dinámica de *domain walls* en $2 + 1$ dimensiones. A diferencia del caso anterior, la solución estática que interpola entre los vacíos del potencial es extensa en una dirección espacial: se trata de una cuerda. El espectro de perturbaciones alrededor de esta solución consta nuevamente de modo cero, modo *shape* y modos de *scattering*, pero en este caso las perturbaciones pueden tener cierta longitud de onda en la dirección de la cuerda. Los modos cero y *shape* vuelven a corresponderse con fluctuaciones de la posición y el grosor del objeto, pero ahora pueden propagarse a lo largo de él. Los modos cero pueden interpretarse como la versión linealizada de las llamadas ondas Vachaspati-Vachaspati. Estas son soluciones exactas de la ecuación de movimiento, y representan perturbaciones de forma y amplitud arbitrarias que viajan sobre la *domain wall* a la velocidad de la luz.

La energía almacenada en los modos cero y *shape* se pierde principalmente mediante dos mecanismos: el acoplo no-lineal a los modos de *scattering* y aniquilación en regiones de alta curvatura en la cuerda. Este último corresponde a un proceso de emisión de radiación no-perturbativa que se intensifica cuando el radio de curvatura de la cuerda es comparable a su grosor. Sin embargo, cabe señalar que esto no ocurre para las ondas Vachaspati-Vachaspati, ya que no pueden dar lugar a radiación por ser soluciones exactas de la ecuación de movimiento.

A bajas energías, cuando el modo *shape* no es excitado, se espera que el único grado de libertad dinámico sea la posición de la cuerda. Si además se desprecian efectos de radiación, la acción que debería describir la dinámica de la cuerda es la acción de Nambu-Goto. Para comprobar su validez, se han simulado colisiones de ondas que se propagan a lo largo de la *domain wall*, manteniendo siempre curvaturas bajas. Además de poner de manifiesto la no-linealidad de la ecuación de Nambu-Goto, estos experimentos confirman que la cuerda reproduce perfectamente el comportamiento predicho por esta acción. Esto deja de ser cierto si se desarrollan zonas de alta curvatura. También se ha comparado la dinámica de la cuerda en una configuración de onda estacionaria con la predicción de Nambu-Goto, de nuevo manteniendo la curvatura pequeña. En este caso, el acuerdo es especialmente bueno si la frecuencia de la onda está por debajo de la mitad de la masa del bosón de la teoría. En caso contrario, el acoplo a los modos de *scattering* es a orden cuadrático y la energía de la *domain wall* es emitida más rápidamente. Para este tipo de configuraciones también se ha calculado la potencia de radiación emitida como función de la frecuencia de la onda estacionaria. Contrariamente a lo que uno podría pensar a priori, se observa que la potencia está altamente suprimida para frecuencias mayores a la masa del bosón.

La dinámica de la cuerda puede cambiar drásticamente si el modo *shape* está excitado. En efecto, la ecuación de estado de la *domain wall* se ve modificada en este caso. En promedio, y a orden más bajo en las perturbaciones, la densidad de energía de la cuerda aumenta, mientras que su tensión permanece constante. Esto implica que ondas que se propagarían a la velocidad de la luz en ausencia de modo interno ven su velocidad reducida. Además, la variación temporal de la tensión puede inducir amplificaciones de pequeños desplazamientos de la cuerda. Se ha demostrado que un modo *shape* homogéneo es capaz de amplificar un modo cero de frecuencia igual a la mitad de la frecuencia del modo interno hasta prácticamente triplicar su amplitud, la cual obedece una ecuación tipo Mathieu. Por otra parte, una configuración de onda estacionaria para el modo *shape* decae en dos modos cero de distinta frecuencia. Estos fenómenos de resonancia hacen que la energía extra (la guardada inicialmente en el modo *shape*) se libere más rápido en forma de radiación.

Así pues, el modo *shape* podría alterar la dinámica de las cuerdas en tiempos típicos de simulación. Sin embargo, la escala de tiempo durante la cual tendría relevancia es insignificante en comparación a la edad del universo. Por tanto, es importante cuestionarse si el modo *shape* puede reexcitarse de forma dinámica a tiempos largos. Para contestar a esta pregunta, se han simulado colisiones de modos cero sobre la cuerda y se ha observado que el modo *shape* solo se excita en la región de interacción si la frecuencia de las ondas es cercana a la mitad de la frecuencia del modo interno. Como no se espera tener estructura a estas escalas a tiempos largos durante la evolución cosmológica, es razonable pensar que este modo no se reexcita, y por tanto, que no juega un papel relevante en un contexto cosmológico.

Este estudio se recoge en el artículo

Daniel Jiménez-Aguilar et al. *The dynamics of domain wall strings.*
https://arxiv.org/abs/2210.02556

En el capítulo 4 se estudian las excitaciones internas de vórtices globales en $2 + 1$ dimensiones. Como en este caso el campo escalar es complejo, existen perturbaciones tanto de su parte radial como de su parte angular. En el vacío tiene sentido asociarlas respectivamente a fluctuaciones con masa y sin masa. El comportamiento asintótico del potencial efectivo de las perturbaciones en el problema de Schrödinger lineal es tal que existe un número infinito de modos ligados para la parte radial, de los cuales solo se analizan los dos de frecuencia menor (el tratamiento numérico del resto resulta complicado, ya que tienen una extensión espacial demasiado grande). Por el contrario, solo existen estados de *scattering* para la parte angular.

De nuevo, la amplitud de los modos ligados como función del tiempo puede estimarse analíticamente mediante el método de la función de Green. Se encuentra que la escala de tiempo del decaimiento por el acoplo no-lineal a los estados de *scattering* es mucho mayor a la anchura del vórtice, y crece a medida que aumenta la frecuencia del modo ligado.

Curiosamente, los modos ligados de la parte radial pueden excitarse al interaccionar con radiación sin masa, mecanismo que entra en acción en simulaciones de vórtices en contextos realistas. Se ha calculado el nivel de excitación de los vórtices en tres situaciones: su formación en una transición de fase, su interacción con un baño térmico y su evolución cosmológica en un universo dominado por radiación. De manera similar a lo que se observó en el caso del *kink*, la energía almacenada en los modos ligados aumenta linealemente con la temperatura hasta que satura a un valor constante, cercano al nivel de excitación obtenido en la transición de fase. En este caso, así como a lo largo de la evolución cosmológica, la energía extra almacenada es muy pequeña en comparación a la masa efectiva del vórtice (inferior al

1 %).

Los resultados fueron publicados en el artículo

J.J. Blanco-Pillado, D. Jiménez-Aguilar, J. Queiruga, J. Urrestilla. *Internal excitations of global vortices.*
JCAP 10 (2021) 047. https://arxiv.org/abs/2107.02215

En el capítulo 5 se demuestra tanto analíticamente como numéricamente que los fenómenos de resonancia descubiertos en el capítulo 3 también ocurren en el caso de cuerdas globales en $3+1$ dimensiones. Además de radiación masiva, estos defectos topológicos pueden emitir radiación sin masa, correspodiente a fluctuaciones de la parte angular del campo. Estas partículas sin masa se asocian al axión, uno de los candidatos más atractivos para constituir la materia oscura. Debido a la amplificación resonante del modo cero, la energía inicial contenida en el modo *shape* vuelve a liberarse más rápidamente, pero en este caso por la emisión de radiación sin masa además de la masiva. Por tanto, este fenómeno puede dar lugar a un aumento de la producción de materia oscura axiónica.

Este estudio se detalla en el artículo

J.J. Blanco-Pillado, D. Jiménez-Aguilar, J. Queiruga, J. Urrestilla. *Parametric resonances in axionic cosmic strings.*
Aceptado para publicación en JCAP. https://arxiv.org/abs/2212.06194

Finalmente, en el capítulo 6 se analiza específicamente la problemática de los *loops* en las simulaciones de redes de cuerdas cósmicas locales, comparando directamente el movimiento de los *loops* en teoría de campos con la predicción de la acción de Nambu-Goto. Se han estudiado dos tipos de *loops*, a los que hemos llamado primordiales y no-primordiales. Los primeros se crean justo después de un periodo de difusión, por lo que se hallan inicialmente en reposo. Los segundos, en cambio, se forman más adelante como resultado de las intersecciones de las cuerdas de la red. Por un lado, los *loops* primordiales siguen exactamente la trayectoria Nambu-Goto hasta que su radio de curvatura es comparable a su grosor. En ese momento, el *loop* empieza a emitir radiación masiva y desaparece. Se presume que el periodo de fricción al que han estado expuestos estos *loops* ha eliminado la estructura a pequeña escala y la energía contenida en modos internos que pudieran estar presentes. Por otro lado, los *loops* no-primordiales sí cuentan con una cantidad significativa de energía extra. Se han analizado varios *loops* de este tipo y en todos los casos se observa que la predicción de Nambu-Goto solo falla en las regiones de alta curvatura. Esto confirma la sospecha, fundada en los resultados del estudio de *domain walls* en $2 + 1$ dimensiones, de que los modos internos no acaban jugando un papel relevante en la dinámica de los *loops*. Tras los eventos de evaporación en estas zonas de las cuerdas, se vuelve a empezar la reconstrucción de Nambu-Goto y se observa acuerdo entre las dos descripciones hasta que vuelve a desarrollarse curvatura alta. En base a los resultados obtenidos, concluimos que los *loops* en las simulaciones de teoría de campos se forman con una cantidad considerable de energía extra a escalas pequeñas, y especulamos lo siguiente: cuando el *loop* ha liberado toda esta energía emitiéndola en forma de radiación masiva, ya empieza a comportarse como predice la acción de Nambu-Goto, siempre y cuando sea lo suficientemente grande. Sin embargo, lo que ocurre en las simulaciones de teoría de campos es que el *loop* se ha hecho demasiado pequeño para entonces, con lo cual sigue evaporándose y desaparece. Por tanto, se requieren simulaciones de teoría de campos en volúmenes mayores donde puedan encontrarse *loops* que sigan siendo grandes tras deshacerse del exceso de energía. Sin embargo, este análisis es preliminar y se necesita más trabajo para confirmar esta conjetura.

Los detalles y resultados de este estudio se recogen en el artículo

J.J. Blanco-Pillado, D. Jiménez-Aguilar, J. Lizarraga, A. Lopez-Eiguren, K. D. Olum, A. Urio, J. Urrestilla. *Nambu-Goto dynamics of field theory cosmic string loops.*
https://arxiv.org/abs/2302.03717

List of publications

1. J.J. Blanco-Pillado, D. Jiménez-Aguilar, J. Urrestilla. *Exciting the domain wall soliton.*
   JCAP 01 (2021) 027. https://arxiv.org/abs/2006.13255
2. J.J. Blanco-Pillado, D. Jiménez-Aguilar, J. Queiruga, J. Urrestilla. *Internal excitations of global vortices.*
   JCAP 10 (2021) 047. https://arxiv.org/abs/2107.02215
3. J.J. Blanco-Pillado, D. Jiménez-Aguilar, J. Queiruga, J. Urrestilla. *The dynamics of domain wall strings.*
   https://arxiv.org/abs/2210.02556
4. J.J. Blanco-Pillado, D. Jiménez-Aguilar, J. Queiruga, J. Urrestilla. *Parametric resonances in axionic cosmic strings.*
   Accepted for publication in JCAP. https://arxiv.org/abs/2212.06194
5. J.J. Blanco-Pillado, D. Jiménez-Aguilar, J. Lizarraga, A. Lopez-Eiguren, K. D. Olum, A. Urio, J. Urrestilla. *Nambu-Goto dynamics of field theory cosmic string loops.*
   https://arxiv.org/abs/2302.03717

Chapter 1

Introduction

The main goal of this work is to explain the current discrepancies between field theory and Nambu-Goto simulations of cosmic strings, based on the conjecture that the internal perturbations of these objects play a relevant role on their dynamics. For this purpose, this thesis covers a detailed study of the dynamics of excited solitons in different number of spacetime dimensions, from $1+1$ dimensional kinks to $3+1$ dimensional strings.

In this introductory chapter, after establishing in section 1.1 the units and conventions adopted throughout the thesis, we will present the main properties of this kind of field theory solutions, known generically as topological defects, and how they are formed in a cosmological setting. This is done in section 1.2, along with a brief discussion of their relevance to constrain field theory models. We will then provide the basic notions of global and local cosmic strings in section 1.3, followed by a more detailed description of the Nambu-Goto approximation in section 1.4. In section 1.5, we give a historical overview of the tension between field theory and Nambu-Goto simulations of cosmic strings, and clearly state the differences and limitations of both approaches. Finally, the structure of the thesis is sketched in section 1.6.

1.1 Units and conventions

- Natural units ($c = \hbar = k_B = 1$) will be used throughout this thesis. This implies that all fields, coordinates and parameters have dimensions of energy (E) to some power. In particular,

  $$[x^\mu] = E^{-1}, \quad [\phi] = E^{D/2-1}, \tag{1.1}$$

  where D is the number of spacetime dimensions.

- The signature for the metric will be taken to be $(+,-,-,-)$.
- Sum over repeated indices will be assumed unless otherwise stated.

1.2 Topological defects

Topological defects are solitonic solutions of the equations of motion of a classical field theory. In simple terms, defects constitute regions of space in which the energy of the fields gets trapped in the aftermath of their formation process, which is typically a phase transition. The term "solitonic" generally refers to a solution with localized, non-dispersive energy density that travels undistorted in shape even after scattering. These objects resemble extended particles in many respects. For instance, the energy density of this kind of solutions is typically concentrated in a region of spatial extent comparable to the Compton wavelength of the massive particle of the theory, and this lump of energy moves at contant velocity in the absence of external forces.

The concept of soliton is not uniquely defined in the literature, but here we will provide the definition given in [1]. Firstly, we need to introduce the term "solitary wave". A solitary wave is a solution of any non-linear field equation whose energy density, as well as being localized[1], takes the form $\rho\left(t,\vec{x}\right)=\rho\left(\vec{x}-\vec{u}t\right)$, where $\vec{u}$ is some velocity vector. A soliton is essentially a solitary wave with the added requirement that its energy density profile remains unchanged after scattering. Therefore, solitons are a very special class of solitary waves. Strictly speaking, the defects that we will investigate in this thesis are not solitons, but solitary waves. However, we will refer to them as solitons, as it is generally done in the literature.

These solutions owe their stability to the topology of the vacuum manifold. In this regard, solitons are typically characterized by some topological index related to their behaviour at spatial infinity. This number constitutes a conserved quantity, in the sense that a field configuration with topological charge Q cannot be continuously deformed into another configuration with index $Q'\neq Q$. In order to exemplify this important property of solitons, as well as some of the other properties mentioned above, let us briefly introduce the simplest defect arising in field theory: the kink solution. Although it will be our main subject of

---

[1] By localized we mean that it is finite in some region of space and falls asymptotically to zero rapidly enough to be integrable. As will see, global strings do not satisfy this condition, but we will still refer to them as solitons.

study in chapter 2, we find it expedient to outline its main properties in this introductory chapter.

1.2.1 The $\lambda\phi^4$ kink

The kink soliton arises in the so-called $\lambda\phi^4$ theory for a real scalar field ϕ in $1+1$ dimensions, for which the action reads

$$S = \int d^2x \left[\frac{1}{2}\eta^{\mu\nu}\partial_\mu\phi\partial_\nu\phi - V(\phi)\right], \tag{1.2}$$

where $\eta^{\mu\nu}$ is the inverse of the Minkowski metric tensor, and the potential energy density $V(\phi)$ is given by

$$V(\phi) = \frac{\lambda}{4}\left(\phi^2 - \eta^2\right)^2, \tag{1.3}$$

where the constants λ and η are, respectively, the quartic self-coupling and the vacuum expectation value of the field. This double-well potential is plotted in figure 1.1. The mass of small fluctuations about the vacua is given by $m = \sqrt{2\lambda}\eta$.

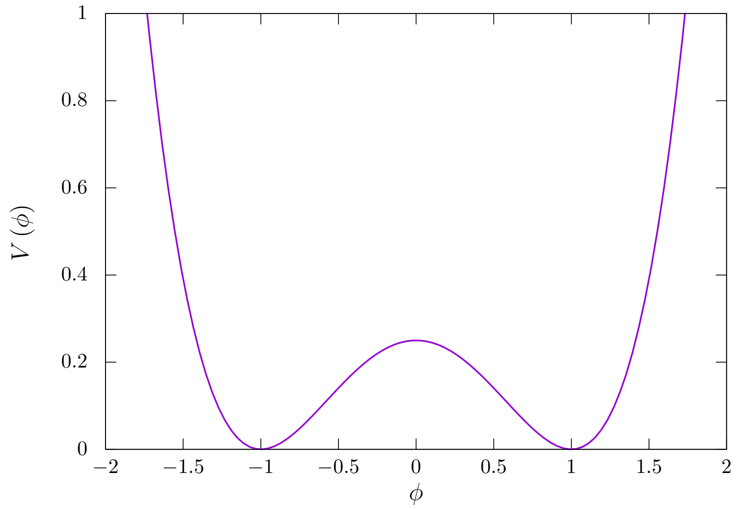

Figure 1.1: Potential energy density (1.3), in units of $\lambda\eta^4$. The value of the field in the horizontal axis has been rescaled by η.

From the action (1.2) it is clear that the Lagrangian is invariant under the transformation $\phi \to -\phi$; it has $\mathbb{Z}_2$ symmetry. The equation of motion for ϕ reads

$$\ddot{\phi} - \phi'' + \lambda\left(\phi^2 - \eta^2\right)\phi = 0, \tag{1.4}$$

where dots and primes respectively denote derivatives with respect to time and space. With the boundary conditions $\phi\left(x\to\pm\infty\right)=\pm\eta$, there is a static solution to this equation that interpolates between the two minima of the potential. This is the kink solution:

$$\phi_k\left(x\right)=\eta\tanh\left(\sqrt{\frac{\lambda}{2}}\eta x\right). \tag{1.5}$$

The so-called antikink solution, $\phi_{ak}=-\phi_k$, is a static solution of the equation of motion with the opposite boundary conditions. The kink solution is shown in figure 1.2 together with its associated energy density, which can be found to be

$$\mu_k\left(x\right)=\frac{\lambda\eta^4}{2}\,\mathrm{sech}^4\left(\sqrt{\frac{\lambda}{2}}\eta x\right). \tag{1.6}$$

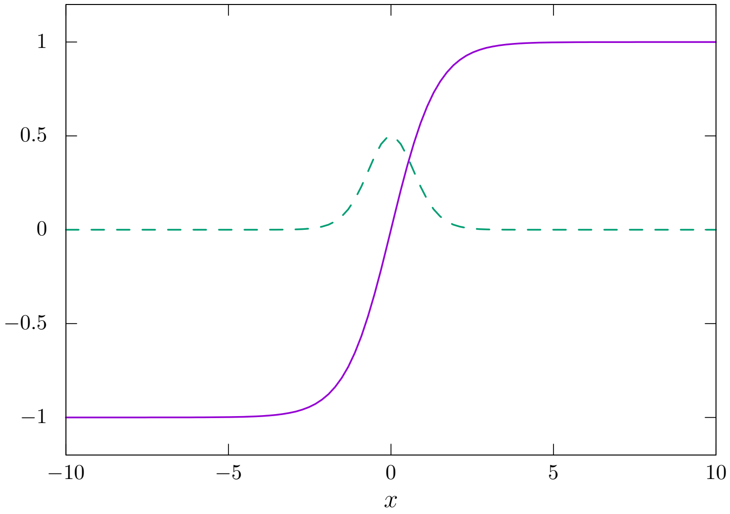

Figure 1.2: The solid purple line corresponds to the kink solution (1.5), rescaled by η. The dashed green line is the energy density of the kink, (1.6), displayed in units of $\lambda\eta^4$. The spatial coordinate x in the horizontal axis is given in units of $1/\sqrt{\lambda}\eta$.

Note that the energy density is exponentially localized around the core of the kink, which has a thickness $\delta\sim m^{-1}$. The energy density decays by a factor greater than 10^3 between $x=0$ and $x=5m^{-1}$. Given the boundary conditions, the continuity of the field forces the existence of this lump of energy. Indeed, since ϕ varies continuously from $-\eta$ to η, there must be a point where $\phi=0$, i.e., a point where the field is sitting at the top of the potential. Therefore, although this lump of energy can certainly move and shrink due to Lorentz contraction, it cannot dissipate. This simple argument shows that the existence of the defect can be determined merely by the knowledge of the values of the field at spatial infinity. One can define a conserved topological charge Q as

$$Q \equiv \frac{\phi\,(x \to \infty) - \phi\,(x \to -\infty)}{2\eta}. \tag{1.7}$$

Note that the kink solution, with $Q = 1$, cannot be continuously deformed into another configuration with a different topological charge. For instance, $Q = 0$ corresponds to a configuration in which the two asymptotic values of the field coincide. Getting such a state from the kink solution is not possible, as the change would require an infinite amount of energy. Roughly speaking, one would have to bring an infinite amount of points from one vacuum to the other one. The simplest possibilities with $Q = 0$ are the homogenous vacuum configurations $\phi = \pm\eta$, but we can also have vanishing topological charge in a "network" of kinks and antikinks (on its own, an antikink has $Q = -1$), as long as the total number of defects is even. Consider for instance the kink-antikink system shown in figure 1.3. Note that such a configuration can be continuously deformed into a vacuum state as a result of kink-antikink annihilation.

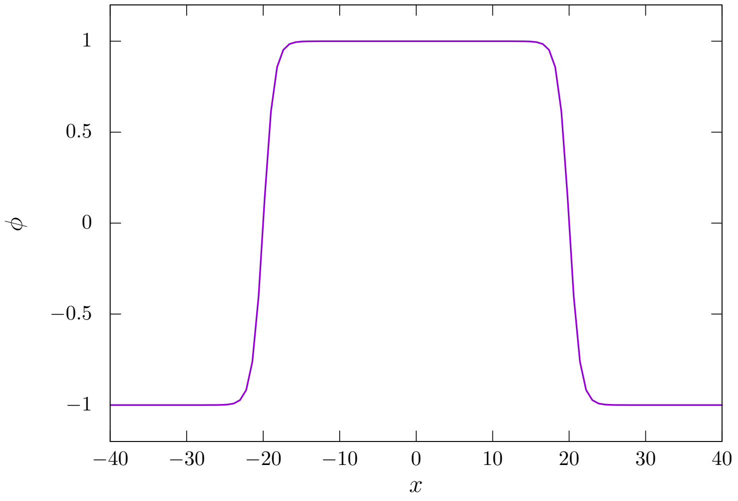

Figure 1.3: A kink-antikink configuration, with topological charge $Q = 0$. The field is rescaled by η and the x coordinate is given in units of $1/\sqrt{\lambda}\eta$.

One can interpret this topological index in terms of a mapping from the set of spatial infinities $S = \{-\infty, +\infty\}$ to the vacuum manifold $\mathcal{M} = \{-\eta, +\eta\}$. The $Q = 0$ configuration can be identified with the mapping of both elements in S to the same element in $\mathcal{M}$. For instance, the case shown in figure 1.3 corresponds to associating both $-\infty$ and $+\infty$ to the element $-\eta$ in $\mathcal{M}$. The $Q = 1$ case corresponds to the mapping $-\infty \to -\eta, +\infty \to +\eta$, and the case $Q = -1$ to $-\infty \to +\eta, -\infty \to +\eta$.

In general, the so-called nth homotopy group $\pi_n(\mathcal{M})$ classifies different mappings from the n-dimensional sphere S^n to the vacuum manifold M. The elements of $\pi_n(\mathcal{M})$ are equivalence classes (homotopy classes) that contain the set of maps that are continuously deformable into each other. In 3+1 dimensions, point-like, one-dimensional and two-dimensional defects are called monopoles, strings and domain walls, respectively. Their classification according to homotopy considerations is shown in table 1.1.

Topological defect	Topology of the vacuum manifold	Relevant homotopy group
Domain wall	S^0 (two points)	$\pi_0(\mathcal{M})$
String	S^1 (a circle)	$\pi_1(\mathcal{M})$
Monopole	S^2 (a sphere)	$\pi_2(\mathcal{M})$

Table 1.1: Classification of topological defects in the context of homotopy theory.

Elaborating further on the specific mathematical details and variants of this classification would be a digression for the purposes of this thesis, so let us end up this subsection by simply pointing the interested reader to references [2, 3, 4, 5], where this topic is discussed in depth.

1.2.2 Formation of defects

As mentioned at the beginning of this introduction, topological defects can be formed in cosmological phase transitions in the early universe. This process is associated to the spontaneous breaking of some symmetry (for instance, a $\mathbb{Z}_2$ symmetry in the case of domain walls or a $U(1)$ symmetry in the case of strings), which is rooted at the temperature dependence of the potential for the scalar field ϕ. In the background of a thermal bath of particles, the scalar field potential gets temperature-dependent terms which may change its shape. According to the hot Big Bang model, the universe starts at a very high temperature such that this effective potential $V_{\text{eff}}(\phi, T)$ is minimized for $\phi = 0$. However, as the universe expands and cools down below some critical temperature T_C, new minima may appear. The field can then undergo a sequence of symmetry breakings, as the new vacuum states may not share the symmetries of the initial one. The field can transition to the new global vacuum in a first-order or in a second-order phase transition, illustrated in figure 1.4. These processes can lead to the formation of topological defects by means of the Kibble mechanism [6].

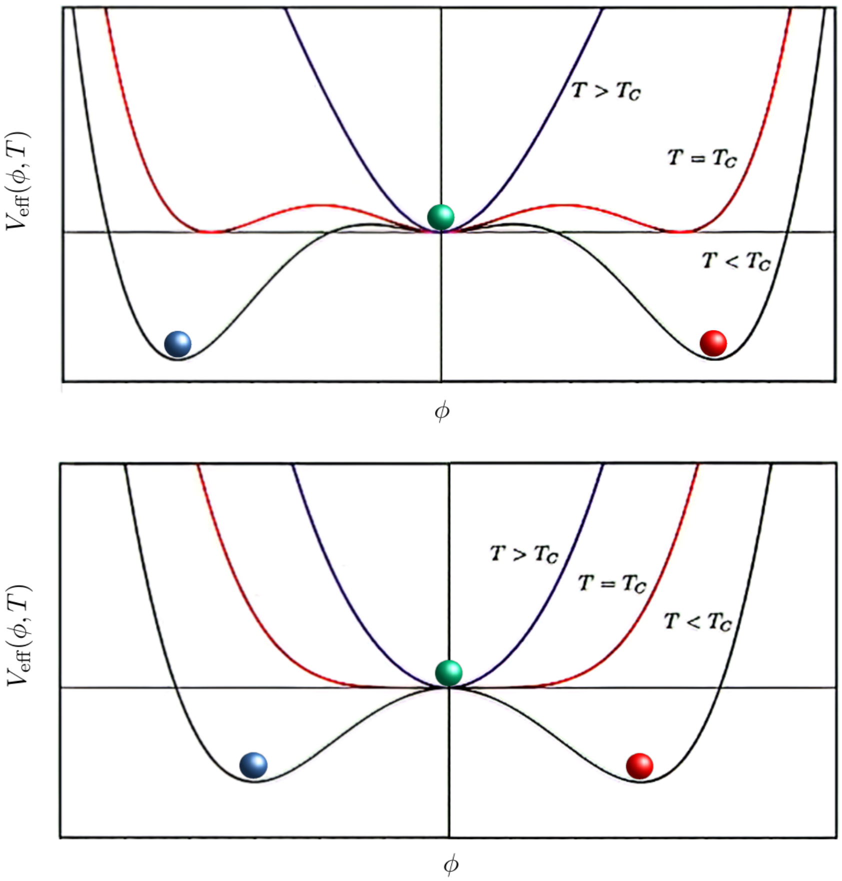

Figure 1.4: Effective potential for a first-order (top panel) and a second-order (bottom panel) phase transition. This figure is adapted from [7].

In a first-order phase transition, the global minimum of the potential at high temperature becomes a local minimum at low temperature. This means that the initial state becomes metastable at the critical temperature. The field can transition from $\phi = 0$ to the global minima either by the influence of an external perturbation or by quantum tunneling. In either case, the phase transition proceeds via the nucleation and growth of bubbles of the true vacua in the false vacuum background (see figure 1.5). It is important to note that ϕ will not pick up the same vacuum value in all bubbles if there is more than one stable phase. As a consequence of the continuity of the field, the coalescence of two bubbles of different vacuum will give rise to the formation of a domain wall defect between the centers of the bubbles. Eventually, the system consists of a network of walls of false vacuum which separates spatial domains filled with different true vacua.

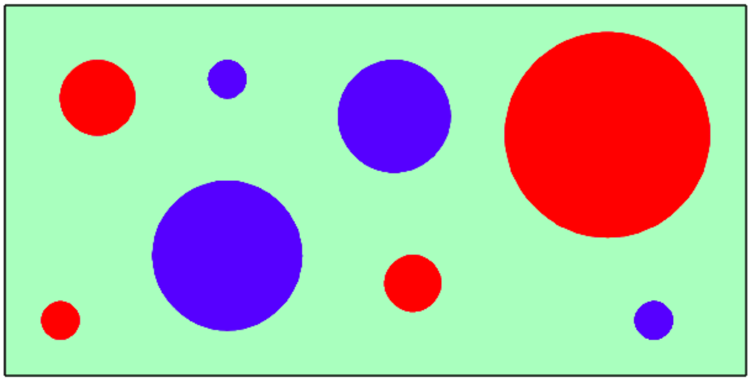

Figure 1.5: Schematic representation of a first-order phase transition (see top panel in figure 1.4). There are two types of bubbles (red and blue), corresponding to different true vacuum values of ϕ. The background is filled with the metastable vacuum $\phi = 0$ (green).

In a second-order phase transition, the minimum of the potential at high temperature becomes a maximum at low temperature, and the field changes continuously from $\phi = 0$ to its vacuum value. For concreteness, let us suppose that the $T < T_C$ potential in the right panel of figure 1.4 is that of the $\lambda\phi^4$ theory, given in equation (1.3). When the temperature drops below T_C, the field has to choose whether it falls to $\phi = -\eta$ or $\phi = +\eta$, depending on the local fluctuations of the field and the field velocity at each point in space. Regions separated by a distance greater than some correlation length ξ will not necessarily fall into the same vacuum, so different regions of space will be filled with different values of ϕ. Continuity of the field requires that $\phi = 0$ at the surfaces that separate different vacuum domains, and a network of domain walls is formed. These are regions of space in which the energy of the old phase has been trapped. We illustrate this in figure 1.6 for the simpler case of a $2 + 1$ dimensional universe. In the case of a complex field in $3 + 1$ dimensions, this mechanism gives rise to cosmic strings, as we shall discuss in the following section.

Estimating the correlation length $\xi(t)$ is relevant because the number density of defects, and hence their contribution to the energy density of the universe, depends on this scale. The causality bound $\xi(t) < d_H(t)$ [8], where $d_H(t)$ is the particle horizon, has to be certainly satisfied, as correlations cannot be established between regions separated by a distance greater than that travelled by light in the full history of the universe. However, $\xi(t)$ strongly depends on the specific dynamics of the phase transition and could be well below this causal upper bound. One can also estimate the correlation length by finding the so-called Ginzburg length [9]. In this case, the basic idea is to obtain the minimum length over which thermal fluctuations are unable to bring the field to another vacuum value. When this happens, the defects effectively “freeze out”, so this scale defines the typical distance between neighbouring defects, and hence their number density. Finally, let us also mention Zurek’s approach [10, 11, 12], in which $\xi\left(t\right)$ is estimated by making the observation that the difference between this scale and the “particle correlation length” (defined as the characteristic scale along which the field changes coherently) should increase proportionally to the temperature-dependent sound speed in the thermal bath.

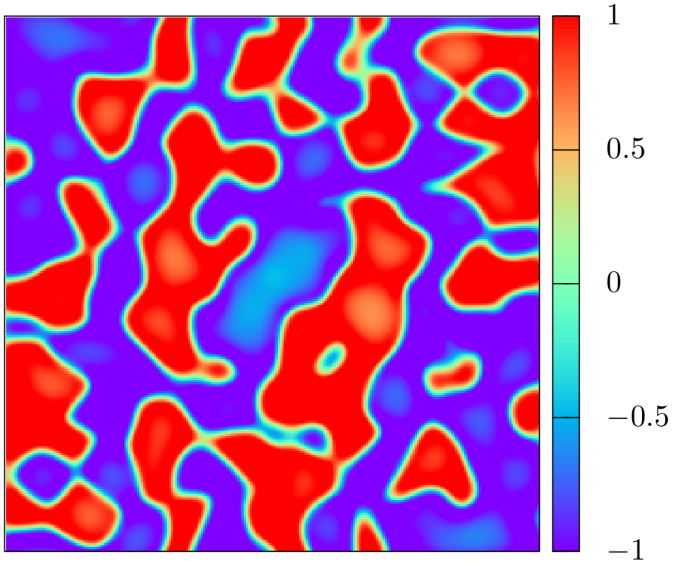

Figure 1.6: A network of $2+1$ dimensional domain walls formed in a second-order phase transition (see bottom panel in figure 1.4). The color palette represents the value of ϕ/η.

Knowing the abundance of topological defects can be a powerful tool to constrain the particle physics models that predict such phase transitions. Consider, for instance, the formation of a network of domain walls in the universe. Since two vacua in different cosmological horizons are uncorrelated, one should expect at least one domain wall per horizon volume. If σ and S are respectively the energy per unit surface and the area of the wall, its energy density today is given by

$$\rho^{0}_{\text{wall}} \sim \frac{\sigma S}{H_0^{-3}} \sim \sigma H_0 \sim \sqrt{\lambda}\eta^3 H_0, \tag{1.8}$$

where H_0 is the current value of the Hubble rate. Therefore, for realistic values of the coupling constant λ and the symmetry breaking scale η, the energy density of a single wall is several orders of magnitude bigger than the critical density today. This is unacceptable for several reasons. The obvious one is that this is in contradiction with the fact that the universe is entering a period of exponential expansion. In fact, the scale factor $a\left(t\right)$ in a domain-wall dominated universe can be shown to be proportional to the cosmic time squared: since the number density of walls scales as a^{-3} and the area as a^2, the energy density of the network is proportional to a^{-1}. Then, from the Friedmann equation $H^2 = (\dot{a}/a)^2 \propto a^{-1}$ it follows that $a \propto t^2$. Even if the walls come to overclose the universe earlier, this time dependence of the scale factor could spoil the processes of large-scale structure formation. In the domain wall domination era we would have $\ddot{a} > 0$, which implies that super-horizon density perturbations are prevented from re-entering the horizon, and thus from starting their growth. The amplification of sub-horizon modes would also be damped by the positive acceleration of the universe. Another problem is that such a domain wall is way more massive than the matter within the present horizon, and it would lead to excessively large fluctuations in the Cosmic Microwave Background. It is therefore clear that the field theory model parameters λ and η can be severely constrained by not contradicting cosmological observations. Another important example where this kind of considerations is made is the widely known monopole problem in the case of magnetic monopoles, which can also overwhelm the energy density of the universe [13].

Some decades ago, interest in topological defects was spurred by their potential role as seeds for cosmic structure formation (see, for instance, [14, 15, 16, 17] for the case of cosmic strings). However, it is currently accepted that gravitational instability around defects is not the mechanism that gave rise to the galaxies and clusters of galaxies we observe today. Indeed, accurate measurements of the temperature fluctuations in the Cosmic Microwave Background favour the theory of inflation as the leading candidate for explaining structure formation in the universe [18, 19, 20, 21]. In the inflationary scenario, the seeds for the growth of cosmic structures originate from the amplification of quantum fluctuations. Simple models of the theory provide an excellent fit to the observed power spectrum [22], thus relegating cosmic strings and other topological defects to play, at most, a secondary role in these processes.

The quasi-exponential expansion of the universe in the inflationary era would have diluted any topological defects formed before that epoch. However, if they are created at sufficiently late times during inflation, this might not be the case. Formation of defects during inflation is possible, for instance, if the field that experiences the symmetry breaking is coupled to the inflaton [23, 24]. A key point for the phase transition to happen is that the effective mass of the symmetry breaking field, which depends on the value of the inflaton, becomes negative at some point. Interestingly, defects could also result from the coupling of the inflaton to the Ricci scalar [25, 26] by similar arguments, and also as a consequence of quantum fluctuations [27, 28, 29] and quantum tunnelling [30]. The interested reader is also referred, for example, to [31] and [32], where the gravitational wave signal from cosmic string networks diluted by inflation is discussed.

1.3 Field theory strings

In this section, we will briefly present the essential features of the two prototypical examples of field theory cosmic strings: global and local strings.

1.3.1 Global strings

Global strings can arise when a global $U(1)$ symmetry is spontaneously broken. A simple example where these objects can be found is the $\lambda\phi^4$ model for a complex scalar field ϕ:

$$S = \int d^4x \left[g^{\mu\nu}\partial_\mu\phi^*\partial_\nu\phi - \frac{\lambda}{4}\left(\phi^*\phi - \eta^2\right)^2 \right] , \tag{1.9}$$

where $g^{\mu\nu}$ is the inverse of the metric tensor. Note that the Lagrangian is invariant under the transformation $\phi\left(t,\vec{x}\right) \to e^{i\alpha}\phi\left(t,\vec{x}\right)$ with constant α. Continuity of the field implies that strings form whenever there is a closed loop in physical space along which the phase of the field changes from 0 to $2\pi n_w$, where n_w is an integer which is often called the winding number. As we shall see in more detail in chapters 3 and 5, there is a static, straight string solution of the equations of motion whose radial part varies from 0 to the vacuum value η, while the angular part is proportional to $n_w\theta$, where θ is the polar angle. A transverse slice of this solution is illustrated in figure 1.7.

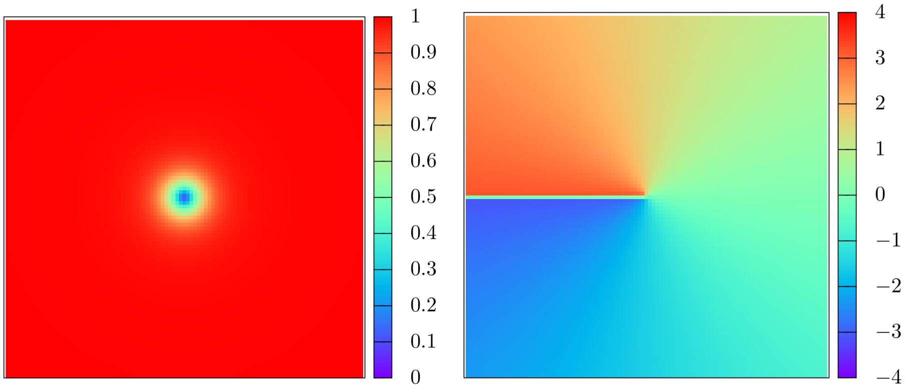

Figure 1.7: Two-dimensional slice of the radial and angular parts (left and right panels, respectively) of the global string solution with unit winding number. The value of the fields is displayed in units of η.

One has to visualize the string as an extension of this configuration along the perpendicular direction. Then, the string is identified with the line where the radial part of the field vanishes. Far from the core, the radial and angular fields can be expanded about their vacuum values in order to obtain the Lagrangian for their corresponding perturbations. This simple exercise reveals that the fluctuations of the radial part are massive, with mass $m = \sqrt{\lambda}\eta$, whereas that of the angular part are massless. Therefore, perturbing the static string configuration can lead to the emission of both massive and massless radiation.

These massless particles, associated with perturbative excitations of the angular part of the complex field in the vacuum, correspond to the so-called axions. Axions are relic pseudo-Goldstone bosons that arise as a consequence of the spontaneous breaking of the Peccei-Quinn symmetry, which is added to the Standard Model in order to solve the strong CP-problem [33]. The Lagrangian in (1.9) leads to the breaking of this symmetry at high energies. Later on, at the QCD crossover at temperature $T \sim 200$ MeV, where quarks and gluons are confined into hadrons, the Mexican-hat potential is distorted by a periodic dependence on the angular (axion) field, which then acquires a mass. The axion turns out to be one of the leading candidates for cold dark matter in the universe, this being the reason why global strings have attracted quite a lot of attention from the astrophysical point of view.

The energy density of the global string is mostly concentrated in a region of size $\delta \sim m^{-1}$. However, there is an important contribution of the winding of the angular field on large distances. This contribution is responsible for the total energy of the string to diverge logarithmically with the radial distance from the core rescaled by the string thickness δ. In practice, the strings are formed in a network and this divergence is cut off by the presence of another string at some distance R. In a realistic cosmological setting, we could easily have $R \sim 10^{50}\delta$, and hence an angular contribution to the energy density of $\ln(R/\delta) \sim 100$. This difference of scales poses a serious problem in computational terms as current field theory simulations can only reach $\ln(R/\delta) \lesssim 7$. As we will point out in the following sections, Nambu-Goto-type simulations can prove very useful in this regard.

1.3.2 Local strings

Here we present the simplest gauge theory in which strings can form: the Abelian-Higgs model [34]. The Lagrangian density is given by

$$\mathcal{L} = \left(D_\mu \phi\right)^* D^\mu \phi - \frac{\lambda}{4}\left(\phi^*\phi - \eta^2\right)^2 - \frac{1}{4q^2} F_{\mu\nu} F^{\mu\nu}, \tag{1.10}$$

where ϕ is a complex scalar field and the covariant derivative D_μ and the field strength tensor $F_{\mu\nu}$ are given by $D_\mu = \partial_\mu - iA_\mu$ and $F_{\mu\nu} = \partial_\mu A_\nu - \partial_\nu A_\mu$, with A_μ a vector field and q a coupling constant. In this case, the Lagrangian is invariant under the gauge or local transformation

$$\phi\left(t, \vec{x}\right) \rightarrow e^{i\alpha(t,\vec{x})}\phi\left(t, \vec{x}\right), \quad A_\mu \rightarrow A_\mu + \partial_\mu \alpha\left(t, \vec{x}\right) , \tag{1.11}$$

where $\alpha\left(t, \vec{x}\right)$ is a real function. With the proper choice of the function $\alpha\left(t, \vec{x}\right)$, $\phi\left(t, \vec{x}\right)$ becomes real after the transformation. One can then exploit the gauge symmetry of the theory with this specific $\alpha\left(t, \vec{x}\right)$ and find the Lagrangian for the perturbations of the real scalar field about the vacuum. The particle spectrum for the broken-symmetry vacuum can be directly read from the resulting Lagrangian and consists of a massive Higgs field with mass $m_s = \sqrt{\lambda}\eta$ and a massive vector field with mass $m_v = \sqrt{2}q\eta$. One can easily verify that the vector field has acquired a mass because of the expansion of the scalar field about a non-zero value. Note also that the breaking of the symmetry does not lead to a massless Goldstone boson as in the previous case. Its absence can be traced to the fact that we have selected a particular gauge, and the corresponding degree of freedom is encoded in the vector field, which is now massive and consequently has three allowed polarization states instead of the two it began with. All this implies that, contrary to what happens for global strings, no massless decay channel is available.

There exists a static, cylindrically symmetric solution of the equations of motion called the Nielsen-Olesen vortex [35]. A crucial difference of this solution with respect to the global one is that the energy density is much more localized around the core of the string, and, indeed, the energy of the configuration does not diverge. Another important difference is that the local string has a quantized magnetic flux.

1.4 Nambu-Goto strings

Nambu-Goto strings are relativistic, line-like objects with no internal structure. The dynamics of these infinitely thin strings is dictated by the so-called Nambu-Goto action [36, 37, 38]. The usual expectation is that a field theory string can be well approximated by a Nambu-Goto string when its radius of curvature is much greater than its thickness[2]. In this case, the string can be regarded as a one-dimensional object, and the spacetime region it sweeps out as it moves (the string worldsheet) can be represented by a two-dimensional surface,

$$X^\alpha = X^\alpha\left(\zeta^a\right) , \tag{1.12}$$

with $a = 0, 1$. In other words, the position 4-vector X^α of the string can be parametrized with two coordinates ζ^0 and ζ^1. The spacetime interval between two nearby points on the worldsheet is

$$ds^2 = g_{\alpha\beta}\partial_a X^\alpha \partial_b X^\beta d\zeta^a d\zeta^b \, , \tag{1.13}$$

where ∂_a denotes differentiation with respect to ζ^a and $g_{\alpha\beta}$ is the four-dimensional metric of the spacetime in which the string is embedded. From (1.13) we identify the worldsheet metric tensor as

$$\gamma_{ab} = g_{\alpha\beta}\partial_a X^\alpha \partial_b X^\beta . \tag{1.14}$$

The Nambu-Goto action is given by

$$S = -\mu \int \sqrt{-\gamma}\, d^2\zeta \, , \tag{1.15}$$

where μ is the energy per unit length of the string and γ is the determinant of the worldsheet metric γ_{ab}. Note that this is the generalization to an extended, one-dimensional object of the relativistic point-like particle action. The equations of motion for the string can be obtained by varying (1.15) with respect to $X^\alpha\left(\zeta^a\right)$:

$$\frac{1}{\sqrt{-\gamma}}\partial_a\left(\sqrt{-\gamma}\gamma^{ab}\partial_b X^\alpha\right) + \Gamma^\alpha_{\beta\lambda}\gamma^{ab}\partial_a X^\beta \partial_b X^\lambda = 0, \tag{1.16}$$

where $\Gamma^\alpha_{\beta\lambda} = \frac{1}{2}g^{\alpha\tau}\left(\partial_\lambda g_{\tau\beta} + \partial_\beta g_{\tau\lambda} - \partial_\tau g_{\beta\lambda}\right)$ are the Christoffel symbols associated to $g_{\alpha\beta}$. In Minkowski spacetime, the Christoffel symbols vanish and we are left with

$$\partial_a\left(\sqrt{-\gamma}\gamma^{ab}\partial_b X^\alpha\right) = 0. \tag{1.17}$$

---

[2] In the case of global strings, this condition may suppress the emission of massive radiation, but not the massless one. This problem is usually solved by supplementing the Nambu-Goto action with a Kalb-Ramond term [39].

On the other hand, the energy-momentum tensor can be obtained by varying the action with respect to $g_{\alpha\beta}$:

$$T^{\alpha\beta}\sqrt{-g} = \mu \int d^2\zeta \sqrt{-\gamma}\gamma^{ab}\partial_a X^\alpha \partial_b X^\beta \, \delta^{(4)}\left(X^\lambda - X^\lambda\left(\zeta^a\right)\right) \,, \tag{1.18}$$

where g denotes the determinant of $g_{\alpha\beta}$.

Equations (1.16) and (1.17) are the equations of motion for the spacetime position coordinates of the string for a general parametrization of the worldsheet. As we will show in the following subsection, these equations take the simple form of the wave equation for a particular parametrization known as the "conformal gauge". In what follows, we will take $g_{\alpha\beta}$ to be the Minkowski metric. For the simplification of the string equations of motion in the case of a general metric, the reader is referred to [38].

1.4.1 Equations of motion in the conformal gauge

The string worldsheet metric γ_{ab} is a 2×2 symmetric tensor, so it has three independent entries. This means that the parametrization of the worldsheet will be completely specified by imposing three gauge conditions. Two of them can be chosen in such a way that the metric takes a conformally flat form, namely,

$$\gamma_{ab} = \sqrt{-\gamma}\eta_{ab}, \quad \gamma^{ab} = \frac{1}{\sqrt{-\gamma}}\eta^{ab}, \tag{1.19}$$

where η_{ab} is the 2-dimensional Minkowski metric. This implies that

$$\gamma_{01} = 0, \quad \gamma_{00} + \gamma_{11} = 0\,. \tag{1.20}$$

Substituting (1.19) into the equation of motion, (1.17), yields

$$\ddot{X}^\alpha - X^{\alpha''} = 0, \tag{1.21}$$

where dots and primes respectively denote derivatives with respect to ζ^0 and ζ^1.

So far, we have imposed the two gauge conditions (1.20). The remaining condition can follow from the association of ζ^0 with the Minkowski time t: $\zeta^0 = t$. Note that this identification is consistent with equation (1.21). Now, let us rename the other worldsheet coordinate as $\zeta^1 = \sigma$, which will label the points along the string. The equation of motion then reads

$$\ddot{\vec{X}} - \vec{X}'' = \vec{0}, \tag{1.22}$$

and the gauge conditions (1.20) reduce to

$$\dot{\vec{X}} \cdot \vec{X}' = 0\,, \tag{1.23}$$

$$\dot{\vec{X}}^{\,2} + \vec{X}'^{2} = 1\,. \tag{1.24}$$

In this guage, the energy-momentum tensor (1.18) is given by

$$T^{\alpha\beta}\left(t, \vec{X}\right) = \mu \int d\sigma \left(\dot{X}^{\alpha}\dot{X}^{\beta} - X^{\alpha\prime}X^{\beta\prime}\right)\delta^{(3)}\left(\vec{X} - \vec{X}\left(t,\sigma\right)\right), \tag{1.25}$$

so the energy of the string is found to be

$$E = \int T^{00} d^3X = \mu \int d\sigma\,. \tag{1.26}$$

Therefore, σ is proportional to the string energy measured from some arbitrary point on the string. Since equation (1.24) tells us that

$$d\sigma = \frac{dl}{\sqrt{1 - \dot{\vec{X}}^{\,2}}}\,, \tag{1.27}$$

where $dl = |d\vec{X}|$, the energy of the string can be written as

$$E = \mu \int \frac{dl}{\sqrt{1 - \dot{\vec{X}}^{\,2}}}\,. \tag{1.28}$$

On the other hand, equation (1.23) implies that the velocity of each point on the string is perpendicular to the tangent vector at that point. Finally, the equation of motion (1.22) rewritten in the local rest frame of an element of string reads $\ddot{\vec{X}} = d^2\vec{X}/dl^2$, because $d\sigma = dl$ in this frame. This implies that the acceleration of this string segment is inversely proportional to its curvature radius. Note also that $\ddot{\vec{X}}$ points to the local center of curvature, and thus a curved string tends to straighten. As a consequence, it develops a velocity and starts to oscillate.

The general solution of the wave equation (1.22) is

$$\vec{X}\,(t,\sigma) = \frac{1}{2}\left[\vec{a}\,(\sigma - t) + \vec{b}\,(\sigma + t)\right], \tag{1.29}$$

and the conditions (1.23) and (1.24) give the constraint

$$|\vec{a}\,'| = |\vec{b}\,'| = 1. \tag{1.30}$$

The functions $\vec{a}$ and $\vec{b}$ are the so-called left and right movers.

Taking the time derivative of (1.29), one can obtain the velocity of the point on the string labelled by σ at time t:

$$\dot{\vec{X}}\,(t,\sigma) = \frac{1}{2}\left[\vec{b}\,'(\sigma + t) - \vec{a}\,'(\sigma - t)\right]. \tag{1.31}$$

On the other hand, the tangent vector at each point is proportional to

$$\vec{X}'\,(t,\sigma) = \frac{1}{2}\left[\vec{a}\,'(\sigma - t) + \vec{b}\,'(\sigma + t)\right]. \tag{1.32}$$

1.4.2 Loops of string

For the case of closed loop solutions, the parameter σ varies in the finite range $0 \leq \sigma < L$, where L is called the invariant length of the loop. This is a conserved quantity, as the total energy of the loop is

$$E = \mu \int_0^L d\sigma = \mu L. \tag{1.33}$$

For a loop, it is evident that the condition $\vec{X}\,(t, \sigma + L) = \vec{X}\,(t,\sigma)$ must be satisfied. This implies that

$$\vec{b}\,(\sigma + L + t) - \vec{b}\,(\sigma + t) = \vec{a}\,(\sigma - t) - \vec{a}\,(\sigma + L - t)\ . \tag{1.34}$$

Consider now the following vector:

$$\vec{\Delta} = \frac{1}{2}\int_0^L d\sigma\left[\vec{b}\,'(\sigma + t) - \vec{a}\,'(\sigma - t)\right]\ . \tag{1.35}$$

In view of equation (1.31), this vector is clearly proportional to the momentum of the loop. Expanding the integrals and making use of (1.34), one is led to

$$\vec{a}\,(\sigma + L - t) = \vec{a}\,(\sigma - t) - \vec{\Delta} \tag{1.36}$$

and

$$\vec{b}\,(\sigma + L + t) = \vec{b}\,(\sigma + t) + \vec{\Delta}. \tag{1.37}$$

In the center-of-mass reference frame of the loop, $\vec{\Delta} = \vec{0}$ and $\vec{a}$ and $\vec{b}$ are periodic functions. In this case, combining equations (1.36) and (1.37) yields

$$\vec{X}\,(t, \sigma) = \vec{X}\,(t + L/2, \sigma + L/2)\,, \tag{1.38}$$

which implies that the loop oscillates in time with period $T = L/2$. A loop that starts out at rest can be easily shown to collapse to a double line at $t = T/2 = L/4$ [40].

Remarkably, it is possible that points on the loop reach momentarily the speed of light. From equations (1.31), (1.32) and (1.30) it follows that

$$|\dot{\vec{X}}|^2 = \frac{1}{2}\,(1 - \cos\Omega) \tag{1.39}$$

and

$$|\vec{X}'|^2 = \frac{1}{2}\,(1 + \cos\Omega) = |\dot{\vec{X}}|^2 + \cos\Omega, \tag{1.40}$$

where Ω is the angle between $\vec{a}'\,(\sigma - t)$ and $\vec{b}'\,(\sigma + t)$. At any time, since $\vec{a}'\,(\sigma - t)$ and $\vec{b}'\,(\sigma + t)$ are unit vectors (see equation (1.30)), these functions of σ can be thought of as curves on the surface of the unit sphere. For a particular $\sigma = \sigma_*$, if at some time $t = t_*$ we have $\Omega = \pi$, that is, if $\vec{a}'\,(\sigma_* - t_*)$ and $\vec{b}'\,(\sigma_* + t_*)$ point exactly to opposite directions, then the velocity of that point σ_* on the loop moves at the speed of light, and the tangent vector vanishes at that point. Such a point is called a cusp.

Other well-known features of string loops are kinks. A kink is a propagating discontinuity in the tangent vector, or in other words, a sharp corner that moves around the loop in one direction. As illustrated in figure 1.8, loops can form when two string collide, in which case they reconnect exchanging partners, or when a string self-intersects. In either case, kinks are formed at the intersection points, and they can propagate in opposite directions to eventually collide. For a loop that has kinks, the vectors $\vec{a}'$ and $\vec{b}'$ are discontinuous functions.

The shape of cusps and kinks is illustrated in figure 1.9. Evidently, the Nambu-Goto approximation is not expected to be accurate in the regions of a field theory string where a cusp forms or two kinks collide. Indeed, the field theory string will self-annihilate and produce bursts of particle radiation at these events (see, for instance, [41, 42, 43, 44]).

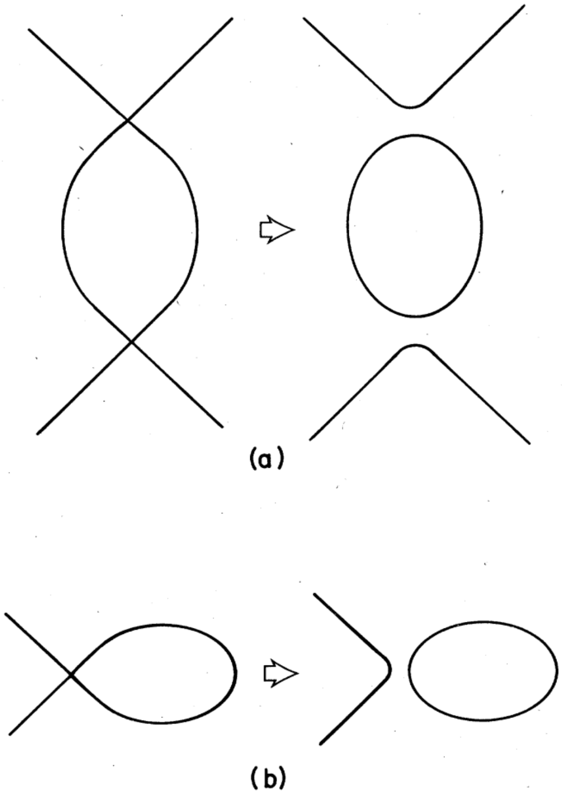

Figure 1.8: Formation of a loop when (a) two strings collide and intersect at two different points or (b) a string self-intersects by curling back on itself. This figure is taken from [45].

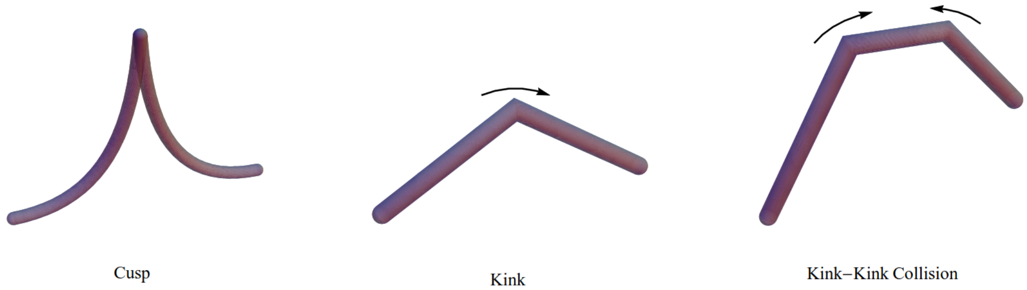

Figure 1.9: Illustartion of a cusp, a kink and the collision of two kinks on a loop. This figure is taken from [43].

1.5 Overview of the tension between field theory and Nambu-Goto simulations of cosmic strings

Numerical simulations of cosmic strings began a long time ago, motivated by the possibility that these objects could serve as the seeds for the inhomogeneities around which cosmic structures could form. In this picture, put forward by Zel'dovich and Vilenkin [14, 15, 16, 17], matter clumps around an oscillating loop of string which has to be sufficiently long-lived. This requires that the main energy loss mechanism is gravitational radiation rather than particle radiation. That such long-lived loops could actually exist was first shown by Kibble and Turok [46, 47], who found a large class of non-self-intersecting loops in the Nambu-Goto approximation.

As we have seen in the previous sections, the spontaneous breaking of a $U(1)$ symmetry leads to the formation of a network of cosmic strings. The study of the gravitational effects and, in general, of the cosmological implications of strings, required the understanding of the statistical properties of the networks. The picture that emerged from the first Nambu-Goto simulations of cosmic strings consists, at formation, of a network of infinite, Brownian strings and a scale-invariant distribution of closed loops [45, 48, 49]. Such a network is illustrated in figure 1.10. By "scale-invariant distribution" we mean that the size distribution of these loops is invariant under a rescaling of the correlation length ξ. In turn, it should be understood that the values taken by the phase of the symmetry breaking field are uncorrelated in points separated by a distance greater than ξ. Regarding the strings, "Brownian" means that the arc length s between two points on the string separated by a distance r scales as $s \propto r^2$. These infinite strings were found to constitute about 80% of the total length of string in the simulations, while the remaining 20% was in the form of loops.

These early investigations seemed to imply that the Nambu-Goto networks evolved towards a scaling regime in which the interstring distance, or the correlation length ξ, is proportional to the horizon size, i.e., $\xi \propto t$. Scaling was also observed later on in field theory simulations of both local and global strings [51, 52, 53], and also in domain wall networks [54, 55, 56]. Such a period of scaling requires an efficient loss of energy from the network, and it is crucial to avoid that the energy density in the strings comes to dominate over radiation in the early universe. The mechanism that allows for a sufficiently fast decay of the energy density of the system of strings is the production of closed loops by intercommutations. The probability associated to this phenomenon was shown to be close to one [57]. Another important consequence of scaling is that the long-term behaviour of the network is insensitive

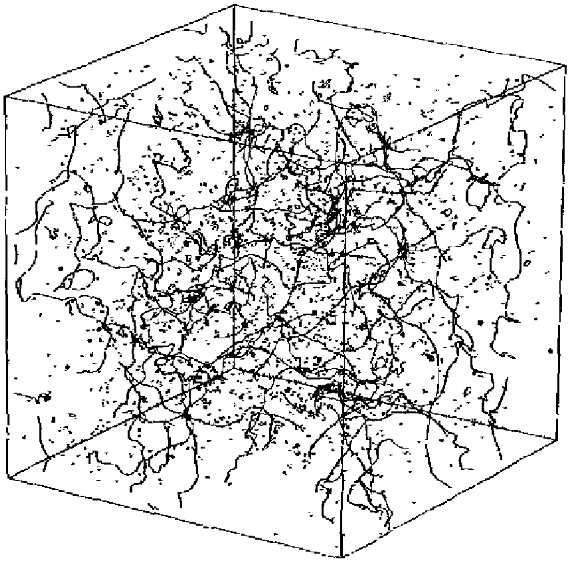

Figure 1.10: A cosmic string network in a Nambu-Goto simulation. This figure is taken from [50].

to the initial conditions that gave rise to it. Moreover, it may allow a cosmological extrapolation of the results obtained in the numerical simulations, which inevitably have a limited dynamic range. It is possible, however, that this computational restriction prevents us from seeing deviations from $\xi \propto t$ at late times (for instance, it has been recently claimed that the proportionality factor could increase logarithmically with time in the case of global strings). The resolution to this conundrum is currently under debate [58, 59, 60, 61, 62, 63, 64].

Subsequent work in the late 90s gave further evidence for scaling, although there were important discrepancies regarding the energy density in strings. In any case, there was no consensus on the physical mechanisms that gave rise to the scaling regime. Bennett and Bouchet [65] noticed that infinite strings were losing significant amounts of energy directly into small loops, as opposed to the standard scenario, where loops were thought to form at larger scales, comparable to the horizon. A possible explanation for that was the presence of short-wavelength structure in the form of kinks that emerged whenever strings crossed. This new picture was also found in later work [66, 67, 68, 69, 70], until Vincent, Hindmarsh and Sakellariadou claimed that the dominant energy loss mechanism of the string networks was direct particle production [71]. Without restrictions on the minimum loop size, loop production occurred at the smallest physical scale, the string width, and the loops would consequently decay into particles shortly after their formation. This claim was backed up by simulations of standing waves in the Abelian-Higgs model [51], but this direct radiation from the strings was later found to be a consequence of an "inaccuarte" choice of initial conditions [72, 73]. In these papers, it was shown that particle radiation was strongly suppressed for long wavelength modes, in agreement with qualitative expectations.

Whether the loops in the scaling regime are mostly produced at the smallest scales or at significant fractions of the horizon size is not clear. The loop component of the networks scales much later than the long-string component. Large-scale Nambu-Goto simulations [74, 75, 76] seemed to suggest that loops produced at the smallest scales (those determined by the scale of the initial conditions) would be more and more scarce at late times, and that the final scaling distribution of loops would be peaked at sizes comparable to the horizon. However, even for the big dynamic range achieved in those simulations, the reported results were still far from that limit.

In the scenario suggested by Nambu-Goto simulations, the scaling regime was thought to be achieved through the production of loops and their subsequent decay into gravitational radiation. However, field theory simulations of the Abelian-Higgs model seemed to indicate that direct particle radiation from strings was the main process that allowed for scaling [77]. While there was evidence for a stable population of non-self-intersecting loops in Nambu-Goto simulations [75], these have never been found in field theory simulations. In the Abelian-Higgs model, a decay channel through scalar and gauge modes of the fields is available, and simulations seem to indicate that loops evaporate within a Hubble time. As a consequence, the number of loops is highly suppressed in field theory simulations and the predicted power in gravitational waves is significantly smaller than in the Nambu-Goto approach [78]. Moreover, the imposition of bounds on the tension μ of cosmic strings (which gives information about the symmetry breaking energy scale η: $\mu \sim \eta^2$) is hampered by this uncertainty, as they are based on the gravitational wave background from loops [79, 80, 81].

The perdurance of cosmic string loops has been recently analyzed in full field theory simulations. In [82], the authors reported that the lifetime τ of Abelian-Higgs loops scaled as $\tau \propto \ell^n$, where ℓ is the initial length of the loop and $n \approx 2$. This law was found to be consistent with episodic particle emission events from kink collisions. However, it was later shown in [83] that this behaviour only applied for artificially created loops. Indeed, the loops in [82] were designed by colliding four straight strings wrapping the simulation box[3]. In [83], the authors showed that loops that chop off naturally from a local string network decay in a much shorter time scale: $\tau \propto \ell$.

---

[3] Following this scheme, the result for global string loops was found to be $\tau \sim \ell$ [84].

Why do loops disappear in Abelian-Higgs simulations? Nobody disagrees on the fact that they can evaporate by radiating particles, but this should only happen when regions of the loop are curved to scales comparable to the string thickness, or when self-intersections take place. If the dynamic range of the simulations is not big enough, a loop that repeatedly self-intersects is doomed to evaporate completely, as the radius of curvature of its descendants will end up being of the same order of magnitude as the width of the string. These self-intersections do happen in field theory simulations, and, indeed, non-self-intersecting loops have not been found so far. This is the main discrepancy between Abelian-Higgs and Nambu-Goto simulations of cosmic strings. Loops completely disappear in field theory simulations, while in the Nambu-Goto case one finds a population of non-self-intersecting loops. Why are the field theory counterparts of the latter not found? Are the conditions that lead to particle radiation and reiterated self-intersection unavoidable in field theory simulations?

In table 1.2 we summarize the main differences between Abelian-Higgs and Nambu-Goto simulations.

Abelian-Higgs simulations	**Nambu-Goto simulations**
Account for field theory effects	Disregard field backreaction
Small dynamic range	Big dynamic range
Network loses energy by particle radiation	Network loses energy by loop production
Absence of non-self-intersecting loops	Presence of non-self-intersecting loops
Low gravitational wave signal	High gravitational wave signal

Table 1.2: Summary of the discrepancies between Abelian-Higgs and Nambu-Goto simulations of cosmic strings.

The problem of small dynamic range in field theory simulations could be responsible for the absence of non-self-intersecting loops. In lattice field theory simulations it is important to have a high resolution in the core of the strings in order to evolve them correctly and to be sure that we are not spoiling or missing physical processes that could take place at that scale. Therefore, the lattice spacing Δx should be smaller than the string thickness δ: $\Delta x < \delta$. However, at the same time, we need a simulation box with sides of length L much longer than δ: $L >> \delta$. Thus, L has to be substantially bigger than Δx (at least $L \gtrsim 400\Delta x$, say), and the total number of lattice points that we need, which is of the order of $(L/\Delta x)^3$, is huge. This requires long computation times, and implementing code parallelization is almost mandatory for practical purposes. This computational problem limits our choice of box size roughly to $L \sim 100\delta$, so loops obtained in field theory simulations have lengths not bigger than a few hundred times the string thickness. In Nambu-Goto simulations, since the strings are assumed to be infinitely thin, these computational limitations are absent and loops can be much longer than the field theory ones. The great majority of the Nambu-Goto loops produce daughter loops as a consequence of self-intersections, which in turn give rise to new generations of smaller loops, again by self-intersections. This cascade process ends up in a generation of non-self-intersecting loops. In field theory simulations, this process starts way below. Consequently, the early generations of daughter loops may very easily have radius of curvature comparable to their thickness, and this will make them radiate until they completely disappear.

A key assumption to justify the use of the Nambu-Goto approximation is that the strings do not radiate. For local strings, this is indeed the case as long as the radius of curvature is much greater than the thickness of the string. This behaviour can be attributed to the fact that the radiated particles are massive, and one has to curve the string to frequencies comparable to that mass scale in order to generate perturbations that can propagate in the vacuum. However, the situation is different for global strings because of the presence of the massless Goldstone boson in the particle spectrum. As previously anticipated, this particle will be radiated even for smooth string configurations, so the Nambu-Goto action has to be supplemented with a Kalb-Ramond term that accounts for the coupling of the string worldsheet to the massless field. Taking into account these considerations, the tension between field theory and Nambu-Goto simulations of local strings, for which there is a mass gap, is even more puzzling.

What is more, field theory simulations of individual local strings have shown conclusively that these strings follow almost exactly the Nambu-Goto dynamics [85, 86]. This prompted some authors to suggest that field theory strings in networks may behave differently due to the influence of the internal modes of these objects [87, 83]. Strings may be endowed with a significant amount of extra energy in the form of localized excitations, either as a consequence of their formation process at a phase transition or during cosmological evolution. This extra energy could potentially alter the equation of state of the strings, and thus modify their expected (Nambu-Goto) dynamics. In particular, the scarcity of loops in field theory simulations could be a consequence of this fact. This is the possibility we investigate in depth in this thesis.

1.6 Structure of the thesis

This thesis is structured as follows:

- Chapter 2: we study $1+1$ dimensional kinks to exemplify that topological defects can be formed with a significant amount of energy in their cores. We also show that this extra energy remains stored in the defects for very long periods of time.
- Chapter 3: we compare in detail the field theory and Nambu-Goto trajectories for $2+1$ dimensional domain walls, and investigate the influence of internal modes in the dynamics of these defects. In particular, we find a self-regulated resonance phenomenon due to the non-linear interaction of the modes.
- Chapter 4: we extend the analysis made in chapter 2 to global vortices in $2+1$ dimensions.
- Chapter 5: we study the resonant effects found in chapter 3 in the case of $3+1$ dimensional global strings.
- Chapter 6: we compare the motion of Abelian-Higgs loops directly extracted from field theory simulations with the predictions of the Nambu-Goto approximation.
- Chapter 7: we end up with a summary of the main conclusions and possible research directions for the future.

Chapter 2

Internal excitations of $1 + 1$ dimensional kinks

Many solitonic configurations in field theory have localized bound states in their spectrum of linear perturbations. This opens up the possibility of having long-lived excitations of these solitons that could affect their dynamics. We start the study of these bound states and their influence in the simple configuration of the $\lambda\phi^4$ kink in $1 + 1$ dimensions. This solution has been already introduced in the previous chapter (see section 1.2.1). In this second chapter, we show that the kink has a single bound state and study its slow decay rate in flat space. We then simulate, in an expanding background, the formation of these defects in a cosmological phase transition to find that they get formed with a 20% excess of energy with respect to their lowest energy configuration. We also explore the kink solution interacting with a thermal bath and extract the amplitude of the bound state as a function of temperature. We note that the energy of the excitation increases with temperature, but it saturates around 20% of the mass of the kink at high temperatures. Finally, we argue that this extra energy may have important consequences in the subsequent evolution of defects.

2.1 Introduction

Solitonic solutions of non-linear field theories are present in many areas of physics, from condensed matter [88] to particle physics [89], string theory [90] or cosmology [38]. As discussed in chapter 1, these solutions can be obtained by considering the lowest energy configurations of the fields involved with a particular boundary condition at infinity which guarantees their stability. These objects have been extensively studied in the literature in the past decades. In $3 + 1$ dimensions, one can find solitonic objects of different dimensionality like domain walls [8], cosmic strings [35] or monopoles [91, 92][1].

Solitons are not the only long-lived localized structures that can exist in non-linear field theories. Many of the same models that have solitons also support lump-like field arrangements that could have extremely long lifetimes. One of the most prominent examples of this type of objects are oscillons[2] [93, 94, 95, 96]. These configurations are approximate solutions of the equations of motion about the vacuum, and present a very slow radiating process that allows the energy to leak to infinity by means of small amplitude oscillations of the field.

In some field theories, it is natural to expect the existence of excited soliton solutions whose properties resemble in many cases the oscillon-like objects. In fact, we will show that the interactions between solitons and oscillons would give rise to these excited states, which decay with a characteristically long time scale. These localized excitations could become relevant for the dynamics of the solitons, specially if they last for long periods of time. In particular, as pointed out in the previous chapter, bound states on cosmic strings could be responsible for significant deviations from the Nambu-Goto dynamics.

In this chapter, we take a step back and study the excited states of $\lambda\phi^4$ kinks in $1+1$ dimensions, and we will argue that this simple field theory has many of the properties that are important to understand the cosmic string scenario. This model possesses solitonic solutions that can be in an excited state. In the following sections, we will show that these excited states have a very long lifetime that can affect the long term evolution of the solitons. However, in order to understand the impact of these perturbation modes, one should first show that they can be dynamically excited. We start this investigation by looking at the possible excitation of the kinks through their cosmological formation in lattice field theory simulations.

The organization of this chapter is the following. In section 2.2, we complete the introduction of the kink solution presented in chapter 1. In section 2.3, we describe the spectrum of excitations of this soliton and their physical interpretation. In section 2.4, we comment on the possible existence of breather solutions in the $\lambda\phi^4$ theory that we are studying. We study numerically the non-linear decay of the bound state in flat spacetime in section 2.5, and we comment on the kink solutions in an expanding universe in section 2.6. In section

---

[1] One could also consider instantons and textures as part of this family of solutions. However, we do not have much to add about this type of objects in this thesis.

[2] Depending on the theory, they are also called quasi-breathers or pulsons.

2.7, we simulate the formation of these kinks in a phase transition in an expanding universe. We can then obtain the average level of excitation of the kinks at formation. In section 2.8, we also explore the process of excitation when the kinks are in contact with a thermal bath and look at the dependence of the excitation with the background temperature. We conclude in section 2.9 with a brief discussion of the possible impact of these results.

The animations corresponding to some of the simulations described in the following sections can be found at `http://tp.lc.ehu.es/earlyuniverse/kink-simulations/`.

2.2 The kink solution in $\lambda\phi^4$

The action of the $\lambda\phi^4$ model in $1+1$ dimensions is given by (1.2):

$$S = \int d^2x \left[\frac{1}{2}\eta^{\mu\nu}\partial_\mu\phi\partial_\nu\phi - \frac{\lambda}{4}\left(\phi^2-\eta^2\right)^2\right], \tag{2.1}$$

The dimensions of the scalar field and the parameters are the following: $[\phi] = [\eta] = E^0$ (dimensionless), $[\lambda] = E^2$.

As shown in equation (1.3) and figure 1.1 in chapter 1, the potential energy density $V(\phi)$ in this model has two degenerate minima at $\phi = \pm\eta$, and the fluctuations of the field around these minima are characterized by perturbative excitations of mass $m = \sqrt{2\lambda}\eta$.

Apart from these excitations, it is also well known that this theory possesses non-perturbative states that interpolate between both vacua. For example, the kink solution interpolates between the $\phi = -\eta$ and the $\phi = +\eta$ minima as x grows. Due to translational invariance, the position of the kink is a free parameter. The solution centered at the point x_0 is given by [1]

$$\phi_{k,x_0}(x) = \eta \tanh\left[\sqrt{\frac{\lambda}{2}}\eta(x-x_0)\right] = \eta\tanh\left[\frac{m}{2}(x-x_0)\right] . \tag{2.2}$$

We will be mostly dealing with the kink centered at the origin ($x_0 = 0$): $\phi_k \equiv \phi_{k,0}$.

As mentioned in the introductory chapter, these solitonic solutions have an energy density which is exponentially localized around their center, and one can estimate their width to be $\delta_k \sim \sqrt{\frac{2}{\lambda}}\eta^{-1}$. The total energy of the kink configuration can be found by integrating its energy density (1.6):

$$M_k = \frac{2\sqrt{2\lambda}}{3}\eta^3 \quad . \tag{2.3}$$

One can also find the solutions that interpolate between these vacua with the opposite boundary conditions at infinity: the antikink solutions. We will refer to both kinks and antikinks generically as kinks, unless the distinction is relevant.

Many different aspects of kink and antikinks and their interactions have been extensively studied in the literature over the years using a combination of analytic and numerical techniques [97]. One interesting point about the $\lambda\phi^4$ model is its lack of integrability, which makes it quite different in many respects to its integrable counterpart, the Sine-Gordon (SG) model [98]. One can see the difference between these models in the interaction between a kink and an antikink. On the one hand, in the SG model, the two solitons scatter off each other without any radiation. On the other hand, in the $\lambda\phi^4$ model, one has a complicated outcome of the collision that depends on the initial state [99, 100, 101]. In the latter case, kinks get excited and radiate upon their interactions.

Another important difference between these models is the existence of breather solutions. In the SG case, one can find analytic solutions describing a bound state of kink and antikink oscillating around their center of mass [1]. In the $\lambda\phi^4$ model, one can show that there is no stable configuration of this form [102]. This does not mean, however, that there are not long lasting configurations of this type. In fact, one can easily create these localized oscillating states that slowly decay by emitting radiation. Furthermore, their interpretation as kink-antikink bound states was also given after some of the first numerical experiments performed in this model [93]. This type of solutions will be further discussed later on in this chapter in relation to the kink excitations.

2.3 The spectrum of excitations around the kink

Let us characterize the small perturbations about the static kink solution. We will assume the field to be separated into the kink solution plus perturbations as

$$\phi(t,x) = \phi_k(x) + \psi(t,x)\,, \tag{2.4}$$

where $|\psi| << \eta$. The linearized equation of motion for these perturbations becomes

$$\ddot{\psi} - \psi'' + \lambda\left[3\phi_k^2(x) - \eta^2\right]\psi = 0\ , \tag{2.5}$$

where the dots and primes denote derivatives with respect to time and space, respectively. Taking an oscillatory ansatz for the perturbations of the form $\psi(t,x) \propto e^{-i\omega t} f(x)$, the equation for the transverse profile of the perturbations has the form of a Schrödinger-like equation:

$$- f''(x) + U(x) f(x) = \omega^2 f(x) \ , \tag{2.6}$$

with effective potential

$$U(x) = \lambda \left[3\phi_k^2(x) - \eta^2 \right] \ . \tag{2.7}$$

This turns out to be a completely solvable potential (see [103]). Its spectrum is composed of two discrete modes and a continuum of scattering states [1]. The two discrete modes are

$$f_0(x) = \text{sech}^2\left(\frac{mx}{2}\right) \qquad \text{with} \qquad \omega_0 = 0 \ , \tag{2.8}$$

and

$$f_1(x) = \sinh\left(\frac{mx}{2}\right) \ \text{sech}^2\left(\frac{mx}{2}\right) \qquad \text{with} \qquad \omega_1 = \frac{\sqrt{3}}{2} m \ , \tag{2.9}$$

and the continuum of scattering states has a functional form given by

$$f_k(x) = e^{ikx} \left[3\tanh^2\left(\frac{mx}{2}\right) - 1 - \frac{4k^2}{m^2} - i \ \frac{6k}{m} \ \tanh\left(\frac{mx}{2}\right) \right] \ , \tag{2.10}$$

where $\omega_k^2 = k^2 + m^2$. Thus, their frequencies are in the range $\omega_k \in (m, \infty)$. These functions become the plane wave solutions for asymptotically large values of x. These plane waves are the ones associated with the continuum of perturbative fluctuations around the vacuum, the asymptotic particle states.

The physical interpretation of the two discrete modes (plotted in figure 2.1) is straightforward. The zero mode describes small rigid perturbations of the position of the soliton itself. One can see this by computing the change of the field distribution due to a small shift in the kink position, namely,

$$\phi_k(x + \delta x) \approx \phi_k(x) + \frac{d\phi_k(x)}{dx} \delta x \ , \tag{2.11}$$

and noticing that

$$\frac{d\phi_k(x)}{dx} \delta x \propto \text{sech}^2\left(\frac{mx}{2}\right) = f_0(x) \ . \tag{2.12}$$

The other discrete state modifies the width of the kink. One can also build some intuition for the spatial profile of this mode by performing a small variation Δ of the thickness of the kink solution to get

$$\phi_k\left(\frac{x}{1+\Delta}\right) \approx \phi_k(x) - x\frac{d\phi_k(x)}{dx}\Delta \approx \phi_k(x) - \frac{m\eta}{2} x\,\mathrm{sech}^2\left(\frac{mx}{2}\right)\Delta\,. \tag{2.13}$$

Direct comparison between this last expression and the bound state $f_1(x)$, given in (2.9), shows that they have a very similar profile. This suggests the name "shape mode"[3] for this bound state. Throughout this chapter, we will refer to this state as "shape mode", "bound state" or "internal mode".

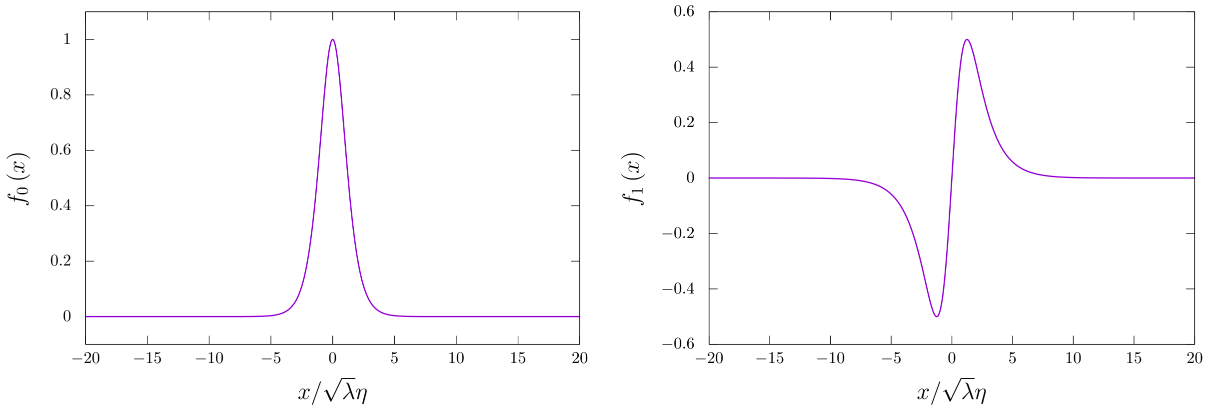

Figure 2.1: Zero mode (left panel) and shape mode (right panel) perturbations as given in equations (2.8) and (2.9), respectively.

2.4 Breather solutions

As previously mentioned, this model has other type of interesting configurations with an extraordinarily long lifetime, first discovered by numerical experiments a long time ago in [93]. They describe the oscillation of the kink and the antikink around each other and they share many of the properties of the SG breather exact solutions [1]. This motivated the pursue of approximate expressions for these type of time-dependent configurations, as well as their numerical exploration by several groups [100]. In [98], the authors gave an approximate ansatz for these objects as a perturbative expansion in the (small) amplitude. However, it was shown in [102] that all these attempts to construct these periodic, localized

---

[3] A collective coordinate approach can also be used to single out the translation and the width degrees of freedom. It is interesting to see that this approach yields a spectrum quite similar to the linear field theory calculation (see, for example, [104]).

solutions were flawed by the presence of a radiating tail[4]. This implied that all these oscillating solutions had a finite lifetime, although in some cases they could stay around for a long time, possibly long enough to play a significant role in the dynamics. One can think of these configurations as the $1+1$ dimensional version of the pulson [94, 95] or the oscillon [96] that appear in many higher dimensional field theories.

Since we will later on encounter these objects in the course of our simulations, it is useful to describe them now. One can find the equation of motion for perturbations $\xi\left(t,x\right)$ about the vacuum by substituting $\phi\left(t,x\right)=\eta+\xi\left(t,x\right)$ into (1.4). The result is

$$\ddot{\xi}-\xi''+2\lambda\eta^2\xi+3\lambda\eta\xi^2+\lambda\xi^3=0\,. \tag{2.14}$$

Following [98], an approximate solution of this equation is

$$\xi_B\left(t,x\right)=\frac{2\eta\epsilon}{\sqrt{3}}\operatorname{sech}\left(\omega_B\epsilon x\right)\sin\left(\omega_B t\right)-\epsilon^2\operatorname{sech}^2\left(\omega_B\epsilon x\right)\left[1+\frac{1}{3}\cos\left(2\omega_B t\right)\right]\,, \tag{2.15}$$

where

$$\epsilon=\sqrt{\frac{m}{2\pi}t-1} \tag{2.16}$$

is taken to be small and

$$\omega_B=\frac{m}{\sqrt{1+\epsilon^2}}\,. \tag{2.17}$$

It is clear from this relation that these solutions always oscillate with frequency lower than the mass of the perturbative excitations in the vacuum: $\omega_B<m$. This means that, at the lowest order, these excitations are not able to emit radiation (see the discussion on scattering states in the previous section). However, it is clear that $O(\epsilon^2)$ terms or higher could make them decay by coupling these solutions to the scattering modes. This is why these configurations have such a slow decay rate and last for such a long time.

It is interesting to note that, when $\epsilon\approx1/\sqrt{3}$, the term linear in ϵ in equation (2.15) multiplied by the kink solution $\phi_k\left(x\right)$ becomes proportional to the shape mode, $f_1\left(x\right)$. Moreover, it oscillates momentarily at the frequency of the bound state: $\omega_B=\omega_1=\sqrt{3}m/2$. This suggests that the internal mode of the kink might be regarded as a breather trapped in the core of the soliton. The relation between these breathers and internal modes has been recently explored in the literature [105].

---

[4] This is why many people refer to these configurations as quasi-breathers to remark their lack of true periodicity.

2.5 Numerical investigations in Minkowski spacetime

2.5.1 Dimensionless variables

Since we will make extensive use of numerical simulations throughout the chapter, it will be convenient to reformulate our theory in terms of the following dimensionless variables:

$$\tilde{\phi} = \frac{\phi}{\eta} \qquad \tilde{x} = \sqrt{\lambda}\eta x = \frac{m}{\sqrt{2}}x \qquad \tilde{t} = \sqrt{\lambda}\eta t = \frac{m}{\sqrt{2}}t \quad . \tag{2.18}$$

With these redefinitions, the action becomes

$$S = \eta^2 \int d^2\tilde{x} \, \left[\frac{1}{2}\partial_\mu\tilde{\phi} \, \partial^\mu\tilde{\phi} - \frac{1}{4}\left(\tilde{\phi}^2 - 1\right)^2\right] , \tag{2.19}$$

where the partial derivatives are now with respect to the dimensionless variables. The equation of motion in terms of the rescaled quantities is free of parameters:

$$\ddot{\tilde{\phi}} - \tilde{\phi}'' - \tilde{\phi} + \tilde{\phi}^3 = 0 \ . \tag{2.20}$$

Note that, in these units, the mass of perturbative excitations about the vacua is $\tilde{m} = \sqrt{2}$, and, for example, the frequency of the shape mode is $\tilde{\omega}_1 = \sqrt{\frac{3}{2}}$. The dimensionless period for the shape mode is then $\tilde{P} = 2\pi/\tilde{\omega}_1 \approx 5.1302$, which will be used as a unit of time in most of the subsequent plots. In the rest of the chapter, we will only work with dimensionless variables unless otherwise specified. However, for simplicity of the notation, we will drop the tildes over them.

The solution of the equation of motion (2.20) will describe the evolution of the physical system in any point of the two-dimensional space of field theories parametrized by η and λ. Note that, even though the factor η^2 is absent from the dimensionless classical equations of motion, it appears as an overall coefficient in the action, and, therefore, it does have implications at the quantum level[5]. This will be of importance in sections 2.7 and 2.8.

2.5.2 Extracting the amplitude of the shape mode

In the following sections, we will describe different lattice simulations that we have performed to understand the level of excitation that the kink solutions can acquire. Therefore,

---

[5] In fact, η plays the role of the inverse of a coupling constant, so the weak coupling regime corresponds to the $\eta >> 1$ limit. One can see this by looking at the ratio of the soliton and elementary excitation masses, namely, $M_k/m \sim \eta^2$.

it is paramount for us to be able to quantify this in a precise way. We do this by computing the amplitude of the shape mode of the kink directly from the simulation data.

We first note that the solutions to the Schrödinger-like equation for the linear perturbations (2.6) constitute an orthonormal basis. Thus, the general expansion for a linear perturbation around the kink can be written in our dimensionless scheme as

$$\delta(t,x) = \hat{A}_0 \bar{f}_0(x) + \hat{A}_1 \bar{f}_1(x)\cos(\omega_1 t) + \int \mathrm{d}k \hat{A}_k Re[\bar{f}_k(x) e^{-i\omega_k t}] \ , \tag{2.21}$$

where we have denoted by $\bar{f}_i(x)$ the normalized mode functions. For instance, the dimensionless, normalized shape mode function is given by

$$\bar{f}_1(x) = \frac{\sqrt{3\sqrt{2}}}{2} \sinh\left(\frac{x}{\sqrt{2}}\right) \operatorname{sech}^2\left(\frac{x}{\sqrt{2}}\right) \ . \tag{2.22}$$

However, since the model is non-linear, the interaction between different modes will make the $\hat{A}_i$ coefficients above time-dependent:

$$\begin{aligned} \delta(t,x) &= \hat{A}_0(t) \bar{f}_0(x) + \hat{A}_1(t) \bar{f}_1(x)\cos(\omega_1 t) + \int \mathrm{d}k \hat{A}_k(t) Re[\bar{f}_k(x) e^{-i\omega_k t}] = \\ &= A_0(t)\bar{f}_0(x) + A_1(t)\bar{f}_1(x) + f_r(t,x) \, , \end{aligned} \tag{2.23}$$

where, in the last line, we have absorbed all the time dependence into the $A_i(t)$ and we have defined the integral carrying the information for the radiation as f_r.

To extract the values of A_i (in particular, $A_1(t)$) given a configuration $\phi(t,x)$ consisting of a kink plus excitation, we first obtain the point x_0 where the field ϕ goes through zero, and define that as the center of the kink. We then calculate the perturbations around the kink as

$$\phi_{\text{pert}}(t,x) = \phi(t,x) - \phi_{k,x_0}(t,x) \tag{2.24}$$

and finally project the perturbations over the shape mode by computing

$$A_1(t) = \int_{-L/2}^{L/2} dx \, \phi_{\text{pert}}(t,x) \ \bar{f}_1(x - x_0) \ , \tag{2.25}$$

where L is the size of the simulation box. This amplitude is the quantity that we will follow during the evolution of the kink in different situations and that we will compare with analytic predictions in the subsequent sections.

The energy stored in the shape mode can be easily found by substituting the field configuration $\phi(t,x) = \phi_k(x) + A_1(t)\bar{f}_1(x)$ into the 00 component of the energy-momentum tensor of the scalar field, which is given by

$$T_{\mu\nu} = \partial_\mu\phi\partial_\nu\phi - \eta_{\mu\nu}\left[\frac{1}{2}\eta^{\alpha\beta}\partial_\alpha\phi\partial_\beta\phi - V(\phi)\right]. \tag{2.26}$$

At the linear level, we have $A_1(t) \approx \hat{A}\cos(\omega_1 t)$, and the energy of the perturbation can be shown to be

$$E_1 \approx \frac{3}{4}\hat{A}^2 . \tag{2.27}$$

2.5.3 Some comments on computational limitations

Throughout this work, we have solved the equation of motion (2.20) in a lattice. The details of its implementation can be found in appendix A, but here we would like to emphasize a few points that will become important in the rest of the chapter. Since we are dealing with a $1+1$ dimensional lattice, we can use a large array of points in the spatial direction without too much computational cost. Moreover, we have written the code in a parallelized fashion so we can use many nodes to implement the evolution of a large volume. The combination of these two facts has allowed us to explore a considerable large volume in our simulations while still being able to faithfully represent the dynamics of the fields.

This will become more advantageous later on in this chapter, since some of our simulations will be performed in an expanding background. In that situation, there is a well-known problem: the comoving size of the solitons shrinks with time. This means that, by the end of the simulation, one could have too small a number of comoving lattice points in the relevant central region of the kink. That is why the use of a large number of points, and a parallel code, are helpful to make sure that our final configurations had at least 20 points covering the important central region where the bound state has its support.

A somewhat popular way to deal with this issue is the so-called "fat string algorithm" [54], where the equations of motion are modified to change the rate of contraction of the soliton width in comoving coordinates. This allows the possibility to track down the position of the solitons without introducing more points in the lattice. However, this method affects, by construction, the physical width of the soliton in the simulation. This will clearly distort the level of excitation of the shape mode in an artificial way, and hence we refrain from using such algorithms here.

It is also worth emphazising that we use absorbing boundary conditions [106] in our simulations. As their name indicates, these conditions work in such a way that they mimic the absorption of waves by the boundary. As we will shortly see, we will need to simulate the system for times much, much longer than the light-crossing time of the box. This poses a numerical problem since we do not want the radiation energy to bounce back from the edge of the simulation. This is a particularly important concern in this case because in one spatial dimension there will not be any dilution of the radiation. Since we will be mostly dealing with the frequencies of the radiation coming from the shape mode, we have tuned these boundary conditions in such a way that they will be most effective at those specific frequencies (see the discussion in appendix A).

2.5.4 Lifetime of the excitation

Our starting point is a detailed study of the shape mode excitation of the kink and its decay. In order to do that, we initialize our $1+1$ dimensional lattice field with a kink at the center of the box and we add to it a small perturbation of the form of the linear shape mode described earlier:

$$\phi(t=0,x) = \phi_k(x) + A(0) \times \bar{f}_1(x)\,. \tag{2.28}$$

We are taking a small amplitude, $A(0) < 1$, and we do not give the field any initial velocity. Following the discussion on linear modes given earlier, one would think that this configuration should stay oscillating without dissipation. The reason for this is that the value of its frequency is smaller than the ones that are allowed to propagate outside of the kink towards infinity. However, the full system is non-linear, so the amplitude of this bound state is expected to decrease over time by emitting radiation at a small rate.

At the lowest order, the non-linear terms will produce a radiation field with a frequency which doubles that of the bound state and a quadratically suppressed amplitude. This clearly indicates that the lifetime of these perturbations will be much, much longer than the typical scale of the problem, i.e., the light-crossing time of the width of the soliton. Actually, it is likely to be a much longer time than the light-crossing time of the simulation box as well. This is why we use the aforementioned absorbing boundary conditions (see appendix A).

The problem of studying the decay of a small fluctuation like the one we just presented has been analyzed by Manton and Merabet [107] using analytical techniques. Their conclusion was that the amplitude of the shape mode should decrease with time following the expression[6]

$$\frac{3}{4}\frac{d\hat{A}^2}{dt} = -0.0112909\ \hat{A}^4\,, \tag{2.29}$$

which means that the amplitude should have the following time dependence:

$$\hat{A}^{-2}(t) = \hat{A}^{-2}(0) + 0.0150546\ t\ . \tag{2.30}$$

Using the results in [107], we can also obtain the predicted form of the radiation field to be

$$f_r\,(x,t) = \frac{3\sqrt{3}\,\pi\hat{A}^2}{8\sinh\left(\pi\sqrt{2}\right)}\cos\left[2\sqrt{\frac{3}{2}}\,t - 2x - \arctan\left(\sqrt{2}\right)\right]\ . \tag{2.31}$$

We have run several simulations starting with different values of the parameter $A(0)$ in order to check the accuracy of these theoretical expectations. In each case, we extracted the value of the amplitude from the simulation by finding the perturbations around the kink and then projecting them over the shape mode (see equation (2.25)).

Our simulations demonstrate that the analytic predictions work perfectly in the case of a small initial amplitude for the bound state. In figure 2.2 we show the comparison between the numerically time-dependent amplitude $A(t)$ extracted using equation (2.25) and the analytic prediction for $\hat{A}(t)$ (2.30). Remember that $A(t)$ carries information about the oscillatory part of the amplitude, whereas $\hat{A}(t)$ follows the envelope created by the maxima of the oscillations. Note that we have evolved this numerical computation for 2×10^5 times the period of the oscillation of the bound state.

We also show in figure 2.3 a snapshot of the perturbation field around the kink, as defined in equation (2.24). The central region can clearly be identified as the waveform of the shape mode (equation (2.9)), while the radiative small contribution far from the core is almost exactly a wave of twice the frequency of the shape mode, in accordance with equation (2.31).

---

[6] We give in appendix C a derivation of this expression following the calculations in [107] and adapting them to our current notation.

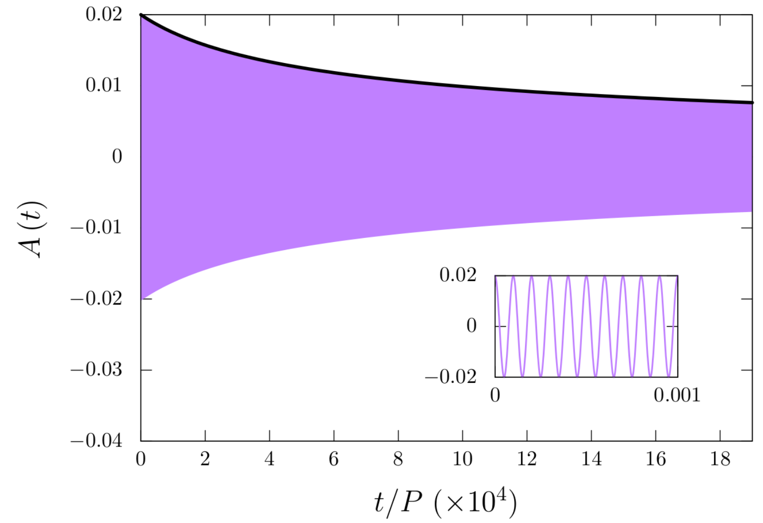

Figure 2.2: Amplitude of the shape mode $A(t)$ as a function of time (displayed as number of periods or oscillations). The black curve corresponds to the analytical second order approximation to $\hat{A}(t)$, namely, equation (2.30) with $A(0) = \hat{A}(0) = 0.02$. Also shown is a zoom of the first oscillations of the amplitude of the internal mode.

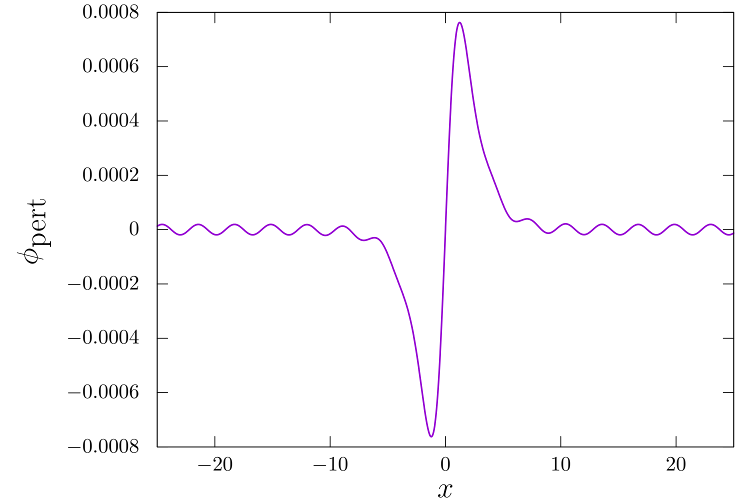

Figure 2.3: Snapshot of the perturbation ϕ_{pert} around the kink after several oscillations of the bound state.

We have also run simulations for larger values of the initial amplitude. The agreement with the analytic estimate is quite accurate all the way to $A(0) \approx 1$. This is somewhat surprising since the amount of energy stored in the perturbation in this case is above the kink rest mass, so there is no reason to expect this linear-type behavior at this point. We show in figure 2.4 the time evolution of the perturbation with $A(0) = 1$, as well as the analytic prediction for the envelope amplitude $\hat{A}(t)$.

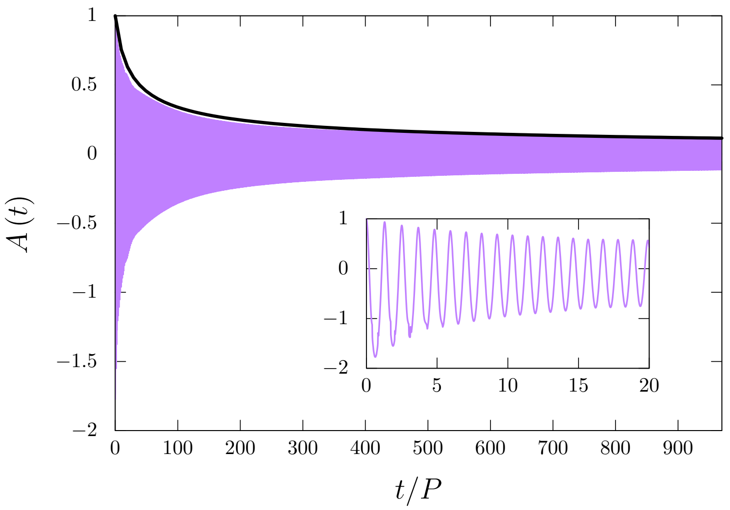

Figure 2.4: Amplitude of the shape mode $A(t)$ as a function of time (displayed as number of periods or oscillations) for $A(0) = 1$. We show in the inset figure the first few oscillations of the amplitude, where an initial asymmetric behaviour is clearly visible. This is a non-linear effect due to the initial large amplitude.

2.5.5 Non-linear evolution

One can ask the question of what happens when one starts with a value of the amplitude well beyond the linear regime. As we mentioned earlier, going to such high values of the amplitude of the perturbation means that the energy of the configuration is not a small fraction of the energy of the kink solution. In fact, for high enough values of $A(0)$, the energy of the initial state could be higher than the rest mass of three kinks. This means that there is enough energy to create a kink pair leaving behind an antikink at the center and still have a configuration consistent with the boundary conditions at infinity.

We have performed several simulations with those high initial energies and we have found that, for $A(0) > 1.334$, the final configuration is made of a central antikink with a couple of kinks flying away to infinity in opposite directions. This clearly indicates that one can think of the shape mode on a kink as a bound state of kink-antikink-kink [107]. In fact, this is the way in which this type of mode was first discovered by numerical experiments in this model [108]. A collection of snapshots of the evolution of this process is given in figure 2.5.

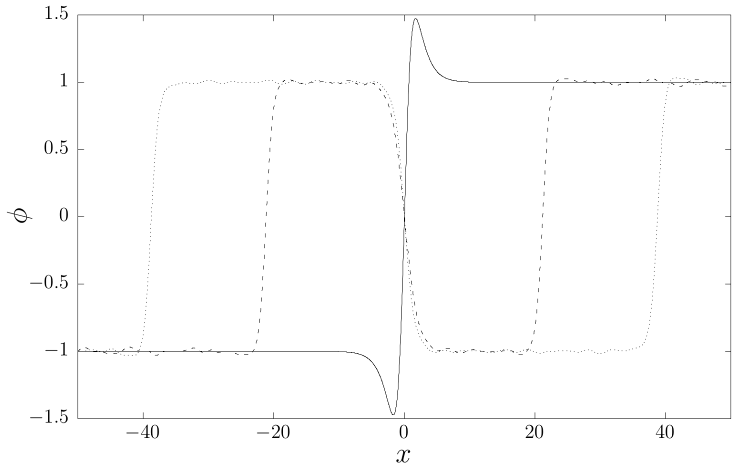

Figure 2.5: Field profile at different time steps for $A(0) = 1.35$. A kink-antikink-kink system forms, and the kinks get away from the antikink in the middle. The solid line corresponds to the initial state, while the dashed and dotted lines correspond respectively to the profile at $t = 80$ and $t = 160$ (15.6 and 31.2 in units of the period of the shape mode P).

This non-linear process shows that there is a maximum amount of energy that can be stored in this long-lasting bound state. Beyond that, the energy is shed by the soliton at a much faster rate in a time scale comparable to the light crossing time of the width of the soliton (one oscillation period). However, it is interesting to note that this maximum amount of energy could be even higher than the rest mass of the kink. This suggests that these modes could play a significant role in the dynamics of the solitons. We shall, therefore, study next how these modes can get excited and to what extent this can happen in a realistic setting.

2.6 Numerical investigations in an expanding background

Our main goal in this section is to characterize the excitation of solitons in a cosmological setting. As a first step, we investigate the kink solution in a dynamic spacetime. The $\lambda\phi^4$ action in a generic curved background reads

$$S = \eta^2 \int d^2x \sqrt{-g} \left[\frac{1}{2} g^{\mu\nu} \partial_\mu \phi \partial_\nu \phi - \frac{1}{4} \left(\phi^2 - 1 \right)^2 \right] , \tag{2.32}$$

where g denotes the determinant of the $1+1$ dimensional metric, which is given by

$$ds^2 = dt^2 - a^2(t)\ dx^2\ . \tag{2.33}$$

We will take this spacetime as a fixed background, that is, we will disregard any backreaction of the matter fields on this metric. Following this prescription, we will specify the functional form of the scale factor $a(t)$ and explore how it affects the dynamics of the field in an attempt to simulate the influence of the different cosmological spacetimes one encounters in $3+1$ dimensions. Our findings should be taken as an illustration of the possible effects one would encounter in a full $3d$ evolution.

The equation of motion for the scalar field in this background becomes

$$\ddot{\phi} + H(t)\dot{\phi} - \frac{1}{a(t)^2}\phi'' + \phi\left(\phi^2 - 1\right) = 0 \ , \tag{2.34}$$

where dots and primes respectively denote derivatives with respect to the dimensionless cosmic time and comoving space and $H(t) = \dot{a}(t)/a(t)$ is the Hubble rate[7]. In a slowly expanding spacetime, one can approximate the soliton by a solution of fixed physical width, namely, a solution of the form

$$\phi(t,x) = \tanh\left[a(t)\frac{x}{\sqrt{2}}\right] \ . \tag{2.35}$$

Here it is manifest that, in an expanding universe, the width of the soliton shrinks in comoving coordinates. This is exactly the effect we mentioned in the previous section. One should be able to faithfully reproduce this evolution numerically if one is interested in studying excitations of the width of the soliton in an expanding universe.

In the following, we will investigate the evolution of the kink solution in different spacetimes and with different initial conditions in order to see whether the particular behaviour of the scale factor and the environment can influence the presence of the shape mode or not.

2.6.1 The kink in de Sitter space

One of the simplest expanding spacetimes that we can study and that will become useful in our future simulations is a $1+1$ dimensional de Sitter space. In this case, the Hubble rate is constant and the metric is given by

$$ds^2 = dt^2 - e^{2Ht}dx^2 \ . \tag{2.36}$$

---

[7] Note that H is also written in dimensionless form. It is related to the physical Hubble rate by the relation $H_{\text{physical}} = \sqrt{\lambda}\eta H$.

The equation of motion for the scalar field in our dimensionless coordinate system becomes

$$\ddot{\phi} + H\dot{\phi} - e^{-2Ht}\phi'' + (\phi^2 - 1)\phi = 0 \ . \tag{2.37}$$

Following the description above, we can parametrize the solution of this equation as

$$\phi_{dS}(t, x) = \varphi_{dS}\left[Ha(t)x\right], \tag{2.38}$$

so the function $\varphi(\xi)$ satisfies

$$(1 - \xi^2)\varphi''_{dS} - 2\xi\varphi'_{dS} = \frac{1}{H^2}\left(\varphi^3_{dS} - \varphi_{dS}\right) \ , \tag{2.39}$$

where now the primes denote derivatives with respect to the coordinate $\xi = Ha(t)x$.

This type of equation was originally found in [109] in a $3+1$ dimensional context. The results here are compatible with that situation as the directions parallel to the wall do not play a significant role. We can solve this equation numerically for different values of the Hubble parameter. For small values of H, the horizon distance H^{-1} is much larger than the width of the kink, and, therefore, one expects the solution to be close to the adiabatic solution of a kink of constant physical width. In figure 2.6, we plot the results for $H = 0.1$. We observed that, in this case, the deviation of the exact solution from the adiabatic one is very small. These deviations can be shown to scale with H^2. Furthermore, similarly to what was found in [109], it can be seen that there is a maximum value of H beyond which there is no stationary kink solution. We will not explore this regime further in this chapter.

We have checked that our numerical code for a kink in a de Sitter universe reproduces the exact scaling solution given by equation (2.39). We have evolved the discrete equations of motion over several Hubble times without any visible excitation of the shape mode. See figure 2.6 for a sample of solutions in comoving space.

Furthermore, in the regime where there is a separation of scales between the width of the soliton and the horizon size, we have also observed that an initial excitation of the internal mode lasts for long periods of time, following the same type of behaviour we have seen in Minkowski space[8]. In order to show this, we consider an initial configuration made up of a

---

[8] Note that, in this case, the bound state profile would be distorted as well. However, in the regime we are interested in, it is sufficient to consider the same waveform as in flat space. This shape oscillates in the same way as before, keeping the same physical width over time.

kink in de Sitter space, with $H = 0.1$, and we add a perturbation in the form of the shape mode with amplitude $A(0) = 0.5$. This configuration is evolved for some time in de Sitter space until we perform a smooth transition from de Sitter to Minkowski space, in such a way that the final scale factor has grown by a factor of ≈ 30.

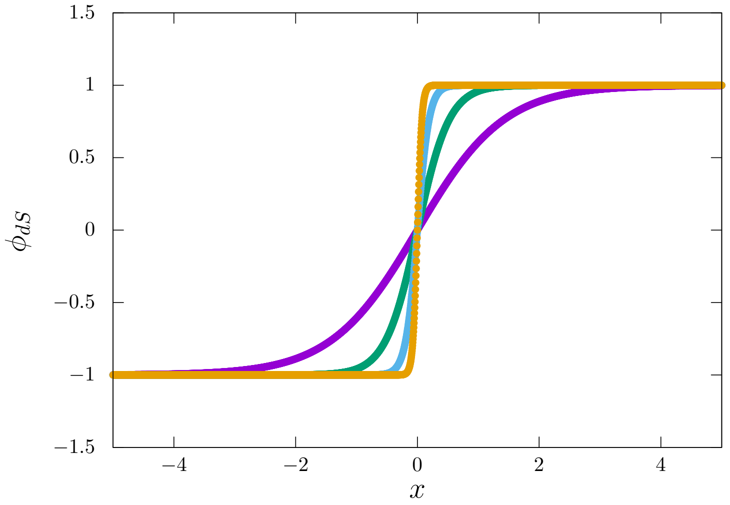

Figure 2.6: Evolution of the kink solution in an expanding de Sitter space with $H = 0.1$. The different profiles correspond to expansion factors of 1, e, e^2 and $e^{2.96}$ (purple, green, blue and orange curves respectively). The solution matches perfectly the one obtained from equation (2.39).

There is a subtlety when performing transitions between different spacetimes. By definition, these transitions change the Hubble parameter and could themselves excite the shape mode of the kink solution. A fast transition from a de Sitter universe to flat space, for example, could trigger some excitation of the internal mode of the soliton. In order to have this effect under control, the final transition to Minkowski space has been designed to be a smooth evolution on a time scale larger than the period of the oscillation of the bound state. We note that, in this way, the final result we read off from the simulation for the amplitude of the internal mode does not depend in any appreciable way on the details of the transition. We obtain the amplitude of the shape mode by projecting out on the perturbation, as explained in equation (2.25). During the expanding phase, we use the same type of projection assuming a fixed physical size of the soliton. As it can be seen in figure 2.7, the amplitude of the shape mode stays quite constant during all this cosmological evolution.

These two numerical experiments allow us to conclude that evolving a kink in de Sitter spacetime of Hubble radius a few times larger than its characteristic size does not have much effect on the amplitude of the shape mode.

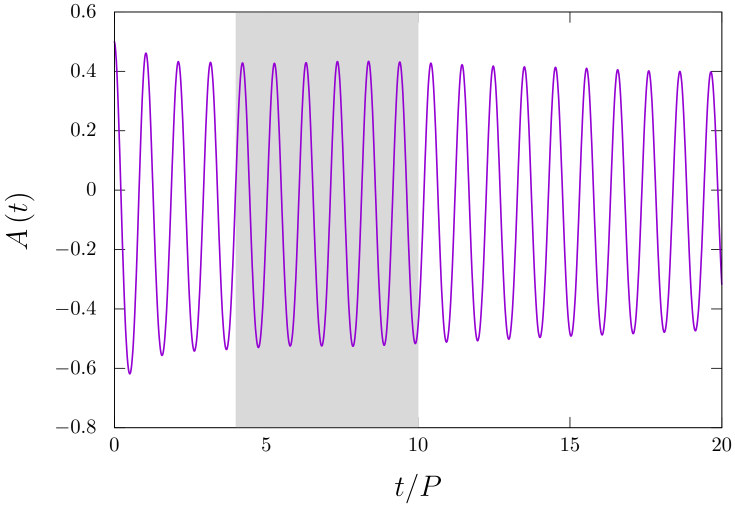

Figure 2.7: Amplitude of the bound state $A(t)$ in an expanding de Sitter background with a small expansion rate $H = 0.1$. We then switch from de Sitter space to Minkowski space in a smooth way (shaded region) to find that the amplitude is not altered by the transition. Time is given in units of the oscillation period of the shape mode P.

2.6.2 The kink in a radiation-dominated universe

We have also studied a power-law behavior of the scale factor of the form $a(t) \propto t^{1/2}$. We refer to this spacetime as a "radiation dominated universe" for its close analogy with the $3+1$ dimensional case. The important point about this type of expansion is that the Hubble rate changes over the course of the evolution, in contrast to what happens in de Sitter space. We have not been able to find an exact expression for the kink profile in this spacetime. However, we can approximate the solution by taking an adiabatic ansatz of the form

$$\phi_r(t,x) = \varphi_r\left[a(t)x\right] \, , \tag{2.40}$$

which leads to the equation

$$\left[1 - H^2(t)y^2\right]\varphi_r'' = \varphi_r^3 - \varphi_r \, , \tag{2.41}$$

where $y = a\,(t)\,x$. This equation can be used to find an approximate initial configuration for the kink in this expanding universe by solving it at a particular value of time with $H = H\,(0)$. This allows us to investigate the possible evolution of the bound state in this spacetime.

We performed the simulations using our parallel code so as to ensure a fine enough grid to accurately resolve the kink width in an expanding background. We also carefully changed the background from radiation domination to Minkowski in order not to excite the shape mode in the process, as explained earlier. Our numerical results indicate that, starting with a Hubble length somewhat larger than the width of the kink, the expansion of the universe does not affect significantly the amplitude of the bound state. This is in agreement with the results in de Sitter space and the intuition that an expansion rate $H < \omega_1$ cannot have much influence on the dynamics of the shape mode.

2.7 Phase transitions in an expanding background

We are now ready to investigate the main topic of this chapter: the formation and perdurance of excitations on a kink in a cosmological setting where the soliton is embedded in a dynamical background. In this section, we will study numerically the formation of kinks in a phase transition and extract their level of excitation in this process.

In order to simulate the phase transition, we will assume that the potential for the scalar field changes abruptly at some particular moment in time according to the following prescription[9]:

$$V(\phi) = \begin{cases} \frac{\lambda\eta^4}{4} + \frac{1}{2}m^2\phi^2 & \text{for } t < 0\,, \\ \frac{\lambda}{4}\left(\phi^2 - \eta^2\right)^2 & \text{for } t > 0\,. \end{cases} \tag{2.42}$$

Moreover, we will take $m = \sqrt{2\lambda}\eta$ to be the mass of the field in the first stage of the evolution. Note that this also corresponds to the mass of the perturbative excitations of the field around the vacua after the symmetry breaking transition.

The initial conditions will correspond to a thermal state of the field at the bottom of the $t < 0$ potential, at some temperature T. There are many ways in which this thermal state can be implemented, and we will discuss some of them in the following section. Here we will take an approach similar to the one in [110], where the formation of oscillons was discussed. In our lattice field theory representation of the scalar field, this means that we will consider the initial state given by

$$\phi\left(t = 0, x_j\right) = \sum_{n=-N/2+1}^{N/2} \frac{1}{\sqrt{2L\omega_n}}\left(\alpha_n e^{ik_n x_j} + \alpha_n^* e^{-ik_n x_j}\right)\,, \tag{2.43}$$

---

[9] In this section, we re-introduce dimensionful variables to clarify the physical content of the theory that we will simulate.

$$\dot{\phi}\left(t=0,x_j\right)=\pi\left(t=0,x_j\right)=\sum_{n=-N/2+1}^{N/2}\frac{1}{i}\sqrt{\frac{\omega_n}{2L}}\left(\alpha_n e^{ik_n x_j}-\alpha_n^* e^{-ik_n x_j}\right), \tag{2.44}$$

where, as usual, we have discretized our box of size L on a lattice with spatial grid size Δx, so that the N sites of the lattice, x_n, are labeled by the index $n=-N/2+1,\ \ldots\ , N/2$. With this notation, the possible wave numbers of the reciprocal lattice are given by $k_n=2\pi n/L$. Given the finite difference scheme described in appendix A, one can see that the propagating free scalar field modes are parametrized by the frequencies

$$\omega_n=\sqrt{\left[\frac{2\sin\left(\frac{k_n\Delta x}{2}\right)}{\Delta x}\right]^2+m^2}\quad . \tag{2.45}$$

Finally, the coefficients of the mode expansion α_n are given by a Gaussian Random Field whose two-point function corresponds to a thermal spectrum of the Bose-Einstein form:

$$\langle|\alpha_n|^2\rangle=\frac{1}{e^{\omega_n/T}-1}=\frac{1}{2}\left[\coth\left(\frac{\omega_n}{2T}\right)-1\right]\ . \tag{2.46}$$

Rewriting this initial configuration in terms of our dimensionless variables, the spectrum now reads

$$\langle|\tilde{\alpha}_n|^2\rangle=\frac{1}{2\eta^2}\left[\coth\left(\frac{\tilde{\omega}_n}{2\eta^2\Theta}\right)-1\right]\ , \tag{2.47}$$

where $\tilde{\omega}_n=\omega_n/\sqrt{\lambda}\eta$ are the dimensionless angular frequencies of the modes and Θ, defined below, is the dimensionless temperature. Therefore, this thermal state is fully specified by two dimensionless parameters:

$$\Theta=\frac{T}{\sqrt{\lambda}\eta^3}\qquad\text{and}\qquad\eta\ . \tag{2.48}$$

Note that the former controls the ratio of the typical thermal energy to the energy scale associated with the kink solution (see the expression of the mass of the soliton in equation (2.3)). The explicit appearance of η can be traced to the fact that our distribution takes into account the quantum effects of the Bose-Einstein distribution. Indeed, in the classical limit ($\omega_n << T$, i.e., when no modes are suppressed), the distribution becomes the Rayleigh-Jeans one and the explicit dependence on η disappears.

In the following simulations, we will choose the parameters in such a way that the amount of thermal energy is subleading with respect to the potential energy of the initial vacuum state. Moreover, we will also take the quantum cutoff of the Bose-Einstein distribution at high frequencies so that it corresponds to a wavelength slightly larger than the lattice spacing. Both these facts will ensure that our initial conditions are dominated by a classical regime, and the use of classical equations of motion to obtain the distribution of defects in the transition is justified. We will fix Θ and η so that both these requirements are satisfied in our simulations (we refer the reader to appendix B, where we give a detailed description of the thermal state and its implementation).

2.7.1 Evolving in an expanding background

The formation of kinks in a cosmological phase transition involves, of course, an expanding universe. In that regard, it is interesting to perform our numerical simulations in this type of background. However, there is another reason for doing that: the expanding background provides a natural friction term. In fact, the background energy density present at the beginning of the simulation is very large compared to the average energy density expected at the end of the simulation, and a mechanism for dissipation is needed in order to identify the kinks which have been formed. Without an efficient dissipation, kinks would acquire large kinetic energies and would annihilate with each other easily, leaving behind a large collection of perturbative excitations. Even if we manage to create a simulation with large enough volume where some of the kinks would survive for long time, the background energy would continuously excite the internal modes of the kink. In such case, it would not be clear when to stop the simulation to obtain an accurate evaluation of the level of excitation of any internal modes present in the defects.

One may fix this problem by simulating the transition with some added friction term, but this is somewhat arbitrary since one would be able to control the final result by adjusting the amplitude and duration of the friction. This is why simulating the transition in an expanding spacetime is advantageous. With the natural friction it provides, the background energy density slowly depletes. Furthermore, as we showed in the previous section, taking a sufficiently small expansion rate does not affect much the amplitude of the internal mode of the kinks.

This cosmological friction term also induces a horizon size, so kinks and antikinks present at distances larger than this distance are not to annihilate. Their velocities are redshifted until they are comoving with the background.

All these effects will allow us to obtain a much more realistic final configuration of the transition where kinks are well separated and almost at rest with respect to the simulation grid. This is a simple configuration that can be used to extract the amplitude of the bound state of the kinks.

As a final step in the simulation, we also consider a smooth transition of the background to $1+1$ dimensional Minkowski spacetime, as explained earlier. We run the simulation for large periods of time with absorbing boundary conditions, and track the amplitude of the shape mode of the kinks during the evolution.

2.7.2 Results

We have run several simulations of $N = 5000$ points with $\Delta x = 0.01$, starting from an initial thermal state at a dimensionless temperature of $\Theta = 10^{-3}$ and a symmetry breaking scale $\eta = 250$. For these values of the parameters, the initial amount of thermal energy is of the order of 15% of the total background energy density. This also means that the thermal modes are substantially suppressed for wavelengths smaller that $\lambda_T \approx 10\Delta x$. This implies that the thermal spectrum at the scale of the soliton is correctly represented by a classical thermal state.

We have evolved these initial configurations in an expanding de Sitter background with dimensionless Hubble rate $H_i = 0.04$. This means that the associated horizon size is substantially larger than the width of the soliton, which is of the order of $m^{-1} = \sqrt{2}$. Based on the numerical experiments we described in the previous section, we are confident that any initial amplitude of the internal mode of the kink produced by the dynamics of the phase transition will survive in this background. Moreover, the background energy density of perturbative excitations is heavily suppressed during this time.

We show in figure 2.8 a few snapshots of the field at different times for a particular realization of this setup. We notice that, as time passes, the field settles on one of the vacua in different regions of space. This leads to the formation of a "network" of alternating kinks and antikinks. Furthermore, this transition also leads to the generation of localized oscillating lumps around each of the vacua. These are nothing more than the breather-type solutions we discussed in previous sections. They are readily produced by the relaxation mechanism of the system and also by the collision and merging of nearby kinks and antikinks.

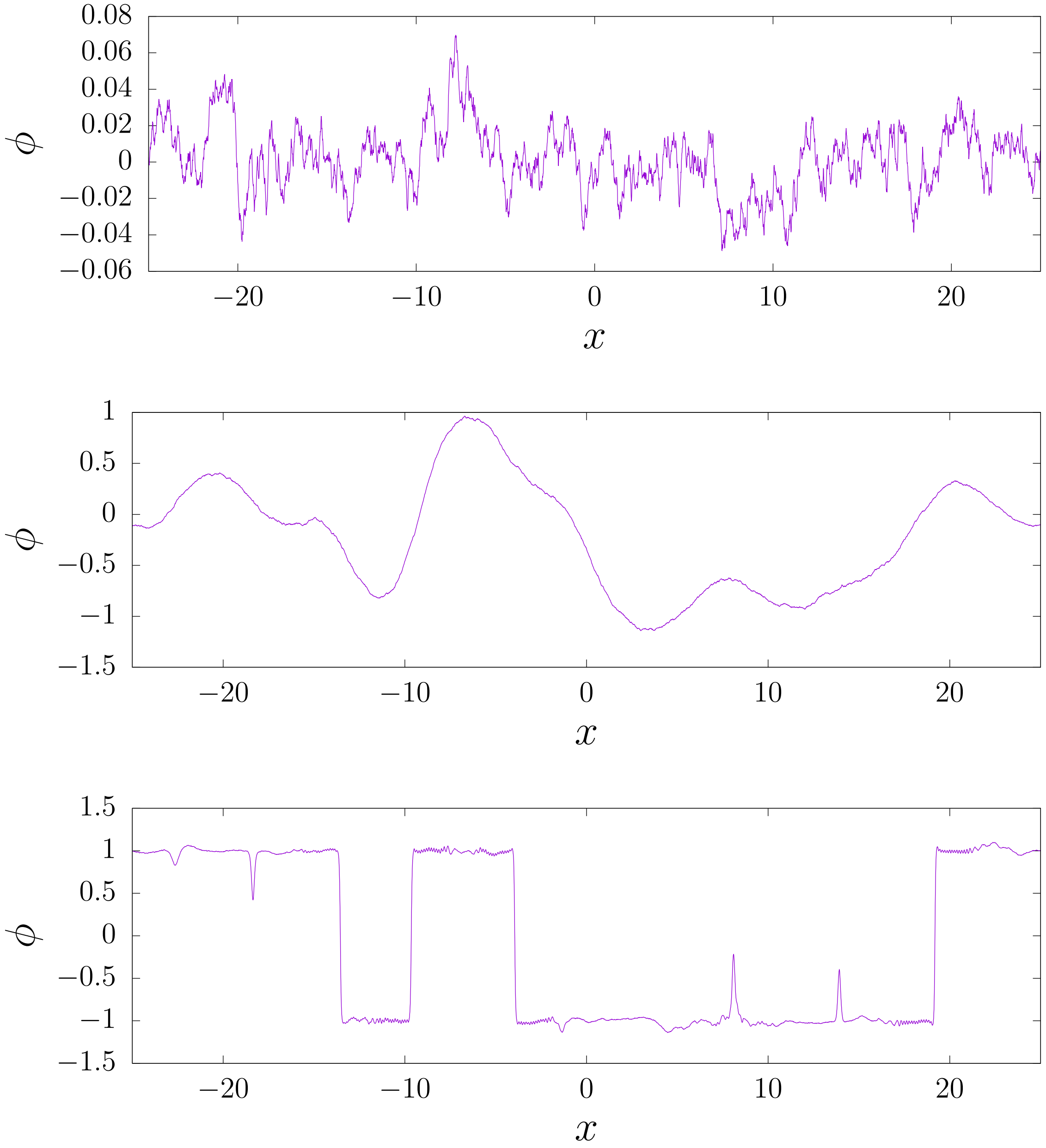

Figure 2.8: Three snapshots of the field profile during the phase transition. The top one corresponds to the initial conditions. The middle one is at some intermediate step during the de Sitter phase and the bottom one is at cosmic time $t = 140$ (27.3 in units of the oscillation period of the shape mode P). This last instant of time already corresponds to the Minkowski stage. Several kinks and antikinks have been created.

We let the system evolve until $t \approx t_* = 80$, and then we relax the expansion of the universe smoothly into flat Minkowski space, similarly to what we did in the previous section. The particular time dependence of the expansion rate we employed is the following:

$$H\left(t\right) = \frac{H_i}{2}\left[1 - \tanh\left(\frac{t - t_*}{w}\right)\right] , \tag{2.49}$$

which corresponds to a scale factor

$$a\left(t\right) = e^{\frac{H_i}{2}t}\left[\frac{\cosh\left(\frac{t_*}{w}\right)}{\cosh\left(\frac{t-t_*}{w}\right)}\right]^{\frac{H_i w}{2}} . \tag{2.50}$$

These functions are plotted in figure 2.9 for our choice of parameters.

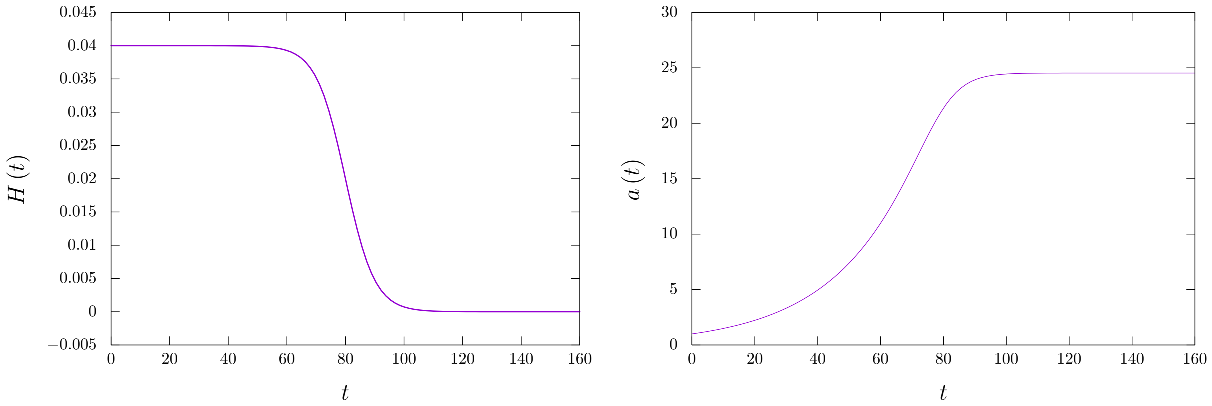

Figure 2.9: Hubble rate (left) and scale factor (right) as a function of cosmic time for $H_i = 0.04$, $t_* = 80$ and $w = 10$. The transition from de Sitter to Minkowski space takes place on a time scale larger than the oscillation period of the shape mode.

By $t = t_*$, the background energy has already decreased substantially and one can observe the kinks forming. We also use absorbing boundary conditions in order for radiation to leave the simulation box as it reaches the boundaries. The late time result of this simulation is a system of well separated kinks and antikinks, pretty much at rest with respect to one another, plus a collection of breathers.

We concentrate on each of the kinks and investigate their level of excitation by extracting the amplitude of the internal mode using the expression given in equation (2.25) locally. The results for the amplitudes of the kinks in the realization shown in figure 2.8 are displayed in figure 2.10. We notice that the resulting amplitudes for the different kinks are quite similar.

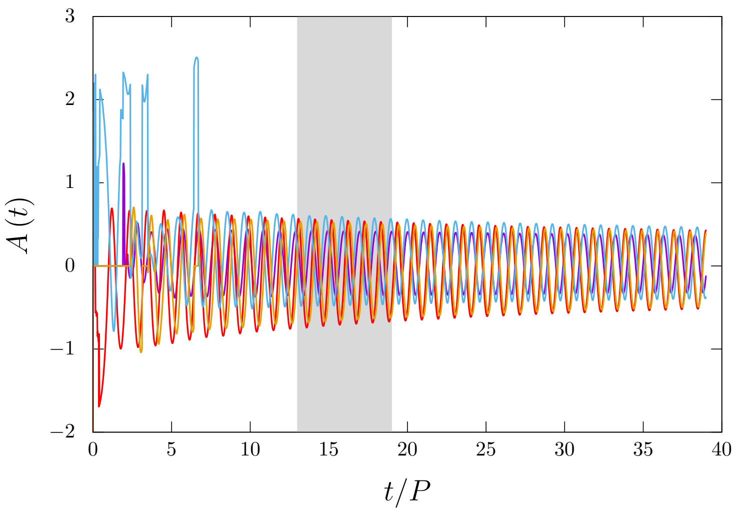

Figure 2.10: Amplitude of the shape mode $A(t)$ as a function of time, for each of the four kinks in figure 2.8. The color correspondence is purple, red, blue and orange as we encounter the kinks going from left to right in figure 2.8. Time is given in units of the oscillation period of the shape mode P, and the shaded region represents the smooth transition from de Sitter to Minkowski space. The error at early times is a consequence of the fact that the position of the center of the kink is not yet well defined.

In order to find the average value of the amplitude of the shape mode, we have run 500 realizations with a thermal distribution of initial perturbations with $\Theta = 10^{-3}$ to get

$$\langle \, \hat{A} \, \rangle_{\text{formation}} = 0.5 \pm 0.1 \ . \tag{2.51}$$

We have also investigated the dependence of this quantity on the initial conditions by changing the temperature of the initial thermal state in such a way that the percentage of extra initial energy due to the perturbations was smaller by a factor of 2. However, the final result for the average amplitude of the bound state of the kink was pretty insensitive to these changes. This may be attributed to the fact that the relevant energy scale in the process of kink formation is the background energy associated with the initial vacuum state. In other words, the initial thermal fluctuations are important to induce inhomogeneities that lead to the formation of kinks and antikinks, but not do not seem to contribute to the final energy stored in them.

We have also run simulations with a “radiation domination” scale factor, that is, $a\,(t) \propto t^{1/2}$. The results are qualitatively similar to the case of de Sitter space.

The animations produced from these simulations show that the excitation of the kinks is mainly due to two effects. The first one is the interaction of the kinks with the perturbative excitations that pass through them. At a linear level, these modes should not excite the kinks. However, at a non-linear level, these waves are able to excite the zero mode and the shape mode. We have actually tested this by recreating this type of interactions on isolated kinks that we irradiated with wave packets of different frequencies. These scattering experiments indeed produced some motion of the kinks, as well as an excitation of the internal mode. The second mechanism for kink excitation is more non-linear in nature and has to do with the collision between breathers and kinks. As we pointed out in section 2.4, one can consider the shape mode as a breather trapped inside the kink. Therefore, it should not come as a surprise that the collisions of breathers with kinks are a good place to see the amplification of the energy stored in the internal mode. We show in figure 2.11 three different snapshots of the evolution of the field for one such type of event. The initial configuration consists of a kink and a breather at a short distance from one another. As times passes, the breather comes closer to the kink and overlaps with it for a while. One can see that this triggers a big resonance effect on the amplitude of the internal mode, so the final state of the kink is substantially more energetic. See figure 2.12 for the evolution of the amplitude of the internal mode as a function of time in this process. Note that the kink translational mode is also excited.

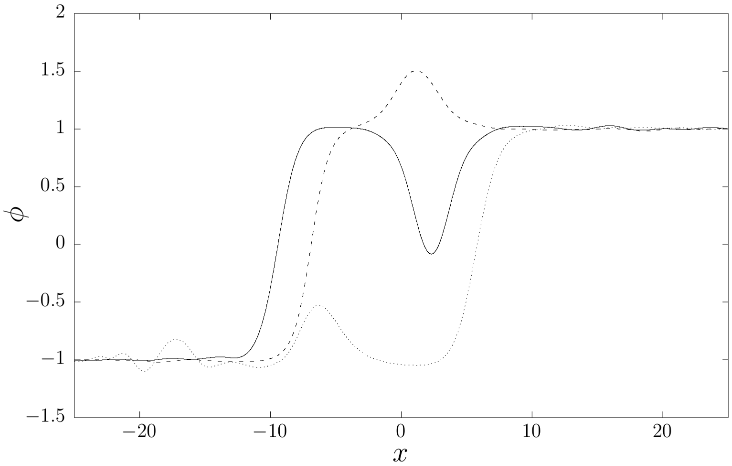

Figure 2.11: Thee different snapshots of the field showing the interaction between a kink and a breather. The solid line is the initial configuration, the dashed line illustrates the two objects coming together, and the dotted line represents the result after they have passed through one another. The resulting amplitude of the shape mode in this scattering process is given in figure 2.12.

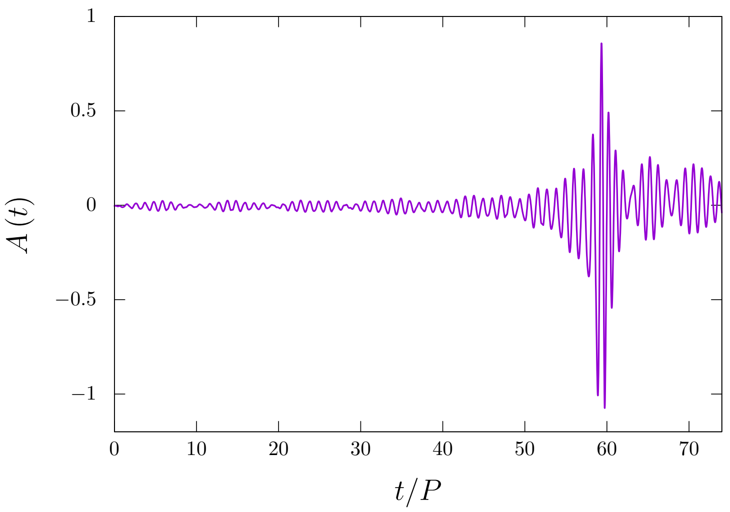

Figure 2.12: Amplitude of the shape mode $A(t)$ as a function of time during a collision of a kink with a breather. Time is given in units of the oscillation period of the shape mode P.

The combination of these two effects leads to the final amplitude of the shape mode on a typical phase transition. At formation, the kinks seem to have around 20% more energy than the lowest energy configuration. This is not a negligible amount of energy, and it could easily have important consequences for the subsequent evolution. In particular, as we showed in section 2.5.4, this kind of extra energy will stay in the kink for long periods of time as compared to the natural time scale of the kink, which is given by $\tau \sim 1/m$.

2.8 Heating up the kink

Another interesting scenario is the possible excitation of the solitons due to their interaction with a thermal bath. This could happen, for example, in the formation of defects in a cosmological setting during reheating [111]. Alternatively, this could also be useful to estimate the possible degree of excitation in numerical simulations where there is a substantial amount of radiation in the background[10].

There are several ways in which a thermal background can be simulated. Following the description in the previous section, we can approximate the solution of a kink in a thermal bath as a sum of the lowest energy configuration for the soliton together with a state of the form given by equation (2.43). One could object that the presence of a kink would distort

---

[10] In this work, we have run the simulations with a thermal spectrum, but the analysis in this section could be easily extended to some other spectra.

the spectrum of the perturbations around the solution, possibly affecting the amplitude of the bound state that we want to find. We have addressed this concern by simulating the interaction of the kink with a thermal bath using the Metropolis algorithm [112]. We give the details of this procedure in appendix B. This is procedure is, computationally, more expensive than the one described above, since the lattice needs to be swept many times over before a configuration that resembles the thermal state is reached[11]. We have done this for several realizations and compared the results with the analytic setup of the thermal state described in the previous section. We found that both methods lead to comparable results for the amplitude of the shape mode.

We show in figure 2.13 a typical example of such initial configuration of a kink at a dimensionless temperature $\Theta = 0.01$. Another important point to note is that the interaction with the thermal fluctuations imprints an initial velocity for the kink as well. We have checked that the distribution of initial velocities is in agreement with the expectation that the average translational kinetic energy is given by $T/2$, as for a massive point particle. In practice, this initial velocity complicates the simulation in Minkowski space as the kink will eventually reach the boundary of our box and leave it, specially for high temperatures.

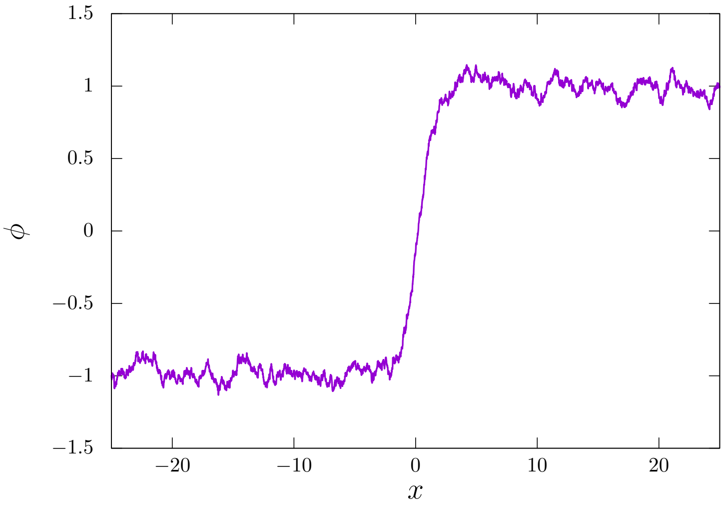

Figure 2.13: Initial field configuration. It has been generated by means of the Metropolis algorithm, at temperature $\Theta = 0.01$.

In order to alleviate this problem, we decided to run the simulations in a de Sitter background with a small expansion rate. As we learned before, this does not have much of an effect on the amplitude of the shape mode, and the kink is slowed down. This technique

---

[11] This method has been previously used in the literature in similar models like [113].

allows us to reliably extract the value of the amplitude of the bound state. We have run 100 realizations for each temperature ranging from $10^{-4} < \Theta < 2$ and obtained the average value of the amplitude. The results are plotted in figure 2.14.

An analytic estimate of the average value of the amplitude as a function of the dimensionless temperature is given in appendix B. This is done by looking at the projection of the thermal fluctuations over the bound state mode. This simple description implies that $\langle \hat{A} \rangle \propto \Theta^{1/2}$. This is a good fit to our results at low temperatures, but deviates from the actual numerical results at higher values of the temperature. This is a somewhat expected result since our analytic estimate is based on the assumption that the background radiation has small amplitude, and this breaks down as one approaches large temperatures.

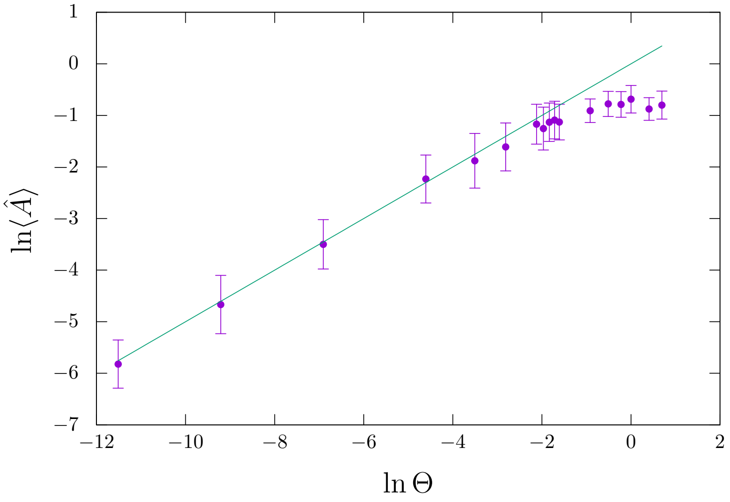

Figure 2.14: Log-Log plot for the average amplitude of the shape mode as a function of temperature. The amplitude is observed to tend to a constant value $\langle \hat{A} \rangle \approx 0.5$ in the high temperature limit. Each purple point corresponds to the average of 100 realizations, and the green line has slope 1/2 to show the $\langle \hat{A} \rangle \propto \Theta^{1/2}$ dependence in the low-temperature regime.

As we increase the temperature, we notice that the energy stored in the thermal fluctuations is not negligible compared to the mass of the kink. This means that, in some realizations, there are fluctuations that generate a kink-antikink pair directly from the background. For temperatures above $\Theta = 0.2$, the number of these pairs is large.

We have performed these numerical simulations for temperatures as large as $\Theta = 2$. In this case, the initial kink is "irrelevant" because the thermal energy is so high that the typical fluctuations can go over the maximum of the potential. However, simulating this in an expanding background and with absorbing boundary conditions, we are able to end up with a collection of isolated kinks. We see that the amplitude of the kinks formed this way is $\langle \hat{A} \rangle \approx 0.5$. This is quite similar to the value we obtained in the previous simulations of the phase transitions.

It is interesting to note that one does not seem to be able to reach the strong non-linear regime for the shape mode amplitude in our numerical simulations. This is indeed the case for both cases, the phase transition and the thermal bath interaction. One is tempted to speculate that, even though the bound state could store much more energy, natural initial conditions for cosmology do not lead to such situations.

One can also simulate this interaction of the kink and a thermal bath using the Langevin equations (see for example [114]). It would be interesting to see if the results for the amplitude of the bound state in this case are in agreement with our simulations. We leave this question for future investigations.

2.9 Conclusions

One of the most interesting properties of solitonic solutions for cosmological applications is their long lifetimes compared to the fundamental time scale of the underlying theory. This is typically due to the fact that they correspond to the lowest energy configuration associated with a topological charge that ensures their stability. In many field theory models, this long perdurance is also shared by other type of localized configurations in the vacuum called breathers or oscillons. The reason for these other objects to have such a long lifetime is different: they are field configurations that oscillate with a frequency which is below the frequency of the propagating modes in the vacuum.

Here we study a sort of hybrid configuration, one that owes its long duration to dynamical reasons but lives on a soliton configuration. The simplest example of this state is perhaps the localized excitation of the kink solution in $\lambda\phi^4$ theory. One can show that, at a linear level, there is such a bound state associated with the width of the kink solution and whose frequency is below the lowest frequency of the scattering states in the vacuum. This means that, as in the case of oscillons, their decay is due to non-linear interactions.

In this chapter, we have studied the full non-linear evolution of the shape mode of the kink in Minkowski space. We have been able to do this over long periods of time by using a $1 + 1$ dimensional lattice with absorbing boundary conditions. We have shown that one could store quite a large portion of extra energy on this bound state for times much longer than the natural time scale of the problem (the width of the kink). The similarities with the breather solutions in the theory makes us think of these bound states on the kink as a breather trapped in the core of the soliton.

We have also explored the evolution of these kink solutions in several cosmological backgrounds. In particular, we have run a large number of realizations to simulate a cosmological phase transition that leads to the formation of these defects. We found that the solitons will typically get formed with an approximately 20% of extra energy due to the presence of a substantial amplitude of the shape mode.

We have also simulated the interaction of the kink solution with a thermal bath and computed the average value of the expected amplitude of the bound state as a function of the temperature. As one increases the thermal energy of the background, the amplitude of the bound state grows following the relation $\langle \hat{A} \rangle \propto T^{1/2}$, but it saturates when the extra energy of the soliton is also about 20%. This suggests that a purely thermal formation of solitons would also create them with some extra energy at this 20% bound.

Our results suggest that, in a realistic setting, solitons will always be formed in an excited state with some extra energy stored in their bound state modes. This could have important consequences for the subsequent evolution of these objects. In particular, if this type of behaviour persists in higher dimensions, adding some extra energy to the solitonic configurations can easily affect their equation of state and hence their dynamics.

The solitons could easily remain excited for the whole span of field theory simulations. However, even though the lifetime of the bound states is very long compared to any time scale of the simulation, it is many orders of magnitude smaller than any relevant cosmological time. This means that one should also investigate whether there is any mechanism that maintains the level of excitation of the solitons throughout their cosmological evolution. Therefore, it remains to be seen if this initial energy that we report in this work has a cosmological relevance or is just a short transient effect. We will comment more on this in the following chapters.

Chapter 3

Dynamics of $2+1$ dimensional domain walls

In this chapter, we study the dynamics of domain walls in the $2+1$ dimensional $\lambda\phi^4$ theory. In this case, the kinks we have presented in the previous chapter become extended along one of the spatial directions, so they behave as strings. For this reason, we will call them domain wall strings.

In this work, we show analytically and numerically that the amount of radiation from the propagation of wiggles on these objects is negligible except for regions of high curvature. Therefore, at low curvatures, the domain wall strings behave almost exactly as the Nambu-Goto action predicts. We show this explicitly with different numerical experiments of the evolution of these objects in a lattice. We then explore their dynamics in the presence of internal mode excitations. We do this again by performing field theory simulations and identify an effective action that captures the relevant interactions between the different degrees of freedom living on the string. We uncover a new parametric resonance instability that transfers energy from the internal mode to the position of the domain wall. This instability is shown to enhance the radiation from the internal mode. We also explore the possibility of exciting the bound state with the collision of wiggles on the domain wall. Our numerical experiments indicate that this does not happen unless the wiggles have a wavelength of the order of the string thickness. Finally, we comment on the possible relevance of our findings to cosmological networks of defects. We argue that our results cast some doubts on the significance of the internal modes in cosmological applications beyond a brief transient period right after their formation. This, however, should be investigated further.

3.1 Introduction

In the previous chapter, we exemplified how solitons can have long-lived excitations spatially localized around their core. Furthermore, for the case studied there (the $\lambda\phi^4$ kink), we saw that these internal modes can store a significant fraction of the rest mass of the defect in them. Therefore, the macroscopic behaviour of the excited soliton could be easily influenced by this extra energy. However, the non-linear coupling between the internal mode and the scattering states allows the excited soliton to slowly relax to the lowest energy configuration.

Depending on the particular model and the dimensionality of spacetime, solitons could appear as extended objects. For instance, as previously mentioned, the kink in $2+1$ dimensions becomes a domain wall string. The presence of these longitudinal directions allows for possible excitations of the soliton to propagate along them. In particular, in the $2+1$ dimensional scenario, the shape mode perturbation described in the previous chapter can be in the form of waves travelling along the string. In addition, since the presence of the object breaks the translational invariance of the theory, Goldstone modes living on the worldvolume of the soliton will appear. All these modes propagating on the object would mutually interact and possibly emit or absorb radiation. In order to understand the dynamics of the excited soliton, one would need to identify the conditions under which these perturbations become important and obtain the effective theory that governs their dynamics and interactions.

A traditional strategy to find the effective action relies on the separation of scales between the different sets of perturbations present in these objects. The excitations localized on the core of the solitons typically have masses of the order of the inverse width of the defect. However, the perturbations that represent wiggles on the solitons are, by definition, massless from the point of view of the effective theory on the worldvolume. At low energies, one can assume that the massive modes are not excited. In this case, the dynamics of the soliton should be governed by an effective action that only captures the interactions of the massless modes. In the case of strings, this approach leads to the use of the Nambu-Goto action. However, as explained in chapter 1, large-scale Nambu-Goto simulations of cosmic strings seem to be in tension with full field theory simulations. The conjecture that the reason for the discrepnacies is the presence of internal excitations in the strings, as well as the results obtained in the previous chapter, argues for a possible extension of the effective theory by including these extra massive modes.

In this chapter, we will investigate this issue in a simpler setting in $2 + 1$ dimensions. Nevertheless, since the objects we will study here are string-like domain walls, the problem at hand shares many of the effects that are at play in the $3+1$ dimensional case. The effective action for domain wall strings within the thin-wall approximation is identical to the Nambu-Goto action for $3+1$ dimensional strings. Furthermore, as we will see, the $\lambda\phi^4$ walls we will investigate have bound state excitations stuck to their core that decay slowly into radiation. Therefore, this lower-dimensional problem has all the ingredients that have been presented in the hypothetical resolution of the local cosmic string puzzle. Taking all this into account, we hope that some of our results and conclusions can be extrapolated to the actual problem with local strings.

This chapter is structured as follows. In section 3.2, we will present the domain wall string solution and the spectrum of perturbations around it. In section 3.3, we will discuss the different mechanisms by which the excited domain wall string can lose energy. In section 3.4, we will investigate the dynamics of the walls in the absence of internal excitations, and we will compare their motion with the predictions of the Nambu-Goto action. In section 3.5, we include the presence of massive excitations in the effective action and discuss their possible dynamical implications. In section 3.6, we explore the non-linear interactions between the excitations on the string and their Goldstone modes. In particular, we demonstrate the existence of resonance effects between them. In section 3.7, we study the possible excitation of the internal mode from the interaction of Goldstone modes. Finally, in section 3.8, we summarize our results and briefly discuss the relevance of these effects for cosmological networks.

Some of the simulations we discuss in this chapter can be found at `http://tp.lc.ehu.es/earlyuniverse/dynamics-of-domain-wall-strings`.

3.2 The domain wall string solution and its excitations

We will study the $2+1$ dimensional $\lambda\phi^4$ model for a real scalar field $\phi(t,x,y)$:

$$S = \int d^3x \left[\frac{1}{2}\eta^{\mu\nu}\partial_\mu\phi\partial_\nu\phi - \frac{\lambda}{4}\left(\phi^2-\eta^2\right)^2 \right] , \tag{3.1}$$

In this case, the dimensions of the field and the parameters are the following: $[\phi] = E^{1/2}$, $[\eta] = E^{1/2}$, $[\lambda] = E$.

The equation of motion coming from this action is

$$\frac{\partial^2 \phi}{\partial t^2} - \frac{\partial^2 \phi}{\partial x^2} - \frac{\partial^2 \phi}{\partial y^2} + \lambda \left(\phi^2 - \eta^2\right) \phi = 0 \ . \tag{3.2}$$

From this equation, one can immediately identify the existence of two vacua at $\phi = \pm\eta$. As in the previous chapter, the mass of perturbative excitations about these vacua is given by $m = \sqrt{2\lambda}\eta$. Therefore, this theory has a gap: there are no massless propagating modes in vacuum. This will have important implications since, as will discuss later on, the only decay channel available for the perturbations is massive.

Evidently, the kink solution we studied in the previous chapter is also an exact solution to the equation of motion (3.2):

$$\phi_k(x) = \eta \tanh\left(\frac{mx}{2}\right) \ . \tag{3.3}$$

Since this configuration does not depend on the y coordinate, one should think about this soliton as an extended object along this direction. Therefore, this is a line-like defect, and indeed, one can easily see that its energy density is mostly concentrated within a narrow area of thickness $\delta \sim m^{-1}$ around the line defined by $\phi = 0$. Even though this field configuration is a domain wall that separates two different vacua, it will dynamically behave as a string.

From the energy-momentum tensor, given in equation (2.26), one can compute the energy per unit length μ and the tension τ of the string:

$$\mu = \int_{-\infty}^{\infty} dx T^{00} = \frac{2\sqrt{2\lambda}}{3}\eta^3 \, , \tag{3.4}$$

$$\tau = \int_{-\infty}^{\infty} dx T^{22} = -\frac{2\sqrt{2\lambda}}{3}\eta^3 \, . \tag{3.5}$$

Therefore, the equation of state of the domain wall string solution is $\mu = -\tau$.

Let us now study the spectrum of small perturbations around this static solution. In order to do this, we will start by considering the following ansatz:

$$\phi(t, x, y) = \phi_k(x) + f_n(x) e^{i(k_n y - \omega_n t)} \ . \tag{3.6}$$

Inserting this expression in the equation of motion (3.2), and keeping only first-order terms, we obtain

$$-f_n''(x) + U(x) f_n(x) = \Omega_n^2 f_n(x)\,, \tag{3.7}$$

where

$$U(x) = \lambda \left[3\phi_k^2(x) - \eta^2\right] \tag{3.8}$$

is the effective potential for this Schrödinger problem and the associated eigenvalues are given by

$$\Omega_n^2 = \omega_n^2 - k_n^2\ . \tag{3.9}$$

This eigenvalue problem is formally identical to the one discussed in the previous chapter. Its spectrum consists of two bound states whose properly normalized eigenfunctions are

$$\bar{f}_0(x) = \sqrt{\frac{3m}{8}}\,\mathrm{sech}^2\left(\frac{mx}{2}\right) \qquad \text{with} \qquad \Omega_0 = 0 \tag{3.10}$$

and

$$\bar{f}_1(x) = \sqrt{\frac{3m}{4}}\,\sinh\left(\frac{mx}{2}\right)\mathrm{sech}^2\left(\frac{mx}{2}\right) \qquad \text{with} \qquad \Omega_1 = \frac{\sqrt{3}}{2}m\,, \tag{3.11}$$

and a continuum of scattering states starting at $\Omega_n = m$ that are associated with radiation coming out of the soliton.

The spatial profile of the eigenfunctions above was shown in figure 2.1. On the one hand, the zero modes, with eigenvalue $\Omega_0 = 0$, represent local rigid displacements of the domain wall, and constitute wiggles that propagate at the speed of light along the longitudinal direction of the string. The homogeneous zero mode perturbation (i.e., with $k_0 = 0$), is simply a rigid displacement of the whole object. On the other hand, the internal or shape mode, with $\Omega_1 = \frac{\sqrt{3}}{2}m$, represents travelling perturbations of the width of the soliton.

A generic linear excitation around the static solution would be given by a combination of all these modes with their corresponding amplitudes. In the following, we aim to understand how to describe the dynamics of the domain wall string in the presence of some of these perturbations and their possible interactions.

3.3 Radiation from domain wall excitations

As we explained in the introduction of this chapter, we are interested in finding an effective action that describes the dynamics of the domain wall string taking into account the influence of the internal modes. This effective theory on the two-dimensional string worldsheet disregards the possibility of energy leaking into the bulk, so in order to be able to quantify the regime of validity of this approach, one should first understand the processes by which the soliton can radiate.

3.3.1 Radiation from zero mode excitations

The zero mode excitations represent the Goldstone modes associated with the wiggles of the domain wall string. An interesting result due to Vachaspati and Vachaspati [115] shows that one can obtain the fully non-linear description of these excitations at the field theory level. They found that the configuration

$$\phi(t,x,y) = \phi_k\left[x - \psi(y \pm t)\right] \ , \tag{3.12}$$

where the travelling wave ψ has arbitrary shape and amplitude, is an exact solution to the equation of motion. The zero modes given in (3.10) are the linearized version of this solution. The wiggle represented by ψ moves at the speed of light in one direction along the domain wall with its shape undistorted, and since the energy is conserved, no radiation is emitted while the wiggle travels. However, in general, we will have zero mode excitations propagating in opposite directions on the string. In this case, we expect some radiation to be emitted from the domain wall.

In order to study this radiation in a quantitative manner, we will start by investigating the energy loss from zero modes in the form of standing waves. We will consider the field configuration

$$\phi(t,x,y) = \phi_k\left(\frac{x - \psi_0(t,y)}{\sqrt{1 + {\psi_0'}^2 - {\dot{\psi_0}}^2}}\right) \ , \tag{3.13}$$

where $\psi_0(t,y)$ corresponds to a standing wave displacement with amplitude $\hat{D}$ and frequency ω_0:

$$\psi_0(t,y) = \hat{D}\cos(\omega_0 y)\cos(\omega_0 t) \ . \tag{3.14}$$

The reason why we consider the configuration (3.13) is that the transverse displacement ψ_0 can be shown to approximately follow the Nambu-Goto equation of motion. This is proven in appendix D along with other remarkable properties of this ansatz. We could have also taken the ansatz

$$\phi(t,x,y) = \phi_k(x) + \psi_0(t,y) \times \bar{f}_0(x) \ , \tag{3.15}$$

which is the linear approximation of the one we used. The results in this case are qualitatively similar to the ones presented here.

For small enough $\hat{D}$, we expect these waves to behave like a free field on the worldsheet, as the linear theory predicts. Their oscillation will then act as a source for radiation at a quadratic order in their amplitude. In appendix C, we estimate analytically the power per unit length emitted by the domain wall string in the configuration (3.13) as a function of the frequency ω_0.

We have also investigated this perturbative radiation in a lattice field theory simulation. We initialized the field according to (3.13) and (3.14), with different frequencies and small amplitudes. Such an initial state is illustrated in figure 3.3.1, although in this example we have chosen a big amplitude in order to clearly visualize the form of the string. In this plot, as well as in the rest of the plots where the domain wall is depicted in this chapter, the horizontal direction corresponds to the y axis.

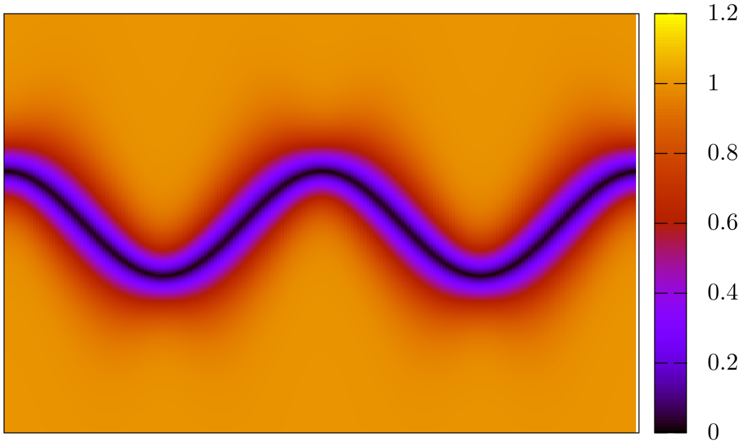

Figure 3.1: A standing wave on the domain wall string, as given in equation (3.13). The color palette indicates the value of $|\phi|/\eta$. The domain wall string is extended along the y direction, which here corresponds to the horizontal axis.

One can easily see that, since these perturbations couple quadratically to the scattering states, the wavelength of the radiation in the x direction is approximately given by $\lambda_{\rm rad} = 2\pi/\sqrt{4\omega_0^2 - m^2}$. This wavelength is large for ω_0 sufficiently close to $m/2$, so one needs the simulation box to be large in the transverse direction (x) in order for the emitted radiation to fit in. Moreover, we are interested in the radiation very far away from the soliton. For these reasons, we chose the size of the box in the x direction to be $L_x = 200$, which is more than enough to avoid any problems related to the spatial extent of the radiation.

On the other hand, we varied the size of the box in the y direction, L_y, from 4 to 26 in order to get the desired frequencies for the standing wave[1]. Regarding lattice spacing, we used $\Delta x = 0.02, 0.04$ and $\Delta t = 0.005, 0.01$. We ran the simulations for 2×10^5 time steps and found the radiated power by integrating the energy flux accross the lines $x = \pm 98$ at late times (the string lies at $x \approx 0$.) We employed absorbing boundary conditions in the x direction and periodic conditions in the y direction (see appendix A for the details). All the previous quantities are given in units of $(\sqrt{\lambda}\eta)^{-1}$.

In figure 3.2 we show the comparison of the radiated power found analytically and numerically. Both results are in very good agreement, and they indicate several important facts for us. First and foremost, it is clear that, for a frequency below $m/2$, the radiation is highly suppressed. This can be easily understood by noticing that the source for radiation has a frequency $2\omega_0$ because it is quadratic in the perturbation. Therefore, if $\omega_0 < m/2$, the source oscillates with frequency smaller than m, which is the minimum frequency required for perturbations to propagate in the vacuum. If one increases the frequency of the standing wave beyond this threshold, the string starts radiating slowly and its power grows with frequency. However, at higher frequencies, radiation shuts off. This effect is due to the fact that the corresponding scattering states have a very small projection onto the source of radiation.

We can also take this type of ansatz and extend it beyond its range of expected validity to study waves of high amplitude and curvature. In this case, we have a new source of radiation that has to do with the presence of high curvature, i.e., regions where the local radius of curvature is small compared to the string thickness δ, or even comparable. In this case, we expect non-perturbative radiation to be emitted as different segments of the string are forced to be closer than their own thickness, so they annihilate. This is reminiscent to what happens in high-curvature regions of local cosmic strings [85, 86].

We show in figure 3.3 how the standing wave loses energy in the form of non-perturbative radiation. We choose an angular frequency below $m/2$ so that the zero mode does not couple quadratically to the scattering states, and look at the power emitted by the standing wave as we gradually increase its amplitude. As expected, the radiation is negligible for small amplitudes, but it is greatly enhanced for large amplitudes.

---

[1] Recall that periodic boundary conditions in the y direction force waves on the string to have frequencies given by $2\pi n/L_y$, where n is an integer number.

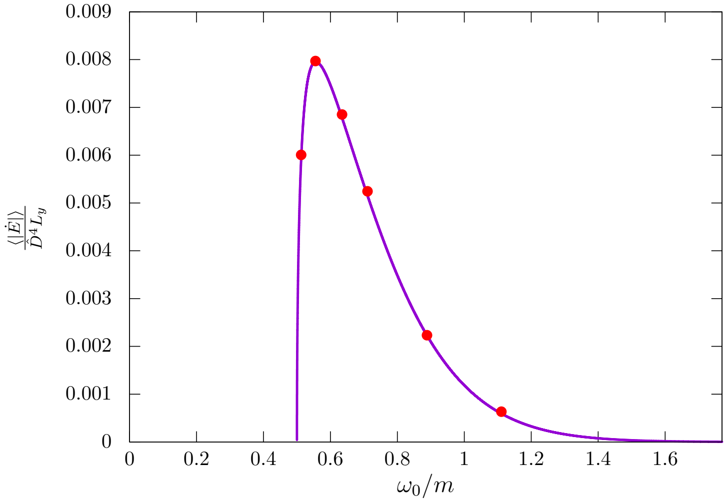

Figure 3.2: Radiated power per unit length as a function of the frequency of the zero mode. The quantity on the y axis is made dimensionless by dividing the power by $\lambda^3\eta^8$. The solid curve corresponds to the analytical estimate (C.26), and the red points represent the power read directly from the numerical simulations.

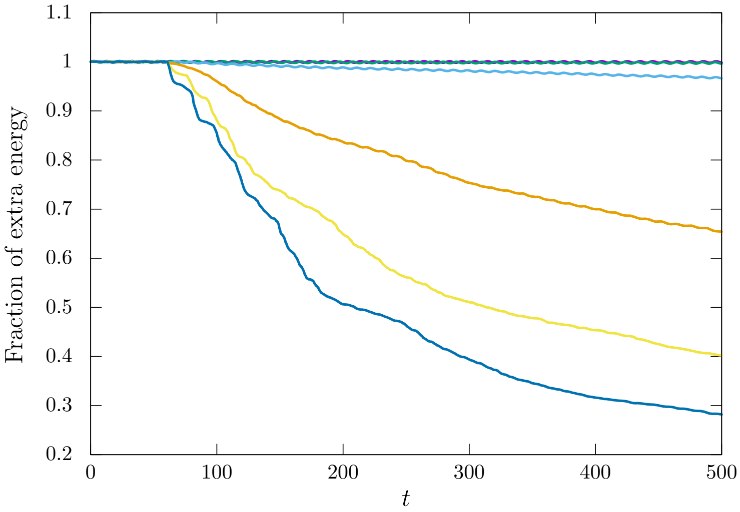

Figure 3.3: Fraction of extra energy as a function of time, given in units of $(\sqrt{\lambda}\eta)^{-1}$, for standing waves with increasing amplitudes. "Extra energy" means total energy inside the box minus energy of the straight domain wall. From top to bottom, the amplitudes of the standing waves are $\hat{D} = 0.5, 1, 2, 4, 6$ and 8, with corresponding curvatures (i.e., ratio of string thickness to radius of curvature) $\kappa = \delta\hat{D}\omega_0^2 = 0.07, 0.14, 0.28, 0.56, 0.84$ and 1.12. In all cases, the frequency of the standing wave is $\omega_0 < m/2$.

3.3.2 Radiation from internal mode excitations

A homogeneous internal excitation on the domain wall (one with zero wave number, or in other words, one that does not depend on the y coordinate) would have an angular frequency $\omega_1 = \Omega_1 > m/2$, as it is clear from (3.9) and (3.11). Therefore, such a perturbation will be able to emit radiation at the quadratic level.

For a homogeneous excitation of the shape mode,

$$\phi(t, x, y) = \phi_k(x) + \hat{A}(t) \cos(\Omega_1 t) \times \bar{f}_1(x) \ , \tag{3.16}$$

the problem of the decay rate of its amplitude due to the non-linear coupling to the scattering states is identical to the $1+1$ dimensional case studied in chapter 2. The amplitude of the internal mode decreases in time following the Manton-Merabet law (2.30):

$$\hat{A}^{-2}(t) = \hat{A}^{-2}(0) + 0.0150546 \ t \ . \tag{3.17}$$

The amplitude decreases slowly compared to the natural time scale of the system, which is the light-crossing time of the thickness of the soliton. This justifies the interest in the amplitude of these modes in field theory simulations, which can be running for a short time compared to this decay time.

We can also look at the evolution of more complicated configurations where the shape mode is excited in the form of a standing wave with some finite wavelength along the y direction. The analytic estimates presented in appendix C show that decay time scale for these inhomogeneous modes is comparable to the one obtained in the homogeneous case for frequencies not too large compared to the mass of the propagating particle in the bulk[2].

All these considerations suggest that we could try to write an effective action for the excited domain walls for small curvatures and time scales smaller than the decay time scale of the bound state. In this regime, the amount of radiation from the domain wall should be subdominant and one could try to find the relevant couplings between the different modes on the string worldsheet. This action would allow us to explore the mechanical backreaction of the shape mode on the strings, which may be the cause of the discrepancies between field

---

[2] We can also think about travelling waves of the shape mode moving in one direction. However, these configurations are related to the standing wave configuration by a boost in the longitudinal direction of the string. Therefore, we could estimate the new time scale associated to their decay by performing this boost on the standing wave mode.

theory and Nambu-Goto simulations. However, before we do that, let us first identify the correct effective action in the absence of any internal excitation. After that, we will add new terms to the action that capture the new dynamics and couplings between the zero modes and the internal modes.

3.4 The dynamics of bare domain wall strings

Let us consider the low-energy dynamics of our domain wall strings. At these low energies, the internal mode will not get excited, so one can assume that the only dynamical degree of freedom is the position of the wall. Furthermore, we will also assume that there are no high-curvature regions excited on the string, so that we can neglect the effects of radiation. If these conditions are met, the expectation is that the domain wall will behave as dictated by the Nambu-Goto action:

$$S = -\mu \int \sqrt{-\gamma}\, d^2\zeta \,, \tag{3.18}$$

where ζ^0 and ζ^1 are the string worldsheet coordinates and γ is the determinant of the worldsheet metric:

$$\gamma_{ab} = \eta_{\alpha\beta}\partial_a X^\alpha \partial_b X^\beta \,. \tag{3.19}$$

Here, $X^\alpha\left(\zeta^0, \zeta^1\right)$ denotes the position 3-vector of the string and the partial derivatives are taken with respect to the worldsheet coordinates.

As explained in chapter 1, the Nambu-Goto equations of motion for a generic parametrization of the string worldsheet are given by

$$\partial_a\left(\sqrt{-\gamma}\gamma^{ab}X^\mu_{,b}\right) = 0 \,. \tag{3.20}$$

Our goal in this section is to compare the solution of these equations to the actual motion of the domain wall string in field theory.

In section 1.4, we showed that the equations of motion (3.20) reduce to the linear wave equation in the conformal gauge, in which the string worldsheet is parametrized by $\zeta^0 = t$ (the usual Minkowski time) and $\zeta^1 = \sigma$ (the string energy measured from an arbitrary point on the string). In this case, the solution takes the simple form (1.29):

$$\vec{X}\left(t, \sigma\right) = \frac{1}{2}\left[\vec{a}\left(\sigma - t\right) + \vec{b}\left(\sigma + t\right)\right] \,, \tag{3.21}$$

with the constraints (1.30):

$$|\vec{a}\,'|= |\vec{b}\,'|= 1. \tag{3.22}$$

We will use this solution in terms of left and right movers to obtain the Nambu-Goto trajectory given some initial conditions for the position of the string in field theory. The details of this Nambu-Goto reconstruction can be found in appendix E.

3.4.1 Colliding wiggles on a straight domain wall

Here we will closely follow the setup studied in the case of local cosmic strings in [86] and discuss the collision of wiggles on a straight domain wall. In order to accurately compare the evolution of the soliton with the Nambu-Goto prediction, we need to start with an initial condition that is close enough to an exact solution of the full field theory equations. Otherwise, the possible deviations from the Nambu-Goto dynamics could just be due to the lack of precision in the initial configuration. Using the results presented in [115], we can set an initial condition that is extremely close to an exact solution of the non-linear scalar field theory. Consider the configuration

$$\phi(t,x,y) = \phi_k\left[x - \psi_+(y+t) - \psi_-(y+t)\right], \tag{3.23}$$

where $\psi_+(y+t)$ and $\psi_-(y-t)$ represent wiggles propagating in opposite directions on the wall. From the Vachaspati-Vachaspati solution (3.12), it is clear that (3.23) is in fact a configuration that can be made to be arbitrarily close to an exact solution provided that the two functions $\psi_+(y+t)$ and $\psi_-(y-t)$ do not have significant overlap, or in other words, if the wiggles are sufficiently far away from each other.

If the wiggles are very mildly curved, so that the curvature of the domain wall is always small even when the waves overlap, there will be no radiation and the Nambu-Goto prediction should be accurate. Note that this is also the expectation even if the wiggles have large amplitudes, provided that their curvature is kept small.

For low-amplitude wiggles, one would expect them to propagate at the speed of light almost unaffected by the presence of the other one. This expectation is based on the fact that, in this limit, the Vachaspati-Vachaspati wiggle reduces to the linear zero mode perturbation given in (3.10). However, the generic Nambu-Goto equations (3.20) are non-linear, so we would like to explore the regimes where we can probe these non-linearities.

Looking at the Nambu-Goto solution in the conformal gauge, given in (3.21), one might conclude that arbitrary wiggles colliding on a straight domain wall just pass through one another unaffected in their shape. In this case, it is not clear what the non-linearities do even for large-amplitude wiggles. This puzzle can be resolved by looking at the particular form of the Nambu-Goto equation in the "static gauge", defined by the parametrization

$$\zeta^0 = t \,, \qquad \zeta^1 = y \ . \tag{3.24}$$

In this case, the Nambu-Goto action reads

$$S_{\text{static gauge}} = -\mu \int dt\; dy \sqrt{1 + \psi'^2 - \dot{\psi}^2} \,, \tag{3.25}$$

which is the action for a scalar field $\psi(t, y)$ (the x coordinate) with a $1 + 1$ dimensional Born-Infeld-like Lagrangian. The equation of motion coming from this action is

$$\partial_t \left(\frac{\dot{\psi}}{\sqrt{1 + \psi'^2 - \dot{\psi}^2}} \right) - \partial_y \left(\frac{\psi'}{\sqrt{1 + \psi'^2 - \dot{\psi}^2}} \right) = 0 \ . \tag{3.26}$$

It is clear that a particular set of solutions of this equation is given by functions of the form $\psi(y \pm t)$, i.e., by waves moving at the speed of light along the domain wall. In this way, we recover the Vachaspati-Vachaspati solution within the Nambu-Goto description. Note that the equation is clearly non-linear, and only when we have small amplitudes we will approximately recover the linear wave equation for a generic configuration $\psi(t, y)$.

The effect of the non-linearities is simply to create a delay in the wiggles as they pass through one another. One can understand this intuitively by noticing that the wiggles travel at the speed of light in (t, σ) space (employed in the conformal gauge), not in (t, y) space. The σ parameter traversed by each wiggle is greater than the y distance by an amount given by the invariant length of the other wiggle. This difference is then translated as a temporal delay. The conserved Hamiltonian coming from the action (3.25) can be easily shown to be

$$H = \mu \int dy \frac{1 + \psi'^2}{\sqrt{1 + \psi'^2 - \dot{\psi}^2}} \,, \tag{3.27}$$

and the delay experienced by one of the wiggles can be found by subtracting the length of the string in the y direction from the length H/μ corresponding to the other wiggle.

Thinking in terms of the conformal gauge solution helps us understand the scattering process. Since the theory is integrable, the wiggles cannot change their shape or produce $1+1$ dimensional radiation in the collision, so this is the only possible outcome of the interaction between the asymptotic waves. This type of behaviour is reminiscent of the interaction of solitons in integrable models like the Sine-Gordon equation [1].

We have checked these predictions of the Nambu-Goto approximation by performing field theory simulations of the collision of wiggles on the domain wall string. As previously mentioned, we need a large initial separation between the wiggles in order for them to be as close as possible to exact Vachaspati-Vachaspati solutions. We evolve the initial configuration given in equation (3.23) with

$$\psi_+\left(y+t\right) = \frac{-8}{\sqrt{\lambda}\eta}\left[\tanh\left(\frac{\sqrt{\lambda}\eta\, y+\sqrt{\lambda}\eta\, t-120}{12}\right)-\tanh\left(\frac{\sqrt{\lambda}\eta\, y+\sqrt{\lambda}\eta\, t-80}{12}\right)\right], \tag{3.28}$$

$$\psi_-\left(y-t\right) = \frac{8}{\sqrt{\lambda}\eta}\left[\tanh\left(\frac{\sqrt{\lambda}\eta\, y-\sqrt{\lambda}\eta\, t+120}{12}\right)-\tanh\left(\frac{\sqrt{\lambda}\eta\, y-\sqrt{\lambda}\eta\, t+80}{12}\right)\right]. \tag{3.29}$$

For these simulations, we chose $L_x = 100/(\sqrt{\lambda}\eta)$, $L_y = 400/(\sqrt{\lambda}\eta)$ for the size of the box and $\Delta x = 0.1/(\sqrt{\lambda}\eta)$, $\Delta t = 0.05/(\sqrt{\lambda}\eta)$ for the lattice spacing and time step. We ran for thousands of time steps in order to let the wiggles collide several times, taking advantage of the periodic boundary conditions in the y direction and the absorbing conditions in the x boundaries.

The wiggles (3.28) and (3.29) are quite flat even for big amplitudes, which is convenient because we want to avoid high curvatures that could spoil the comparison with the Nambu-Goto dynamics. For these particular wiggles, the curvature (i.e., the ratio of the string thickness to the radius of curvature) during interaction is around 0.12 (at most).

A comparison between the field theory and the Nambu-Goto trajectories is shown in figure 3.4. We see almost perfect agreement. We also exemplify the delay generated by the non-linearity of the Nambu-Goto equation by plotting the position of the string according to the linear wave equation. This delay is also shown in figure 3.5, where we plot the position of the center of the wiggles in a (t, y) spacetime diagram. Using (3.27) and (3.28) or (3.29), we checked that the delay in this simulation is indeed given by

$$\frac{H}{\mu} - L_y = \int_{-L_y/2}^{L_y/2} dy\, \psi_{\pm}'^2 \approx \frac{13.7}{\sqrt{\lambda}\eta}\,. \tag{3.30}$$

Finally, we have also explored the scattering of wiggles when high-curvature regions are produced. We show in figure 3.6 the amount of energy in the box in our numerical simulations. We see that energy is emitted in bursts of radiation from the high-curvature region that emerges every time the wiggles collide. This behaviour is very similar to the one observed in [86]. After each collision, the domain wall behaves again like a Nambu-Goto string with wiggles of different shape.

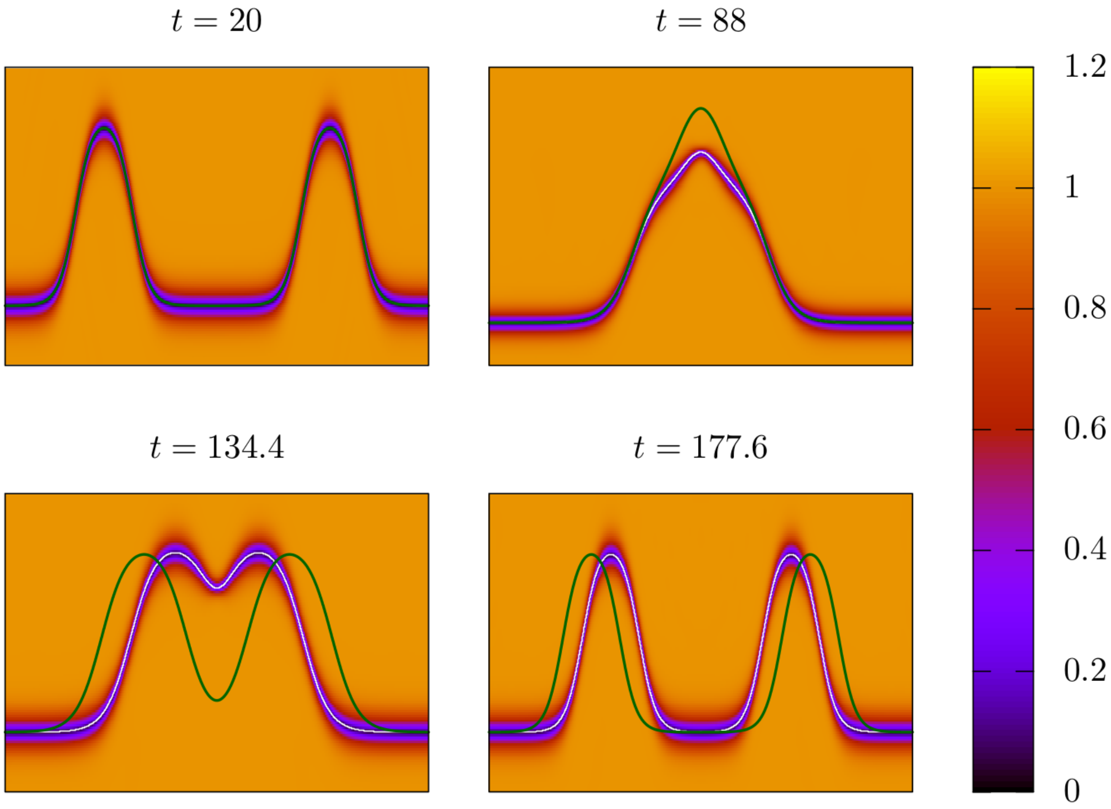

Figure 3.4: Field theory simulation of the collision of low-curvature wiggles propagating on a straight domain wall string. We show the absolute value of the field, $|\phi|/\eta$, in the two-dimensional simulation space. The white curve represents the position of the domain wall according to the Nambu-Goto action, while the green curve corresponds to the solution of the linear wave equation. The time labels are displayed in units of $(\sqrt{\lambda}\eta)^{-1}$, and the ranges of x (vertical axis) and y (horizontal axis) in these units are the following: $y \in [-150, 150]$ and $x \in [-5, 20]$ for the $t = 20$ and $t = 177.6$ panels, $y \in [-100, 100]$ and $x \in [-5, 30]$ for the $t = 88$ panel, and $y \in [-100, 100]$ and $x \in [-5, 20]$ for the $t = 134.4$ panel.

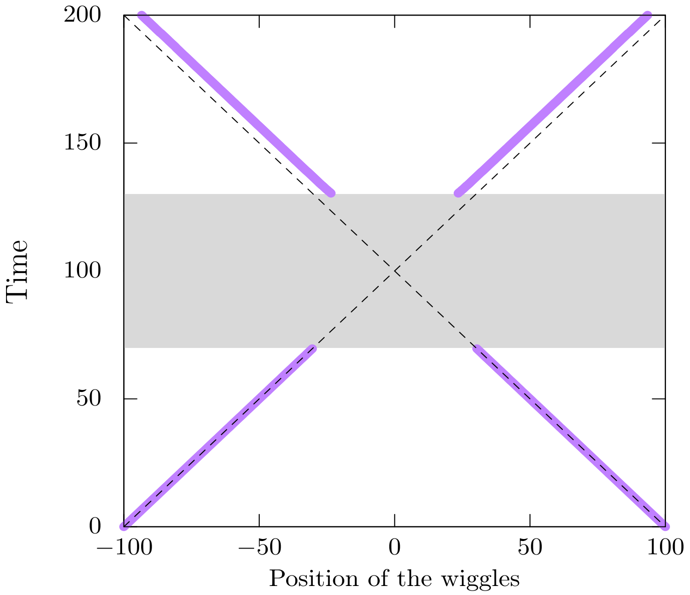

Figure 3.5: Spacetime diagram for the position of the wiggles propagating on the straight domain wall string obtained directly from the field theory simulation (in purple) and for speed of light propagation (dashed line). The shaded grey region indicates the time during which the wiggles overlap.

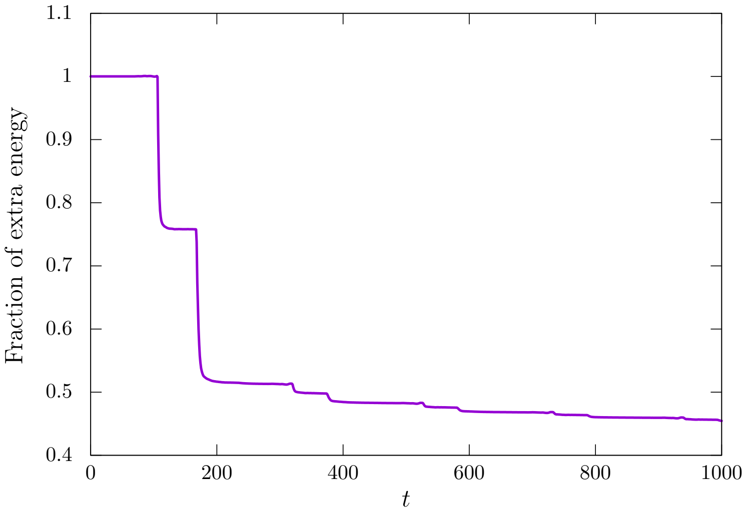

Figure 3.6: Fraction of extra energy as a function of time, displayed in units of $(\sqrt{\lambda}\eta)^{-1}$, for high-curvature wiggles colliding on the wall. "Extra energy" means total energy inside the box minus energy of the straight domain wall, or in other words, the energy of the wiggles on the straight domain wall. In this case, the maximum ratio of string thickness to radius of curvature is approximately $\kappa \approx 0.44$ at the moment of the collision.

In summary, we have checked explicitly that the non-linear behaviour of the Nambu-Goto action reproduces almost perfectly the field theory solution in the case of a low-curvature domain wall string.

3.4.2 Standing waves

We also compared the evolution of a standing wave in the Nambu-Goto description with the actual solution in field theory. Similarly to what we did in section 3.3, we took our initial conditions for the standing wave in field theory to be the ones described by equation (3.13). Choosing the amplitude $\hat{D}$ and the frequency ω_0 of the standing wave with some care, we can study the behaviour of solutions within the small-curvature regime where the Nambu-Goto action should be valid. Our results can be summarized as follows:

- For $\omega_0 < m/2$, the field theory and Nambu-Goto trajectories coincide for very long periods of time. This is reasonable as the radiation in this case is quartic in the amplitude of the perturbation.
- For $m/2 < \omega_0 \lesssim m$, the field theory and Nambu-Goto trajectories coincide for some oscillations, but then they cease to be in phase. We attribute this to the fact that the zero mode couples quadratically to the scattering states, so the energy radiated per unit time is higher than in the previous case.
- For $\omega_0 > m$, the agreement between the field theory and Nambu-Goto trajectories lasts again for very long periods of time. This is also expected as the radiated power is suppressed for high frequencies of the standing wave (see figure 3.2).

3.5 Effective theory including the internal mode

As previously mentioned, internal modes could add a substantial amount of energy to the domain wall, and, consequently, its dynamics may be significantly altered. This is somewhat similar to what happens with superconducting cosmic strings, where the current on the string core effectively modifies the equation of state of the string [116, 117].

One can easily calculate how the equation of state of the domain wall string changes when the shape mode is excited. Here we will consider a homogeneous shape mode perturbation with amplitude $A(t) \approx \hat{A}\cos(\Omega_1 t)$. If one inserts the field configuration

$$\phi(t,x,y) = \phi_k(x) + A(t) \times \bar{f}_1(x) \tag{3.31}$$

in the energy-momentum tensor of the scalar field, given in equation (2.26), one can obtain the energy per unit length and the tension of the excited wall as a function of the amplitude of the internal mode. After integrating over the transverse x direction, one gets, at quadratic order in the amplitude,

$$\mu_A = \mu \left(1 + \frac{9}{8\sqrt{2}} \frac{\sqrt{\lambda}}{\eta} \hat{A}^2 + ... \right) \tag{3.32}$$

and

$$\tau_A(t) = -\mu \left(1 + \frac{9}{8\sqrt{2}} \frac{\sqrt{\lambda}}{\eta} \hat{A}^2 \cos(2\Omega_1 t) + ... \right) , \tag{3.33}$$

One can also obtain these results by postulating the following effective action for a scalar field θ that lives on the string worldsheet and represents the amplitude of the internal mode:

$$S = \int d^2\zeta \sqrt{-\gamma} \left[-\mu + \frac{1}{2}\gamma^{ab}\partial_a\theta\partial_b\theta - \frac{1}{2}m_\theta^2\theta^2 \right] . \tag{3.34}$$

As before, the coordinates ζ^0 and ζ^1 parametrize the string worldsheet and γ_{ab} is the induced metric. On the other hand, the mass of the scalar field $\theta\left(\zeta^0, \zeta^1\right)$ is $m_\theta = \Omega_1 = \sqrt{3}m/2$.

At the linear level, this theory describes the free degrees of freedom propagating on the straight domain wall, namely, the massless Goldstone modes and the massive internal mode. Taking it beyond the linear order, the theory describes a non-trivial interaction between these modes which could lead to interesting effects.

It is important to note that, since this effective action disregards the presence of radiation, it should only be valid for small amplitudes of the internal perturbation θ. In the following subsection, we aim to test the validity of this action by simulating the collapse of circular domain wall in the full field theory.

3.5.1 Domain wall ring collapse

Note that the massive mode in this $1+1$ dimensional theory introduces a new time scale associated with its oscillating period $\tau_m \sim 1/m_\theta$. For times much larger than this, the average effect of the shape mode excitation on a straight domain wall is to increase its energy density, but it does not modify its tension. For a uniformly excited wall, this would seem to decrease the speed of propagation of the transverse excitations of the string. In the case of a closed loop, this suggests that its collapse would be slowed down. We have performed field theory simulations of the collapse of a circular domain wall and this is indeed the case:

the larger the initial amplitude of the internal mode, the slower the collapse. However, since this effective action disregards the presence of radiation, we should only restrict to small amplitudes.

The spacetime position of the circular domain wall can be parametrized as follows:

$$X^\mu(t,\tilde{\sigma}) = (t, R(t)\cos(\tilde{\sigma}/R_0), R(t)\sin(\tilde{\sigma}/R_0)) \ , \tag{3.35}$$

where $\tilde{\sigma}$ is proportional to the arc length and $R(t)$ is the radius of the loop. Initially, $R(0) = R_0$. Without any excitation, or in other words, with $\theta = 0$ everywhere in the loop, the previous action yields the equation

$$\dot{R}^2 = 1 - \left(\frac{R}{R_0}\right)^2 \ , \tag{3.36}$$

which is satisfied for

$$R(t) = R_0 \cos\left(\frac{t}{R_0}\right) \ . \tag{3.37}$$

This represents the evolution of a static ring that collapses under its own tension in a time $t_c = \pi R_0/2$.

Let us now consider the case of a ring with some extra energy due to the presence of an excited internal mode. In our language, this means that $\theta(t=0) \neq 0$. In this case, the equation of motion coming from the effective action is

$$\begin{aligned}\ddot{R}(t) = -\frac{(1-\dot{R}^2)}{R} \times \Bigg[\frac{1}{F(\theta) + \frac{\dot{\theta}^2}{2\mu}\frac{1+2\dot{R}^2}{1-\dot{R}^2}} \Bigg(F(\theta) + \frac{1}{2\mu}\dot{\theta}^2 \left(\frac{2\dot{R}^2 - 1}{1-\dot{R}^2}\right) + \\ + \frac{R\dot{R}\dot{\theta}}{\mu}\left(\frac{\ddot{\theta}}{1-\dot{R}^2} + m_\theta^2\theta\right)\Bigg)\Bigg] \ ,\end{aligned} \tag{3.38}$$

$$\ddot{\theta} + \dot{\theta}\frac{\dot{R}}{R}\left(1 + \frac{R\ddot{R}}{1-\dot{R}^2}\right) + (1-\dot{R}^2)m_\theta^2\theta = 0 \, , \tag{3.39}$$

where

$$F(\theta) = \left(1 + \theta^2\frac{m_\theta^2}{2\mu}\right) \ . \tag{3.40}$$

If the equation for θ is rewritten in terms of the time coordinate in the rest frame of the collapsing wall, $\tau = t/\Gamma = t\sqrt{1-\dot{R}^2}$, it takes the form of the equation of a real scalar field in a $1+1$ dimensional Friedmann-Lemaître-Robertson-Walker universe with scale factor $R(\tau)$. As one can easily check, this exercise yields

$$\frac{d^2\theta}{d\tau^2} + \frac{1}{R}\frac{dR}{d\tau}\frac{d\theta}{d\tau} + m_\theta^2\theta = 0\,. \tag{3.41}$$

Note that this $1+1$ dimensional universe is collapsing, so the second term in this equation is an anti-fricton term that will drive θ to higher amplitudes.

We compared the prediction of the coupled equations (3.38) and (3.39) with the results obtained in a field theory simulation. Taking advantage of the symmetry of the problem, we solved the field theory equation of motion in a $1+1$ dimensional lattice, assuming that the scalar field ϕ is only a function of time and the radial coordinate. We took the initial radius of the domain wall loop to be very large compared to its thickness. In this limit, the kink solution centered at this radius is pretty close to an exact solution for the radial profile of the field. Therefore, the shape mode excitation is also a good approximation for the initial perturbation. We imposed an absorbing boundary condition at infinity and a vanishing value of the derivative of the field at the center of the loop, and we ran the simulation in a box of size $L = 1200$, with lattice spacing $\Delta x = 0.012$ and time step $\Delta t = 0.004$. The initial radius was chosen to be $R_0 = 1000 \gg \delta \sim 1$. All these quantities are given in units of $(\sqrt{\lambda}\eta)^{-1}$.

The results and the comparison with the solution of equations (3.38) and (3.39) are shown in figure 3.7. The effective action seems to be an accurate description of the collapse provided that one starts with a relatively small value of the amplitude of the shape mode. For larger amplitudes, the effective description is spoiled by the presence of a significant amount of radiation. However, it is also possible that the effective action (3.34) may need some correction.

3.5.2 Parametric resonance within the effective action description

Let us conclude this section by indicating another important effect that is already hinted in our effective action approach. As one can see in equation (3.33), the tension of the excited domain wall string oscillates when internal modes are present. This suggests that one could have parametric resonance effects that would trigger the appearance of transverse excitations in the position of the wall. This is analogous to the non-relativistic string resonance already discussed a long time ago in [118]. Indeed, one can easily identify this behaviour by looking

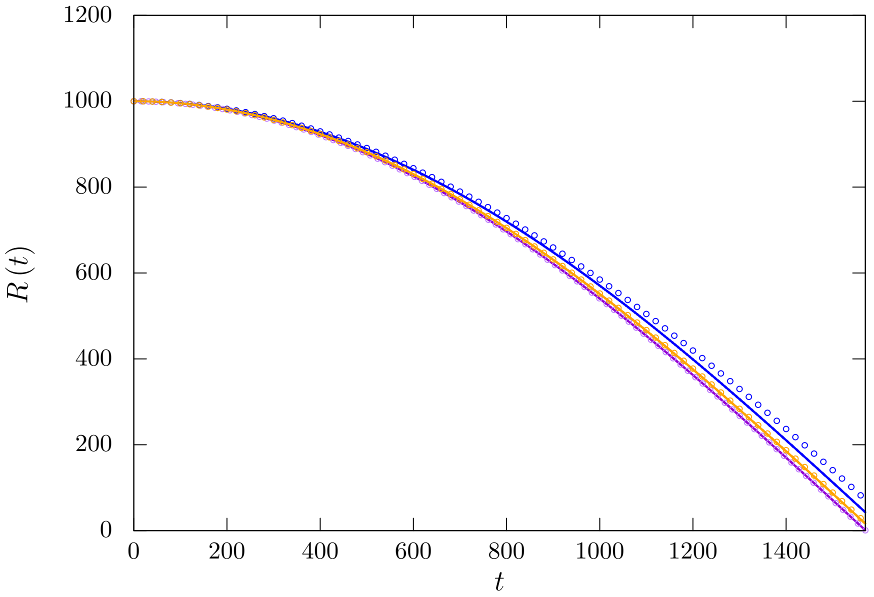

Figure 3.7: Radius of the ring as a function of time for $\theta\,(t=0)=0$ (purple), $\theta\,(t=0)=0.2$ (orange) and $\theta\,(t=0)=0.4$ (blue). The solid curves are the result of the field theory simulation, while the ones with circles correspond to the solution of the coupled equations (3.38) and (3.39). Time and the radius of the loop are displayed in units of $(\sqrt{\lambda}\eta)^{-1}$.

at the equation of motion for the position of the wall coming from the effective action (3.34):

$$\partial_a\left[\sqrt{-\gamma}(\mu\gamma^{ab}+T^{ab})\partial_b X^\mu\right]=0\,, \tag{3.42}$$

where T^{ab} is the effective energy-momentum tensor associated with the scalar field θ representing the bound state amplitude, which is given by

$$T^{ab}=\gamma^{ab}V\left(\theta\right)-\frac{1}{2}\gamma^{ab}\gamma^{cd}\partial_c\theta\partial_d\theta+\gamma^{ac}\gamma^{bd}\partial_c\theta\partial_d\theta\,, \tag{3.43}$$

with

$$V\left(\theta\right)=\frac{1}{2}m_\theta^2\theta^2\,. \tag{3.44}$$

Let us parametrize the spacetime position of the string, which lies along the y direction, as $X^\mu(t,y)=(t,\psi(t,y),y)$. For simplicity, let us take the transverse displacement of the string to be $\psi(t,y)=D(t)\cos(\omega_0 y)$. Substituting this in (3.42), one gets

$$\ddot{D}(t)+\omega_0^2\left(1-\frac{\dot{\theta}^2}{\mu}\right)D(t)=0\,. \tag{3.45}$$

If we approximate the amplitude of the shape mode by the lowest-order solution, $\theta\left(t\right) = \hat{A}\cos\left(\Omega_1 t\right)$, this equation takes the form of the Mathieu equation. This means that the internal mode would trigger the amplification of a standing wave with frequency $\omega_0 = \Omega_1$ in the position of the string.

In the following section, we will explore the presence of this type of renonance phenomena in field theory simulations.

3.6 Parametric resonances in field theory simulations

3.6.1 Dimensionless variables

From now on, to make the comparison to our numerical simulations more direct, we will work with the following set of dimensionless variables:

$$\tilde{\phi} = \phi/\eta, \quad \tilde{t} = \sqrt{\lambda}\eta t, \quad \tilde{x} = \sqrt{\lambda}\eta x, \quad \tilde{y} = \sqrt{\lambda}\eta y\,. \tag{3.46}$$

With this rescaling, the action reads

$$S = \frac{\eta}{\sqrt{\lambda}} \int d^3\tilde{x} \left[\frac{1}{2}\partial_\mu\tilde{\phi}\partial^\mu\tilde{\phi} - \frac{1}{4}\left(\tilde{\phi}^2 - 1\right)^2\right]\,, \tag{3.47}$$

where the partial derivatives are now with respect to the dimensionless spacetime coordinates. The mass of small fluctuations about the vacuum, the energy per unit length of the static domain wall solution and the angular frequency of the homogeneous shape mode are now given by $\tilde{m} = m/(\sqrt{\lambda}\eta) = \sqrt{2}$, $\tilde{\mu} = \mu/(\sqrt{\lambda}\eta^3) = \sqrt{8/9}$ and $\tilde{\Omega}_1 = \Omega_1/(\sqrt{\lambda}\eta) = \sqrt{3/2}$, respectively. Moreover, the amplitude of the shape mode will be rescaled as $\tilde{\hat{A}} = \lambda^{1/4}\hat{A}/\sqrt{\eta}$, which is still dimensionless.

After this rescaling, the equation of motion (3.2) is free of parameters:

$$\frac{\partial^2\tilde{\phi}}{\partial\tilde{t}^2} - \frac{\partial^2\tilde{\phi}}{\partial\tilde{x}^2} - \frac{\partial^2\tilde{\phi}}{\partial\tilde{y}^2} + \left(\tilde{\phi}^2 - 1\right)\tilde{\phi} = 0\,. \tag{3.48}$$

In the following, we will drop the tildes for simplicity, but all variables will refer to these new dimensionless quantities.

3.6.2 Parametric instability for a homogeneous internal excitation

As we pointed out in the previous section, perturbing the domain wall with the shape mode can lead to the subsequent excitation of a particular zero mode. This type of parametrically resonant excitations of the transverse position of the string by perturbations on its tension have been known and studied for a long time. In fact, this is one of the first examples of parametric resonance events in the history of physics [118].

The simplest way to identify this phenomenon in our field theory context is to assume the following particular ansatz for the perturbations around the static straight domain wall:

$$\phi(t,x,y) = \phi_k(x) + A(t)\bar{f}_1(x) + D(t)\bar{f}_0(x)\cos(\omega_0 y) \ , \tag{3.49}$$

where $\bar{f}_0(x)$ and $\bar{f}_1(x)$ are given by the wave functions found in section 3.2.

We will consider the string to be in a box with periodic boundary conditions along the y direction. This is, of course, a particular truncation of the most generic ansatz we can write. In particular, we are disregarding any coupling of this configuration to any radiating mode. Therefore, we have to consistently assume that the amplitudes of the modes involved in this calculation are sufficiently small.

Substituting (3.49) in the Lagrangian density and integrating in the x and y directions (from $-L_y/2$ to $L_y/2$ in the latter case) yields the following mechanical Lagrangian L for the amplitudes:

$$\begin{aligned} \frac{2}{L_y}L \quad = \quad & -\frac{4\sqrt{2}}{3} + \dot{A}^2(t) - \frac{3}{2}A^2(t) + \frac{1}{2}\dot{D}^2(t) - \frac{1}{2}\omega_0^2 D^2(t) - \frac{3}{2}C_1 A^2(t)D^2(t) \\ & -\frac{3}{4}C_1 A^4(t) - \frac{9}{16}C_1 D^4(t) - 3C_2 A(t)D^2(t) - 4C_2 A^3(t) \, , \end{aligned} \tag{3.50}$$

where

$$C_1 = \int_{-\infty}^{\infty} dx \bar{f}_1^2\,(x)\,\bar{f}_0^2\,(x) = \frac{3\sqrt{2}}{35} \, , \tag{3.51}$$

$$C_2 = \int_{-\infty}^{\infty} dx\, \phi_k\,(x)\,\bar{f}_1\,(x)\,\bar{f}_0^2\,(x) = \frac{3\sqrt{3}\pi}{64 \times 2^{3/4}} \, . \tag{3.52}$$

The Euler-Lagrange equations then read

$$\ddot{A}(t) + \frac{3}{2}\left[1 + C_1 D^2(t)\right] A(t) + 6C_2 A^2(t) + \frac{3C_1}{2}A^3(t) + \frac{3C_2}{2}D^2(t) = 0 \, , \tag{3.53}$$

$$\ddot{D}(t) + \left[\omega_0^2 + 6C_2 A(t) + 3C_1 A^2(t)\right] D(t) + \frac{9C_1}{4} D^3(t) = 0\,. \tag{3.54}$$

Suppose that we start out with a small homogeneous excitation of the shape mode and an even smaller "seed" zero mode perturbation in the form of a standing wave. Neglecting higher-order terms, the equations above reduce to

$$\ddot{A}(t) + \frac{3}{2} A(t) = 0\,, \tag{3.55}$$

$$\ddot{D}(t) + \left[\omega_0^2 + 6C_2 A(t)\right] D(t) = 0\,. \tag{3.56}$$

The amplitude of the shape mode oscillates harmonically with frequency $\Omega_1 = \sqrt{3/2}$, that is, $A(t) = \hat{A}\cos(\Omega_1 t)$, and the amplitude of the zero mode obeys a Mathieu equation [119]. As we will see below, this implies that a zero mode with a particular frequency will be amplified. However, the simplified equations (3.55) and (3.56) only hold for the short-term evolution of the system. As $D(t)$ grows, $A(t)$ must decrease in order for the energy associated to the reduced mechanical Lagrangian (3.50) to be conserved. At some point, the term proportional to $A(t)$ in equation (3.56) becomes irrelevant and the source term proportional to $D^2(t)$ in equation (3.53) cannot be ignored anymore. Then, the coupled equations become

$$\ddot{A}(t) + \frac{3}{2} A(t) + \frac{3C_2}{2} D^2(t) = 0\,, \tag{3.57}$$

$$\ddot{D}(t) + \omega_0^2 D(t) = 0\,. \tag{3.58}$$

Now, the zero mode has stopped growing and the shape mode has become a forced harmonic oscillator. Therefore, $A(t)$ will start growing and $D(t)$ will decrease. This will take the system back to the regime of validity of the set of equations (3.55) and (3.56), and the cycle will start again.

The Mathieu equation (3.56) predicts that the zero mode amplifies exponentially for particular values of ω_0 and $\hat{A}$. Indeed, in this type of equations, the parametric resonance is identified with instability bands in the frequency-amplitude space. For our particular problem, the stability chart of equation (3.56) is shown in figure 3.8.

The zero mode is then expected to amplify for frequencies and amplitudes of the shape mode falling in these bands. Note that the unstable frequency $\omega_0 = \Omega_1$ found from the effective action in the previous section is also obtained here.

We simulated the evolution of a domain wall string with a homogeneous excitation of the shape mode by solving the full field theory equation of motion in a lattice. The initial conditions are

$$\phi\left(x,y,t=0\right)=\phi_k\left(x\right)+A(0)\bar{f}_1(x)+D(0)\bar{f}_0(x)\cos\left(\omega_0 y\right)\ , \tag{3.59}$$

$$\dot{\phi}\left(x,y,t=0\right)=0\,. \tag{3.60}$$

As exemplified in figure 3.9, the parametric resonance does indeed take place. For this particular example, we chose $\omega_0=2\pi/10$, $A(0)=0.5$ and $D(0)=0.02$, and we ran the simulation in a box with sides of length $L_x=L_y=20$, lattice spacing $\Delta x=0.01$ and time step $\Delta t=0.005$.

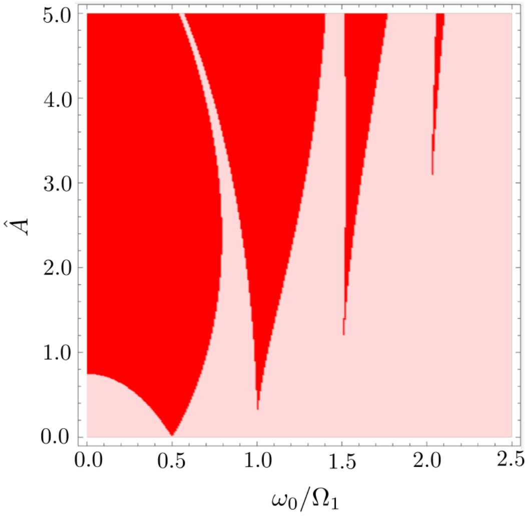

Figure 3.8: Mathieu chart for equation (3.56). The red bands indicate the regions of instability, and they are peaked at zero mode frequencies satisfying $\omega_0/\Omega_1=n/2$, where n is a natural number. These peaks are actually located at $\hat{A}=0$, but they are so narrow that this is impossible to visualize in the graph.

We also performed simulations with smaller initial amplitudes for the homogeneous shape mode perturbation in order to test the analytical equations (3.53) and (3.54). The comparison of the analytical solution with the amplitudes extracted directly from the full field theory simulation are shown in figure 3.10. Although the first pulse is predicted almost perfectly by the coupled equations, there is some deviation for the subsequent ones. Presumably, the reason for that radiation is emitted in this process, and this effect is not taken into account in our analytical approach.

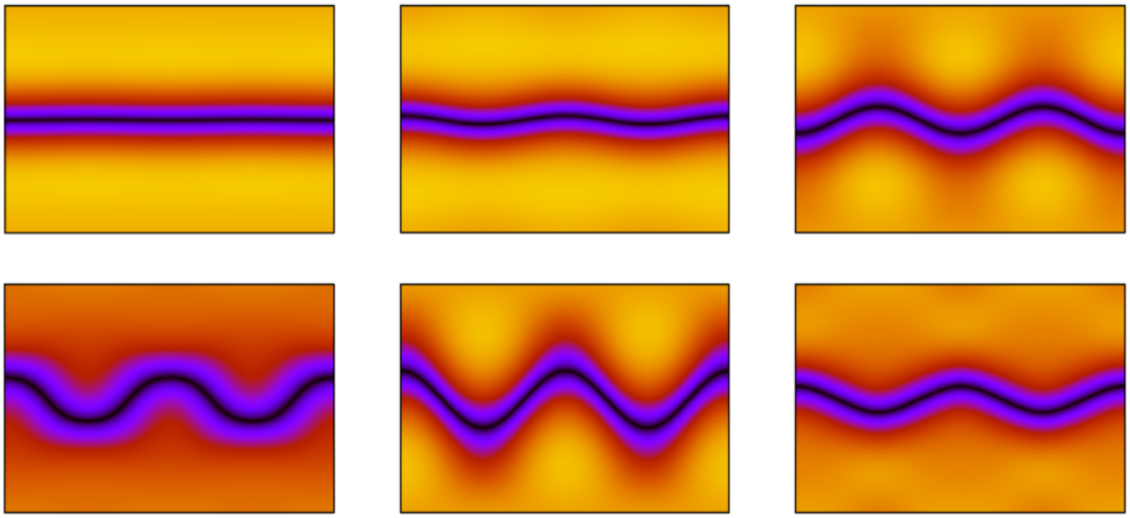

Figure 3.9: Parametric resonance excitation of a standing wave for the position of the domain wall string from a homogeneous shape mode perturbation. In these plots, x ranges from -4 to 4 (vertical axis), and y from -10 to 10 (horizontal axis).

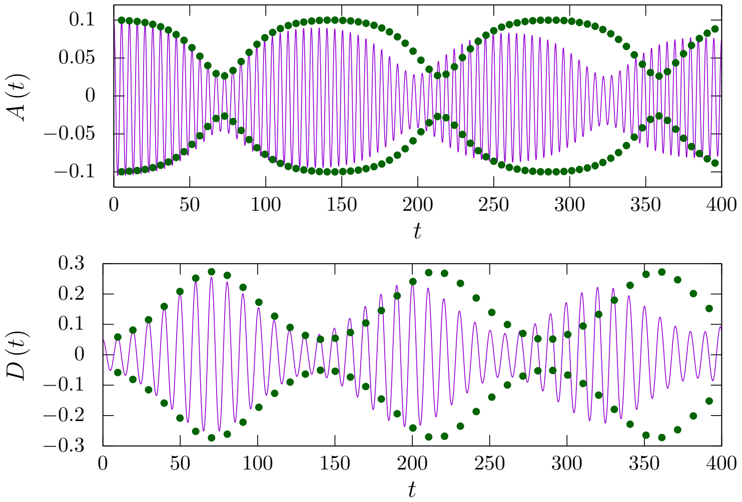

Figure 3.10: Amplitude of the shape mode (top panel) and the resonant zero mode (bottom panel) as a function of time. The values read from the simulation are shown in purple, and the green dots correspond to the solution of the coupled equations (3.53) and (3.54). In the latter case, we only show the envelope in order to make the comparison easier.

This parametric resonance can also be triggered by small thermal fluctuations surrounding an initially straight domain wall string, and also in the formation process of the walls in a phase transition (see figure 3.11). In these cases, as well as in the rest of our simulations, we always observed the amplification of a zero mode with frequency $\omega_0 \approx \Omega_1/2$.

Higher-frequency modes which are also allowed to grow in accordance to the Mathieu chart never showed up. We attribute this to the fact that, in a discrete lattice, where the zero mode frequencies are quantized, it is very hard to fall into the instability bands peaked at frequencies $\omega_0 > \Omega_1$, because they are extremely narrow for small amplitudes of the shape mode.

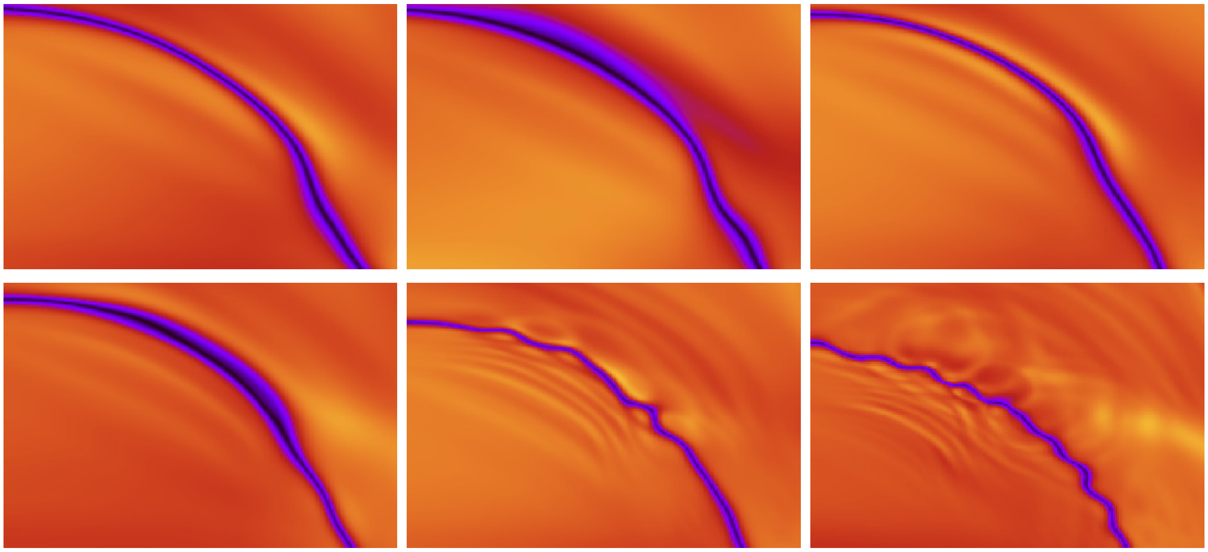

Figure 3.11: Several snapshots of the evolution of a domain wall soon after its formation in a cosmological phase transition. The shape mode is clearly excited in the segment of string shown. After a few oscillations, a zero mode of frequency $\Omega_1/2$ is amplified.

Finally, let us point out that the amplitude of the resonant zero mode can be estimated analyically. At the lowest order, the energy per unit length stored in the shape mode and the zero mode are respectively given by

$$E_s/L_y = \frac{3}{4}\hat{A}^2\,, \tag{3.61}$$

$$E_z/L_y = \frac{\omega_0^2}{4}\hat{D}^2\,. \tag{3.62}$$

Taking $\omega_0 = n\Omega_1/2$ and assuming that the shape mode transfers all its energy to the zero mode, one gets

$$\hat{D}_{\max} = \frac{2\sqrt{2}}{n}\hat{A}\,. \tag{3.63}$$

For $n = 1$, this is approximately what we get in figure 3.10.

3.6.3 Parametric instability for an inhomogeneous internal excitation

We will now consider a situation where the internal mode has the form of a standing wave. In this case, one can show that the initially straight domain wall develops an instability towards the formation of a standing wave with a couple of different wavelengths (see the snapshots in figure 3.12).

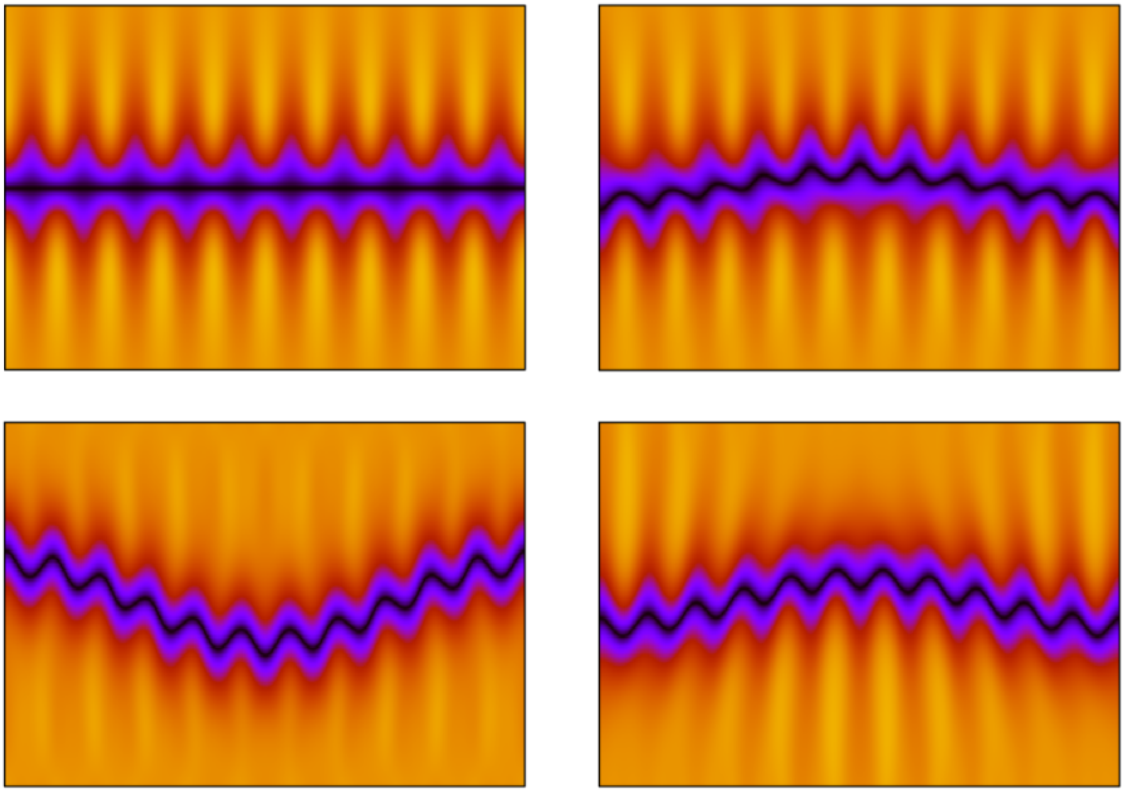

Figure 3.12: Standing wave in the internal mode decaying into a standing wave in the position of the domain wall string with two different frequencies. In these plots, x ranges from -5 to 5 (vertical axis), and y from -17 to 17 (horizontal axis).

We can explain this behaviour by substituting the ansatz

$$\phi(t,x,y) = \phi_k(x) + A(t)\bar{f}_1(x)\cos(k_s y) + D_1(t)\bar{f}_0(x)\cos(k_1 y) + D_2(t)\bar{f}_0(x)\cos(k_2 y) \quad (3.64)$$

into the Lagrangian. Dismissing terms proportional to the product of four amplitudes, this yields

$$\begin{aligned}\frac{2}{L_y}L &= -\frac{4\sqrt{2}}{3}+\frac{1}{2}\dot{A}^2(t)+\frac{1}{2}\dot{D}_1^2(t)+\frac{1}{2}\dot{D}_2^2(t)-\frac{1}{2}\left(\frac{3}{2}+k_s^2\right)A^2(t)- \\ &\quad -\frac{1}{2}k_1^2D_1^2(t)-\frac{1}{2}k_2^2D_2^2(t)-\frac{3C_2}{2}\left[C_3^{(1)}A(t)D_1^2(t)+C_3^{(2)}A(t)D_2^2(t)\right]- \\ &\quad -3C_2C_3^{(3)}A(t)D_1(t)D_2(t)\,, \end{aligned} \tag{3.65}$$

where C_1 and C_2 are given by (3.51) and (3.52), and

$$C_3^{(1)}=\begin{cases}0 & \text{if } k_1\neq k_s/2,\\ 1 & \text{if } k_1=k_s/2,\end{cases} \tag{3.66}$$

$$C_3^{(2)}=\begin{cases}0 & \text{if } k_2\neq k_s/2,\\ 1 & \text{if } k_2=k_s/2,\end{cases} \tag{3.67}$$

$$C_3^{(3)}=\begin{cases}0 & \text{if } k_1+k_2\neq k_s \text{ and } |k_1-k_2|\neq k_s,\\ 1 & \text{if } k_1+k_2=k_s \text{ or } |k_1-k_2|=k_s.\end{cases} \tag{3.68}$$

The equations of motion coming from this Lagrangian are

$$\ddot{A}(t)+\left(\frac{3}{2}+k_s^2\right)A(t)+3C_2D_1(t)D_2(t) = 0\,, \tag{3.69}$$

$$\ddot{D}_1(t)+k_1^2D_1(t)+3C_2A(t)D_2(t) = 0\,, \tag{3.70}$$

$$\ddot{D}_2(t)+k_2^2D_2(t)+3C_2A(t)D_1(t) = 0\,. \tag{3.71}$$

These are the correct equations for the amplitudes as long as the following three conditions are met: (i) $k_1\neq k_s/2$, (ii) $k_2\neq k_s/2$ and (iii) $k_1+k_2=k_s$ or $|k_1-k_2|=k_s$. This kind of system of coupled equations has been discussed before in the literature in connection with mechanical systems (see, for example, [120]). The results in these papers indicate that one can find solutions where a simultaneous resonant amplification of two different modes is possible provided that their wavenumbers satisfy the condition

$$k_1+k_2=\sqrt{\frac{3}{2}+k_s^2}\,. \tag{3.72}$$

In fact, one can find bands of instability quite similar in nature to the ones in the Mathieu equation, so this condition does not have to be completely sharp. If we also take into account condition (iii) above, we should expect amplification of two zero modes with frequencies

$$k_1 = \frac{k_s + \sqrt{\frac{3}{2} + k_s^2}}{2} \tag{3.73}$$

and

$$k_2 = \frac{-k_s + \sqrt{\frac{3}{2} + k_s^2}}{2} \,. \tag{3.74}$$

This is exactly what we found in our full field theory simulations.

In these simulations, the field was initialized according to equation (3.64). We performed two groups of simulations corresponding to two different wave numbers for the shape mode: $k_s = 2\pi/3.4$ and $k_s = 2\pi/5$. For each group we took several values for the length of the box in the y direction: $L_y = 17, 34, 51, 68$ for the former and $L_y = 20, 50, 75, 85, 100$ for the latter, with typical lattice spacing of $\Delta x = 0.03$ and time step $\Delta t = 0.01$.

3.6.4 An effective action including higher-order interactions

The effective action (3.34) discussed in the previous subsections does not capture the parametric resonance of the zero mode with frequency $\omega_0 = \Omega_1/2$. This discrepancy can be traced to the relevant oscillatory term in the associated Mathieu equations. In the effective theory description, that term is quadratic on the amplitude of the internal mode. However, in the field theory Lagrangian approach, the relevant term is linear. This explains the doubling of the resonant frequency between both models.

An interesting question that we might ask is whether we can supplement the effective action given in (3.34) in such a way that it can accommodate the coupling between the modes that we have uncovered in the field theory simulations. One possibility could be the presence of terms that couple the scalar field representing the internal mode amplitude, θ, and the Ricci scalar of the string worldsheet, $\mathcal{R}$. Note that $\mathcal{R}$ depends on derivatives of the position of the domain wall string. Therefore, this term describes a coupling between the shape mode and the Goldstone modes on the wall. Terms of this form, without the scalar field θ, have been proposed already in the context of higher-order corrections to the Nambu-Goto action [121, 122, 123, 124].

With this type of term, the effective action reads

$$S = \int d^2\zeta\sqrt{-\gamma}\left[\left(\alpha + \beta\theta\right)\mathcal{R} - \mu + \frac{1}{2}\gamma^{ab}\partial_a\theta\partial_b\theta - V\left(\theta\right)\right] , \tag{3.75}$$

where α and β are real constants and $V\left(\theta\right)$ is given in (3.44). Varying this action with respect to the coordinates of the string position, $X^\mu\left(\xi^0, \xi^1\right)$, we get the following equations of motion:

$$\partial_b\left[\sqrt{-\gamma}\left(M^{ab} - 2\beta F^{ab}\right)\partial_a X^\mu\right] = 0\,, \tag{3.76}$$

where the symmetric tensors M^{ab} and F^{ab} are given by

$$M^{ab} = 2\left(\alpha + \beta\theta\right)G^{ab} + \mu\gamma^{ab} + T^{ab}\,, \tag{3.77}$$

$$F^{ab} = \gamma^{ac}\gamma^{bd}\partial_c\partial_d\theta - \gamma^{ab}\partial_c\left(\gamma^{cd}\partial_d\theta\right)\ . \tag{3.78}$$

On the one hand, $G^{ab} = R^{ab} - \frac{1}{2}\gamma^{ab}\mathcal{R}$ in equation (3.77) is the Einstein tensor, which vanishes in $1+1$ dimensions. On the other hand, T^{ab} is the energy-momentum tensor of the scalar field, given in equation (3.43).

Assuming that θ is only a function of time, the expansion of equation (3.76) for $X^1 = \psi\left(t, y\right)$ to lowest order in θ and ψ reads

$$\ddot{\psi} - \left(1 + \frac{2\beta}{\mu}\ddot{\theta}\right)\psi = 0\,. \tag{3.79}$$

Finally, using the approximation $\theta\left(t\right) = \hat{A}\cos\left(\Omega_1 t\right)$ and assuming that $\psi\left(t, y\right) = D\left(t\right)\cos\left(\omega_0 y\right)$, we find a Mathieu equation for the amplitude of the zero mode:

$$\ddot{D}\left(t\right) + \omega_0^2\left[1 - \frac{2\beta\Omega_1^2}{\mu}\hat{A}\cos\left(\Omega_1 t\right)\right]D\left(t\right) = 0\,. \tag{3.80}$$

Therefore, amplification occurs for waves of frequency $\omega_0 = \Omega_1/2$, as observed in our lattice field theory simulations. It should be stressed, however, that this result does not imply that (3.75) is the correct effective action for the dynamics of the excited domain wall string. All we can say is that this action is consistent with the phenomenon observed in field theory simulations.

3.6.5 New time scale of radiation

In the previous sections, we have shown that shape mode excitations can trigger the resonant amplification of Goldstone modes. This non-linear process can potentially lead to radiation from the domain walls. Here we show that this is indeed what happens.

We first performed a simulation in $1+1$ dimensions of a kink initially excited with a shape mode perturbation of amplitude $A(t=0)=0.3$. The energy stored in the internal mode decays due to the non-linear coupling to the scattering states in accordance with the Manton-Merabet law. On the other hand, we performed a simulation in $2+1$ dimensions with the initial state of a straight domain wall string perturbed homogeneously with an internal mode of the same amplitude, $A(0)=0.3$. Furthermore, contrary to the previous simulation, we allow for the parametric resonance to happen. Then, we compare the decay of the energy stored in the bound state in the $1+1$ simulation with the energy per unit length in the bound state in the $2+1$ simulation. This is shown in figure 3.13.

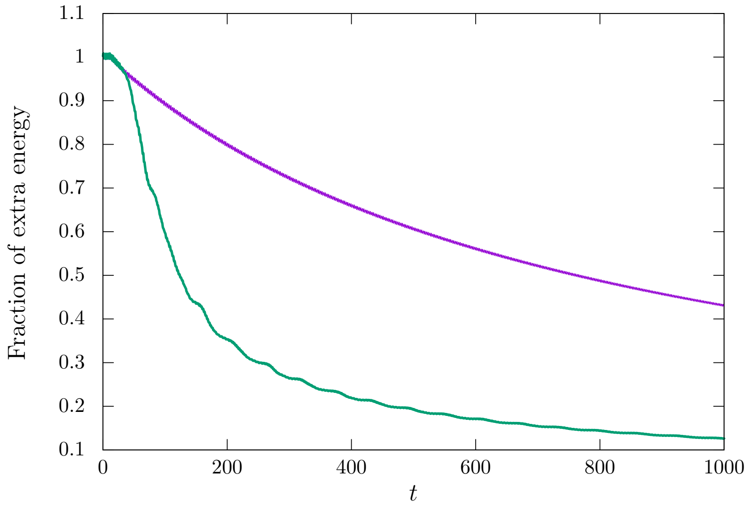

Figure 3.13: Fraction of extra energy inside the box as a function of time in a $1+1$ simulation (purple curve) and in a $2+1$ simulation where the resonance occurs (green curve). “Extra energy” means additional energy with respect to the static domain wall solution.

Therefore, when the domain wall is allowed to resonantly oscillate along the y direction, the rate of radiation is higher. In other words, this interaction between the shape mode and the zero mode reduces the lifetime of the internal excitations.

3.7 Dynamical excitation of the internal modes

One of the interesting points about the existence of internal excitations in these models is their relatively long lifetime. We have shown that, for small amplitudes, these excitations could survive for a time much larger than the natural time scale of the problem, m^{-1}. This makes these modes potentially relevant for numerical simulations since the time scale of the runs is shorter than their lifetime.

As it is clear from figure 3.11, the internal mode can be excited when the domain walls are formed in a cosmological phase transition, and the resonance phenomena studied in the previous sections take place. As we have seen, these processes enhance the emission of radiation from the strings, so it seems reasonable to expect that this mechanism would effectively shut off in a time scale smaller than the Manton-Merabet time associated to the natural non-linear decay of the amplitude of the shape mode. However, even the Manton-Merabet time scale is very small compared to the age of the universe, so one may conjecture that the internal modes do not play a relevant role in the dynamics of defects at late, cosmological times.

In this section, we ask whether there exists any mechanism that replenishes the internal modes of the defects in the course of their cosmological evolution. If this was the case, the shape mode could still have relevance in the long-term dynamics of the solitons.

In order to study this possibility, we first consider a relaxed domain wall string and investigate whether the interaction between Goldstone modes could lead to a transfer of energy to the internal mode. We do this by simulating the collision of wave packets of specific frequencies travelling at the speed of light in opposite directions on the string. After the collision, we inspect the straight segment of the domain wall left behind after the wiggles have passed through one another (see figure 3.14). One can look for the possible excitation of the internal mode in this segment by projecting out the scalar field configuration onto the shape mode. Note that the computation of the amplitude of the shape mode during the time that the wiggles overlap (the shaded region in figure 3.15) is problematic due to the rapid motion of the domain wall. However, we are only interested in the result after the collision. The projection can be trusted then.

We simulated these collisions in a lattice with $L_x = 32$, $L_y = 800$, $\Delta x = 0.08$ and $\Delta t = 0.02$.

The initial state is given by equation (3.23) with

$$\psi_+ (y+t) = -\frac{B}{4}\left[\tanh\left(\frac{y+t-220}{25}\right) - \tanh\left(\frac{y+t-180}{25}\right)\right]\cos\left[\omega\left(y+t\right)\right] , \qquad (3.81)$$

$$\psi_- (y-t) = \frac{B}{4}\left[\tanh\left(\frac{y-t+220}{25}\right) - \tanh\left(\frac{y-t+180}{25}\right)\right]\cos\left[\omega\left(y-t\right)\right] . \qquad (3.82)$$

These are sinusoidal wiggles with amplitude controlled by B and angular frequency ω. We performed three groups of simulations: wiggles with frequency $\omega = 2\pi/20$ (below the resonance frequency), $\omega = 2\pi/10$ (very close to the resonance frequency) and $\omega = 2\pi/5$ (above the resonance frequency). In each case, B was adjusted to get the desired ratio of string thickness to radius of curvature of the order of 0.1.

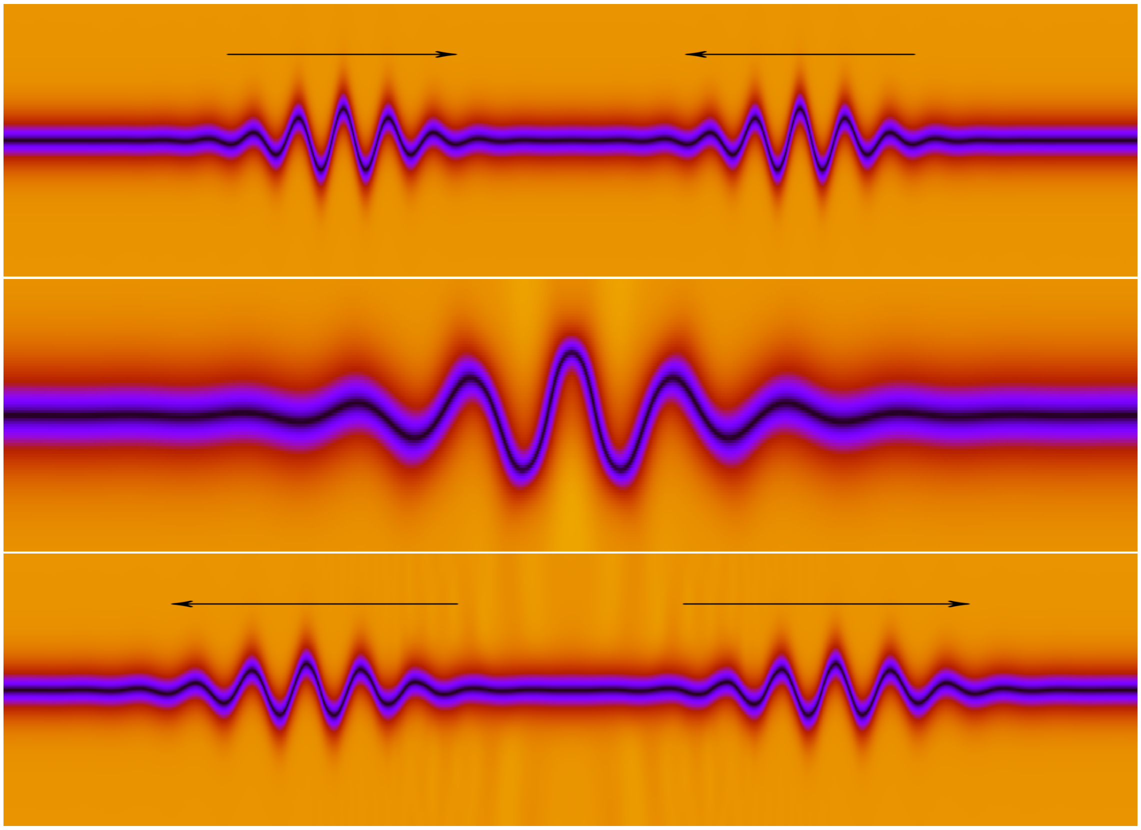

Figure 3.14: Collision of two sinusoidal wave packets on the domain wall. We show the initial conditions at the top panel, the moment of maximum overlap in the middle and a configuration after the collision at the bottom. From top to bottom, the vertical axis x ranges from -8 to 8, -4 to 4 and -8 to 8, while the horizontal axis y ranges from -250 to 250, -100 to 100 and -200 to 200.

Our results indicate that the internal mode is not excited by any appreciable amount except in one particular situation: if the frequency of the wiggles is half of the frequency of the internal mode, the domain wall segment left behind after the collision is excited. This can be understood from equations (3.53) and (3.54), by noticing that the zero mode acts as a driving source for the internal mode. When the two wiggles overlap, one forms a standing wave for a short period of time with the appropriate frequency to resonantly excite the amplitude of the internal mode. Other frequencies do not lead to an amplification of the shape mode, as shown in figure 3.15.

Since one does not expect a big number of such high-frequency Goldstone modes at late times, the dynamical transfer of a significant amount of energy to the internal modes of the defects seems unlikely. Therefore, it is reasonable to conclude that shape mode excitations do not play a relevant role in the long-term dynamics of the solitons in a realistic setting.

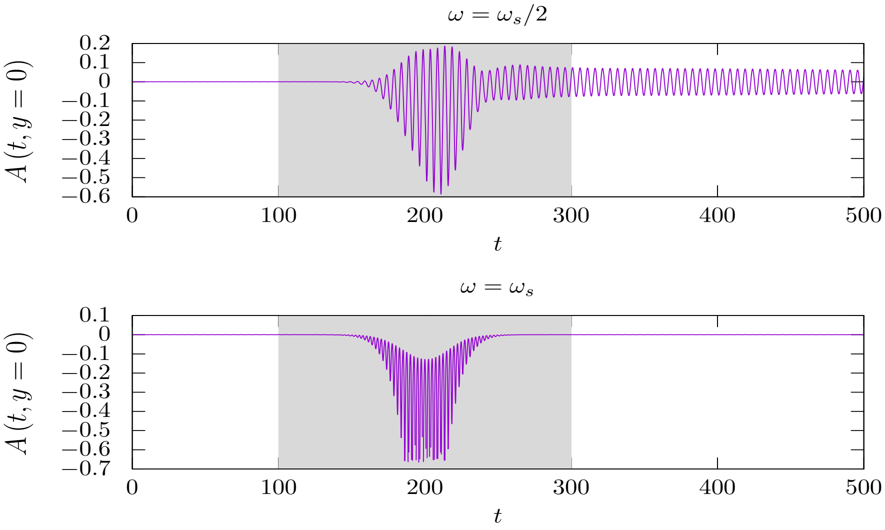

Figure 3.15: Amplitude of the shape mode as a function of time at $y = 0$, the center of the box. The shaded region represents the time during which the wiggles overlap. The internal mode remains excited after the collision only when the frequency of the wiggles is $\omega = \Omega_1/2$.

3.8 Conclusions

In this chapter, we have investigated the dynamics of domain walls in a scalar field theory in $2+1$ dimensions. We began our study by finding the static domain wall string solution and the spectrum of perturbations around it. This spectrum consists of the shape mode, associated with propagating fluctuations in the string thickness; the zero mode, representing local displacements of the string that also travel along the object, and scattering modes, which correspond to vacuum excitations that propagate freely to infinity (radiation).

Both the shape mode and the zero mode couple non-linearly to the scattering states, and this makes their amplitude slowly decay in time. The time scale associated to this decay is much larger than the natural time scale of the problem, given by the width of the soliton, or, equivalently, by the inverse of the mass m of perturbative excitations of the field in the vacuum. We analyzed the decay of small-amplitude zero modes in the form of standing waves and obtained the corresponding radiated power per unit length as a function of the frequency ω_0 of the wave. This power is highly suppressed for $\omega_0 < m/2$, in which case the emitted radiation is quartic in the amplitude of the perturbation, and for $\omega_0 > m$. In the latter case, this behaviour is due to the small overlap between the corresponding scattering states and the source of radiation.

The domain wall string can also radiate non-perturbatively in regions of high curvature. We have shown that, in the absence of such regions and provided that the shape mode is not excited, the dynamics of the wall is well described by the Nambu-Goto action.

The excitation of the shape mode modifies the equation of state of the domain wall string solution. In particular, this induces an oscillatory tension. Averaging over the oscillation period of the internal mode, one sees that the perturbation increases the energy per unit length of the soliton, whereas the tension stays the same. This suggests that wiggles on the string would propagate slower than in the absence of excitation. Moreover, the periodic time dependence of the tension can lead to resonance effects. In order to analytically describe the dynamics of the excited wall, we postulate an effective action that couples the position of the string to a massive scalar field that represents the amplitude of the shape mode and lives in the $1 + 1$ dimensional string worldsheet. This effectve action seems to capture both effects. On the one hand, we simulated in full field theory the collapse of a circular domain wall and found that the shape mode perturbation slows down the collapse. However, since the effective action disregards the presence of radiation, we can only test it for small amplitudes of the internal mode. In this regime, the radius of the wall as a function of time is accurately described by the effective equations of motion. On the other hand, the effective action predicts that the shape mode can trigger the amplification of a standing wave in the position of the string. The amplitude of this wave follows a Mathieu equation. For a homogeneous excitation of the internal mode, the resonant zero mode is predicted to have the frequency of the shape mode. We conjecture that such resonance phenomena could also take place in other effective theories as, for instance, in the context of braneworlds.

Our lattice field theory simulations of excited domain wall strings show that these parametric resonances do indeed take place in the full theory. However, the frequency of the amplified zero mode is found to be half of the frequency predicted by the effective action. This resonance at half the frequency of the shape mode is confirmed by our analytical calculations based on a reduced Lagrangian for the amplitudes of the modes. Therefore, one should include new couplings to the effective action in order for it to predict the correct resonance frequency. We have shown that a linear coupling between the scalar field representing the amplitude of the shape mode and the Ricci scalar of the string worldsheet does the job. This seems to indicate that such a term should indeed be present in the effective theory.

Our Lagrangian approach reveals that this resonance phenomenon is actually a self-regulated process: the zero mode borrows energy from the shape mode and gets amplified, but at some point it stops growing and gives the energy back to the internal mode, and then the cycle starts again. This analytical model is based on an ansatz for the scalar field which disregards the presence of radiation, so the exchange of energy between the modes is perpetual. However, radiation is actually emitted in this process. Indeed, we have shown that the energy initially stored in the shape mode decays faster than expected as a consequence of the resonance.

This faster decay of the energy stored in the shape mode suggests that the internal modes would only play a transient role in a cosmological context. However, this conclusion may change if there is any mechanism that is able to populate these modes later on in the evolution of the defects. We have investigated this possibility by simulating collisions of wiggles on the straight domain wall. Our results indicate that the shape mode is excited in the region of interaction only if the wiggles have the specific frequency of resonance. Long wavelength wiggles expected to be present at late times do not seem to have the capacity to populate the internal modes, so we conclude that these are only relevant for a short-term dynamics of the defects.

In chapter 5, we will see that the resonance phenomena discovered in this work are also present in $3+1$ dimensional strings. It should be noted that there are other processes that might excite the internal modes in that case. In particular, it was suggested in [84] that intercommutation processes (when a loop forms) could lead to internal excitations. At first, this might not seem to be enough to significantly affect the evolution of the loop as a whole. However, one should investigate this further.

Chapter 4

Internal excitations of $2+1$ dimensional global vortices

Here we extend the analysis of the internal modes of kinks in chapter 2 to global vortices in $2+1$ dimensions. Therefore, our investigations in this chapter concern a complex scalar field.

We study the spectrum of linearized excitations of these objects and identify the existence of localized excitation modes. Then, we compute the decay time scale of the first two and compare the results to the numerical evolution of the full non-linear equations. We also show numerically how the interaction of vortices with an external source of radiation or other vortices can excite these modes dynamically. Moreover, as we did in chapter 2, we simulate the formation of vortices in a phase transition and their interaction with a thermal bath and estimate the amplitudes of the internal modes in each case. These numerical experiments indicate that, even though vortices are capable of storing a large amount of energy in these internal excitations, this does not seem to happen dynamically. We finally explore the evolution of a network of vortices in a $2+1$ dimensional expanding background which expands as a $3+1$ dimensional universe dominated by radiation. We find that vortices are barely excited in the course of this cosmological evolution: the extra energy they store in these cosmological simulations never exceeds the 1% level of the total mass of the core of the vortex.

4.1 Introduction

Global vortices are the lower-dimensional counterparts of global strings. As explained in chapter 1, these cosmic strings are formed whenever a $U(1)$ global symmetry is spontaneously broken, and, very importantly, they are coupled to a long range field, the massless Goldstone mode associated with fluctuations in the angular part of the complex field [125]. After formation, the network of global strings will evolve losing energy by the emission of these massless modes, the would be axion particles. One of the most interesting aspects of this scenario is the idea of associating the axion to the dark matter in the universe [126, 127, 128]. In order to give an accurate calculation of the density of axions, one needs to understand the evolution of these networks. This program is currently being pursued by several groups that have used lattice field theory simulations to infer the long-term behaviour of the networks [59, 60, 58, 64, 129, 130, 131, 62, 63] (for earlier studies see [132, 133, 134, 52, 53]). Some of the properties of these networks are still under debate. In particular, there is currently some controversy about the asymptotic nature of the scaling regime and the spectrum of axions being produced by the network.

One of the key issues in this debate is whether one is able to have a sufficiently large dynamic range to be able to extrapolate the results from a small simulation to a cosmological setting. This is particularly important for the proper evolution of strings since they will eventually dominate the axion spectrum. Therefore, it is crucial to understand the underlying physics that controls the dynamics of these axionic strings. The effective theory for the string dynamics in these models is complicated by its coupling to low energy degrees of freedom propagating outside of the string, the axions. This means that the Nambu-Goto action for relativistic strings should be supplemented by a Kalb-Ramond term [39]. This coupling is important not only to understand the string radiation, but also its subsequent motion [135, 136, 137]. In this approach, one disregards the dynamics of the massive (radial) modes of the complex scalar field by assuming that the string is not significantly curved to excite them. These ideas have been investigated numerically. For instance, in [138, 139], the authors analyzed the dynamics of sinusoidally displaced string configurations in field theory simulations. Their results seemed to be in excellent agreement with radiation predictions using the Kalb-Ramond action [140, 141, 142]. However, recent simulations of global string loops created from the intersection of long strings in a box suggest a different picture, where a combination of massless and massive radiation has been observed [84]. This represents an important departure from the aforementioned Kalb-Ramond effective theory for a global string, which does not consider any massive radiation. It has been suggested that this could be due to the presence of internal excitations that lead to a transfer of energy from the string motion to massive states leaving the string. This chapter will be devoted to the analysis of these internal excitations in $2 + 1$ dimensional vortices as a preliminary step to understand the influence of these modes on the dynamics of global strings in $3 + 1$ dimensions, which will be our subject of study in chapter 5.

The organization of this fourth chapter is the following. In section 4.2 we provide the field theory model for the global vortices and the static solution. In section 4.3 we obtain the linearized equations of motion for the perturbations around this solution and identify their bound states, whose decay rates are found analytically and numerically in section 4.4. In section 4.5 we explore the possible excitation of the bound states by different external sources, and in section 4.6 we quantify the excitation in three realistic situations: when the vortices are formed in a phase transition, when they interact with a thermal bath and when they undergo cosmological evolution as part of a network. Finally, we conclude in section 4.7 with a brief discussion of the results and their impact regarding the evolution of axionic strings in numerical simulations as well as in a realistic cosmological setting.

Some examples of the simulations we have performed in this paper can be found at `http://tp.lc.ehu.es/earlyuniverse/global-vortex-simulations/`.

4.2 The global vortex solution

The simplest field theory model that allows for global vortex configurations is

$$S = \int d^3x \left[\eta^{\mu\nu} \partial_\mu \phi^* \partial_\nu \phi - \frac{\lambda}{4} \left(\phi^* \phi - \eta^2 \right)^2 \right] . \tag{4.1}$$

We will be using the following representation of the scalar field:

$$\phi = \frac{\phi_1 + i\phi_2}{\sqrt{2}}, \tag{4.2}$$

as well as the Argand representation:

$$\phi = \frac{\varphi}{\sqrt{2}} e^{i\frac{\alpha}{\eta}}. \tag{4.3}$$

Therefore, $\varphi = \sqrt{\phi_1^2 + \phi_2^2}$ and α will denote the radial and the angular parts of the field, respectively. The dimensions of the fields and the parameters are the following: $[\phi_1] = [\phi_2] = [\varphi] = [\alpha] = E^{1/2}$, $[\eta] = E^{1/2}$, $[\lambda] = E$.

Note that the model is invariant under a global $U(1)$ symmetry. However, the potential leads to spontaneous symmetry breaking, and the vacuum state is parametrized by $|\phi|^2 = \eta^2$. One can identify two degrees of freedom in the vacua: the one associated with radial excitations of the field and the one corresponding to the perturbations of the angular part. The former has a mass $m_r = \sqrt{\lambda}\eta$, whereas the latter is a massless Goldstone boson.

The equations of motion arising from the action (4.1) can be found to be

$$\frac{\partial^2\phi_{1,2}}{\partial t^2} - \frac{\partial^2\phi_{1,2}}{\partial x^2} - \frac{\partial^2\phi_{1,2}}{\partial y^2} + \frac{\lambda}{2}\left(\frac{\phi_1^2+\phi_2^2}{2} - \eta^2\right)\phi_{1,2} = 0, \tag{4.4}$$

or, in cylindrical coordinates (ρ, θ),

$$\frac{\partial^2\phi_{1,2}}{\partial t^2} - \frac{\partial^2\phi_{1,2}}{\partial \rho^2} - \frac{1}{\rho}\frac{\partial\phi_{1,2}}{\partial \rho} + \frac{1}{\rho^2}\frac{\partial^2\phi_{1,2}}{\partial \theta^2} + \frac{\lambda}{2}\left(\frac{\phi_1^2+\phi_2^2}{2} - \eta^2\right)\phi_{1,2} = 0. \tag{4.5}$$

The static vortex solution is given by

$$\phi_v\left(\rho,\theta\right) = \eta f(\rho) e^{i n_w \theta}\ , \tag{4.6}$$

where n_w is the winding number. After rescaling the radial coordinate by defining $r = \sqrt{\lambda\eta^2}\rho = m_r\rho$, the field equation for the profile function $f(r)$ in this ansatz is given by

$$\frac{d^2 f}{dr^2} + \frac{1}{r}\frac{df}{dr} - \frac{n_w^2}{r^2} f - \frac{1}{2}\left(f^2 - 1\right) f = 0. \tag{4.7}$$

We will take the appropriate boundary conditions with $f(0) = 0$ at the center of our coordinate system, so that the solution remains smooth there, and $f(r \to \infty) = 1$, so that the solution approaches the vacuum asymptotically. Using the equation of motion, one can show that the approximate behaviour of $f(r)$ for $r \to \infty$ is $f(r) = 1 - n_w^2/r^2 + \mathcal{O}(1/r^4)$, while for $r \to 0$, $f(r) = c\, r^{n_w} + ...$, where c is a constant. We show in figure 4.1 the profile function for the case $n_w = 1$. This solution, together with the angular part $(\alpha = \theta)$, is represented in the xy plane in figure 1.7 in the introductory chapter.

In the model studied in this chapter, the energy-momentum tensor for the complex scalar field reads

$$T_{\mu\nu} = \partial_\mu\phi^*\partial_\nu\phi + \partial_\nu\phi^*\partial_\mu\phi - \eta_{\mu\nu}\left[\eta^{\alpha\beta}\partial_\alpha\phi^*\partial_\beta\phi - V\left(\phi\right)\right]. \tag{4.8}$$

One can easily find the energy of the vortex solution by substituting $\phi = \phi_v$ in the energy density T^{00} and integrating over the plane. The result is

$$E_v = 2\pi\eta^2 \int_0^\infty r dr \left[\left(\frac{df}{dr}\right)^2 + \frac{n_w^2}{r^2} f^2 + \frac{1}{4}\left(f^2 - 1\right)^2\right]\ . \tag{4.9}$$

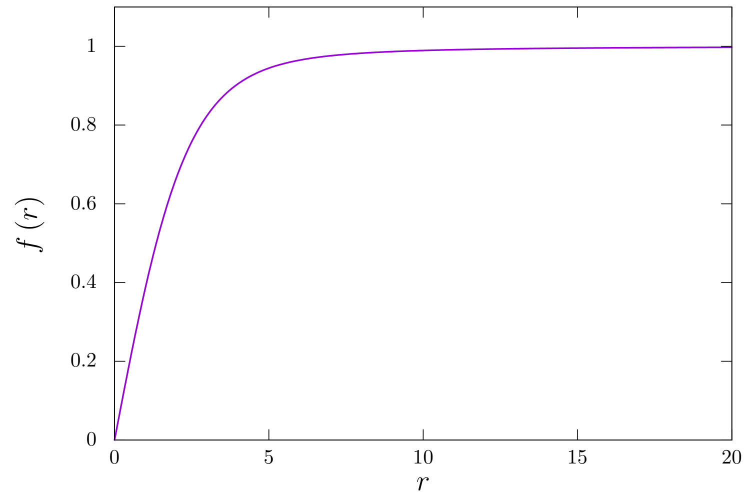

Figure 4.1: Profile function $f(r)$ for a static vortex with unit winding.

Plugging the profile for the function $f(r)$ in this expression, one can see two different contributions to the energy: one that is concentrated in the center of the vortex, in the region $r \lesssim 1$, associated with the massive degree of freedom, and another one that comes from the variation of the angular part (the f^2/r term). The first one gives a finite contribution to the energy, while the second one leads to a logarithmic divergence. In a realistic context, this divergence is cured by the presence of another string at some distance $r = R$. In that case, for the $n_w = 1$ vortex solution, we get

$$E_v \approx E_{\mathrm{core}} + 2\pi\eta^2 \ln\left(\frac{R}{\tilde{\delta}}\right) \, , \tag{4.10}$$

where $\tilde{\delta} \sim m_r\delta$, with δ denoting the dimensionful core thickness. Using the profile for the function $f(r)$ and calculating the integrals in equation (4.9), we can fit the values of the two different parts of the energy of the global vortex to

$$E_v \approx 4.9\eta^2 + 2\pi\eta^2 \ln\left(\frac{R}{2.15}\right) . \tag{4.11}$$

For $3+1$ dimensional global strings, this becomes the energy per unit length. The existence of these two different contributions is also reflected in the description of the dynamics of the strings. The Nambu-Goto effective action for relativistic strings is, in this case, supplemented by the existence of a term that describes the coupling of the string to the Goldstone mode. It turns out that there is a somewhat simpler description of this coupling in terms of a 2-form potential $B_{\mu\nu}$ that is dual to the Goldstone mode in four dimensions [143]. This field is naturally coupled to the string worldsheet through the so-called Kalb-Ramond action

[135, 143]. This effective action can thus be used to compute the radiative decay of these strings into the massless mode.

The global vortices are point-like objects in two spatial dimensions, and their coupling to the Goldstone boson can be described by assigning these vortices an electric charge. Their motion and radiation can then be studied in this limit where the massive radiation is neglected. One can then compare this simplified dual description with the full numerical evolution in terms of the complex scalar field.

4.3 Spectrum of perturbations

In this section, we aim to identify the spectrum of perturbations around the background solution of the global vortex with unit winding discussed above. This spectrum is composed of discrete bound states, translational zero modes and a continuum of scattering states.

Any generic perturbation around the global vortex solution can be split into its modification of the modulus of the field and the variation of the phase. Such separation makes sense especially when we look at the solution asymptotically. There, these degrees of freedom decouple and one can identify each of these fluctuations as part of the massive or the massless sector in the vacuum. This approach is analogous to the analysis of the spectrum of perturbations done in [144] for global strings.

Let us start with cylindrically symmetric perturbations, i.e., proportional to $e^{i\theta}$. This type of perturbations will correspond to fluctuations of the radial part of the field:

$$\phi(t,\rho,\theta) = \eta\left[f(\rho) + s(\rho)\cos\left(\omega t\right)\right]e^{i\theta}\,. \tag{4.12}$$

Here we are taking the function $s(\rho)$ to be a real function of the radial coordinate. Substitution into the equation of motion (4.5) yields, at linear order,

$$-s''(\rho) - \frac{s'(\rho)}{\rho} + U(\rho)s(\rho) = \omega^2 s(\rho), \tag{4.13}$$

with

$$U\left(\rho\right) = \frac{m_r^2}{2}\left[3f^2\left(\rho\right) - 1\right] + \frac{m_r^2}{\rho^2}\,. \tag{4.14}$$

This effective potential goes asymptotically to $U(r\to\infty) = m_r^2$, so we can expect that the spectrum has a set of bound states with $\omega^2 < m_r^2$, and a continuum of states beyond this point. This continuum will match asymptotically the vacuum solutions obtained by setting $f = 1$ in the previous equations, which in our case reduce to the Bessel functions of the first kind $J_1(k\rho + \omega t)$, with $\omega^2 = k^2 + m_r^2$.

It can be shown that, due to the slow decay of the potential at large distances from the core, there are infinitely many bound modes below the threshold $\omega = m_r$ (see page 117 of [145] for a description of this type of behaviour in quantum mechanics). A numerical scan of the possible frequencies has uncovered the existence of the first two bound states with frequencies

$$\omega_1^2 = 0.8133\, m_r^2\,, \tag{4.15}$$

$$\omega_2^2 = 0.9979\, m_r^2\,. \tag{4.16}$$

The first bound state had been already identified in [144] and more recently in [84], but the higher ones appear to have been missed by these earlier papers. Higher frequency modes belonging to the infinite set of bound states are all packed very close to the threshold of scattering states[1]. More importantly, they are highly delocalized with respect to the vortex core. This implies that, in order to study them numerically, one would need very large simulation boxes. Therefore, we will restrict the subsequent numerical analysis to the first two bound states, although the basic properties obtained for them may be easily extended to the other modes. We show the profile of these two first excitations in figure 4.2, as a function of the dimensionless radial coordinate $r = m_r\rho$. We will denote them as $s^{(1)}(r)$ and $s^{(2)}(r)$.

Note that there is quite a big difference between these two bound states, not only in their extent, but also in their shape. The first state represents a fairly localized mode with support mostly over the core of the vortex. Furthermore, since it is a solution of the linearized equations of motion for the perturbations, one may think that this localized state will oscillate forever without dissipation. This suggests an interpretation of this mode as a massive particle trapped in the core of the vortex. On the other hand, the effect of exciting this mode creates an oscillation of the apparent width of the vortex. In many respects, this mode is very similar to the shape mode found in chapters 2 and 3 for the kink and the domain wall strings.

---

[1] One can use the asymptotic behaviour of the effective potential (in our case, $U(\rho)/m_r^2 \approx 1 - 2/r^2$) to estimate the energy separation for these modes. See, for example, [146], vol II, page 1665.

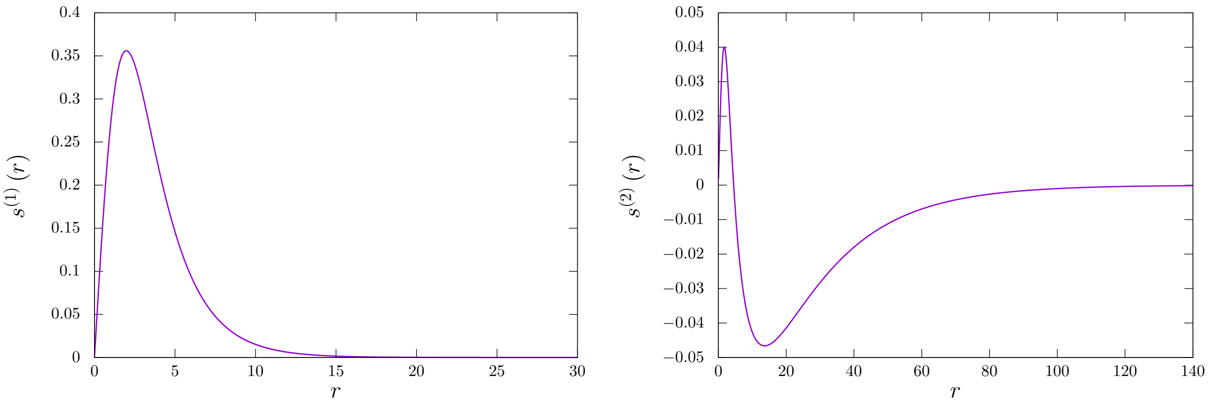

Figure 4.2: Normalized bound state functions $s^{(1)}(r)$ (on the left, with eigenvalue ω_1) and $s^{(2)}(r)$ (on the right, with eigenvalue ω_2). Note the difference of scales between both modes.

The situation for the second mode is somewhat similar, except that it is not so well localized. Its profile spreads over a much larger region than the soliton core. This property can be traced back to the fact that the frequency eigenvalue for this mode is very close to the continuum, so one can say that it is much more loosely trapped by the vortex. Moreover, as expected from a higher excitation mode, it has a node at some distance from the center of the vortex. This also means that its effect on the width of the soliton is less straightforward to interpret. Similar considerations can be made for the higher frequency bound states. We will collectively denote these modes as "internal excitations" of the vortex.

Let us now turn to perturbations associated with a small variation of the phase of the field. Such fluctuations would lead to an excited field configuration of the form

$$\phi(t,\rho,\theta) = \left[f(\rho) + i\bar{s}(\rho)\cos\left(\bar{\omega}t\right)\right]e^{i\theta}\,. \tag{4.17}$$

In this case, the equation of motion for the perturbation is

$$-\bar{s}''(\rho) - \frac{\bar{s}'(\rho)}{\rho} + \frac{\bar{s}(\rho)}{\rho^2} + \frac{m_r^2}{2}\left[f^2(\rho) - 1\right]\bar{s}(\rho) = \bar{\omega}^2\bar{s}(\rho), \tag{4.18}$$

which does not have any bound state (note that the asymptotic decay of the effective potential is now faster than in the case of the massive modes described above). Furthermore, its continuum spectrum starts at $\bar{\omega} = 0$ and the asymptotic states represent the excitations associated with the massless Goldstone mode in the vacuum. The solutions are written in terms of Bessel functions with the relation $\bar{\omega}^2 = k^2$. Finally, there is also a zero mode solution of the form $\bar{s}(\rho) = f(\rho)$, which just signals the invariance of our theory with respect to rigid phase rotations of the full background solution.

We can also consider perturbations with an azimuthal angular dependence. This corresponds to field configurations of the form

$$\phi(t,\rho,\theta) = \left(f(\rho) + \left[s_n^r(\rho)\cos(n\theta) + i s_n^i(\rho)\sin(n\theta)\right]\cos\left(\omega t\right)\right) e^{i\theta}. \tag{4.19}$$

In this case, the real and imaginary parts of the general fluctuation do not decouple and one is led to an eigenvalue problem for the following system of differential equations:

$$-\frac{d^2 s_n^r}{d\rho^2} - \frac{1}{\rho}\frac{ds_n^r}{d\rho} + \frac{s_n^r}{\rho^2}\left(n^2+1\right) + \frac{m_r^2}{2}\left(3f^2-1\right)s_n^r + \frac{2n}{\rho^2}s_n^i = \omega^2 s_n^r, \tag{4.20}$$

$$-\frac{d^2 s_n^i}{d\rho^2} - \frac{1}{\rho}\frac{ds_n^i}{d\rho} + \frac{s_n^i}{\rho^2}\left(n^2+1\right) + \frac{m_r^2}{2}\left(f^2-1\right)s_n^i + \frac{2n}{\rho^2}s_n^r = \omega^2 s_n^i. \tag{4.21}$$

We have scanned these equations for solutions with eigenvalues $\omega < m_r$, which would denote the presence of a bound state for this system. Our numerical investigations show that there are no further bound state solutions for $n < 10$ apart from the $n = 1$ zero modes associated with the rigid translations of the vortex on the xy plane. Although we do not have a definite proof, we conjecture that, indeed, there are no bound states in this system for larger values of n either.

As a final comment, let us mention that vortices with higher winding have a number of negative eigenvalues ($n > 1$) corresponding to the splitting of the object into lower-charge vortices (see [144]).

4.4 Decay rate of the perturbations

In the previous section, we identified two excitations of the vortex that correspond to localized perturbations of the radial degree of freedom of the complex scalar field. The calculation of the corresponding eigenfunctions $s^{(1)}(\rho)$ and $s^{(2)}(\rho)$ at the linear level shows that their frequencies are not large enough to propagate in the vacuum. However, as in the previous chapters, the amplitude of these modes will slowly decay due to the non-linear coupling to the scattering states.

4.4.1 Dimensionless variables

Before presenting our analytical and numerical results regarding the decay of the bound states, it is convenient to redefine the theory in terms of dimensionless variables. As in the previous chapters, we define

$$\tilde{\phi} = \frac{\phi}{\eta} \qquad \tilde{x} = \sqrt{\lambda}\eta x = m_r x \qquad \tilde{y} = \sqrt{\lambda}\eta y = m_r y \qquad \tilde{t} = \sqrt{\lambda}\eta t = m_r t \ , \tag{4.22}$$

and the radial coordinate ρ is correspondingly rescaled as $r = m_r \rho$. With these redefinitions, the action can be written as

$$S = \frac{\eta}{\sqrt{\lambda}} \int d^3\tilde{x} \ \left[\partial_\mu \tilde{\phi}^* \ \partial^\mu \tilde{\phi} - \frac{1}{4} \left(\tilde{\phi}^* \tilde{\phi} - 1 \right)^2 \right] . \tag{4.23}$$

In this expression, the partial derivatives are taken with respect to the dimensionless variables.

In what follows, we employ the dimensionless variables unless otherwise stated. However, once again, we will drop the tildes for the sake of simplicity in notation.

4.4.2 Analytical estimate

As we have already pointed out, the bound states decay slowly by their non-linear coupling to the scattering states. Their decay rate can be estimated analytically by means of the Green's function method. This calculation is very similar to the one we performed for the kink solution in chapter 2, and we present it in full detail in appendix C for the case at hand.

The starting point is to consider the general time-dependent profile for the vortex excited by the presence of the localized mode:

$$\phi(t, r, \theta) = f(r) e^{i\theta} + A_j(t) s^{(j)}(r) e^{i\theta} + \left[\eta_1(t, r) + i \ \eta_2(t, r) \right] e^{i\theta} \,, \tag{4.24}$$

where $j = 1$ or 2 and the functions $\eta_{1,2}(t, r)$ represent the scattering modes that will contribute to the radiation field[2]. Then, the main steps in the derivation of the decay rates are sketched as follows:

1. We substitute the field configuration (4.24) into the equations of motion (4.5). This leads to a differential equation for $\eta_1(t, r)$ and another one for $\eta_2(t, r)$. However, to

---

[2] The scattering states have been taken to possess the same cylindrical symmetry as the source of the perturbations.

second order in the amplitude, the perturbation only constitutes a source term for the former.

2. We find the asymptotic form of $\eta_1(t,r)$ using the Green's function method.

3. We plug this solution in the $0r$ component of the energy-momentum tensor (4.8) to compute the radiation power at spatial infinity.

4. We equate this rate of energy loss and the power corresponding to the configuration

$$\phi(t,r,\theta) = \left[f(r) + A_j(t)s^{(j)}(r)\right] e^{i\theta}\,, \tag{4.25}$$

which corresponds to the initial state, where no radiation is present. The equality between these two rates yields a differential equation for A_j, which we finally solve.

On the one hand, the result for the first bound state, $s^{(1)}(r)$, is

$$\hat{A}_1^{-2}(t) = \hat{A}_1^{-2}(0) + \Omega_1 t \qquad \Omega_1 = 0.00218\,. \tag{4.26}$$

On the other hand, the second mode, $s^{(2)}(r)$, decays according to

$$\hat{A}_2(t)^{-2} = \hat{A}_2^{-2}(0) + \Omega_2 t \qquad \Omega_2 = 2.77 \times 10^{-7}\,. \tag{4.27}$$

Note that the decay time scale of the second mode is much longer. This is basically due to the smaller overlap of the source in this second mode with the profiles of the scattering modes, hence decreasing the coupling of the source to the radiation field. A similar argument may be used for the higher bound modes, which are in fact spread over a much larger distance. This seems to indicate that their decay rate would also be more and more suppressed as one approaches the continuum threshold.

The previous calculation assumes that there is no coupling between these modes, and thus they evolve independently. However, in a realistic situation, there is always a small coupling between them. These couplings between modes of different frequencies will induce a variation or modulation of the amplitude of the modes that will be superimposed on the analytic expectation displayed above. We will show an example of this effect in the next subsection.

From the value of the amplitude, one can extract the energy stored in the bound state. This is done by substituting (4.25) into the 00 component of the energy-momentum tensor

(4.8). After integration over the plane, one gets

$$E_j \approx 2\pi\omega_j^2 \hat{A}_j^2 \, . \tag{4.28}$$

4.4.3 Numerical simulations

The analytical estimates (4.26) and (4.27) rely on a set of approximations. In order to confirm these results, we have conducted a series of numerical simulations with a static initial configuration consisting of the static vortex solution plus bound state perturbation:

$$\phi\left(t=0,r,\theta\right) = \left[f\left(r\right) + A_j\left(t=0\right) s^{(j)}\left(r\right)\right] e^{i\theta}. \tag{4.29}$$

In this case, it is clear that the field configuration should preserve cylindrical symmetry throughout the evolution. Therefore, one can assume that the field will be given by $\phi\left(t,r,\theta\right) = h\left(t,r\right) e^{i\theta}$, and the equations of motion reduce to the following radial equations:

$$\ddot{\phi}_{1,2} = \frac{\partial^2\phi_{1,2}}{\partial r^2} + \frac{1}{r}\frac{\partial\phi_{1,2}}{\partial r} - \frac{\phi_{1,2}}{r^2} - \frac{1}{2}\phi_{1,2}\left(\phi_1^2+\phi_2^2-1\right) \, , \tag{4.30}$$

which can be solved in a $1+1$ dimensional lattice. This is advantageous as it allows for high resolution simulations with bigger dynamic range. In the following sections, however, the assumption of cylindrical symmetry will not hold for some of our numerical experiments, in which case we will resort to a $2+1$ dimensional lattice.

Another important ingredient in our simulation scheme is the use of absorbing boundary conditions [106]. This technique allows us to run simulations for a long period of time without having to worry about the radiation bouncing off the simulation walls and affecting again the vortex. We used this type of boundary conditions in all our simulations except in section 4.6.3, where we employed periodic boundary conditions. The details can be found in appendix A.

In order to check the accuracy of the analytical estimates for the amplitude of the bound states, we need to read off this amplitude directly from the simulation. We do that by first finding at each moment the position of the vortex in our lattice. In $2+1$ dimensions, this is done by identifying the elemental lattice plaquette that has a non-zero winding. This is, of course, not needed in $1+1$ simulations since the vortex is always fixed at the origin by construction. This is the case for the problem at hand. After that, we subtract the background vortex solution centered at that point from the actual field configuration. This gives us all the perturbations present at that moment around that vortex. We can then project this perturbation field over each of the particular excitation modes we are interested in, using the orthogonality condition of the different modes.

We first set up the excitation separately, i.e., we either take $A_1\left(t=0\right)=0.2$ and $A_2\left(t=0\right)=0$, or $A_2\left(t=0\right)=0.2$ and $A_1\left(t=0\right)=0$. In both cases, the extra energy stored in the internal modes for these values of the amplitudes is about 5% of the energy of the vortex core. In the first case, we chose $L=40$, $\Delta x=0.004$ and $\Delta t=0.001$ for the size of the box, the lattice spacing and the time step. In the second case, since the second mode has a much larger spatial extent, we used $L=200$, $\Delta x=0.05$ and $\Delta t=0.01$.

We show in figure 4.3 the comparison between the amplitude $A_j(t)$ extracted directly from the simulation and the analytic predictions for $\hat{A}_j(t)$. We see that the analytic calculations do indeed capture the slow non-linear decay of these perturbations. Interestingly, even if we increase the amplitude beyond the linear regime, meaning taking initial amplitudes of order one, the analytical expressions given earlier are still a pretty good approximation. Therefore, in principle, these bound states can store a large fraction of the energy of the vortex core and still behave in a quasi-linear fashion, getting rid of it in a time scale much larger than the width of the soliton.

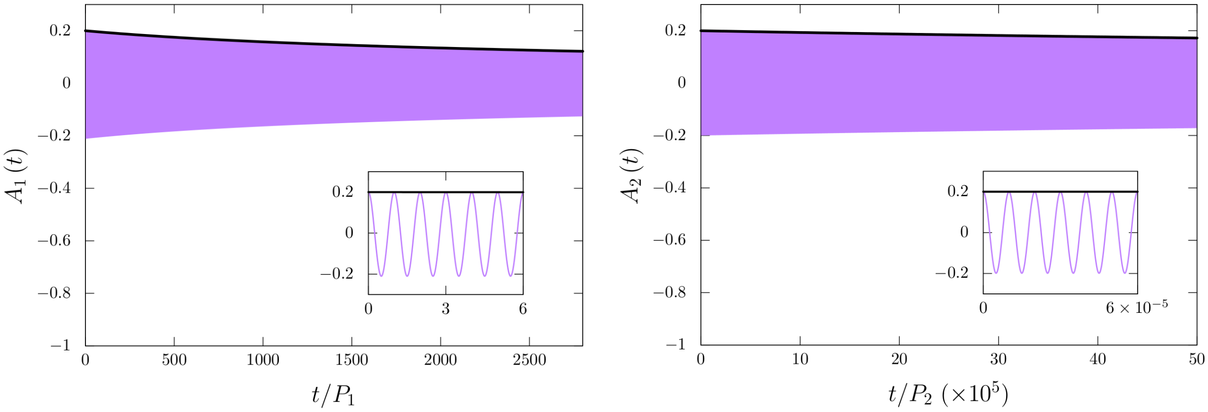

Figure 4.3: Amplitude of the bound modes (purple curve) as a function of time (displayed in units of the corresponding period) and comparison with the analytical estimate (solid black line). The inset shows the first few oscillations for each mode. On the left we show the first mode, whose period is $P_1=2\pi/\omega_1\approx 6.97$. On the right we show the second one, with period $P_2=2\pi/\omega_2\approx 6.29$.

We have analysed the spectrum of the radiation obtained from the decay of the excited vortex. The Fourier analysis of the radiation field demonstrates that most of the energy is radiated away at twice the frequency of the excited modes. Another interesting point to make is that this radiation is almost exclusively produced in terms of massive excitations. This is somewhat expected since the initial state corresponds to a perturbation of the radial part of the field. However, it is important to check that non-linear couplings between these modes do not lead to an appreciable radiation of the massless Goldstone mode. This fact could be used to disentangle the different sources of energy from a generic string state since, according to our simulations, the coupling of the zero mode of the vortex to the Goldstone mode will lead to massless radiation, whereas the internal excitations will mostly emit massive modes.

We have also evolved an initial configuration where both internal modes are excited. In this case, the small coupling between the modes leads to a modulation of their amplitudes. One can clearly see this effect in figure 4.4.

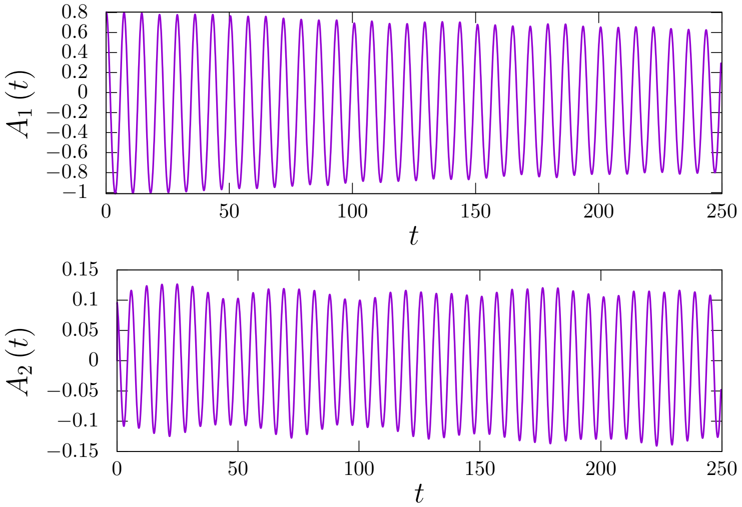

Figure 4.4: Non-linear coupling between the bound states. The first mode is initialized with an amplitude of 0.8 and the second one with an amplitude of 0.1. The amplitude of both modes is modulated by the presence of the other. The effect is more visible on the second mode.

Finally, we have also checked the evolution of these modes in a less symmetric situation by running the same initial conditions on a $2+1$ lattice. The results for the time dependence of the amplitude of the modes and the nature of the radiation emitted are essentially the same.

4.5 Exciting the bound states

Here we will explore some mechanisms that lead to the excitation of the bound states studied in the previous sections.

4.5.1 Exciting the vortex with massive radiation

Since the radiation of the excited states is mostly in the form of massive perturbations of the scalar field (perturbations of its radial part), it is reasonable to expect that the reverse process should also occur. Therefore, we have studied the effect of "illuminating" the vortex with massive radiation. In order to do that, we take advantage of the cylindrical symmetry of the problem and construct an initial state in $1+1$ dimensions consisting of an incoming wave packet directed towards the origin, where we place the background vortex solution. After bouncing off the center, the reflected energy from the scattering state is absorbed in the boundary and we are left with an excited vortex solution.

The specific form of the incoming wave packet is constructed as follows. As mentioned in section 4.3, a solution to the linearized equation for the scattering states in the asymptotic limit is the Bessel function of the first kind $J_1(kr+\omega t)e^{i\theta}$, with $\omega^2 = k^2+1$. Taking this into account, we design the initial condition for the field as

$$\phi(t,r,\theta) = \left[f(r) + B\ \mathcal{W}(r) J_1(kr+\omega t)\right] e^{i\theta}\,, \tag{4.31}$$

where $\mathcal{W}(r)$ is a window function that gives support to the wave on a finite region of space in our simulation, initially away from the core of the vortex. We take this window function to be

$$\mathcal{W}(r) = \frac{1}{4}\left[1+\tanh\left(r-20\right)\right]\left[1-\tanh\left(r-50\right)\right]\ . \tag{4.32}$$

Such an initial state is shown in figure 4.5.

For this particular initial configuration, the amplitude of the first bound state as a function of time is shown in figure 4.6. As we anticipated, the bound state is excited in this process. However, the level of excitation depends on a complicated way on the frequency as well as the amplitude of the incoming wave, and does not seem to follow a simple pattern. This fact seems to resemble the results found in $1+1$ dimensions for the case of the kink soliton in [147], where a fractal-like behaviour was encountered. Our purpose here is just to identify the different physical processes that can excite the bound state for the vortex, so we will not study this in more detail.

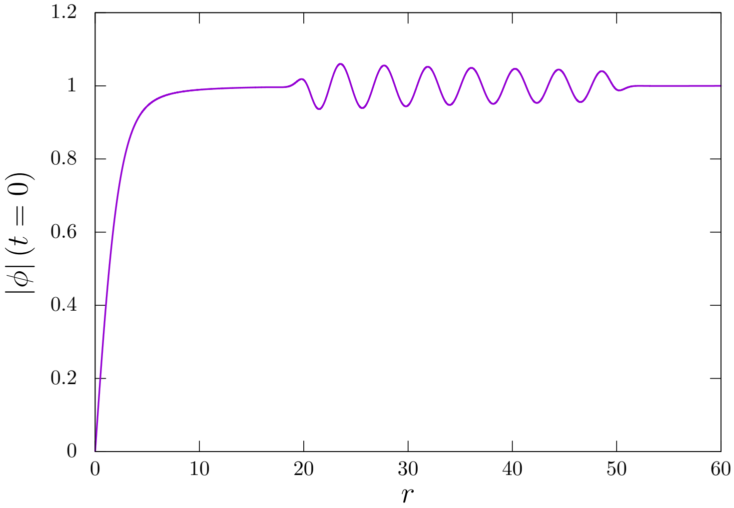

Figure 4.5: Radial part of the field at $t = 0$. The massive wave has amplitude $B = 0.46$ and angular frequency $\omega = 2\omega_1$ and moves towards $r = 0$.

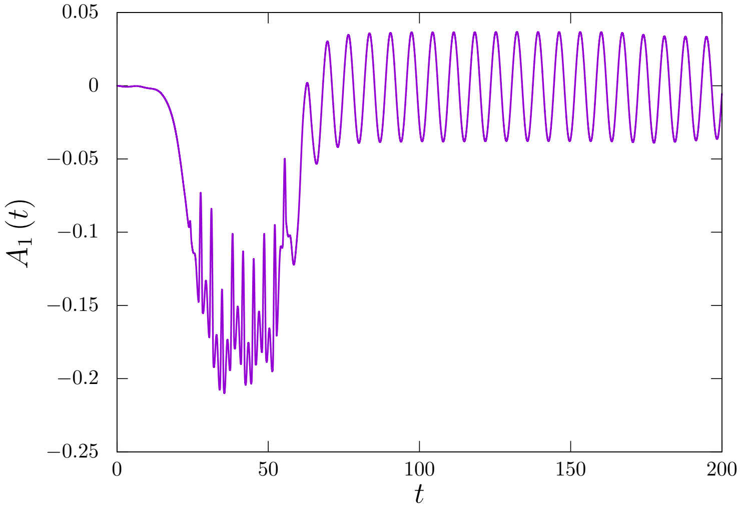

Figure 4.6: Amplitude of the first bound state as a function of time. After an interval of overlapping with the vortex, situated at $r = 0$, the wave recedes to infinity (being absorbed at $r = 60$) leaving the bound mode excited.

We have also run similar experiments in $2+1$ dimensions to make sure that the effect does not depend on the restricted symmetry of the radiation. In this case, we use a plane symmetric wave colliding with the vortex. The result of this scattering process is complicated by the fact that the vortex is displaced by the incoming wave. In other words, it is not only the bound state that is excited, but also the translational zero mode.

These numerical experiments have also uncovered an interesting effect due to the non-linear interaction of the radiation and the vortex. As the massive wave passes by the vortex, the soliton reacts by moving in the direction of the incoming wave. Although this may sound counterintuitive, this is a process that has already been observed to happen in the case of kinks in 1+1 dimensions and has been dubbed in the literature as negative radiation pressure [148, 149, 147, 150, 151].

In these simulations, the length of the simulation box was chosen to be $L = 60$, with lattice spacing and time step $\Delta x = 0.003$ and $\Delta t = 0.001$. We used the same values for the simulations in the following subsection.

4.5.2 Exciting the vortex with massless radiation

It is interesting to ask whether one can excite the localized bound states by illuminating them with a wave of the massless field, the Goldstone mode. This does not seem to be possible at the linear level, but it could happen in the non-linear regime.

The experiments we have performed in this case are pretty much the same as in the previous subsection. We first send towards the vortex a wave packet constructed from scattering states of the massless field in a cylindrical fashion. Following the description given in the previous subsection and the discussion in section 4.3, one can show that such perturbation can be described by a field configuration of the form

$$\phi(\mathbf{x},t) = \left[f(r) + iB\ \mathcal{W}(r) J_1(kr + \omega t)\right] e^{i\theta}\,, \tag{4.33}$$

where $\omega = k$. Such initial state is shown in figure 4.7 for a particular set of parameters. The results of the interaction of this wave with the vortex is shown in figure 4.8, where we display the amplitude of the first bound state.

This clearly shows that an incoming massless radiation can excite the internal modes. This effect could have important consequences for numerical simulations of string networks, since the motion of the strings creates a background of massless radiation that could transfer part of its energy to the internal modes by this long range interaction of vortices.

Similarly to the case of the massive wave, the amplitude of the bound state at the end of the scattering process depends on the frequency as well as the amplitude of the wave in a complicated way. We have not tried to systematically study this dependence in any detail.

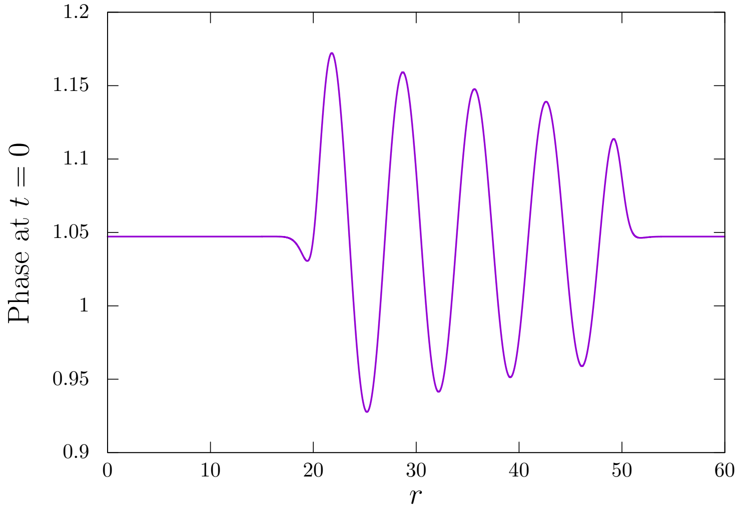

Figure 4.7: Phase profile for the incoming wave given by equation (4.33) with amplitude $B = 0.71$ and angular frequency $\omega \approx \omega_1$.

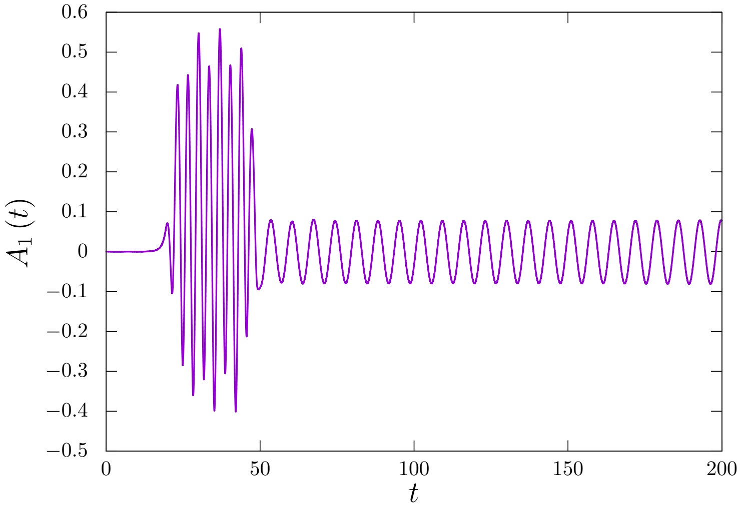

Figure 4.8: Amplitude of the first bound state as a function of time. The massless wave interacts with the vortex and leaves the bound mode excited.

We have also explored this effect in less symmetrical situations where we radiated the vortex with a plane wave of the massless mode. These investigations show that the vortex also becomes excited by the interaction with these waves, so we conclude that this is a generic effect.

Finally, we notice that, in the numerical examples we have performed for this case, we have not found the negative pressure effect. This seems to distinguish the influence of massless radiation on the vortex from the effect of massive radiation.

We have not performed the analogous tests for the second bound state. It is reasonable to expect that only perturbations with a wavelength comparable to the size of the mode will be able to excite them. Given the large spatial extent of the second mode, the simulations in this case would be computationally costly. We will see later on in our cosmological simulations that the second bound state is indeed also excited, so we expect that processes as the ones shown here take place for that mode in a realistic setting. An analogous comment should apply for bound modes with frequencies above ω_2. In an ideal situation, these higher frequency bound states would be excited by even larger wavelengths. However, in practice, they should be cut off by the presence of other vortices at shorter distances or by the size of the simulation box.

Before concluding this section, we would like to comment on another interesting effect that we have observed in our numerical simulations. Apart from the experiments described above, we have also explored the effect of waves impinging on a vortex with the bound state already excited. In the course of these investigations, we noticed that a vortex with a large-amplitude mode that is irradiated with waves does not seem to absorb more energy in the bound state. In fact, in some cases, the system decays faster than it would have done in the vacuum. This sort of stimulated emission process could have important consequences to set the typical level of excitation in vortices in realistic situations. We will comment on this possibility in the next sections.

4.5.3 Vortex-antivortex interaction

As we explained earlier, one can describe the low-energy dynamics of a $2+1$ dimensional global vortex with an effective action similar to the well-known Kalb-Ramond action [152, 153, 130]. In this case, the Goldstone mode is replaced by its dual formulation, which in $2+1$ dimensions is a Maxwell field. Vortices are thus replaced in this effective theory by point-like particles of fixed mass and charged with respect to the gauge field.

In this language, it is easy to understand why vortices would attract or repel each other depending on their relative winding. Radial modes are, by definition, not described in this effective theory. However, the acceleration of vortices moving under the influence of another nearby vortex (or antivortex) can lead to the excitation of the internal modes. We have indeed observed this behaviour in pairs of vortices that we placed initially at a distance larger than their core sizes and that were gradually accelerated away from each other. A quantitative measure of the amplitude of the bound state is complicated by the fact that the vortices acquire a large velocity. One could, in principle, numerically transform our lattice data into the rest frame of the vortex of interest. This would give us the field distribution that an observer moving at the instantaneous velocity of the vortex would see, and we could read the amplitude in this reference frame. However, this is a challenging numerical procedure, specially when we have large variations of the velocity in short periods of time. In this chapter, we will only consider vortices with small velocities, thus making sure that this issue does not affect the numerical estimate of the amplitude of the bound states.

4.6 Formation and evolution in an expanding background

The previous numerical experiments show that the internal states of a vortex can be excited by absorbing part of the radiation impinging on them or by interacting with other vortices. All these effects would be present in realistic situations, possibly creating a sizeable amplitude for these modes. In the following, we will describe the numerical simulations we have performed in order to identify the characteristic amplitude of the bound states when they are formed, and also during cosmological evolution.

4.6.1 Formation of vortices in a phase transition

We are interested in studying the formation of vortices in a $2+1$ dimensional phase transition. As we did in chapter 1, we will assume that the effective potential governing the dynamics of the field changes abruptly at some particular moment:

$$V(\phi_1,\phi_2) = \begin{cases} \frac{\lambda\eta^4}{4} + \frac{1}{2}m_r^2\left(\phi_1^2+\phi_2^2\right) & \text{for } t<0, \\ \\ \frac{\lambda}{4}\left(\frac{\phi_1^2+\phi_2^2}{2}-\eta^2\right)^2 & \text{for } t\geq 0. \end{cases} \tag{4.34}$$

Here, we have momentarily restored the parameters in order to properly specify the details of the potential. Recall that the fields ϕ_1 and ϕ_2 are given by $\phi_1=\sqrt{2}\Re\left(\phi\right)$ and $\phi_2=\sqrt{2}\Im\left(\phi\right)$, and note that we have chosen $m_r=\sqrt{\lambda}\eta$ to be the mass of these fields at the initial vacuum.

Thus, the system is initialized in a thermal state for the massive degrees of freedom at the minimum of the potential, which is initially parabolic. The details regarding the preparation of the thermal state can be found in appendix B. After the transition, we consider the potential that corresponds to the original model in equation (4.1). Influenced by the thermal perturbations, the initially symmetric state $\phi(t = 0, x, y) \approx 0$ rolls down the potential and a network of vortices and antivortices is formed (see figure 4.9).

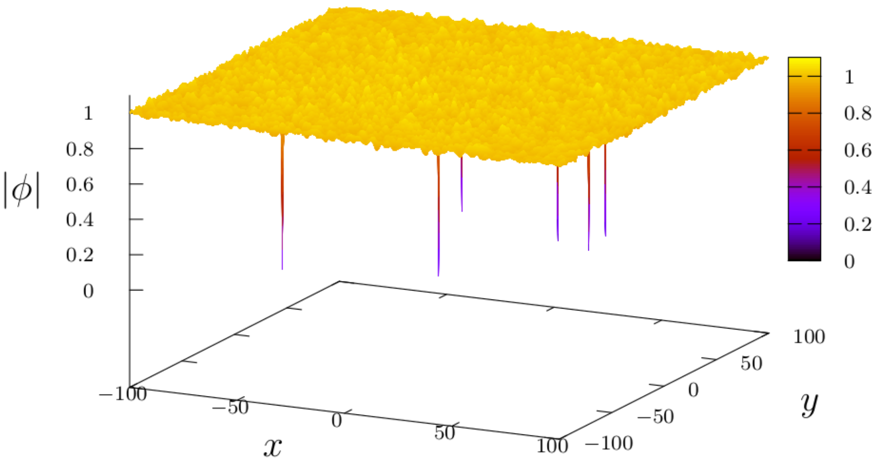

Figure 4.9: Vortices formed in a phase transition. The color palette indicates the modulus of the field. We can clearly identify the presence of a few vortices embedded on a background of small amplitude fluctuations of the field coming from the phase transition.

In an attempt to emulate a realistic setting of vortex formation, we introduce a source of dissipation in our simulations. Following the prescription in chapter 1, we simulate the formation of vortices in a $2+1$ dimensional de Sitter space and finally transition smoothly to a Minkowski background. At this stage, there is no expansion and we can use the usual projection formulas to read off the amplitude of the bound states. We chose an expansion rate given by

$$H(t) = \frac{H_i}{2}\left[1 - \tanh\left(\frac{t - t_*}{\Delta}\right)\right] , \tag{4.35}$$

which corresponds to a scale factor

$$a(t) = e^{\frac{H_0}{2}t}\left[\frac{\cosh\left(\frac{t_*}{\Delta}\right)}{\cosh\left(\frac{t-t_*}{\Delta}\right)}\right]^{\frac{H_0\Delta}{2}} . \tag{4.36}$$

These functions are plotted in figure 4.10 for our choice of dimensionless parameters: $H_i = 0.01$, $t_* = 180$ and $\Delta = 10$.

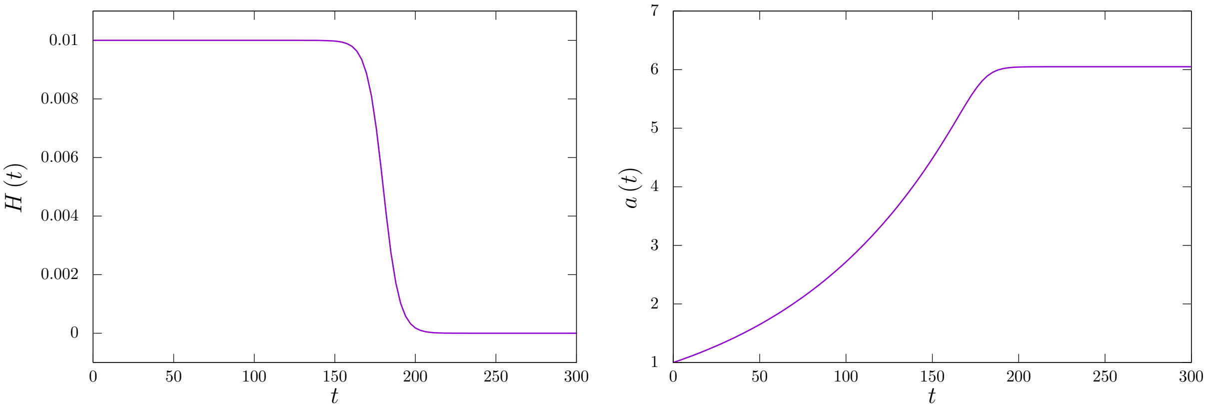

Figure 4.10: Hubble rate (left) and scale factor (right) as a function of cosmic time.

The price to pay for simulating an expanding background in a lattice is well known. The simulation takes place in a comoving lattice, so a physical object with fixed size, like the vortex, will shrink. Therefore, we should make sure that our expansion runs for long enough to do its job of smoothing the background, but not so much that the vortex core is not well resolved.

We have run 10 different initial configurations and obtained the amplitude of both $s^{(1)}(r)$ and $s^{(2)}(r)$ for each of the vortices present in the lattice at the end of the simulation. Each of the realizations contained 2000 lattice points on each direction, with $\Delta x = 0.1$ and $\Delta t = 0.04$.

We found approximately seven vortices per simulations, and their final velocities were very small. Therefore, we are confident that we have been able to correctly extract the level of excitation in each mode. Averaging over all the vortices in our ensemble, we arrived to the following results for the amplitude of the first two bound states:

$$\langle \hat{A}_1 \rangle = 0.164 \pm 0.016 \,, \tag{4.37}$$

$$\langle \hat{A}_2 \rangle = 0.181 \pm 0.060 \,. \tag{4.38}$$

In order to estimate how excited these vortices are, we compare the extra energy stored in these modes (using (4.28)) with the energy the vortices would have in their absence. We do this in two different ways. We first compare the extra energy stored in the bound states with the energy in the core (see equations (4.10) and (4.11)). In this case, we find that a vortex with the amplitudes given in equations (4.37) and (4.38) has of the order of 3% and 4% higher energy than the core mass of the vortex in the minimum energy configuration.

We can also compare the extra energy with the total energy of the bare vortex, i.e., the core energy plus the contribution of the gradient of the phase. As mentioned in section 4.2, this total energy grows logarithmically with the distance from the core and depends on some cutoff scale. For the situation at hand, we choose this cutoff scale to be the average distance between vortices at the end of our simulations. This computation shows that the vortices seem to have a 0.4% and 0.5% of extra energy due to these localized excitations[3].

Our results indicate that the vortices are barely excited at formation, so we do not expect the amount of extra energy stored in the bound states to be relevant for the dynamics. It is interesting to note that this amount of energy is much lower the one we found for the kinks in chapter 1.

In section 4.6.3 we will explore what happens to this level of excitation in the course of the subsequent evolution of the vortices in a cosmological background.

4.6.2 A vortex in a thermal bath

As we showed in section 4.5, the interaction of the vortex with radiation induces the excitation of the bound states. In this section, we aim to extract the amplitude of these modes when the vortex is placed in contact with a thermal bath (see figure 4.11). We give a detailed description of the numerical implementation of this initial thermal state in our lattice in appendix B. This type of configurations could be interesting in the study of defect formation in reheating scenarios [111] and possibly in other realistic situations in condensed matter physics.

It is important to note that this thermal bath of perturbations will also induce a random velocity to the vortex. This limits our ability to read off the amplitude of the bound state for long periods of time since the vortex may end up leaving the simulation box. In order to ameliorate this problem, we run the simulation in a $2+1$ dimensional de Sitter background. We choose the Hubble rate of this spacetime to be small compared to m_r so that it will not affect the amplitude of the bound states, but large enough for the horizon distance to be within our simulation box. This allows us to read the amplitude of the internal modes after their initial "peculiar" thermal velocities have been redshifted away. In figure 4.12 we plot our results for the amplitude of the bound states as a function of temperature. As in the

---

[3] As we mentioned earlier, the size of the bound states beyond the second mode makes the analysis of their excitation during the phase transition numerically unfeasible. However, we do not expect any dramatic effect for those modes in any realistic situation.

previous subsection, we performed these simulations in a 2000×2000 lattice with $\Delta x = 0.1$ and $\Delta t = 0.04$.

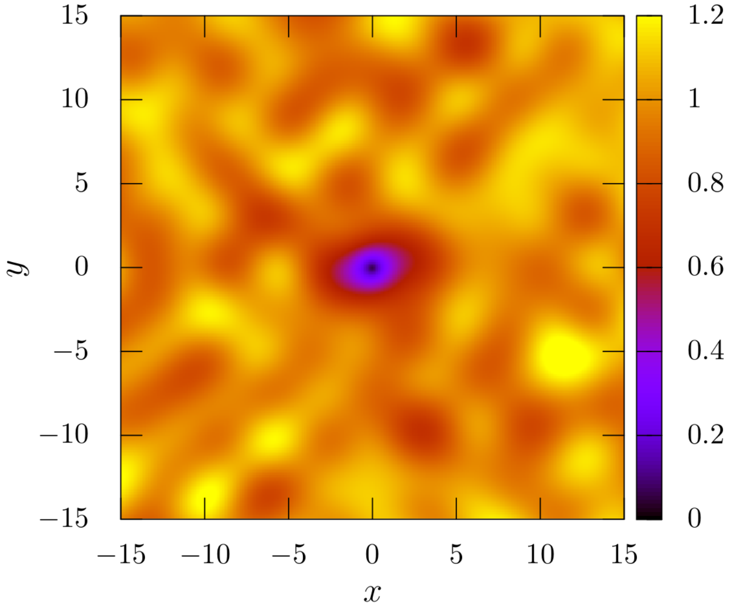

Figure 4.11: Vortex in contact with a thermal bath at temperature $\Theta = T/\eta^2 = 0.1$. The color palette indicates the modulus of the field.

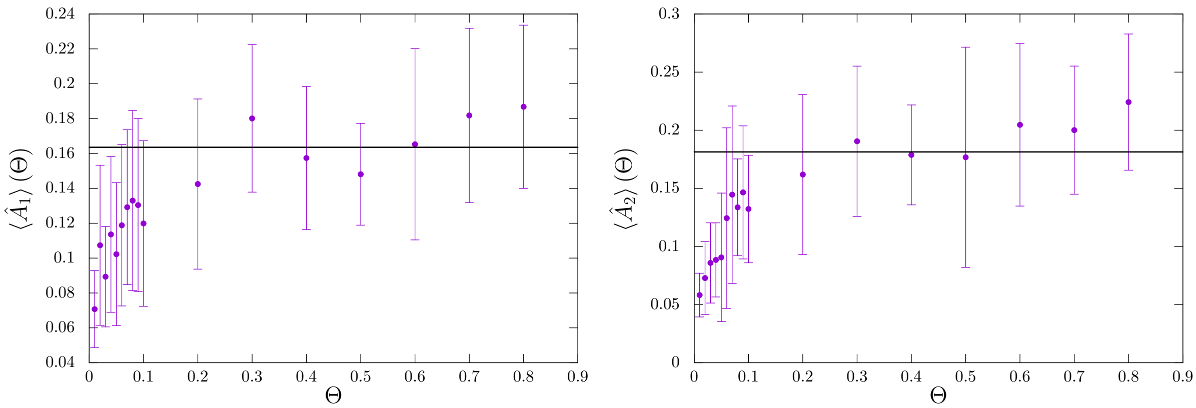

Figure 4.12: Average amplitude of the first (left) and second (right) modes, $\langle \hat{A}_1 \rangle$ and $\langle \hat{A}_2 \rangle$, as a function of the dimensionless temperature $\Theta = T/\eta^2$. The black line corresponds to the average amplitude obtained in the phase transition, given in (4.37) and (4.38).

Note that the amplitude of the internal modes saturates for high temperatures at approximately the same value that is found when the vortices are formed in a phase transition. This result was also observed for the case of $1+1$ dimensional kinks in chapter 1. We attribute this behaviour at high temperatures to the fact that, in this regime, the amplitude of the thermal perturbations is large enough to climb to the top of the potential. In this limit, since there is no much difference between this very hot initial state and the field configuration before the phase transition, it is reasonable to expect that the results in both cases are consistent with one another. In fact, at those very high energies, we have observed the formation of other vortex-antivortex pairs from the vacuum as one would expect if there is enough thermal energy available.

One may wonder why the amplitude saturates to a value which is significantly lower than the maximum possible one. One reason for this may be the phenomenon of stimulated emission we mentioned in the previous section. This process would make high-amplitude states much more unstable than one would imagine by studying their decay in vacuum. This would effectively set a lower maximum amplitude for the bound states in realistic setups where the vortices are typically hit by waves of different frequencies and amplitudes.

4.6.3 Cosmological evolution of a $2+1$ dimensional vortex network

As we explained earlier, the interaction of the vortex with massive and massless radiation seems to induce its excitation. Furthermore, it is also excited when it accelerates under the influence of other vortices. It is therefore clear that the amplitude of the bound states will not only depend on the initial conditions, but also on the subsequent dynamics. We would like to have some idea of the evolution of these excitations as a function of time when all these previously discussed effects are at play. In order to do that, we will take inspiration from the type of evolution we expect to occur for global strings, the three-dimensional counterparts of our vortices, and we will simulate an ensemble of vortices for a period of cosmological expansion. In particular, we will consider a $2+1$ dimensional expanding universe in a "radiation-dominated" state, i.e., we will take the scale factor to grow with cosmic time as $a(t) \propto \sqrt{t}$. This type of simulation has been done before also as a toy model to understand the dynamics of global strings in [154]. There are, however, important differences with the $3+1$ dimensional case that make a direct extrapolation between these models difficult. We will comment more on this in our conclusion section.

Since we are using comoving coordinates, as the system evolves, the vortices shrink (comovingly). Thus, we have to make sure that we resolve the cores for the duration of our simulation. In order to do so, we have simulated the vortex network following one of the simulation techniques found in the literature (see, for example, [155, 62, 63]). This procedure consists of several steps (we refer to the interested reader to the previous citations for details).

The initial conditions correspond to the scalar field in the vacuum manifold, with no velocity, but with random orientation of its phase. This configuration has a very high energy, and in order to approach a scaling regime, a period of diffusion evolution is used. Then, we employ a period in which the core of the defects grows artificially until it reaches the desired width (coregrowth period). It is only then that the proper radiation domination period of the simulation starts. Since the measurements of the amplitudes of the internal modes only make sense in Minkowski space, we smoothly transition from radiation to Minkowski, and then read the corresponding amplitudes. Right after the coregrowth period, we are left with a collection of well separated vortices that start their cosmological evolution with a horizon distance larger than the size of the solitons.

In this work, we did not want to exhaustively study this procedure; we just wanted to analyze whether the outcoming vortices would be excited, and to what approximate level. Thus, we have only chosen one appropriate set of parameters, and have simulated the system 10 times with different initial random conditions, obtaining 100 vortices (on average, 10 ± 4 vortices).

The parameters we have used for our simulations are the following: the simulation box was a square of 8192 points per dimension, and the comoving lattice spacing was $\Delta x = 0.2$. The time resolution was $\Delta\tau = 0.04$ (during diffusion $\Delta\tau = 0.008$). Here, τ denotes conformal time. This choice of parameters ensures that at the end of the simulation, where the vortices have shrunk due to the comoving coordinates and the expansion of the universe, we resolved the core of the vortex with enough precision to obtain the amplitude of the internal modes successfully.

We have used a period of 100 time units in diffusion, and the coregrowth period was from $\tau = 10$ until $\tau = 65$. The radiation domination simulation ran until $\tau = 785$, and then a smooth transition to Minkowski happened until $\tau = 820$. After that, the amplitudes were read for a further 50 time units. We run for a total dynamic range of $a(\tau_f)/a(\tau_i) \sim 10$. With those numbers, we stop the simulation at roughly half light-crossing time of the box, thus avoiding possible finite volume effects that could arise because of the use of periodic boundary conditions.

In the course of cosmological evolution, all the processes of vortex excitation detailed earlier take place. See a sequence of snapshots at different stages of the simulation in figure 4.13.

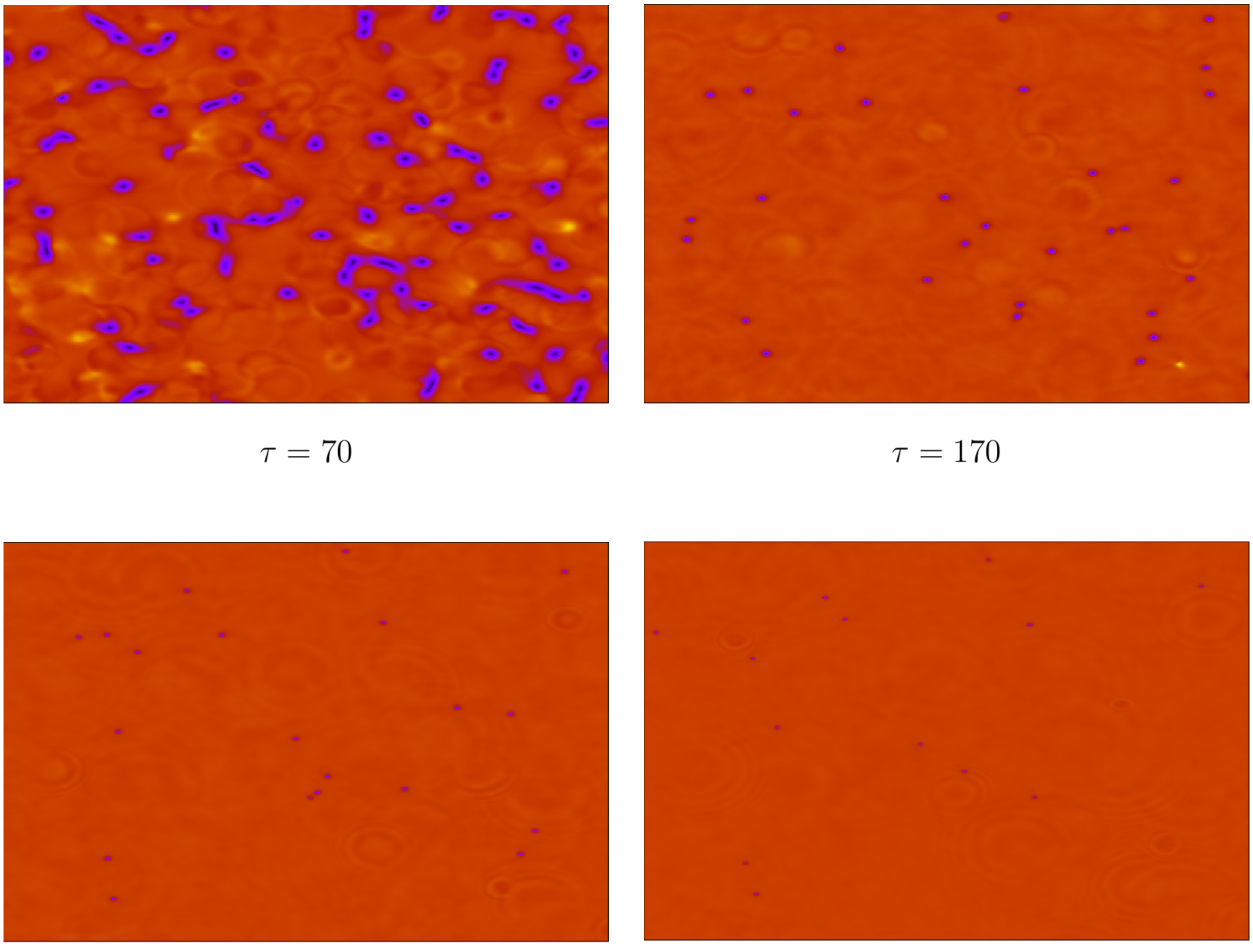

$\tau = 70$

$\tau = 170$

$\tau = 270$

$\tau = 370$

Figure 4.13: A sequence of snapshots of the scalar field evolution during the initial part of the radiation era in one simulation. The pictures show a subregion of side $L/2$ of the simulation at different values of the conformal time, τ.

Vortices move under the influence of other nearby ones and accelerate, acquiring in some cases large velocities. In this motion, they emit radiation in the form of massless (Goldstone) modes, and some vortex-antivortex pairs annihilate emitting a shell of massive radiation[4]. All these waves of radiation affect other vortices and excite their bound states. These processes continue until the energy in these waves is redshifted away by the expansion of the universe.

---

[4] We have not witnessed the appearance of two-dimensional oscillons as a result of these annihilations. This seems to be in agreement with the findings in [156].

Similarly to what happens in $3+1$ dimensional networks of strings, our configurations reach a scaling regime where the number of vortices per Hubble length is roughly constant[5]. This in turn means that the number of vortices should scale as $n(\tau) \propto \tau^{-2}$. We show in figure 4.14 the behaviour of the average number of vortices in our simulations. As the figure shows, our simulations enter a scaling regime pretty early, so the evolution takes place within this stage for a substantial amount of our run-time, thus also factoring in the possibility that internal modes evolve during this period.

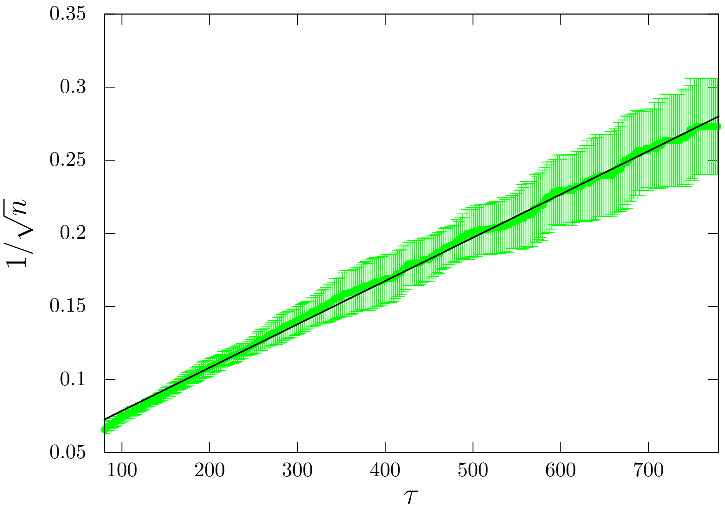

Figure 4.14: Inverse of the square root of the average number of vortices (n) as a function of conformal time. The results are in good agreement with the linear fit $0.05 + 0.0003\tau$ (black line).

Finally, in figure 4.15 we display the amplitude of the bound states as a function of time after the transition to Minkowski space. This was done for low-velocity vortices only. As previously mentioned, we obtained a total number of 100 vortices. Out of those, 65 were moving slow enough for us to reliably obtain the amplitude of the internal modes. The average amplitude for each of the first two bound modes is estimated to be

$$\langle \hat{A}_1 \rangle \approx 0.049 \pm 0.036 \quad , \quad \langle \hat{A}_2 \rangle \approx 0.053 \pm 0.037 \; . \tag{4.39}$$

Following the same type of calculation we did in the case of the phase transition, we can infer that the vortices are, on average, 0.03% (first mode) and 0.04% (second mode) more energetic due to the bound states at the end of our simulations. One can also compare the

---

[5] We do not address the problem of the logarithmic dependence in the thesis. An additional reason for not doing that in this particular chapter is that the case of $2+1$ dimensions is special in this regard [154].

amount of extra energy in the vortex by considering only the core mass of the vortex. In this case, the appropriate percentages are 0.25% and 0.36% respectively. This is clearly a small amount of energy, so it is hard to see how this can significantly affect the dynamics of the vortices.

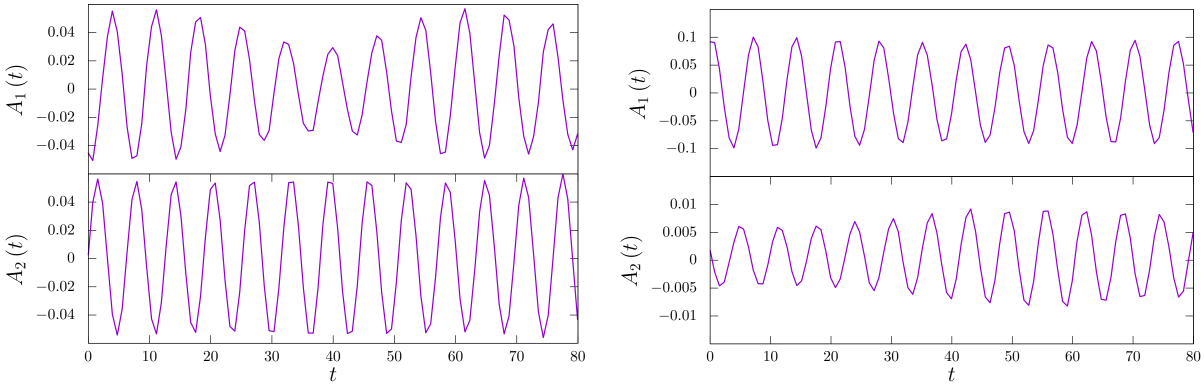

Figure 4.15: Two examples of the amplitude of the bound state modes on a vortex at the end of the radiation era evolution.

These results indicate that bound states seem to survive for the duration of our cosmological simulations. Part of this excitation may come from the initial conditions, and another part from the subsequent interaction with radiation and other vortices. It is interesting to note that, at the end of our cosmological simulations, the amplitudes of the modes seem to be significantly lower than what we found in the process of vortex formation in a phase transition. It would be interesting to investigate the dependence of these results on the procedure we use to set the initial conditions or the expansion history. However, given the low level of excitation of vortices in our simulations, it does not seem likely that the bound states could play a relevant role in the dynamics of the solitons in these other cases.

4.7 Conclusions

In this chapter, we have investigated the spectrum of perturbations around $2+1$ dimensional global vortices. We have found that vortices of unit winding number have localized states whose angular frequency is below the mass of the radial excitations of the field in the vacuum. This means that they will only radiate at the non-linear level. Using similar techniques to the ones developed in [107], we were able to compute the decay rate of the first two bound states analytically. These calculations show that these modes radiate most of their energy in the form of massive radiation at twice their oscillating frequency. Furthermore, the typical time scale of their decay is much longer than the period of oscillation. Numerical simulations of the excited vortex in a field theory lattice, solving the full non-linear equations of motion, reveal a perfect agreement with these analytic predictions.

These internal modes can store a large percentage of the core mass of the vortex for a very long time. It is interesting to evaluate this possibility quantitatively since it could affect the dynamics of the vortices in a realistic setting.

We have explored several mechanisms by which a vortex can get excited dynamically. We first illuminate the vortex solution with wave packets and compute the amplitude of the bound states after the scattering process. Our results indicate that this excitation happens for either massless and massive radiation. Furthermore, the long-range interaction of vortices due to their coupling to the massless Goldstone mode induces forces between them. The presence of acceleration also leads to excitations. However, the amplitude of the bound modes can also decrease due to the interaction with radiation, so it is hard to predict the level of excitation that the vortices could reach in a dynamical background. In order to do this, we have designed a few numerical experiments that can be considered representatives of different realistic situations where these processes can take place.

We first look at the level of excitation of vortices after their formation in a phase transition. We do this by simulating an abrupt change from an initially parabolic potential to the double-well one. This leads to the formation of a network of vortices and antivortices, which are found to be excited. However, the extra energy they store in the bound states is only about a few percent of the core mass of the vortex solution.

We also obtained the level of excitation of these modes when the vortex is in contact with a thermal bath. The results also indicate that the energy transfer from the thermal background to the internal modes is not very efficient. The amount of extra energy is again below the 1% level for all temperatures. This quantity saturates as one increases the temperature and its value is, in fact, very similar to the one obtained at formation in phase transitions.

Finally, we simulated the cosmological evolution of vortices in a 2+1 dimensional "radiation-dominated" universe. In this case, some vortices and antivortices annihilate and disappear leaving behind massive radiation that excites other vortices. Moreover, the interactions between vortices lead them to gain some extra internal energy as well. However, the result at the end of the simulation is, once again, that vortices do not seem to acquire a large amount of extra energy in the form of internal excitations. Therefore, we conclude that this extra energy is not affect significantly the subsequent dynamics of the solitons.

The global vortices we described here can be seen as the cross section of an infinite straight global string, so the perturbation modes we have been discussing are indeed present on the $3+1$ dimensional string as well. As we will see in chapter 5, these modes are solutions to the corresponding Schrödinger problem for strings, and come with some wavelength in the z direction (parallel to the string). This means that part of the conclusions we have presented here can be extended to the $3+1$ dimensional case. Specifically, the typical time scales of the perturbations will be similar to the case studied in this chapter. However, it is difficult to estimate whether the low level of excitation seen here can be extrapolated to the more complicated string network. We think that there are important processes that are missed by our simulations in $2+1$dimensions. In particular, strings have light degrees of freedom living on their worldsheet: the Goldstone modes associated to the position of the string. These wiggle modes could interact and lead to the excitation of the internal modes. Furthermore, strings can self-intersect and reconnect with other strings. These processes lead to the formation of kinks that travel along the string and that could excite the internal modes[6].

Finally, we would also like to comment on the possible applications of our methods for condensed matter vortices. The dynamical results we report here only apply to the relativistic models for vortices that we presented in section 4.2. However, the calculation needed to identify the bound states of global vortices may be useful in the computation of perturbations in condensed matter theories such as the Gross-Pitaevskii equation for superfluids.

---

[6] Indeed, this is what was suggested in [84]. It would be interesting to investigate whether the energy in that case decays following the time scale we obtained in our study in this chapter.

Chapter 5

Dynamics of $3 + 1$ dimensional global strings

In this chapter, we uncover a new parametric resonance of global cosmic strings. This process, analogous to the one we discussed in chapter 3, is triggered by the presence of internal modes that resonantly amplify the transverse displacements of the string. We study this phenomenon analytically and numerically, and we also analyze the massless and massive radiation produced by these excited strings. Our results may be relevant for current numerical simulations of axionic cosmic string networks.

5.1 Introduction

The nature of dark matter remains as one of the biggest puzzles in cosmology. Among the multiple hypothetical particles that have been proposed as dark matter candidates, the axion is perhaps the most promising one. Particle physics models with axions appear in many well motivated extensions of the Standard Model where an extra $U(1)$ symmetry (the so-called Peccei-Quinn symmetry [33]) is added. This symmetry is broken at high energies leading to the appearance of a Goldstone mode. Eventually, this mode becomes massive due to small instanton contributions at low energies (see section 1.3). Therefore, these models predict the existence of a new particle with very weak interactions, thus being a strong candidate for dark matter [157, 158, 159, 160, 161].

On the one hand, if the Peccei-Quinn symmetry is spontaneously broken before inflation, the axionic abundance today would depend on the value of the axion field in our local patch of the universe. On the other hand, if this symmetry is broken after inflation, the phase transition would lead to the formation of axionic cosmic strings [6, 125, 135]. As this cosmological network of strings evolves, it produces a spectrum of Goldstone modes. This happens until the axion acquires its mass, leading to the formation of domain walls attached to the strings. These walls will typically trigger the annihilation of the string network, a process that will also contribute to the axionic abundance[1].

It is clear from this description that, in order to estimate the relic abundance of axions in these models, one needs to have a good understanding of the evolution of the network of axionic strings. This task has been tackled by several groups over the years [132, 133, 52, 134, 53, 129, 130, 131, 59, 58, 60, 61, 62, 64, 63, 163, 164], but their results are not all consistent with one another. One of the issues that is currently under scrutiny concerns the large-scale properties of the network, in particular the density of strings in the scaling regime. This is a key property of the network that directly affects the estimate of the axion abundance in the model.

Another important ingredient needed to compute the density of axions today is the spectrum of Goldstone mode radiation produced by strings. This spectrum has also been estimated by several groups using different techniques, although a quantitative agreement has not been reached yet. In this chapter, we would like to describe a phenomenon that may have some relevance in the dynamics of axionic cosmic strings, and, in turn, in the spectrum of the radiation they produce.

As we mentioned above, these axionic cosmic strings appear as solitonic objects in a field theory model with a $U(1)$ global symmetry. The study of small perturbations around the simplest straight string configuration reveals the existence of two different types of possible excitations. The lowest energy excitations correspond to the transverse displacements of the string. These perturbations can be viewed as massless modes on the $1+1$ dimensional worldsheet of the string and describe wiggles that propagate at the speed of light. The second type of excitations is related to deformations of the shape of the soliton. These are the long-lived internal modes we have been focusing on throughout this thesis.

The dynamics of global strings has been extensively studied in the literature within the thin wall approximation [135, 136, 143, 137, 140, 141, 138]. However, this effective description does not take into account the presence of these massive internal modes. Here, we would like to consider the effect that the presence of both types of excitations can have on

---

[1] The cosmological scenario after the walls are formed strongly depends on the details of the axion potential [162].

strings. In particular, we will show that an internal mode excitation can trigger the resonant amplification of the transverse motion of the string, as we saw for the domain walls studied in chapter 3. This, in turn, could also accelerate the decay process of the extra energy stored in the string.

The organization of the rest of the chapter is the following. In section 5.2 we discuss the field theory model that we will consider as well as the linear perturbations around the relaxed axionic string. In section 5.3, we study an effective Lagrangian that describes the coupling between these modes and investigate the possible appearance of parametric resonances. We also show how these resonances are easily activated in lattice field theory simulations and compare the results with the analytic predictions. In section 5.4 we analyze the radiation emitted by the excited string. Finally, in section 5.5, we end with some conclusions about the possible relevance of these findings to the results obtained in field theory simulations of cosmic string networks.

5.2 Axionic strings and their excitations

We will consider the action (1.9):

$$S = \int d^4x \left[\eta^{\mu\nu} \partial_\mu \phi^* \partial_\nu \phi - \frac{\lambda}{4} \left(\phi^* \phi - \eta^2 \right)^2 \right] . \tag{5.1}$$

As in the previous chapter, we will use the representations (4.2) and (4.3) for the scalar field:

$$\phi = \frac{\phi_1 + i\phi_2}{\sqrt{2}}, \tag{5.2}$$

$$\phi = \frac{\varphi}{\sqrt{2}} e^{i\frac{\alpha}{\eta}}. \tag{5.3}$$

In this case, however, the dimensions are $[\phi_1] = [\phi_2] = [\varphi] = [\alpha] = E$, $[\eta] = E$, $[\lambda] = E^0$ (dimensionless).

The form of the potential leads to spontaneous symmetry breaking. The vacuum manifold is parametrized by the configurations with $|\phi(t, \vec{x})| = \eta$. The spectrum of perturbations about these vacua is composed of a massive (radial) field with mass $m_r = \sqrt{\lambda}\eta$ and a massless Goldstone mode that represents flutuations of the angular part of the field. The equations of motion obtained from the Lagrangian are

$$\ddot{\phi}_{1,2} - \nabla^2\phi_{1,2} + \frac{\lambda}{2}\left(\frac{\phi_1^2+\phi_2^2}{2} - \eta^2\right)\phi_{1,2} = 0. \tag{5.4}$$

As in the previous chapter, we look for static solutions of the form

$$\phi_s(t,\rho,\theta) = \eta f(\rho)e^{i\theta}\,. \tag{5.5}$$

Since this configuration does not depend on z, this is an extended object in this direction. If we rescale the radial coordinate as $r = m_r\rho$, the function $f(r)$ satisfies equation (4.7) with winding number $n_w = 1$.

Our discussion about the energy of this solution in section 4.2 also applies to this case. In particular, recall that the energy of the string diverges logarithmically with the distance from the core. Note, however, that expression (4.11) should be now taken as the energy per unit length of the string.

Let us now consider the possible perturbations around the static solution. The problem is formally equivalent to the one presented in section 4.3, but now the perturbations can have some wavelength in the z direction. One can easily identify the different solutions at the linear level by analogy with the $2+1$ dimensional case. For the radial perturbations, consider the field configuration

$$\phi(t,r,\theta,z) = \eta\left[f(r) + s(r)\cos\left(\omega t - k_z z\right)\right]e^{i\theta}\,, \tag{5.6}$$

where k_z is the wave number in the z direction. Substitution into the equation of motion yields

$$-s''(\rho) - \frac{s'(\rho)}{\rho} + U(\rho)s(\rho) = \Omega^2 s(\rho), \tag{5.7}$$

with $U(\rho)$ given by (4.14) and

$$\Omega^2 = \omega^2 - k_z^2\,. \tag{5.8}$$

We first note that there are zero mode solutions of these equations with $\omega^2 - k_z^2 = 0$. These modes correspond to travelling waves moving at the speed of light along the longitudinal direction of the string, and they can be computed from the derivatives of the static solution (5.5) with respect to the transverse directions x and y:

$$\eta_x^0(r,\theta) \equiv \partial_x\phi_s(r,\theta) \qquad , \qquad \eta_y^0(r,\theta) \equiv \partial_y\phi_s(t,\theta)\,. \tag{5.9}$$

Note that these zero modes are not normalizable. Indeed, this is just a manifestation of the slow decline of the energy density of the global strings.

We also have bound states with $\omega^2 - k_z^2 < m_r^2$. As pointed out in the previous chapter, there is an infinite number of them. Here we will only deal with the first bound state $s^{(1)}(r)$, already found in chapter 4 (see left panel in figure 4.2). The eigenfrequency of this mode is given by $\omega^2 - k_z^2 = 0.8133\, m_r^2 \equiv \omega_s^2$.

Finally, we have a continuum of scattering states starting at $\omega^2 - k_z^2 = m_r^2$. These correspond to fluctuations that can propagate in the vacuum.

As shown in chapter 4, an excited vortex state with a small amplitude of the shape mode, $s^{(1)}(r)$, could take a long time to decay to its ground state. The reason for this is that the frequency of the internal mode is below the mass threshold for radial modes to propagate in the vacuum. However, non-linearities allow for a slow leakage of its energy to infinity. This phenomenon can be directly translated to our $3+1$ dimensional configuration by considering a homogenous excitation of the shape mode along the straight string. The invariance along the z direction of this configuration allows us to use the results from the $2+1$ dimensional problem to infer the decay time scale of this homogeneous perturbation. However, as we will see in the next sections, the story can change completely when the string has some finite wavelength in the z direction.

5.3 Parametric resonances

5.3.1 Dimensionless variables

We first revert to dimensionless variables:

$$\tilde{\phi} = \frac{\phi}{\eta} \qquad\qquad \tilde{x}^\mu = \sqrt{\lambda}\eta x^\mu = m_r x \ , \tag{5.10}$$

where x^μ denotes the time and space coordinates. Now, the action reads

$$S = \frac{1}{\lambda}\int d^4\tilde{x}\ \left[\partial_\mu\tilde{\phi}^*\ \partial^\mu\tilde{\phi} - \frac{1}{4}\left(\tilde{\phi}^*\tilde{\phi} - 1\right)^2\right] \tag{5.11}$$

with the partial derivatives taken with respect to the dimensionless variables.

In the following, all variables should be understood as dimensionless unless the parameters λ and η appear explicitly.

5.3.2 Analytical calculations

Let us first consider the situation of a straight axionic string uniformly excited with the presence of a shape mode. As previously mentioned, this mode will couple non-linearly to the scattering states and its energy will be slowly radiated to infinity in the radial directions. This was already studied in chapter 4. Here we will be interested in studying the coupling between the shape mode and the transverse wiggle excitations of the string. With this idea in mind, we consider a possible excitation of the string of the form

$$\phi(t,r,\theta,z) = f(r)e^{i\theta} + A(t)s^{(1)}(r)e^{i\theta} + D(t)\eta_x^0(r,\theta)\cos(k_z z)\,, \tag{5.12}$$

where $A(t)$ denotes the amplitude of the shape mode and $D(t)$ represents the amplitude of the zero mode, which we take to be in the form of a standing wave. Note that this ansatz disregards completely the presence of any radiation field. This is, of course, an approximation. Taking this into consideration will become important when we compare the results of our numerical simulations with the predictions of this ansatz. Note also that this effective model can be easily extended to describe displacements in any direction in the xy plane by expressing the zero mode perturbations as a linear combination of $\eta_x^0(r,\theta)$ and $\eta_y^0(r,\theta)$.

Inserting this ansatz in (5.1) and integrating along the spatial directions, we obtain the following Lagrangian for the amplitudes of the modes:

$$\begin{aligned} L = -E_s + 2\pi L_z \quad \Big[& \quad \dot{A}^2 - \omega_s^2 A^2 - I_{A,3}A^3 - I_{A,4}A^4 \\ + & \quad I_D(R)\dot{D}^2 - \left(I_{D,2} + I_D(R)k_z^2\right) D^2 - I_{D,4}D^4 \\ - & \quad I_{AD,3}\; AD^2 - I_{AD,4}\; A^2D^2 \Big]\,, \end{aligned} \tag{5.13}$$

where E_s denotes the energy of the straight string solution, L_z is the extent of the string in the z direction and the coefficients $I_{A,3}, I_{A,4}, I_{D,2}$ and $I_{D,4}$ represent the finite higher-order couplings between the amplitudes. These coefficients are computed by performing the following integrals:

$$I_{A,3} = \int_0^\infty dr\, r\, f(r)\left[s^{(1)}(r)\right]^3 \approx 0.197, \tag{5.14}$$

$$I_{A,4} = \frac{1}{4}\int_0^\infty dr\, r\, \left[s^{(1)}(r)\right]^4 \approx 0.0188, \tag{5.15}$$

$$I_{D,4} = \frac{3}{32}\int_0^\infty dr\, r\, \left[\eta_1^4(r) + 4\eta_1^2(r)\eta_2^2(r) + \eta_2^4(r)\right] \approx 7.36\times 10^{-4}, \tag{5.16}$$

$$I_{AD,3} = \int_0^\infty dr\, r\, s^{(1)}(r)\left[\eta_1^2(r) + \eta_1(r)\eta_2(r) + \eta_2^2(r)\right] \approx 0.0904, \tag{5.17}$$

$$I_{AD,4} = \frac{1}{2}\int_0^\infty dr\, r\, \eta_s^2(r)\left[\eta_1^2(r) + \eta_1(r)\eta_2(r) + \eta_2^2(r)\right] \approx 0.0185, \tag{5.18}$$

$$\begin{aligned} I_{D,2} \;&=\; \int_0^\infty dr\, r\, \left[\frac{1}{2}f^2(r)\left(\eta_1^2(r) + \eta_1(r)\eta_2(r) + \eta_2^2(r)\right) + \frac{1}{2}\left(\eta'^2_1(r) + \eta'^2_2(r)\right)\right. \\ &\left. -\frac{1}{4}\left(\eta_1^2(r) + \eta_2^2(r)\right) + \frac{2}{r^2}\eta_2^2(r)\right] \approx -1.86\times 10^{-4}. \end{aligned} \tag{5.19}$$

In these integrals, the functions $\eta_1(r)$ and $\eta_2(r)$ are defined as

$$\eta_1(r) = \frac{1}{2}\left[f'(r) + \frac{f(r)}{r}\right], \quad \eta_2(r) = \frac{1}{2}\left[f'(r) - \frac{f(r)}{r}\right], \tag{5.20}$$

and we have imposed the following normalization of the shape mode:

$$\int_0^\infty r\, dr\, \left[s^{(1)}(r)\right]^2 = 1. \tag{5.21}$$

On the other hand, the coefficient $I_D(R)$ can be shown to be logarithmically divergent with the cutoff distance R:

$$I_D(R) = \frac{1}{2}\int_0^R dr\, r\, \left[\eta_1^2(r) + \eta_2^2(r)\right]. \tag{5.22}$$

The equations of motion we obtain from the Lagrangian (5.13) are given by

$$\ddot{A}(t) + \left(\omega_s^2 + I_{AD,4}\, D(t)^2\right)A(t) + \frac{3}{2}I_{A,3}A(t)^2 + 2I_{A,4}A(t)^3 + \frac{1}{2}I_{AD,3}D(t)^2 = 0\ ,$$

$$\ddot{D}(t) + \left[k_z^2 + \frac{I_{D,2}}{I_D(R)} + \frac{I_{AD,3}}{I_D(R)}A(t) + \frac{I_{AD,4}}{I_D(R)}A(t)^2\right]D(t) + \frac{2I_{D,4}}{I_D(R)}D(t)^3 = 0\ . \tag{5.23}$$

At the lowest order, the amplitudes behave as harmonic oscillators[2]. Going beyond the linear order, we identify the presence of resonance effects between the two modes. Let us start by looking at the zero mode equation. Disregarding the higher order coupling, we get

---

[2] Note, however, that the zero mode amplitude $D(t)$ acquires a small mass term due to the finite cutoff scale R. Taking the limit of $R \to \infty$, this term vanishes.

an equation of the form

$$\ddot{D}(t) + \left[k_z^2 + \frac{I_{D,2}}{I_D(R)} + \frac{I_{AD,3}}{I_D(R)} A(t)\right] D(t) = 0 \ . \tag{5.24}$$

Assuming the unperturbed shape mode time dependence, namely, $A(t) \propto \cos(\omega_s t)$, we immediately notice that this equation is of the Mathieu type [119]. This means that we should expect a parametric resonance behaviour of the string zero mode in the presence of a shape mode excitation. Following the discussion in section 3.6, we conclude that the resonant amplification should take place for a zero mode with frequency k_z satisfying

$$\sqrt{k_z^2 + \frac{I_{D,2}}{I_D(R)}} = \frac{\omega_s}{2} \ . \tag{5.25}$$

In this case, almost all the energy stored in the shape mode is transferred to the zero mode. In this process, the amplitude of the former decreases and the amplitude of the latter grows. Therefore, at some point, higher order terms in $A(t)$ become negligible and the first equation in (5.23) reduces to

$$\ddot{A}(t) + \omega_s^2 A(t) + \frac{1}{2} I_{AD,3} D(t)^2 = 0 \, . \tag{5.26}$$

This means that, at this point, the shape mode will start growing due to the oscillations of the zero mode. In other words, energy can also be resonantly transferred from the zero mode to the internal mode.

This analysis indicates that there are resonant effects in the interaction between these modes. This is completely analogous to the behaviour observed for domain wall strings in chapter 3. Even though we do not expect any runaway process since higher-order terms will tame any dramatic behaviour, this phenomenon will have an effect on the amount of radiation emitted from the string which is not taken into account in the effective Lagrangian.

5.3.3 Numerical simulations

The analysis presented in the previous section suggests that a uniform excitation of the shape mode on a string will induce a parametric excitation of a zero mode of a particular wavelength. In this subsection, we show this is indeed the case by solving the full field theory equation of motion (A.19) in a lattice with absorbing boundary conditions (for the details, see appendix A).

We show in figure 5.1 a few snapshots of the position of the string extracted from our field theory simulation. The static string solution was perturbed initially with the shape mode and a small amplitude zero mode in the x direction:

$$\phi\left(t=0,r,\theta\right)=\left[f\left(r\right)+A\left(t=0\right)s^{(1)}\left(r\right)\right]e^{i\theta}+D\left(t=0\right)\sin\left(k_z z\right)\eta_x^0\left(r,\theta\right)\ , \qquad (5.27)$$

with $A\left(t=0\right)=0.5$, $D\left(t=0\right)=0.01$ and $k_z=6\pi/L_z$. In this simulation, we chose $L_x=L_y=80$ and $L_z=40$, with lattice spacing $\Delta x=0.2$ and time step $\Delta t=0.1$.

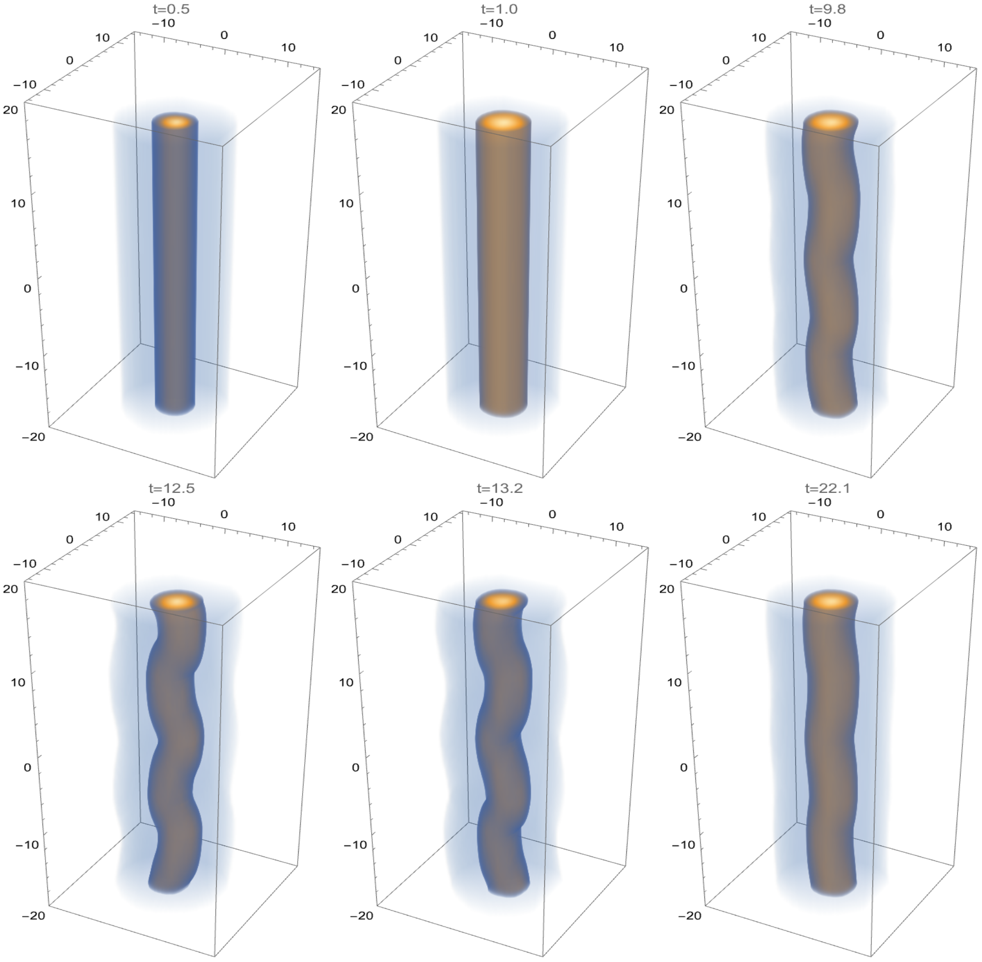

Figure 5.1: Evolution of the string energy density in field theory. The initial state corresponds to an excited state with $A(t=0)=0.5$ and $D(t=0)=0.01$. Top panel, left-to-right, $t=0.5$, 1.0 and 9.8. Bottom panel, left-to-right $t=12.5$, 13.2 and 22.1. The colors indicate the magnitude of the energy density, which goes from 0, in blue, to $0.5\lambda\eta^4$, in yellow.

The small initial value of the amplitude of the zero mode is given in order to accelerate the amplification. We have also performed numerical experiments in which the straight string is placed in a thermal bath at some low temperature (the implementation of such a state is described in appendix B). Even for a thermal energy as small as 0.03% of the energy of the string solution, the amplification of the zero mode occurs. However, it takes place in a longer time scale.

In order to quantitatively test the analytic system, we extract the amplitude of both the shape and zero modes directly from the simulation. We do this as follows. Firstly, we assume that the field configuration at any time is given by

$$\phi(t,r,\theta,z) = f(r)e^{i\theta} + A(t)s^{(1)}(r)e^{i\theta} + D(t)\eta_x^0(r,\theta)\cos(k_z z) + R\left(t,r,\theta,z\right)\ , \tag{5.28}$$

where $R(t,r,\theta,z)$ denotes collectively the scattering states. In order to find the amplitude of the shape mode, $A(t)$, we multiply both sides of (5.28) by $s^{(1)}\left(r\right)e^{-i\theta}$ and integrate the real part over all space to get

$$A\left(t\right) = \frac{1}{2\sqrt{2}\pi L_z}\int_{-L_z/2}^{L_z/2} dz \int_0^{2\pi} d\theta \int_0^{r_{\max}} dr\, r\left[\phi_1\left(t,r,\theta,z\right)\cos\theta + \phi_2\left(t,r,\theta,z\right)\sin\theta\right] s^{(1)}\left(r\right)\ , \tag{5.29}$$

Similarly, the amplitude of the zero mode can be obtained by projecting onto $(\eta_x^0)^*$. The result is

$$D\left(t\right) = \frac{\sqrt{2}\pi}{L_z}\frac{\int_0^{L_z/2} dz \int_0^{2\pi} d\theta \int_0^{r_{\max}} dr\, r\left[\phi_1\left(f'\cos^2\theta + \frac{f}{r}\sin^2\theta\right) + \phi_2\left(f' - \frac{f}{r}\right)\sin\theta\cos\theta\right]}{\int_0^{2\pi} d\theta \int_0^{r_{\max}} dr\, r\left[\left(f'\right)^2 + \left(\frac{f}{r}\right)^2\right]}\ . \tag{5.30}$$

The numerical amplitudes we obtain following this prescription are shown in figure 5.2, where we compare them with the predictions of the system of equations (5.23). For this comparison, we performed a different simulation with a smaller initial amplitude of the shape mode in order to reduce the effects of radiation as much as possible. In this case, we chose $A\left(t=0\right) = 0.1$, $D\left(t=0\right) = 0.1$ and $k_z = 2\pi/L_z$, in a lattice with $L_x = L_y = 80$, $L_z = 13.8$, $\Delta x = 0.1$ and $\Delta t = 0.05$.

We note that the solution of the analytic equations is very sensitive to the numerical values of the coefficients. Indeed, complete agreement in figure 5.2 is not obtained unless we slightly modify a few numbers involved in equations (5.23). In the example we have shown, the required changes are the following:

- $I_{AD,3} \ \rightarrow\ 1.17 \times I_{AD,3}$
- $k_z^2 + I_{D,2}/I_D(R) \approx 0.207 \ \rightarrow\ 0.2077$

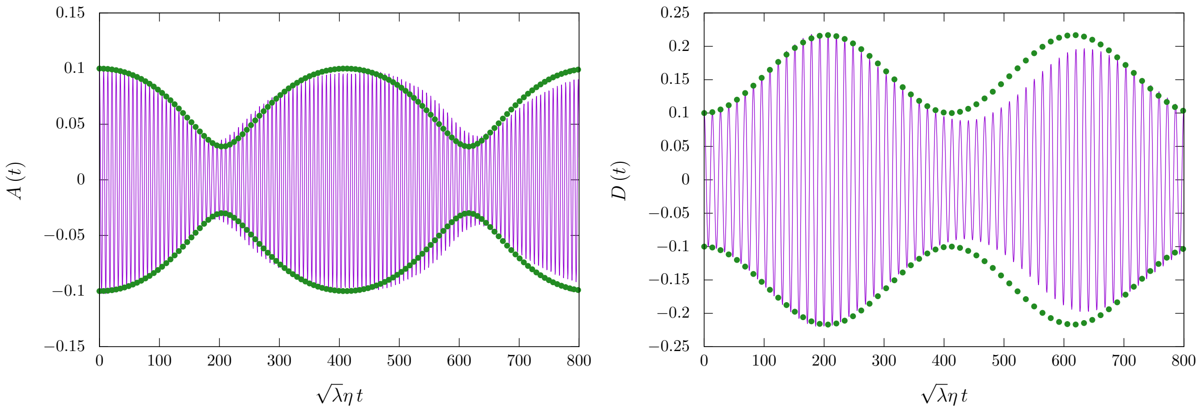

Figure 5.2: Comparison of the measurements of the shape mode (left) and zero mode (right) from the field theory simulation (in purple) with the results predicted using the equations of motion coming from our effective Lagrangian (green).

We attribute these imprecisions to the fact that all the functions involved in the integrals above are found numerically, and thus they come with some degree of uncertainty. The integral $I_{D,2}$ was found to be particularly sensitive to the number of points used for the integrand.

With the new coefficients, we get a very good agreement with the theoretical expectation for the first oscillation. The subsequent slight deviation is also to be expected since the field theory simulation allows for the presence of radiation emitted from the string, and this effect is not included in our analytical treatment.

5.4 Radiation from the excited string

As we explained in the previous sections, an axionic string is coupled to the massless Goldstone mode that propagates in the vacuum. This can be easily seen if one excites a zero mode on the string. The initial amplitude of this excitation will decrease as the string oscillates mainly due to massless radiation. This has been studied in the literature [135, 143, 140, 141], more notably recently with the aid of adaptive mesh refinement techniques in [138, 139]. We have also performed this type of simulations and obtained a similar result. Most of the energy emitted from an initial zero mode excitation occurs in the form of massless modes in the low amplitude regime. Increasing the amplitude of these oscillations, one encounters a mix of massive and massless radiation due to non-perturbative processes. Such massive non-perturbative radiation was observed in chapter 3, when we explored collisions of high-curvature wave packets on the domain wall string.

On the other hand, a string excited with a homogeneous shape mode perturbation will decay mostly in terms of massive radiation. This was demonstrated in the context of $2+1$ dimensional vortices in chapter 4, where we described analytically the slow decrease of the amplitude of this mode as a function of time. We have corroborated that this is the case in our current $3+1$ dimensional setup when the parametric resonance discussed in the previous section is not set off.

The situation becomes more interesting when the parametric resonance takes place. The initial excitation of the shape mode leads to massive radiation due to the coupling of this mode to the massive scattering states. However, the subsequent amplification of the zero mode leads to the appearance of massless radiation. The non-linear coupling of the shape mode and the zero modes gives rise to a mixture of massless and massive radiation. We show in figure 5.3 the different contributions of the total energy radiated by the string.

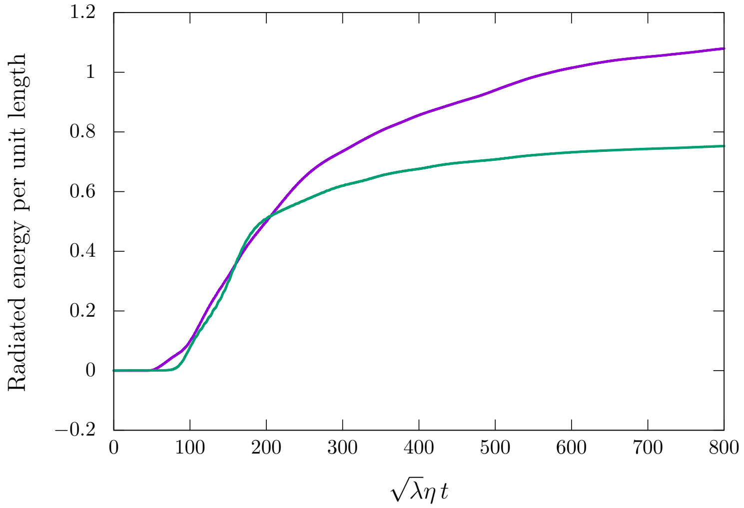

Figure 5.3: Amount of energy radiated in the form of the massive mode (purple) and the massless mode (green) as a function of time. The quantity shown in the y axis is a dimensionless energy per unit length, namely, energy per unit length divided by η^2. In this simulation, the shape mode is initialized homogeneously with amplitude $A(t=0)=0.6$, which corresponds to an initial extra energy per unit length of 2.1 in these units.

The computation of this energy is done by integrating the radiated power over the surface of a distant box surrounding the string. In order to account separately for the energy radiated in massive and massless modes, we follow the prescription given in [138, 139]. The 00 and $0i$ components of the energy-momentum tensor can be written as

$$T^{00} = \Pi_\varphi^2 + (\mathcal{D}\varphi)^2 + \Pi_\alpha^2 + (\mathcal{D}\alpha)^2 + V\left(\phi_1, \phi_2\right) \,, \tag{5.31}$$

$$T^{0i} = 2\left[\Pi_\varphi \left(\mathcal{D}\varphi\right)_i + \Pi_\alpha \left(\mathcal{D}\alpha\right)_i\right] , \tag{5.32}$$

where

$$\Pi_\varphi = \frac{1}{\sqrt{2}} \frac{\phi_1 \partial_t \phi_1 + \phi_2 \partial_t \phi_2}{\sqrt{\phi_1^2 + \phi_2^2}} , \tag{5.33}$$

$$\mathcal{D}\varphi = \frac{1}{\sqrt{2}} \left(\frac{\phi_1 \partial_x \phi_1 + \phi_2 \partial_x \phi_2}{\sqrt{\phi_1^2 + \phi_2^2}}, \frac{\phi_1 \partial_y \phi_1 + \phi_2 \partial_y \phi_2}{\sqrt{\phi_1^2 + \phi_2^2}}, \frac{\phi_1 \partial_z \phi_1 + \phi_2 \partial_z \phi_2}{\sqrt{\phi_1^2 + \phi_2^2}} \right) , \tag{5.34}$$

$$\Pi_\alpha = \frac{1}{\sqrt{2}} \frac{\phi_1 \partial_t \phi_2 - \phi_2 \partial_t \phi_1}{\sqrt{\phi_1^2 + \phi_2^2}} , \tag{5.35}$$

$$\mathcal{D}\alpha = \frac{1}{\sqrt{2}} \left(\frac{\phi_1 \partial_x \phi_2 - \phi_2 \partial_x \phi_1}{\sqrt{\phi_1^2 + \phi_2^2}}, \frac{\phi_1 \partial_y \phi_2 - \phi_2 \partial_y \phi_1}{\sqrt{\phi_1^2 + \phi_2^2}}, \frac{\phi_1 \partial_z \phi_2 - \phi_2 \partial_z \phi_1}{\sqrt{\phi_1^2 + \phi_2^2}} \right) . \tag{5.36}$$

The terms with φ correspond to the contribution of the massive modes, while those with α are identified as the contribution of the massless modes. Therefore, their corresponding radiated powers are given by

$$\begin{aligned} P_{\text{massive}} = 2 \quad \Big[& \int_{-L_z/2}^{L_z/2} dz \int_{-L_y/2}^{L_y/2} dy \, \left(\Pi_\varphi \left(\mathcal{D}\varphi\right)_1 |_{x=-L_x/2} + \Pi_\varphi \left(\mathcal{D}\varphi\right)_1 |_{x=L_x/2} \right) \\ + & \int_{-L_z/2}^{L_z/2} dz \int_{-L_x/2}^{L_x/2} dx \, \left(\Pi_\varphi \left(\mathcal{D}\varphi\right)_2 |_{y=-L_y/2} + \Pi_\varphi \left(\mathcal{D}\varphi\right)_2 |_{y=L_y/2} \right) \Big] , \end{aligned} \tag{5.37}$$

$$\begin{aligned} P_{\text{massless}} = 2 \quad \Big[& \int_{-L_z/2}^{L_z/2} dz \int_{-L_y/2}^{L_y/2} dy \, \left(\Pi_\alpha \left(\mathcal{D}\alpha\right)_1 |_{x=-L_x/2} + \Pi_\alpha \left(\mathcal{D}\alpha\right)_1 |_{x=L_x/2} \right) \\ + & \int_{-L_z/2}^{L_z/2} dz \int_{-L_x/2}^{L_x/2} dx \, \left(\Pi_\alpha \left(\mathcal{D}\alpha\right)_2 |_{y=-L_y/2} + \Pi_\alpha \left(\mathcal{D}\alpha\right)_2 |_{y=L_y/2} \right) \Big] . \end{aligned} \tag{5.38}$$

Due to this resonance phenomenon, the energy stored in the initial internal excitation is radiated away faster than one would have estimated from the calculation in $2+1$ dimensions. We illustrate this effect in figure 5.4 by comparing the extra energy in the simulation box for a string excited with the shape mode in two cases: one where the resonant amplification of the zero mode is allowed and another one where this possibility is prohibited by a small length of the box in the z direction. We clearly see that the extra energy initially stored in the shape mode is radiated faster due to the coupling of the emergent zero mode to the massless Goldstone boson in the vacuum.

In these simulations, we initialized the shape mode with an amplitude of $A\left(t=0\right) = 0.6$, and we used $L_x = L_y = 80$, $\Delta x = 0.1$ and $\Delta t = 0.05$. The cutoff distance in this case is

$R \approx 40$. Therefore, using (5.22) we have $I_D\left(R=40\right) \approx 0.8$ and it follows from (5.25) that the resonant zero mode has wavelength $\lambda_z \approx 14$. The length of the box in the z direction was chosen to be $L_z = 14$ in the case where the amplification is allowed (red curve in figure 5.4) and $L_z = 2$ in the other case (orange curve in figure 5.4).

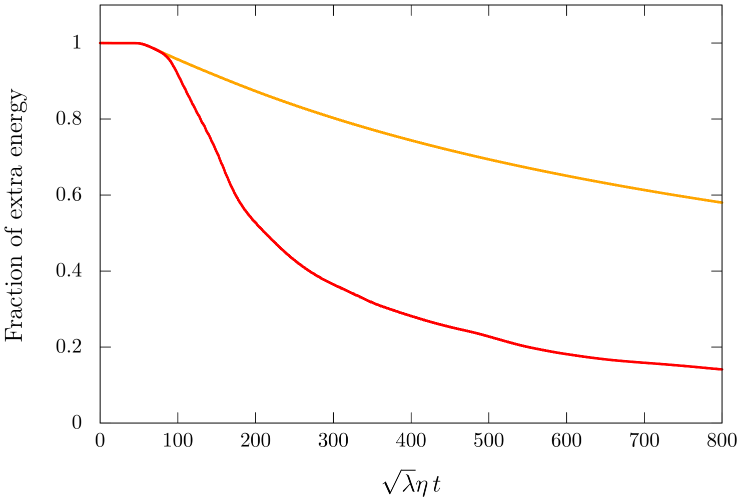

Figure 5.4: Comparison of the extra energy for an excited string with the same initial amplitude of the shape mode but different size in the z direction. In orange we show the fraction of this initial energy in the case of an excited string where the parametric resonance is prevented by the short length of the box in the z direction. In red, we show the case in which the resonance is allowed and kicks in. Both these simulations use absorbing boundary conditions for the (x, y) boundaries of the box.

Let us note that the field configuration we have analyzed, which consists of a string that undergoes parametric resonance starting from a homogeneous excitation of the shape mode, radiates fundamentally at two specific frequencies. On the one hand, the angular frequency of the massive radiation is $\omega_{\text{massive}} \approx 2\omega_s$. On the other hand, the frequency of the resonant zero mode is $\omega_s/2$. Since the source term for radiation is also quadratic in the zero mode (see appendix C), we should expect the angular frequency of massless radiation to be $\omega_{\text{massless}} \approx \omega_s$. This is precisely what we observe in our simulations. We illustrate in figure 5.5 the massive and massless radiation patterns in a case where the instability occurs.

The snaphots in figure 5.5 are taken from a simulation with an initial shape mode excitation of $A\left(t=0\right) = 0.2$, in a lattice with $L_x = L_y = 80$, $L_z = 40$, $\Delta x = 0.08$ and $\Delta t = 0.04$.

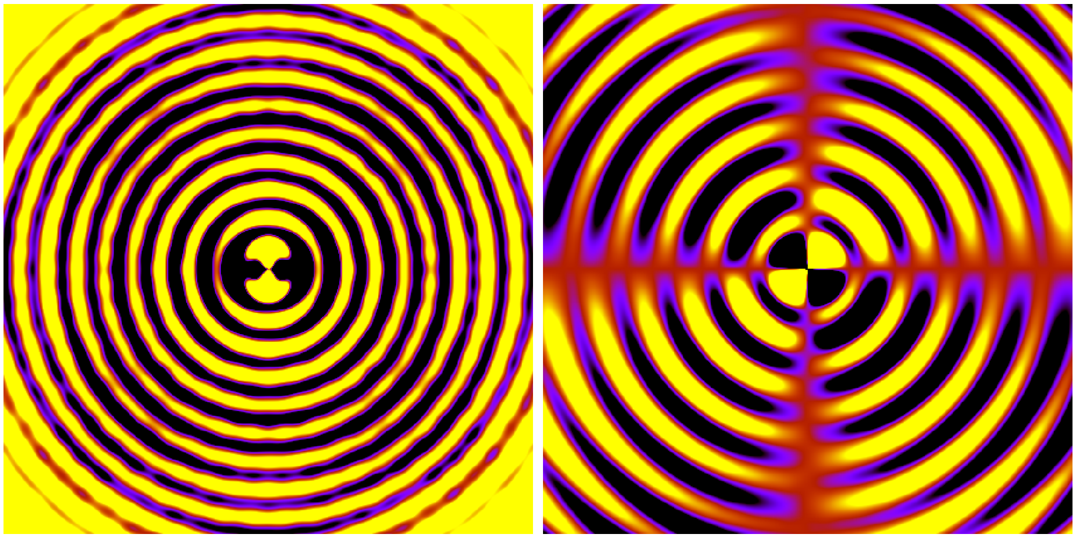

Figure 5.5: Snapshot of the massive and massless radiation (left and right panels, respectively) emitted by a homogeneously excited string which undergoes parametric resonance, on the $z = 0$ plane. On the one hand, the cylindrically symmetric massive radiation field shown is obtained by subtracting at each time step the static string solution and the shape mode with its instantaneous amplitude from the radial part of the field. On the other hand, the massless radiation is obtained by subtracting the polar angle from the angular part of the field. This quadrupole mode for the massless radiation was already identified as the dominant one in [138].

5.5 Conclusions

In this chapter, we have shown that axionic strings can undergo parametric resonance effects due to the interaction between massless modes that parametrize the transverse motion of the string and the massive shape modes that modify the internal structure of the soliton. The presence of this instability leads to quantitative as well as qualitative differences in the spectrum of radiation from axionic strings. Therefore, this study could have important implications on the estimate of axionic dark matter abundance from cosmological global string networks.

In order for this effect to become important, the strings must be in an excited state where part of the energy is stored in the shape mode. One of the instances where this can happen is, of course, during the formation of the strings. In the case of vortices in $2+1$ dimensions, studied in chapter 4, the level of excitation of the shape mode in this process was found to be very low. However, this conclusion may change depending on the way the initial conditions are set. Some lattice field theory simulations of axionic strings use some period of relaxation where these internal modes are presumably heavily suppressed. Others do not have this friction regime and could easily produce strings with internal excitations of higher amplitude. From the results presented in this chapter, one could speculate that this would lead to a transient regime in which both massive and massless radiation is efficiently produced from the network. Indeed, some simulations have found a significant amount of massive radiation in the early stages of their evolution [64]. It would be interesting to understand whether this is due to the excitation of the internal modes of the strings and whether the instability we have discovered here is present.

These effects could also take place in the course of the network's evolution whenever strings intercommute. It is possible that the shape mode absorbs some energy in this type of events. In fact, this has been the claim put forward in [84] based on the formation of loops from the intersection of long strings. Interestingly, in this paper it is shown that part of the spectrum of radiation from these loops is in the form of massive radiation, which would seem to be in agreement with our observations.

The results presented in this chapter are similar to the ones obtained in chapter 3 for the case of domain wall strings. We argued there that the amplification of the zero mode could be captured by adding to the effective action a term that represents the coupling between the scalar field describing the amplitude of the internal mode and the Ricci scalar of the string worldsheet. We conjecture that a similar term could also do the job for axionic strings, and we leave for future work the role of this kind of couplings in an effective action which also includes the Kalb-Ramond term.

Finally, it is reasonable to expect that the mechanism described in this chapter is also present in other field theory models with solitons where there are both types of excitation modes living on the worldvolume of the defects. In particular, it would be interesting to identify whether this can happen in the case of local strings, or more generically in higher-dimensional defects as brane-like objects.

Chapter 6

Dynamics of $3 + 1$ dimensional local string loops

In this chapter, we compare the dynamics of cosmic string loops obtained directly in Abelian-Higgs field theory simulations with their expected motion according to the Nambu-Goto action. We demonstrate that these loops follow the trajectories predicted within the Nambu-Goto effective theory except in regions of high curvature, where energy is emitted from the loop in the form of massive radiation. This energy loss continues for all the loops we have analyzed until they self-intersect or become so small that they disappear well before they complete a single oscillation. We comment on the relevance of this investigation to the interpretation of the results from field theory simulations, as well as their extrapolation to a cosmological context.

6.1 Introduction

As we have seen in the previous chapters, the dynamics of solitons can be explored by performing numerical experiments in lattice simulations. Every point in this lattice is simply evolved according to the full non-linear equations of motion. One can then recover the information of the evolution of the fields in the lattice and interpret the results in terms of a collection of solitons in motion possibly interacting with each other. In this approach, one can probe the profiles of the fields at scales smaller than the characteristic soliton size[1], and also identify whether the solitons are in an excited state or not.

However, in computational terms, this procedure is very expensive if one wants to simu-

---

[1] This is always the case since the lattice spacing is required to be smaller than that scale.

late a volume that is large compared to the size of the soliton. This is particularly relevant in simulations that involve many solitons or whenever one is interested in investigating an effect whose characteristic scale is much larger than the soliton's thickness. In these cases, one is forced to look for some effective theory that captures the degrees of freedom that are relevant for the problem without having to simulate every point in the lattice. Simulations based on effective theories thus handle a much smaller number of degrees of freedom, and consequently, the dynamic range is greatly increased. In turn, this can help us obtain a better understanding of the large-scale dynamics of the system. Nevertheless, one needs to make sure that there are no microphysical effects missed in the effective theory that could potentially become relevant for the large scale-dynamics that one wants to faithfully reproduce in the simulation.

These two types of simulations are, therefore, complementary. One can use the lattice simulations to learn the important field theory effects that need to be accounted for in the effective theory of the solitons. Once this is done, one should be able to find some common ground where both these simulations can be compared and where an agreement can be reached on the important dynamics to study. Once this is achieved, an extrapolation to the relevant scales can be safely done using the effective theory.

In this chapter, we aim to take the first step towards showing this agreement between the lattice and effective approaches in the context of local cosmic string networks. In this case, we will consider the Abelian-Higgs model as the field theory where local cosmic strings appear as solitons [165] and the Nambu-Goto action as the effective theory at low energies [166, 167]. Cosmological simulations of both types, lattice field theory [168, 169, 155, 170, 87, 171, 172, 173] and Nambu-Goto [174, 175, 176, 177, 74, 178, 179, 75, 76, 180], have been extensively studied in the past. However, as we pointed out in chapter 1, there seems to be an important disagreement about the abundance of non-self-intersecting loops between these two numerical approaches. Let us recall that all the loops found so far in field theory simulations self-intersect, and they disappear before completing a single oscillation. On the contrary, a population of non-self-intersecting loops is found in Nambu-Goto simulations. These loops decay by emitting gravitational waves, whereas loops that continually intersect lose energy also via massive radiation. A possible explanation for this discrepancy could be that field theory simulations have not been lucky enough to produce a sufficiently large non-self-intersecting loop. This is reasonable as field theory simulations have much fewer loops in general, and the Nambu-Goto dynamics shows that non-self-intersecting conditions in a random loop are rare compared to self-intersecting ones.

As we have been discussing in the previous chapters, another possibility is the presence of internal excitations on the strings. We have seen that these modes are extremely long-lived and can store significant amounts of energy. Consequently, they can modify the equation of state of the strings, and hence their expected dynamics. In particular, the resonance phenomena described in chapters 3 and 5 exemplify this. Moreover, we have shown that these bound states can be excited when the defects are formed in phase transitions, when they are placed in a thermal bath, and when they interact with other defects and radiation. Collisions of wiggles and kinks on the strings can also give rise to local excitations of the bound states.

In this chapter, we will analyze the evolution of loops extracted directly from field theory simulations. More specifically, we will obtain the position and velocity of some of the largest loops found in the course of a field theory simulation of a network of strings and we will compare their evolution with the one predicted by the Nambu-Goto action. Let us anticipate that our results indicate that these loops follow the Nambu-Goto prediction except in localized regions where the radius of curvature is small compared with the string thickness. By definition, the Nambu-Goto approximation is not good in such regions. Furthermore, we find no evidence for a new equation of state for the strings. This seems to imply that internal modes are barely excited in the simulations.

The organization of this chapter is the following. In section 6.2, we briefly describe the field theory simulations that were used to generate the loops. In section 6.3, we detail the techniques we use to compare the dynamics of field theory loops and the Nambu-Goto prediction. In section 6.4, we present our results with a few snapshots showing simultaneously the field theory and Nambu-Goto trajectories. Finally, in section 6.5, we comment on the implications of these findings for the cosmological extrapolation of the results obtained in field theory simulations of cosmic string networks.

6.2 Field theory simulations of cosmic string loops

The field theory that we will investigate in this chapter is the Abelian-Higgs model in Minkowski space, whose Lagrangian density was already introduced in chapter 1:

$$\mathcal{L} = (D_\mu \phi)^* D^\mu \phi - \frac{\lambda}{4}\left(\phi^*\phi - \eta^2\right)^2 - \frac{1}{4e^2} F_{\mu\nu} F^{\mu\nu} \, . \tag{6.1}$$

This describes the dynamics of a complex scalar field $\phi(t, \vec{x})$ coupled to a vector field $A_\mu(t, \vec{x})$ through the covariant derivative $D_\mu = \partial_\mu - iA_\mu$. The usual field strength for the vector field is given by $F_{\mu\nu} = \partial_\mu A_\nu - \partial_\nu A_\mu$, and we will consider the case $\beta = \lambda/(2e^2) = 1$, which means that the masses of the scalar and vector excitations in the vacuum are equal: $m = m_s = m_v$.

It is well known that the equations of motion obtained from this Lagrangian allow for the existence of solitonic vortices [165]. In $3 + 1$ dimensions, the vortices become strings whose energy is concentrated in a core thickness $\delta \sim m^{-1}$.

In order to compare the dynamics of the loops in this theory with the prediction of the Nambu-Goto action, we take the loops obtained in [83], which are created from some random initial conditions in the lattice. We point the interested reader to [83] for details, but we summarize here the necessary basic information. After discretization of the Hamiltonian that corresponds to the Lagrangian (6.1), the equations of motion are obtained and solved in cubic lattices with periodic boundary conditions.

The initial configuration of the system is chosen to be such that all fields are set to zero except for the scalar field, which is set to be a stationary Gaussian random field with a power spectrum given by

$$P_\phi = Ae^{-kl_\phi} \ , \tag{6.2}$$

where the amplitude A is chosen so that $\left\langle |\phi|^2 \right\rangle = \eta^2$. The free parameter which rules the initial randomness is the correlation length l_ϕ, which can be set initially to different values.

These random initial conditions lead to a considerable excess of energy in the simulation volume. Therefore, a cooling process is applied using a diffusive period of evolution, and once a smooth field distribution is obtained, the network evolves following the true equations of motion in flat space.

It is important to mention that, after the diffusive period, the network is at rest, which means that any loop at this initial stage will start from a static configuration. We will comment on these primordial loops in section 6.4, but let us for now point out that they will not be our main focus as they are not representative of the typical loops in a network simulation. Instead, we will be interested in loops which are formed later on in the evolution of the network, either by self-intersections or intercommutation of long strings.

In order to localize the position of the strings and the subsequent loops, one firsts identifies all the lattice plaquettes with a non-trivial winding in the simulations. Then, the connection between all the centers of these plaquettes will constitute the string. The evolution of the network is followed by outputting the windings, and the formation of loops coming from intersections is confirmed by visual inspection.

Since, as mentioned, the simulations are done using periodic boundary conditions, all the strings in the box can be considered to be closed loops, but these loops can be "broken" by the periodic boundary conditions. Thus, if one were to plot the loop directly, some would not appear to be a connected piece of string. In order to avoid this, the loops that are broken by the periodic boundary conditions were reconstructed by applying spatial translations and assigning new coordinates to the string positions. In this manner, one has a list of connected positions in space for all loops.

In total, we have analyzed seven loops (and their descendants) from the simulations in [83]. These loops were obtained using two different correlation lengths: $l_\phi = 15$ and 25 in η^{-1} units. All of them were produced using lattices of 1024 points per dimension with a spatial resolution of $\delta x = 0.125$ and temporal resolution of $\delta t = 0.2\delta x$, again in η^{-1} units. Moreover, the loops are output at each time step of the evolution so that the field theory information available for the Nambu-Goto reconstruction is as accurate as possible. This data, extracted directly from the field theory simulations, is the starting point of our analysis.

6.3 Comparing the field theory and Nambu-Goto trajectories

The effective action that describes the dynamics of local strings is expected to be the Nambu-Goto action [166, 167]. This can be justified by making a judicious choice of coordinate system around the center of the string and integrating the action along the transverse directions of the string [181]. This yields an action of the Nambu-Goto form. This argument rests on several assumptions that we now list in detail.

First, it assumes that the local radius of curvature R of the string is large compared to its thickness δ. In fact, one can think of the Nambu-Goto action as the lowest-order approximation of an infinite expansion in powers of δ/R. In a cosmological setting, truncating this series keeping only the first term seems quite reasonable since the separation of scales from the microphysical size of the strings to any cosmologically relevant scale is huge. Of course, this separation of scales is not so large in a field theory simulation of a string network.

The second assumption, which is somewhat related to the previous one, is that the string does not lose energy by radiation in the course of its evolution. This is built in the Nambu-Goto action since there is a conservation law for the invariant length of a loop. However, from the point of view of field theory, solitonic strings could lose part of their energy into radiation in the form of propagating modes in the bulk. Evidently, this cannot happen for a relaxed static string, since this is an exact solution to the equations of motion. Boosting this object cannot lead to radiation either. The only way this string can radiate is due to acceleration, which is locally acquired in regions that get curved during the evolution. The question is then a quantitative one. How much energy is radiated due to the typical acceleration of the strings in their evolution? In order to answer this question, we should keep in mind that all the propagating modes in the Abelian-Higgs model are massive (see section 1.3.2). This suggests that one should wiggle the string with a frequency at least of the order of this mass, m in our case, in order to make it radiate. Our results in section 3.3 confirm this expectation for the case of domain wall strings.

Radiation can also be emitted non-perturbatively by intercommutation processes [182], in which strings cross and emerge having changed partners (see figure 1.8 in the introductory chapter). Other processes closely related to these are the formation of cusps and collisions of kinks (figure 1.9). During the formation of the cusp, part of the string annihilates with itself and releases energy in the process [85]. Similarly, kink-kink collisions [82], or in general, the appearance of very high curvature regions [86], lead to a similar energy ejection from the string. All these non-perturbative processes cannot be described by the Nambu-Goto action and need to be accounted for separately.

Finally, another important assumption in the use of the Nambu-Goto action is the general expectation that, in their rest frame, the solitonic strings are well approximated by the static solution of lowest energy. The underlying idea for this expectation is the supposition that excitations on the string will decay in a time scale comparable to the thickness of the soliton. However, as we have showed in the previous chapters, there exist long-lived excitations that can be present for the whole span of numerical simulations. Furthermore, they allow for effects (for instance, parametric resonances) that are not captured by the Nambu-Goto action. Nevertheless, these bound states are not expected to store energy at very late times, so it seems reasonable to assume that they are not relevant in a cosmological context.

Here we set out to investigate the relevance of all these possible effects in the evolution of cosmic string loops. We will compare the evolution of the loops extracted from field theory simulations following the procedure described in the previous section with the one predicted by the Nambu-Goto action. In the next subsection, we will explain how to reconstruct the Nambu-Goto dynamics from the field theory data at any moment in time.

6.3.1 Nambu-Goto reconstruction from field theory data

The Nambu-Goto approximation was presented in full detail in the introductory chapter, in section 1.4. The action is given in equation (1.15):

$$S_{NG} = -\mu \int \sqrt{-\gamma}\, d^2\zeta \,, \tag{6.3}$$

where μ is the energy per unit length of the string and γ is the determinant of the worldsheet metric, which is parametrized by the coordinates ζ^0 and ζ^1. In order to reconstruct the Nambu-Goto trajectory from the field theory data, it is useful to employ the conformal gauge, which corresponds to a parametrization of the string worldsheet given by $\zeta^0 = t$ (the usual Minkowski time) and $\zeta^1 = \sigma$ (proportional to the string energy measured from some arbitrary point on the string; see equations (1.26) and (1.27)). In this gauge, the equation of motion for the string position vector $\vec{X}\,(t,\sigma)$ reduces to the wave equation (1.22), so the solution is given by (1.29):

$$\vec{X}\,(t,\sigma) = \frac{1}{2}\left[\vec{a}\,(\sigma - t) + \vec{b}\,(\sigma + t)\right] \,. \tag{6.4}$$

The gauge conditions (1.23) and (1.24) impose the constraint (1.30) on the sigma derivative of the left and right movers:

$$|\vec{a}\,'| = |\vec{b}\,'| = 1. \tag{6.5}$$

Therefore, in order to obtain the Nambu-Goto trajectory of the loop, all one needs to do in practice is to find the form of the functions $\vec{a}$ and $\vec{b}$ with respect to their arguments. Note that, after obtaining these functions at a particular moment, equation (6.4) will allow us to find the position of the string at any time, provided that no intercommutations take place[2]. This can in turn be compared with the position in field theory.

Another tool that one can use to see whether the loop behaves globally as the Nambu-

---

[2] In this case, one has to compute the new $\vec{a}$ and $\vec{b}$ functions corresponding to the daughter loops and analyze them separately.

Goto action predicts is the invariant length, which is the integral of σ along the whole loop. This is a constant of motion in the Nambu-Goto description.

The starting point for the Nambu-Goto reconstruction is two lists of vectors corresponding to the field theory positions of each point on the loop at $t = 0$ and $t = \Delta t = 8\delta t$. We will use the data in these two time steps to compute the velocity of each point. The reason for taking this time interval bigger than δt is to try to smooth out possible errors in the estimate of the velocity[3]. All the details of the reconstruction algorithm can be found in appendix E. Here we sketch the main steps:

1. We first smooth out the field theory position vectors mentioned above to avoid possible artifacts coming from the discrete nature of the lattice. We do this with a Gaussian window function whose width w is given by a few lattice spacings. We chose Mδx with $M = 2$.

2. Using the smoothed data, we compute the unit tangent vectors from the difference of consecutive position vectors.

3. The next step is to compute the velocity and the Lorentz factor of each point n of the loop at $t = 0$ assuming that the velocity is perpendicular to the tangent vector, in agreement with (1.23). Let $\vec{X}_n$ be the position vector of the loop at $t = 0$. In order to obtain their velocities, we have to find, for each n, the intersection of the plane perpendicular to the tangent vector at that point with the loop at $t = \Delta t$. Let us denote this intersection point by $\vec{\mathcal{X}}^*_n$. The velocity is then estimated as

$$\dot{\vec{X}}_n = \frac{|\vec{\mathcal{X}}^*_n - \vec{X}_n|}{\Delta t}\,, \tag{6.6}$$

   and the Lorentz factor as

$$\Gamma_n = \frac{1}{\sqrt{1 - |\dot{\vec{X}}_n|^2}}\,. \tag{6.7}$$

4. Now, we find the sigma derivative of the position vectors as

$$\vec{X}'_n = \frac{\vec{X}_{n+1} - \vec{X}_n}{\Delta\sigma_n} = \frac{1}{\Gamma_n}\frac{\vec{X}_{n+1} - \vec{X}_n}{|\vec{X}_{n+1} - \vec{X}_n|}\,. \tag{6.8}$$

---

[3] If Δt is taken too small, we may easily find superluminal points. This is, of course, an error induced in regions of high velocity of the string. Note also that regions of self-annihilation would give rise to these problems. However, superluminal motion is expected in this case since in those regions the string does not behave as the Nambu-Goto action predicts, and thus the algorithm should definitely fail.

One can easily check this by considering equation (1.27) for the amount of σ in the string segment n, which we have denoted by $\Delta\sigma_n$.

5. Finally, the left and right movers needed in (6.4) can be computed from

$$\vec{a}\,'(\sigma_n) = \vec{X}'_n - \dot{\vec{X}}_n\,, \tag{6.9}$$

$$\vec{b}\,'(\sigma_n) = \vec{X}'_n + \dot{\vec{X}}_n\,. \tag{6.10}$$

This follows inmediately from equations (1.31) and (1.32).

We can also compute the invariant length as $L = \sum_n \Delta\sigma_n$, where $\Delta\sigma_n$ can be read directly from (6.8).

In the course of the reconstruction, some points are found to have velocities very close to the speed of light, or even higher velocities, as we mentioned earlier. In order to suppress the pathological effect that these points could have on the invariant length, we have decided to put an artificial cap to the velocity of each individual point: we replace any estimate of $|\dot{\vec{X}}_n| > 0.9$ with $v_{\max} = 0.9$. We have tried other regularization procedures and checked that the invariant length of the loop is not significantly altered in these cases.

6.4 Results

6.4.1 Non-primordial loop

Using the techniques we have outlined above, we can compare the evolution of field theory loops from our simulations with the motion predicted by the Nambu-Goto dynamics. Using the data from two time steps in the field theory simulation separated by Δt, we build the functions $\vec{a}(\sigma)$ and $\vec{b}(\sigma)$. This allows us to plot the predicted Nambu-Goto position for all times. This comparison shows that the field theory loop follows the Nambu-Goto solution very accurately for most of the string length. This seems to suggest that these loops extracted directly from the simulation are not endowed with a significant amount of extra energy as conjectured in [83], or at least, not enough to change the trajectory of the string perceptibly. A large amount of energy in bound states would change the equation of state of the string and its local velocity would be modified with respect to the one obtained in Nambu-Goto. This is not observed for most parts of the string length.

However, there are regions of the loop where we observe a departure of the field theory and Nambu-Goto trajectories. Many of the string segments where we see this departure are regions where the Nambu-Goto dynamics predicts the onset of high curvature. The field theory loop would emit non-perturbative radiation in those regions, so it not a surprise that it does not follow the Nambu-Goto prediction there. An example of such local departure from Nambu-Goto dynamics is shown in figure 6.1.

In these snapshots, we represent the field theory string with some thickness of order δ (the width of the solitonic object). For most of the string, the position predicted by the Nambu-Goto action (in red) is hidden inside of the blue tube that gives the position of the field theory loop. The two curves only deviate from one another in a small section of the whole string. In that region, the Nambu-Goto string curves itself at a scale comparable to δ, but the field theory string does not do that and finds a shortcut.

These episodes of high curvature act as a source of energy from the string. Some of these events resemble the cusp annihilation simulated several years ago in [85], while others just correspond to the interaction of wiggles on the string that produce high-curvature regions. In some cases, these interactions lead to the formation of tiny daughter loops that immediately annihilate on the field theory side.

After those episodes, the evolution of the field theory string does not follow the Nambu-Goto prediction. The reason for this is clear: the Nambu-Goto action conserves energy, so it does not account for this energy loss mechanism. This means that the field theory and Nambu-Goto trajectories will start being different in the regions where energy is radiated. As time passes, this departure spreads over the rest of the string. If one waits long enough, the difference becomes quite visible, and if one were to continue the comparison forward, the shapes of the loops would grow more different. However, this is not a real measure of the different local dynamics. To address this issue, we follow a procedure also used in the past in [85]. Once we have identified one of these high-curvature events on the string, we start the Nambu-Goto reconstruction again taking as initial conditions the field theory data when the string has relaxed after the event. This yields different $\vec{a}$ and $\vec{b}$ functions that should be valid for the subsequent evolution. Doing this, what we see is that the field theory trajectory after these events is again accurately described by the new Nambu-Goto data. The new comparison after the event of figure 6.1 is shown in figure 6.2.

This behaviour continues for a while until a new episode occurs. This is shown in figure 6.3, where we clearly see another localized region where the Nambu-Goto prediction deviates from the field theory result. The string in field theory does not want to curve itself so much as the Nambu-Goto action predicts and takes a shortcut. Once again, some fraction of the energy of the string is radiated away in this process.

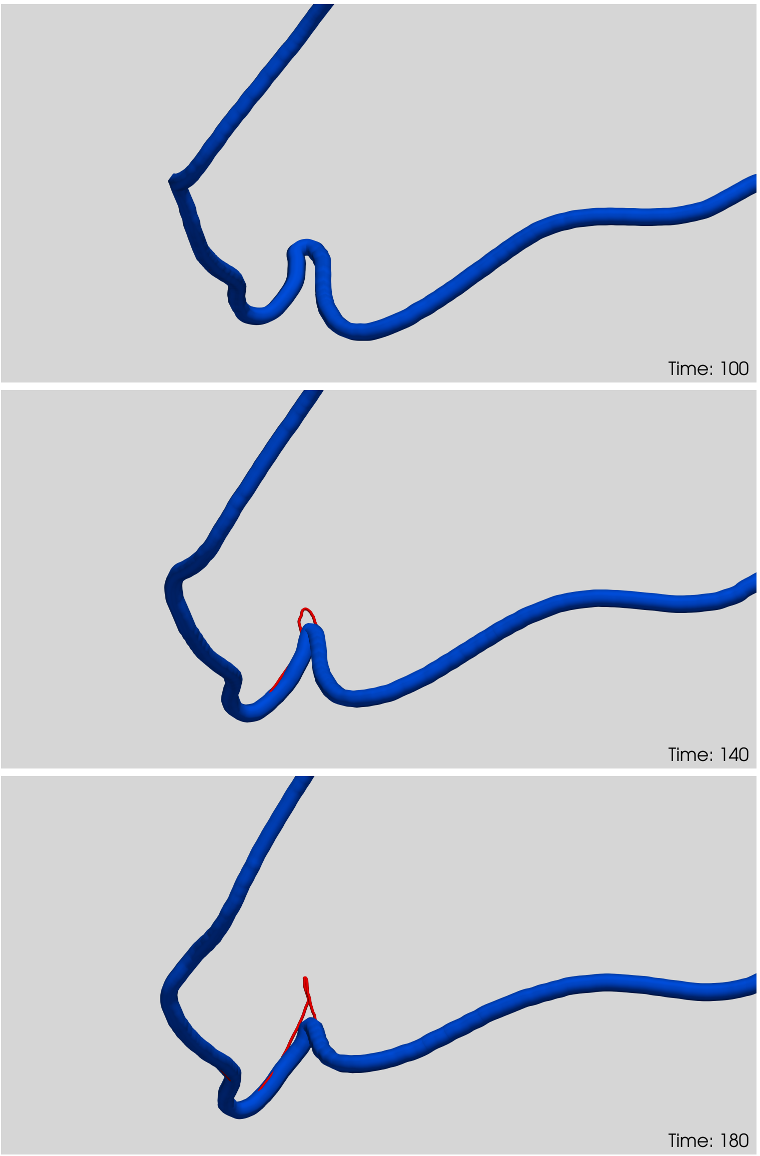

Figure 6.1: Several snapshots of the evolution of one of the field theory loops. We show in blue the position of the string obtained directly from the lattice simulation. In red is the predicted Nambu-Goto position obtained from the reconstruction procedure described in the previous section. The agreement between these two descriptions is very good for most of the loop's evolution. We have zoomed in on a region of the string at a particular moment where there is a visible departure between them.

We have seen a similar behaviour in all our loops. Some of the examples are clear, but some other ones are harder to visualize since more than one of these high-curvature events happen to have some non-trivial overlap in time. In fact, this already happens in our example loop. We show in figure 6.4 a third event which is simultaneous to the one represented in figure 6.3. This third event takes place quite far away in space from the previous one.

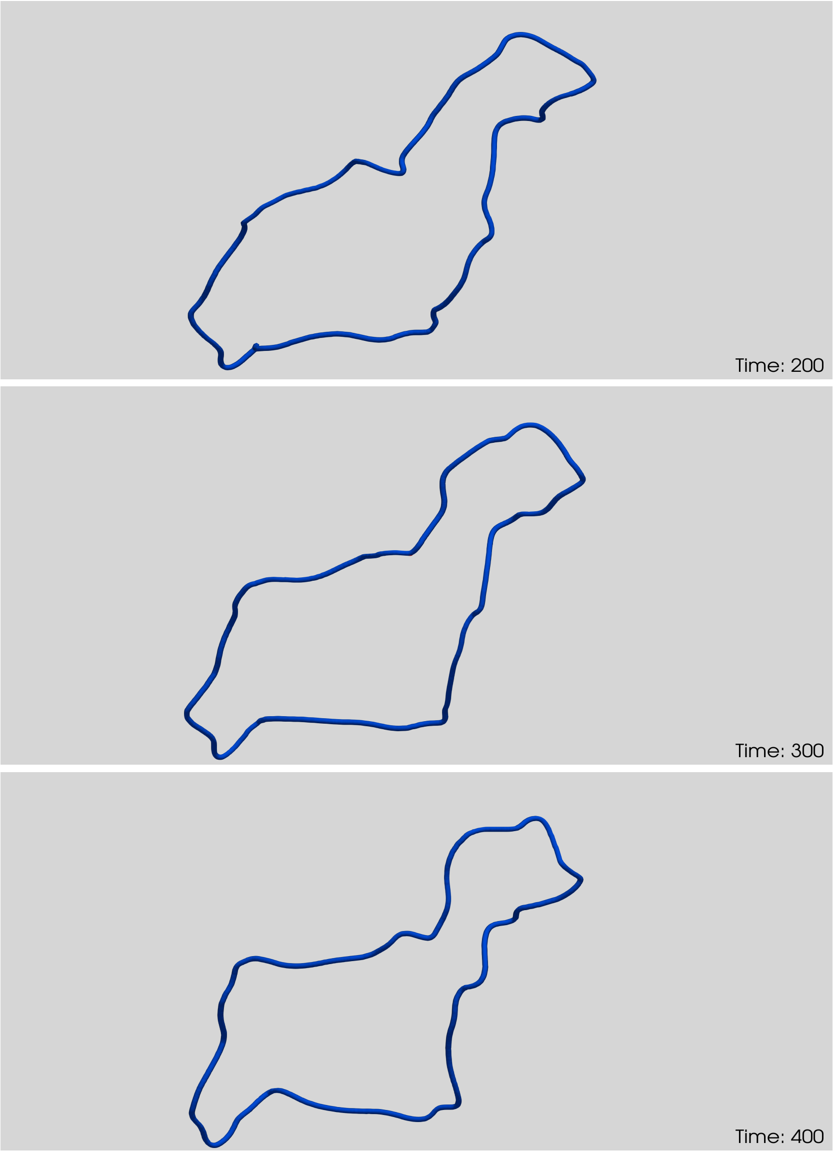

Figure 6.2: The evolution of the field theory loop seems to follow the Nambu-Goto prediction obtained from the reconstruction of the string after the high-curvature event. There is no visible departure between the Nambu-Goto and the field theory descriptions.

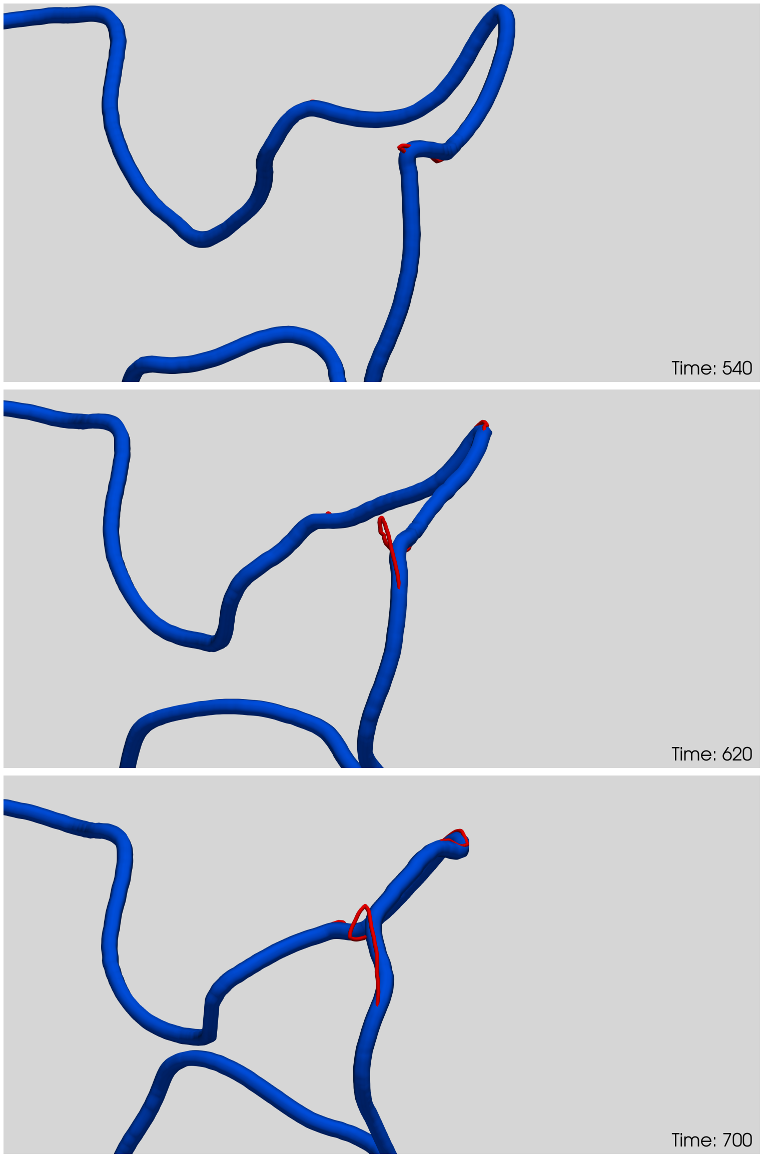

Figure 6.3: Another high-curvature event on the same loop. The Nambu-Goto description (in red) is the one obtained after the first event in figure 6.1. The evolution between these two episodes is well represented by the Nambu-Goto dynamics.

We also looked at the evolution of the invariant length of the loop. This is done by adding up the amount of σ of each string segment, as mentioned in the previous section. For this, we need the velocities of each point of the loop at every time step, so we compute them from the field theory data taken in pairs: we calculate the velocities at $t = 0$ from the field theory positions at $t = 0$ and $t = \Delta t$, the velocities at $t = \delta t$ from the field theory positions at $t = \delta t$ and $t = \delta t + \Delta t$, etc.

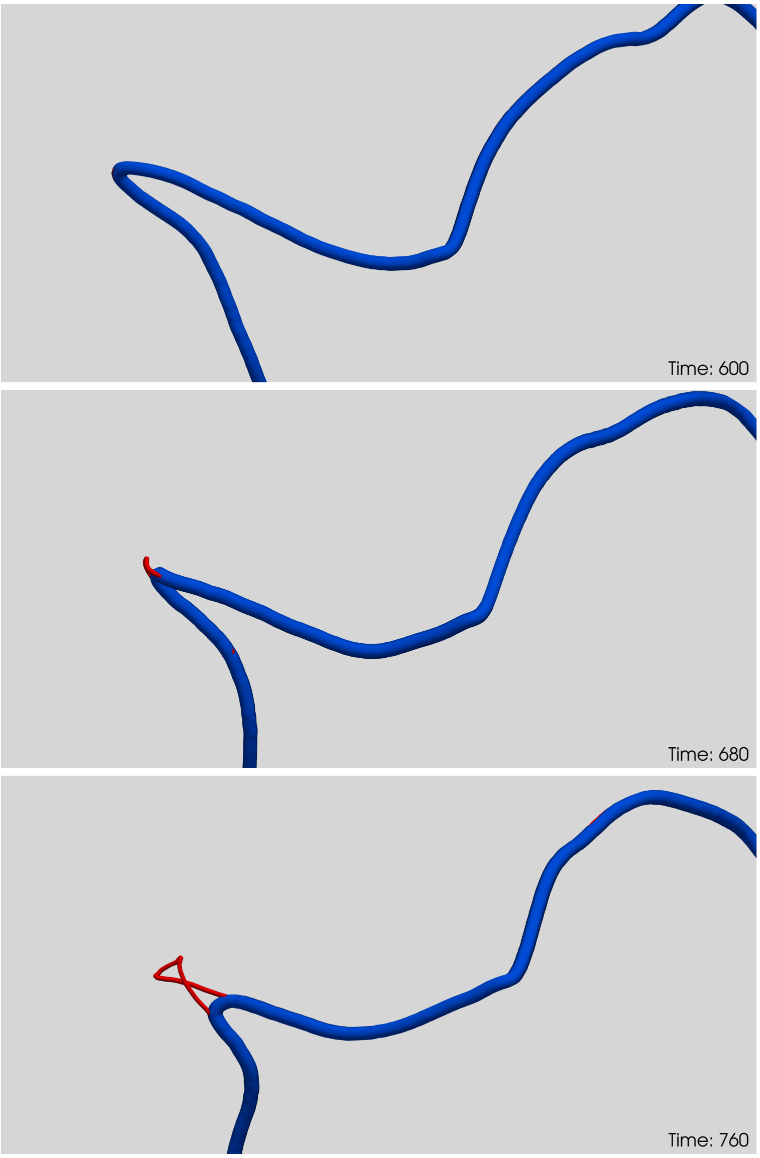

Figure 6.4: Another high-curvature event on the same loop. This one has some overlap in time with the event shown in figure 6.3. The Nambu-Goto description (in red) is the one obtained after the first event in figure 6.1.

In the Nambu-Goto description, the total amount of σ is a constant of motion. We plot in figure 6.5 this energy for the loop we discussed before. We observe that the energy overall tends to go down. There are some episodic events where this decrease is sharper, and some of those can be linked with the high-curvature events. We mark in this figure the three different episodes that we have been discussing above by shading in light purple the ranges of time displayed in figures 6.1, 6.3 and 6.4. Looking at the energy, there seems to be a connection between these events and the periods of time during which the energy decreases more strongly.

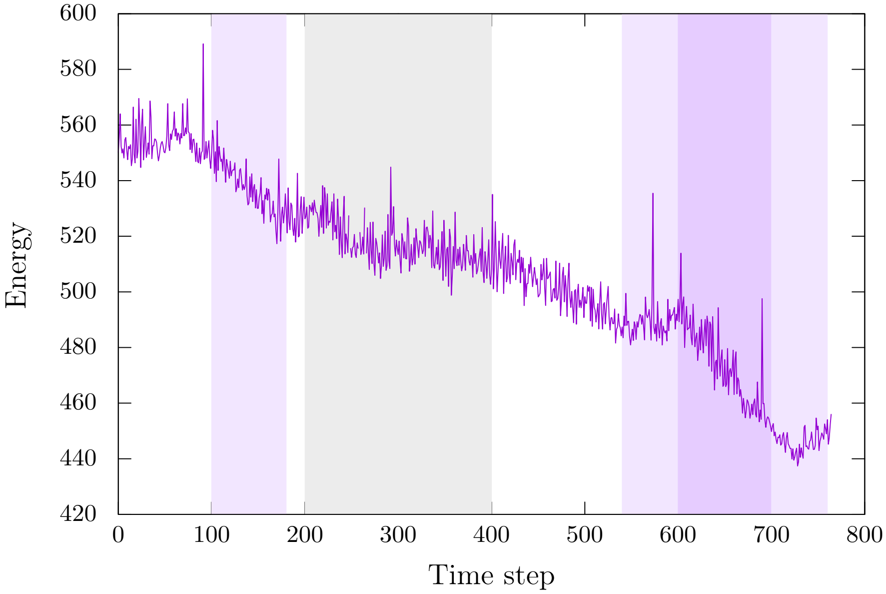

Figure 6.5: Invariant length (total amount of σ) for the Nambu-Goto reconstruction of the field theory data of the loop analyzed in the previous figures. The purple bands correspond to the high-curvature events presented in figures 6.1,6.3 and 6.4. The grey band corresponds to figure 6.2, where the energy remains roughly constant. The white region between time steps 400 and 540) corresponds to figure 6.6, where there is a small deviation from the Nambu-Goto dynamics.

There are other instances (between time steps 200 and 400) where the energy seems to be constant, represented in grey in figure 6.5. These correspond to the times for which the Nambu-Goto reconstruction was made after the first episode, as shown in figure 6.2, where there is a very good agreement with the field theory data.

There are, however, periods of time where the energy slowly decreases that are not so obviously associated with any of these individual high-curvature events (see figure 6.6, which corresponds to time steps 450, 500 and 550). The reasons for the decline of the energy in this case are not so clear. One possibility might be the presence of small-scale structure that leads to radiation. It is remarkable, and somewhat puzzling, that although the energy goes down roughly by the same percentage as in a high-curvature event, the visual inspection of the loop dynamics does show a rather small deviation from the Nambu-Goto trajectory. This could just be due to the combined effect of several smaller regions where the deviation is small instead of a single large event like in the other cases.

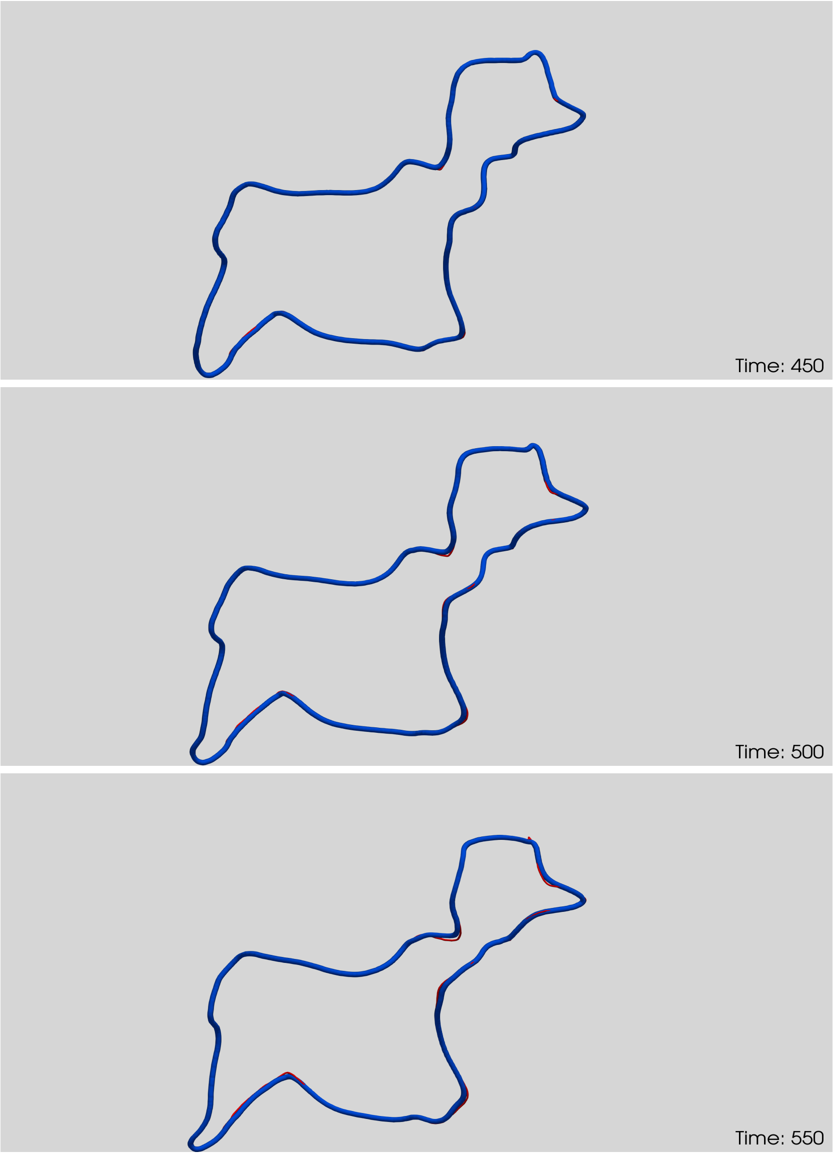

Figure 6.6: Evolution of the field theory string when the decline of the energy is not so obviously related to high-curvature regions.

6.4.2 Primordial loop

As pointed out before, we create our string network with an initial period of diffusion. One can, of course, look at the initial evolution of some of the loops created at this time as well. However, we should note that they are different from the ones we have analyzed in the rest of the chapter in many respects. First of all, they are much smoother due to the period of diffusion, and furthermore, they are created at rest, meaning that all the segments of the string start their evolution with zero initial velocity. The fact that they start evolving at rest makes them rather special from the Nambu-Goto perpective. As mentioned in chapter 1, it is easy to show that an initially static loop will overlap with itself along the entirety of its physical length in a quarter of its period if it moves according to the Nambu-Goto action [40]. Therefore, it is clear that we cannot use this kind of loops to illustrate the typical behaviour of a loop in a realistic cosmological setting. However, we can use these primordial loops to check the validity of our numerical code for the Nambu-Goto reconstruction and our results.

We show in figure 6.7 the comparison of the evolution of one of these primordial loops with the prediction of the Nambu-Goto action. The snapshots clearly show that the field theory and Nambu-Goto trajectories are pretty much identical all the way until they come close to the aforementioned overlap. Note also that this loop is much smoother than the previous ones, this being the reason why no high-curvature events occur until the overlap is inminent. However, in the last stages of collapse, the difference between the field theory and Nambu-Goto trajectories becomes more apparent. This is expected since the interaction of different regions of the string in this pathological self-intersection is not handled by the Nambu-Goto dynamics. Nevertheless, the fact that up to this point both descriptions agree with one another can be seen as a validation of both the field theory and Nambu-Goto reconstruction codes.

We also show in figure 6.8 the invariant length of this loop using the Nambu-Goto reconstruction at each moment in time. We notice that this energy is pretty much constant until time step 40, which is also the moment where we observe the first signal of deviation from Nambu-Goto dynamics in the evolution of the loop (see figure 6.7). From this time on, although the energy of the loop decreases, its trajectory seems to be very close to the one predicted by the Nambu-Goto action. This is somewhat similar to what happens in the case of the non-primordial loop in figure 6.6.

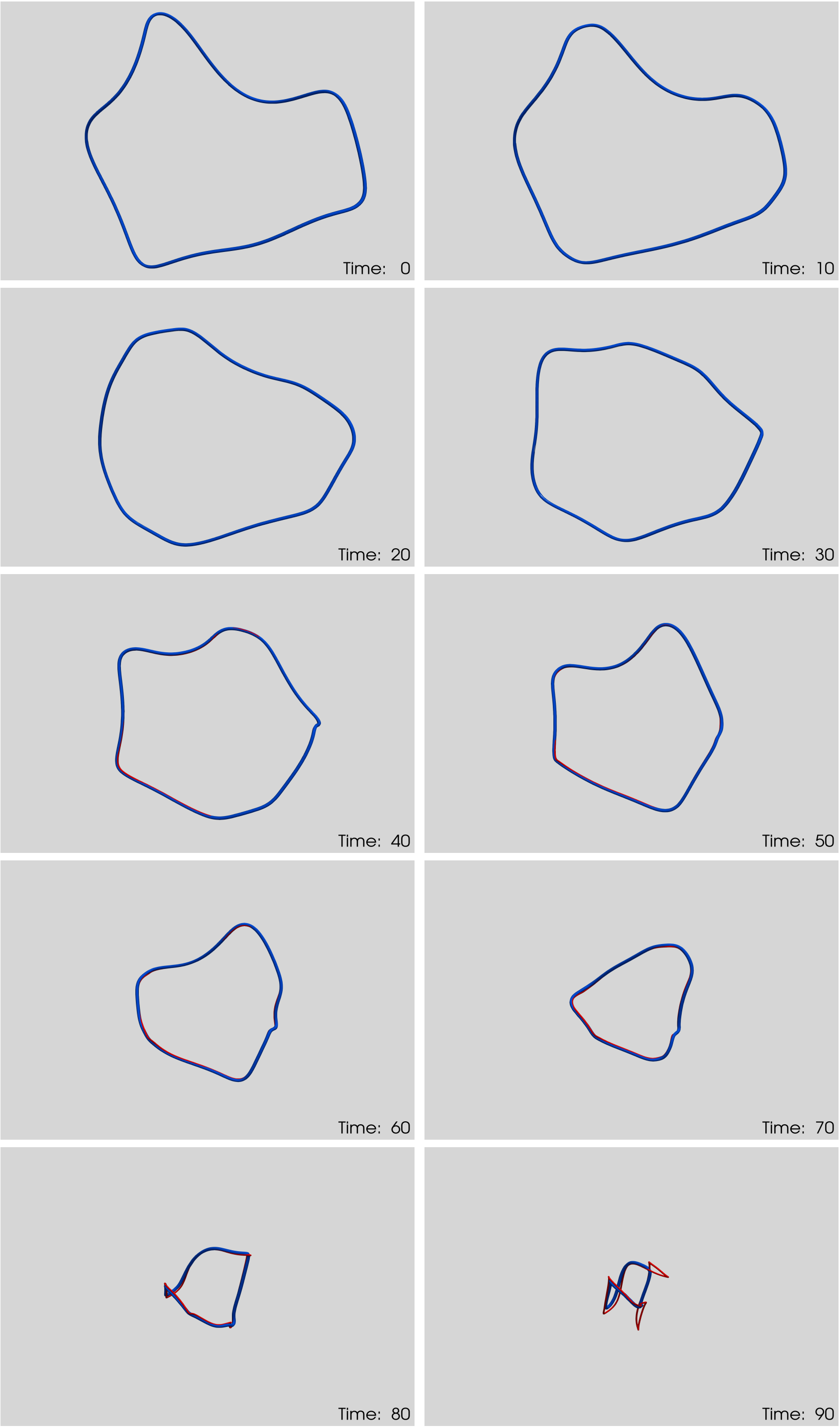

Figure 6.7: Snapshots of the evolution of a primordial loop, which starts out at rest. We notice how its evolution in field theory (blue) is very close to the Nambu-Goto expectation (red) except towards the end of the collapse. A these stages of the evolution, the loop has shrunk by a large fraction and the Nambu-Goto dynamics predicts a complete self-overlap of the string.

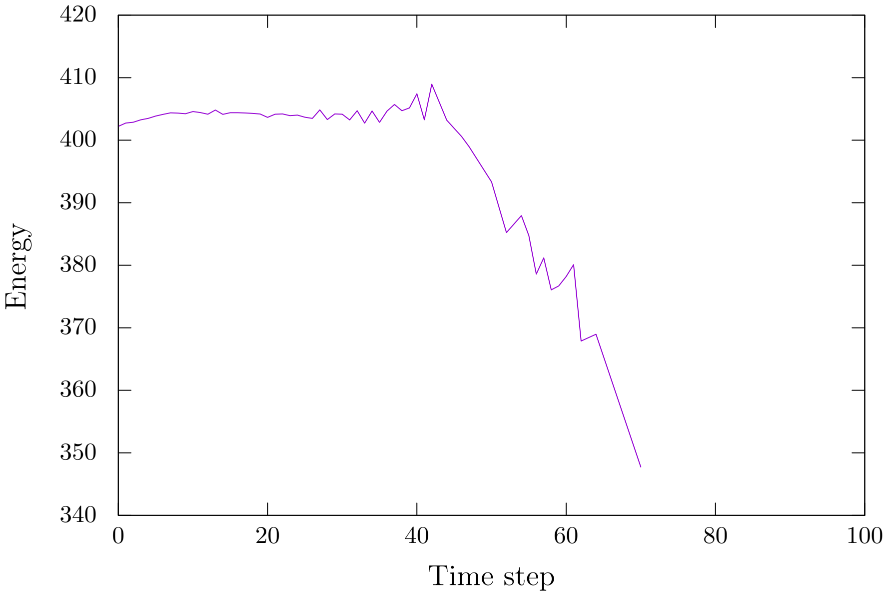

Figure 6.8: Total amount of σ for the Nambu-Goto reconstruction of the field theory data of the primordial loop.

6.5 Conclusions

In this chapter, we have compared the evolution of loops obtained in the course of a lattice field theory simulation with their expected dynamics in the Nambu-Goto approximation. Understanding the discrepancy between these two approaches is of paramount importance in order to make an accurate prediction of the observational signatures of strings. In particular, it is crucial in the estimate of the gravitational wave signature from strings in current and future gravitational wave observatories (see [183] and references therein).

Our investigations show that loops in field theory seem to behave according to the Nambu-Goto action in regions where the curvature is not high. In those regions, the visual comparison with the Nambu-Goto trajectory does not support the need for any departure in the equation of state of field theory loops. The strings move locally as the Nambu-Goto action dictates. However, we have found that the strings lose part of their energy in the course of their evolution. Some of this energy is lost by annihilation of nearby string segments in regions of high curvature. These high-curvature events are indeed predicted by the Nambu-Goto evolution obtained from the original reconstruction of the field theory string. Of course, since the energy of the loop is conserved in the Nambu-Goto approximation, this description cannot account accurately for the subsequent evolution of the field theory loop. This can be bypassed by reconstructing the Nambu-Goto data again after one of these events. Then, the subsequent evolution of the loop seems to be well described by the new Nambu-Goto data. There are other instances where the string loses energy which cannot be so clearly pinpointed as regions of high curvature, at least following our visual inspection. Remarkably, though, the trajectory of the string does not seem to be altered perceptibly in these events. A possible explanation for this behaviour is the presence of small-scale structure, but, in any case, this issue deserves further investigation.

The picture that emerges from our comparison of both descriptions of the string motion is the following. Most of the time, loops behave as the Nambu-Goto action predicts, but there are instances where this description breaks down and one needs to interrupt the comparison for a while until the Nambu-Goto behaviour resumes again. The study of the conserved Nambu-Goto energy backs up that there are instances where the energy drops that correspond to high curvature events.

This localized energy loss mechanism makes the loops shrink and sometimes self-intersect before they have a chance to oscillate for a full period, so at the end, the resultant loops are too small to expect them to behave as Nambu-Goto loops and they finally disappear. This could explain why we do not get any non-self-intersecting loop at the end the simulation even though the dynamics of the loops is well explained by the Nambu-Goto approximation for most of their evolution.

Now, if the loops behave almost everywhere like Nambu-Goto strings, would one expect to get non-self-intersecting loops also in field theory, and thus a large fraction of the energy of the network released as gravitational waves? The direct obvious way of answering this question might be to keep simulating loops of this kind until a non-self-intersecting loop is found in field theory. However, this is not a good strategy since, as indicated in the introduction of this chapter, non-self-intersecting conditions are not so easy to come by. Many large non-self-intersecting loops are found in Nambu-Goto simulations [76] because one simulates a much, much larger volume with many more loops. Unfortunately, we do not have the dynamic range in field theory to do such simulations. Of course, we may be lucky and find one such loop in our simulations after a large number of them.

Another idea would be to start with a different set of loops. For example, we could get loops from field theory simulations in the radiation or matter eras. These loops should be smoother and have a greater chance to become non-self-intersecting.

The best scenario would be to start with a large enough loop that radiates most of the extra energy it has in the form of wiggles in the first few moments of evolution. This would proceed via high-curvature events like the ones we have discussed, thus leaving behind a smoother loop that now should behave mostly as Nambu-Goto (except maybe for the presence of cusps). This expectation is natural given our results in section 3.4, where we performed field theory simulations of collisions of wave packets on the domain wall string. The results indicate that most of the energy is emitted in the first collision. The wiggles then become milder, and their subsequent interaction is not so violent. This argues for a transient period of smoothing of the loops (of the order of an oscillation time, which is roughly given by the invariant length) after which the whole loop would start behaving as predicted by the Nambu-Goto action.

Moreover, as the universe expands, the sizes of structures on the loops would increase proportionally to the horizon distance, while the size of the string core would remain fixed. Thus, over cosmological time, the curvature radii seen on loops would become many orders of magnitude larger than the string thickness, the radiative processes we see here would disappear, and the loop motion would be accurately given by the Nambu-Goto action.

This picture is just a conjecture than can be drawn from the results presented in this chapter. Nevertheless, the study reported here is quite preliminary. We have analyzed only a few loops, and their dynamics is not completely understood. Therefore, other alternative scenarios [168, 170, 87, 83] are still plausible.

Chapter 7

Final remarks

The ultimate goal of this research work is to shed some light on the tension between field theory and Nambu-Goto simulations of cosmic strings, which is mainly due to their radically different results regarding the abundance of non-self-intersecting loops. These are present in Nambu-Goto simulations, but not in field theory ones. Consequently, the predicted gravitational wave signal from cosmic string networks is highly suppressed in the field theory approach.

Nambu-Goto simulations assume that the strings are infinitely thin and disregard any back-reaction of the fields. In particular, radiative processes and non-linear interactions between perturbation modes are missed in the Nambu-Goto approximation. All these effects are taken into account in field theory simulations, albeit at the cost of a much smaller dynamic range. The main advantage of the Nambu-Goto approach is thus a bigger dynamic range which would allow for a cosmological extrapolation of the results obtained in the simulations. Therefore, one should elucidate whether field theory effects are relevant for the dynamics of the strings at the cosmological scales of interest.

All cosmic string loops found in the largest lattice field theory simulations performed to date disappear due to particle radiation in a time scale roughly given by the initial length of the loop. It was conjectured that the reason for this short lifetime might be the presence of extra energy in the loops. This extra energy could modify the equation of state of the strings and have important effects on their dynamics.

This conjecture has been the starting point for our investigations. In the previous chapters, the internal excitations of kinks, domain walls, global vortices and global strings have been extensively studied. We have also compared directly the field theory dynamics of domain walls and local strings to the prediction of the Nambu-Goto action. Our results were already interpreted and discussed at the end of each chapter, in connection with previous related work. Here we will collect the main conclusions and present in a succinct way possible directions for future research.

First and foremost, we have shown that topological defects acquire some extra energy in realistic cosmological settings. This extra energy remains stored in the core of the solitons in the form of bound states for extremely long periods of time, much larger than the natural scale of the problem, which is the width of the object. We have quantified the level of excitation of kinks (chapter 2) and global vortices (chapter 4) in two situations: their formation in a cosmological phase transition and their interaction with a thermal bath at temperature T. While global vortices are barely excited in these processes, the amount of extra energy acquired by the kinks is significant. The results are summarized in table 7.1:

	Phase transition	**Heat bath ($T \ll M$)**	**Heat bath ($T \gtrsim M$)**
Kinks	$0.2M_k$	$T/2$	$0.2M_k$
Global vortices	$0.005M_v$	$T/2$	$0.005M_v$

Table 7.1: Approximate amount of extra energy in the bound states in a phase transition and a thermal bath. M denotes either the mass of the kink solution, M_k, or the mass of the vortex solution, M_v.

We also extracted the level of excitation of global vortices during their cosmological evolution as part of a network. Once again, they do not seem to be significantly excited: the extra energy in the shape mode is found to be less than 1% of the mass of the vortex solution.

The energy stored in the bound states decays due to their non-linear coupling to the scattering modes. We have shown both analytically and numerically that the amplitude of the excitation decreases in time following the Manton-Merabet law. This decay time scale is not only larger than the width of the soliton, but also than the typical span of numerical simulations. This means that the extra energy is present for the entire numerical evolution of the defects.

An excited shape mode can drastically alter the dynamics of defects which are extended in some spatial direction. More specifically, we have shown that string-like solitons can undergo parametric resonances which amplify local transverse displacements (zero modes) of the object by borrowing energy from the internal modes. This can be traced to the fact that the perturbation modifies the equation of state of the string in such a way that its tension becomes oscillatory. Our numerical simulations of excited domain walls and global strings in chapters 3 and 5 reveal that the resonant zero mode has half of the frequency of the shape mode, which means that the string becomes wiggly on scales comparable to its thickness. As a consequence of the resonance, radiation is emitted and the energy initially stored in the bound state decays faster than predicted by the Manton-Merabet law. This non-linear phenomenon can be described by an effective action that couples the massless Goldstone modes corresponding to the wiggles with a massive scalar field that represents the amplitude of the shape mode and lives in the $1+1$ dimensional string worldsheet. A key ingredient needed to describe the amplification of the zero mode with the particular frequency observed in the full field theory simulations is the coupling of the aforementioned scalar field with the Ricci scalar of the string worldsheet.

In the case of global strings, these resonances enhance the emission of massless radiation. Therefore, this could be relevant for calculations of the abundance of axionic dark matter from cosmic string networks.

Another interesting effect of the bound state is to slow down the propagation of wiggles on the string. This is suggested by the fact that, to lowest order, the average effect of the perturbation is to increase the energy per unit length of the string while leaving its tension unaltered. In the case of a circular domain wall, we have seen that its collapse is indeed slowed down by the presence of an excited shape mode along the loop.

Needless to say, all these effects are not captured by the Nambu-Goto action. However, as mentioned above, the energy stored in the shape mode decreases in time following the Manton-Merabet law, or faster if the resonance phenomena take place. Even though this time scale is large in units of the oscillation period of the bound state, it is tiny compared to the age of the universe. Therefore, internal modes should not be relevant for the dynamics of the defects at late times, as long as there is no mechanism that could repopulate them. Our simulations of colliding wiggles on the domain wall string in chapter 3 indicate that this does not happen unless the wavelength of the wiggles is one of the resonant wavelengths, which is at least of the order of the string thickness. Since such high-frequency modes are not expected at late times in a cosmological setting, we conclude that internal modes are probably not important in this case.

In the absence of shape mode excitations and high-curvature regions, which lead to particle radiation, cosmic strings should behave as the Nambu-Goto action predicts. This is backed up by our simulations of bare domain walls in chapter 3 and local string loops in chapter 6. In the latter case, we directly compared the field theory trajectory of loops chopped off from a network of Abelian-Higgs strings with the Nambu-Goto trajectory. What we found is that the two trajectories coincide except in regions of high curvature, and no resonant amplification of zero modes was observed. Presumbaly, internal modes were suppressed in an early period of friction implemented in the field theory simulations.

The disagreement in the number of non-self-intersecting loops and the lack of consensus on the main mechanism of energy loss in cosmic string networks have led to the widespread belief that the loops in large-scale field theory simulations do not move as Nambu-Goto strings. Our analysis in chapter 6 shows that this is not quite right for loops found in state-of-the-art Abelian-Higgs simulations. The reason for the discrepancies may lie at the origin and the influence of the high-curvature regions where the field theory trajectory deviates from the Nambu-Goto prediction, or it could otherwise be alien to the string dynamics. Regarding the first possibility, some questions arise: can these high-curvature events prevent a loop from being non-self-intersecting? Can they trigger the appearance of new high-curvature regions? Is there any mechanism that allows for the regeneration of this structure? If not, a plausible explanation could be that loops in field theory simulations become too small in the process of getting rid of the extra energy in the form of high-curvature wiggles, thus evaporating without having had the chance to become non-self-intersecting. Loops with larger initial lengths might remain sufficiently big after a transient stage in which they would smooth out by ejecting this extra energy. After that, they would presumably behave according to the Nambu-Goto action everywhere. If this is the case, the problem is just a matter of limited dynamic range in field theory simulations.

In any case, although we have made a lot of progress, there is still work to be done to fully resolve this cosmic string puzzle. Let us end up by sketching some sensible follow-up investigations:

- Compare the field theory and Nambu-Goto trajectories of local string loops formed in the radiation or matter eras. These loops should be smoother and have a bigger chance to become non-self-intersecting.
- Study the spectrum of perturbations around the local string configuration and analyze the influence of internal modes on the dynamics of these defects.

- Determine whether intercommutation processes can excite the internal modes, and to what extent this could alter the overall dynamics of the strings.
- Quantify the energy loss in collisions of wiggles on the strings as a function of their curvature. This should be useful to estimate more accurately the time scale needed for the loops to effectively stop radiating.
- Extend our analysis in chapter 6 to global strings. In order to do this, one would have to take into account the emission of massless radiation by supplementing the Nambu-Goto action with a Kalb-Ramond term.
- Understand the massive radiation from global strings in terms of an effective action that incorporates the coupling of the string to the radial degree of freedom of the scalar field.

Appendix A

Discretization of the equations of motion and boundary conditions

In this appendix, we present the discretization schemes that we used to solve the equations of motion in a lattice, as well as the boundary conditions employed. We will display them separately for each chapter.

In all chapters, most of the simulations had to be performed for very long periods of time. Moreover, in some cases, we evolve in an expanding background. As pointed out in the main text, this is a problem because objects of fixed physical size like the solitons we study shrink in comoving coordinates. Therefore, we may not have enough points to accurately resolve them satisfactorily (we may run out of points in the core of the defects). We thus parallelized our codes so that the simulation box is distributed among different processors. We only implement this parallelization in the x direction. Since our finite-difference scheme only relies on nearest neighbours, we only need a one-dimensional halo around the box in each processor. We used Message Passing Interface (MPI) for communication between different processors. A typical processor will share its information with the ones to either side of it, except the first and last processors, which only share their information with one processor (to their right and left, respectively).

A.1 Chapter 2

We want to solve numerically the equation of motion (2.34)

$$\ddot{\phi} + H\dot{\phi} - \frac{1}{a^2}\phi'' + \phi\left(\phi^2 - 1\right) = 0 \, . \tag{A.1}$$

If the evolution takes place in Minkowski spacetime, it suffices to set $a = 1$ and $\tilde{H} = 0$.

We need to discretize this equation into the lattice. In order to discretize the time derivatives, we use the so-called staggered leapfrog method. In order to do that, we need to define the conjugate momentum as

$$\pi\left(t + \frac{\Delta t}{2}, x\right) \equiv \frac{\phi\left(t + \Delta t, x\right) - \phi\left(t, x\right)}{\Delta t} \,. \tag{A.2}$$

Note that the field lives in integer time steps, and the conjugate momentum in half time steps. Now, the equation of motion for π reads

$$\dot{\pi} = \frac{1}{a^2}\phi'' - \phi\left(\phi^2 - 1\right) - H\pi \,. \tag{A.3}$$

First, we discretize the second order spatial derivative of the field using nearest neighbours:

$$\phi''\left(t, x\right) = \frac{\phi\left(t, x + \Delta x\right) - 2\phi\left(t, x\right) + \phi\left(t, x - \Delta x\right)}{\left(\Delta x\right)^2} \,. \tag{A.4}$$

From (A.3) we see that π and $\dot{\pi}$ should be evaluated at the same time step. However, the former lives at half-integer steps, while the latter lives at integer steps, because $\dot{\pi}$ is calculated as the difference of π at two different half-integer time steps:

$$\dot{\pi}\left(t + \Delta t, x\right) = \frac{\pi\left(t + \frac{3}{2}\Delta t, x\right) - \pi\left(t + \frac{\Delta t}{2}, x\right)}{\Delta t}. \tag{A.5}$$

To solve this issue, we simply replace π in the friction term with its average in neighbouring half time steps:

$$\pi(t + \Delta t, x) = \frac{\pi\left(t + \frac{1}{2}\Delta t, x\right) + \pi\left(t + \frac{3}{2}\Delta t, x\right)}{2} \,. \tag{A.6}$$

Now all the terms in the equation for π (A.3) are evaluated at integer time steps. The staggered leapfrog method now consists of solving for the conjugate momentum using (A.3), which explicitly reads

$$\begin{aligned} \pi(t + \frac{3}{2}\Delta t, x) \;\; = \;\; & \left(1 + H\frac{\Delta t}{2}\right)^{-1} \left\{\left(1 - H\frac{\Delta t}{2}\right)\pi(t + \frac{1}{2}\Delta t, x) + \right. \\ & \left. + \Delta t\left[\frac{1}{a(t)^2}\phi''(t, x) - \phi(\phi^2 - 1)\right]\right\} \,, \end{aligned} \tag{A.7}$$

with ϕ'' given by equation (A.4), and then solving for the field, which can be obtained from equation (A.2):

$$\phi(t+\Delta t,x) = \phi\,(t,x) + \Delta t\ \pi\left(t+\frac{\Delta t}{2},x\right). \tag{A.8}$$

A typical simulation in chapter 2 consists of a box of length $L = 50$, with $\Delta x = 0.01$ and $\Delta t = 0.0008$. Thus, the number of points in the box is $N = 5000$, which are usually distributed among 40 processors.

In this chapter, we employed absorbing boundary conditions in all our simulations. The idea behind these boundary conditions is quite simply to force an outgoing wave traveling towards the boundary to be annihilated at that point [106]. These conditions read

$$\left(\frac{\partial\phi}{\partial t} \pm \frac{\partial\phi}{\partial x}\right)\bigg|_{t,x=\pm\frac{L}{2}} = 0\,. \tag{A.9}$$

These are known as Mur boundary conditions [184].

Let us briefly discuss the reasoning behind these absorbing boundary conditions. Far away from the soliton (in the $x \to \pm\infty$ limit), we can assume that the field is described as a perturbation around the vacuum of the form $\phi_\pm\,(t,x) = \pm 1 + \xi_\pm\,(t,x)$. At the linear level, the equation of motion yields a solution for this perturbation as a travelling wave: $\xi_\pm\,(t,x) \propto \cos\left(\omega t \mp kx + \delta\right)$, where $\omega = \sqrt{k^2+m^2}$ and δ is a phase. This wave is a solution to the Mur boundary conditions if $\omega = k$. Therefore, these conditions work better for waves with $k >> m$.

It is possible that the outgoing radiation in a particular problem is monochromatic, with known angular frequency ω. For instance, if our initial condition consists of a kink with its shape mode excited, we know that it will radiate waves with frequency $\omega = 2\,\omega_1 = \sqrt{3}\,m$. In such a situation, the absorbing boundary conditions can be refined as follows:

$$\left(\frac{\partial\phi}{\partial t} \pm \frac{\omega}{\sqrt{\omega^2-m^2}}\frac{\partial\phi}{\partial x}\right)\bigg|_{t,x=\pm\frac{L}{2}} = 0\,. \tag{A.10}$$

As one can easily check, the travelling waves $\xi_\pm$ above are exact solutions to these equations. This means that, for our almost monochromatic radiation, these boundary conditions will be more effective. We have implemented these conditions and, indeed, the absorption gets to be better with these modified absorbing boundary conditions.

Here we show a couple of different situations to illustrate the way these absorbing boundary conditions work. We run our code twice in flat space with an initial condition given by an excited kink, but the excitations in both cases were chosen to be different. In the first case, we excite the kink with a bound state of amplitude $A(0) = 0.332$. In the second case, we use a symmetric perturbation with the same amount of energy[1]. We plot in figure A.1 the energy inside of our simulation box as a function of time. We use the same boundary conditions (A.9) in both cases.

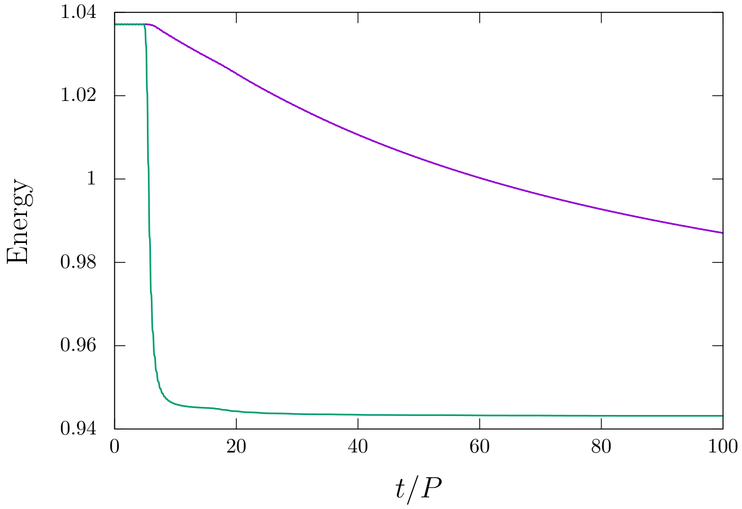

Figure A.1: Total energy inside of the box for two different initial conditions with absorbing boundary conditions. The purple line shows the slow decay of the energy for a kink with a bound state excitation, while the green line represents the configuration of a kink with a symmetric perturbation. The total energy in this case is very quickly emitted from the kink and absorbed almost immediately as it reaches the boundaries. Time is displayed in units of the period of the shape mode.

The results indicate several important points. First, the energy remains constant in both cases before any perturbation reaches the boundary. This means that our code conserves energy in Minkowski space as it should. The energy curve in both cases starts to decline as soon as the first waves arrive to the boundary. However, the total energy from the symmetric perturbation decreases quite rapidly, and in a short period of time, the final energy is the one of the kink itself. This indicates that the generic absorbing conditions work quite efficiently and there is not much energy bouncing around the box. In the other case, the energy curve decreases slowly due to the presence of the bound state, which decays in a long time scale. This slow leakage of energy is also efficiently absorbed in the boundary and the final result

---

[1] The perturbation now is an even function of x, so it has zero projection onto the shape mode. This implies that its energy will be emitted much more efficiently.

is also a very small amount of feedback into the bound state due to energy bouncing off the edges of the box.

A.2 Chapter 3

The equation of motion that we solve throughout chapter 3 can be written in dimensionless form as

$$\frac{\partial^2\phi}{\partial t^2} - \frac{\partial^2\phi}{\partial x^2} - \frac{\partial^2\phi}{\partial y^2} + \phi\left(\phi^2 - 1\right) = 0 \ . \tag{A.11}$$

We solve this equation numerically using the staggered leapfrog method, explained in the previous section, and nearest neighbours for the discretization of the spatial derivatives. Our simulations in this chapter were typically run in lattices with a total number of points of the order of 10^6.

Regarding the boundary conditions, we use periodic boundary conditions in the y direction, along which the domain wall string lies, and absorbing ones in the x direction. The reason for the latter is that an important part of the radiation produced in our simulations is emitted along that direction. Implementing these absorbing boundary conditions allows us to run for very long periods of time without having to worry about the effects of the radiation bouncing off the walls and reexciting the soliton.

The tuning (A.10) of the absorbing boundary conditions turned out to be crucial in our simulations, specially in those of section 3.3. In our simulations of standing waves in that section, we knew the angular frequency of the outgoing radiation produced by the non-linear coupling of the zero mode to the scattering states: $\omega = 2\omega_0$. Here, ω_0 is the frequency of the zero mode. Note that (A.9) and (A.10) are nearly equivalent if $\omega >> m$, or $\omega_0 >> m/2$. However, this may not be the case as we are free to choose the angular frequency of the zero mode to be arbitrarily close to $m/2$. We employed the refined boundary conditions (A.10) for the standing wave experiments in sections 3.3 and 3.4, and the version (A.9) for the rest.

A.3 Chapter 4

As it has been mentioned in the main text in chapter 4, we solve the equations of motion for the field in a $1+1$ or a $2+1$ dimensional lattice depending on the effect we want to study. On the one hand, when the problem can be simulated using cylindrical symmetry, the $1+1$ dimensional lattice can be used. This case allows for a much bigger number of lattice points, and thus, bigger accuracy and dynamical range. However, this approach pins the core of the string to a point, and does not allow for motion of the vortex. On the other hand, $2+1$ dimensional lattices can be used to solve all problems. This allows for situations with no symmetry, it allows for the core to move, and we can have more than one vortex in the simulation. The price to pay is a heavier numerical budget, and thus the accuracy and dynamical range are lower than in the $1+1$ dimensional case.

Let us note that an additional advantage of parallelization in this chapter is that it allowed us to have a large simulation box, which is needed for the second bound state to fit in.

A.3.1 $1+1$ simulations

This type of simulations has been used when the problem presented a cylindrical symmetry. As mentioned in the main text, the equations we have to solve reduce to

$$\ddot{\phi}_{1,2} = \frac{\partial^2 \phi_{1,2}}{\partial r^2} + \frac{1}{r}\frac{\partial \phi_{1,2}}{\partial r} - \frac{\phi_{1,2}}{r^2} - \frac{1}{2}\phi_{1,2}\left(\phi_1^2 + \phi_2^2 - 1\right) . \tag{A.12}$$

We have solved these equations using the staggered leapfrog method described in the first section of this appendix. The boundary conditions applied were $\phi(r=0)=0$ and absorbing boundary conditions at $r=L$, where L is the size of the simulation box. Absorbing boundary conditions are the best suited for the problem at hand, because we do not wish that the radiation emitted by the vortex bounces off the simulation edges back to the soliton. A boundary condition of the form

$$\left(\frac{\partial \phi_{1,2}}{\partial t} + \frac{\partial \phi_{1,2}}{\partial r}\right)\Bigg|_{r=L} = 0 \ , \tag{A.13}$$

would absorb an outgoing cylindrical wave at an asymptotically far boundary. Such a wave would be given by

$$\xi\left(r,t\right) \propto \frac{1}{\sqrt{r}} \cos\left(\omega t - kr + \delta\right) . \tag{A.14}$$

One can understand why equation (A.13) is a good absorbing boundary condition by noticing that $\phi_{1,2} = 1 + \xi$ is its approximate solution for $\omega = k$. This last condition implies that the absorbing boundary condition works better for modes with $k \gg m = 1$.

Once again, one can refine this condition by tailoring the equation to be satisfied at the boundary for a cylindrical monochromatic wave with known angular frequency ω, namely,

$$\left(\frac{\partial \phi_{1,2}}{\partial t} + \frac{\omega}{\sqrt{\omega^2-1}} \frac{\partial \phi_{1,2}}{\partial r} + \frac{\omega}{2\sqrt{\omega^2-1}} \frac{\phi_{1,2}-1}{r} \right) \Bigg|_{r=L} = 0\,. \tag{A.15}$$

We have checked in our simulations that both equation (A.13) and equation (A.15) yield similar results. Both choices seem to be equally efficient at absorbing outgoing radiation.

There have been several instances in which the 1+1 dimensional approach has been useful, mainly in the determination of the decay time scale of the bound modes and the study of their excitation by illuminating the vortex with radiation.

A.3.2 $2+1$ simulations

For these simulations we do not assume any symmetry, so we solve numerically the equations of motion for ϕ_1 and ϕ_2 in an expanding background. The equations read

$$\ddot{\phi}_{1,2} + 2H\dot{\phi}_{1,2} - \frac{1}{a^2}\nabla^2\phi_{1,2} + \frac{1}{2}\phi_{1,2}\left(\phi_1^2+\phi_2^2-1\right) = 0\ , \tag{A.16}$$

where dots denote partial derivatives with respect to cosmic time and $\nabla^2 = \partial_x^2 + \partial_y^2$, with x and y being comoving coordinates; a is the scale factor, and $H = \dot{a}/a$ is the Hubble rate.

A flat space version of these equations of motion in $2+1$ dimensions has been used for all the cases studied in the $1+1$ dimensional setup to make sure that there was not extra dynamics that was lost while imposing cylindrical symmetry. In order to do that, we used the corresponding boundary conditions implemented for the $2+1$ dimensional simulations, which are either the Cartesian version of equation (A.13),

$$\left(\frac{\partial \phi_{1,2}}{\partial t} + \frac{\partial \phi_{1,2}}{\partial x} \frac{x}{\sqrt{x^2+y^2}} + \frac{\partial \phi_{1,2}}{\partial y} \frac{y}{\sqrt{x^2+y^2}} \right) \Bigg|_{x=\pm L/2, y=\pm L/2} = 0\ , \tag{A.17}$$

which is more efficient at absorbing modes with radial incidence, or

$$\left(\frac{\partial \phi_{1,2}}{\partial t} \pm \frac{\partial \phi_{1,2}}{\partial x} \right) \Bigg|_{x=\pm L/2} = 0\ , \quad \left(\frac{\partial \phi_{1,2}}{\partial t} \pm \frac{\partial \phi_{1,2}}{\partial y} \right) \Bigg|_{y=\pm L/2} = 0\,, \tag{A.18}$$

which is more efficient at absorbing modes with normal incidence.

The $2+1$ version was indispensable for the simulations in section 4.5.3 and 4.6.

A.4 Chapter 5

In chapter 5, we solve the dimensionless version of the equations of motion (A.19),

$$\ddot{\phi}_{1,2} - \nabla^2 \phi_{1,2} + \frac{1}{2}\left(\frac{\phi_1^2 + \phi_2^2}{2} - 1\right)\phi_{1,2} = 0\,, \tag{A.19}$$

using once again the staggered leapfrog method and nearest neighbours for the discretization of the spatial derivatives.

We employed periodic boundary conditions in the z direction (along which the string lies) and absorbing boundary conditions in the x and y directions. The latter were implemented by imposing the conditions (A.17) at the boundaries, for every value of the z coordinate. As in the previous cases, these conditions are expected to work better when the wave number is equal to the angular frequency, i.e., for massless radiation. However, massive radiation emitted by the string turned out to be efficiently absorbed as well.

Appendix B

Thermal fluctuations

In this appendix, we explain how to generate thermal fluctuations of the scalar field in one, two and three spatial dimensions. For the case of a $1+1$ dimensional spacetime, we also show how to generate the fluctuations around the kink solution by means of the Metropolis algorithm and present an analytical estimate for the amplitude of the bound state as a function of temperature.

Here, the distinction between dimensionful and dimensionless variables will be explicit, so the latter will always carry a tilde on them.

B.1 Real field in $1+1$ dimensions

B.1.1 Thermal fluctuations about the vacuum

In section 2.7, the field was initialized as a thermal state around the vacuum: $\phi\left(t=0,x\right)=0+\xi\left(t=0,x\right)$, where ξ denotes the thermal fluctuations. Our starting point is the expansion of ξ in imaginary exponentials given in equations (2.43) and (2.44). Let us display them once again here:

$$\xi\left(t=0,x_j\right)=\sum_{n=-N/2+1}^{N/2}\frac{1}{\sqrt{2L\omega_n}}\left(\alpha_n e^{ik_nx_j}+\alpha_n^*e^{-ik_nx_j}\right), \tag{B.1}$$

$$\dot{\xi}\left(t=0,x_j\right)\equiv\pi_\xi\left(t=0,x_j\right)=\sum_{n=-N/2+1}^{N/2}\frac{1}{i}\sqrt{\frac{\omega_n}{2L}}\left(\alpha_n e^{ik_nx_j}-\alpha_n^*e^{-ik_nx_j}\right). \tag{B.2}$$

In these expressions, the angular frequencies ω_n and the wave numbers k_n are given by

$$\omega_n = \sqrt{\left[\frac{2\sin\left(\frac{k_n \Delta x}{2}\right)}{\Delta x}\right]^2 + m^2} \tag{B.3}$$

and

$$k_n = \frac{2\pi n}{L}\,, \tag{B.4}$$

and $m = \sqrt{2\lambda}\eta$ is the mass of perturbative excitations about the vacuum. As mentioned in the main text, the complex coefficients α_n satisfy

$$\langle|\alpha_n|^2\rangle = \frac{1}{e^{\omega_n/T} - 1} = \frac{1}{2}\left[\coth\left(\frac{\omega_n}{2T}\right) - 1\right]\,, \tag{B.5}$$

which is plotted in figure B.1.

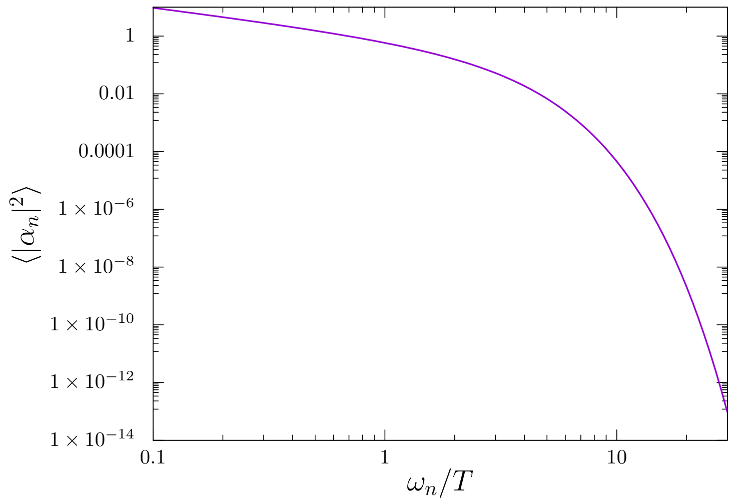

Figure B.1: Two-point function of the complex coefficients α_n in logarithmic scale, as given in equation (B.5). Note that it is highly suppressed for $\omega_n >> T$.

Now we introduce the dimensionless variables. Length scales and frequencies are rescaled by $\sqrt{\lambda}\eta$, and we also redefine $\tilde{\xi} = \xi/\eta$ and $\tilde{\pi}_\xi = \pi_\xi/\sqrt{\lambda}\eta^2$. Moreover, we define the dimensionless temperature Θ as we did in section 2.7:

$$\Theta = \frac{T}{\sqrt{\lambda}\eta^3}\,, \tag{B.6}$$

that is, we rescale temperature with the energy of the kink configuration. Finally, we redefine the complex coefficients as $\tilde{\alpha}_n = \alpha_n/\eta$.

On the other hand, as it is clear from figure B.1, the Bose-Einstein spectrum (B.5) decays exponentially for $\omega_n > T$, which translated into dimensionless variables means $\tilde{\omega}_n > \eta^2\Theta \equiv \tilde{\Omega}$. The spectrum can be rewritten in terms of Θ and $\tilde{\Omega}$ as follows:

$$\langle|\tilde{\alpha}_n|^2\rangle = \frac{\Theta}{2\tilde{\Omega}}\left[\coth\left(\frac{\tilde{\omega}_n}{2\tilde{\Omega}}\right) - 1\right] . \tag{B.7}$$

Now the question is how to generate the random variables $\tilde{\alpha}_n$. Let A_n and B_n be the real and imaginary parts of $\tilde{\alpha}_n$. Then,

$$\langle|\tilde{\alpha}_n|^2\rangle = \langle A_n^2\rangle + \langle B_n^2\rangle\,, \tag{B.8}$$

and it follows from (B.7) that

$$\langle A_n^2\rangle = \langle B_n^2\rangle = \frac{\langle|\tilde{\alpha}_n|^2\rangle}{2} = \frac{\Theta}{4\tilde{\Omega}}\left[\coth\left(\frac{\tilde{\omega}_n}{2\tilde{\Omega}}\right) - 1\right] . \tag{B.9}$$

We want A_n and B_n to be Gaussian independent variables with zero mean and variance given by (B.9). There is a standard procedure to generate such variables. For each n, one has to follow these steps:

1. Generate two variables f_n and g_n uniformly distributed between 0 and 1.
2. Make the following redefinitions: $\gamma_n \equiv 2\pi f_n$ and $r_n \equiv \sqrt{-2\ln(1-g_n)}$.
3. Then,

   $$A_n = \sqrt{\frac{\langle|\tilde{\alpha}_n|^2\rangle}{2}}\, r_n \cos\gamma_n \tag{B.10}$$

   and

   $$B_n = \sqrt{\frac{\langle|\tilde{\alpha}_n|^2\rangle}{2}}\, r_n \sin\gamma_n \tag{B.11}$$

   are Gaussian independent variables with zero mean and variance $\langle|\tilde{\alpha}_n|^2\rangle/2$.

With all the previous redefinitions and other simple manipulations, the thermal fluctuations of the field and the velocity can be finally reexpressed as

$$\begin{aligned}\tilde{\xi}\left(\tilde{t}=0,\tilde{x}_j\right) &= \sum_{n=-N/2+1}^{N/2}\sqrt{\frac{2}{\tilde{L}\tilde{\omega}_n}}\left[A_n\cos\left(\tilde{k}_n\tilde{x}_j\right)-B_n\sin\left(\tilde{k}_n\tilde{x}_j\right)\right]= \\ &= \sum_{n=-N/2+1}^{N/2}\sqrt{\frac{\langle|\tilde{\alpha}_n|^2\rangle}{\tilde{L}\tilde{\omega}_n}}r_n\cos\left(\tilde{k}_n\tilde{x}_j+\gamma_n\right)\ ,\end{aligned} \tag{B.12}$$

$$\begin{aligned}\tilde{\pi}_\xi\left(\tilde{t}=0,\tilde{x}_j\right) &= \sum_{n=-N/2+1}^{N/2}\sqrt{\frac{2\tilde{\omega}_n}{\tilde{L}}}\left[B_n\cos\left(\tilde{k}_n\tilde{x}_j\right)+A_n\sin\left(\tilde{k}_n\tilde{x}_j\right)\right]= \\ &= \sum_{n=-N/2+1}^{N/2}\sqrt{\frac{\tilde{\omega}_n\langle|\tilde{\alpha}_n|^2\rangle}{\tilde{L}}}r_n\cos\left(\tilde{k}_n\tilde{x}_j-\gamma_n\right)\ .\end{aligned} \tag{B.13}$$

These are the exact expressions we employ as initial conditions for the cosmological phase transitions. Note that the amplitude of the thermal modes is proportional to $\sqrt{\langle|\tilde{\alpha}_n|^2\rangle}$, so those with angular frequencies $\tilde{\omega}_n >> \tilde{\Omega}$ are suppressed. In the classical limit, where no modes are suppressed, $\langle|\tilde{\alpha}_n|^2\rangle \to \Theta/\tilde{\omega}_n$ and one can gain some insight into this thermal state by making the following two observations:

- The amplitude of the field thermal modes is proportional to $\sqrt{\Theta}/\tilde{\omega}_n$. For a given temperature, higher frequency modes have smaller amplitudes.
- The amplitude of the velocity thermal modes is proportional to $\sqrt{\Theta}$. For a given temperature, all modes have the same amplitude regardless of their frequency.

To fully specify the initial state with (B.12) and (B.13), note that we only need to choose $\tilde{\Omega}$ and Θ. The choice of these parameters is made in such a way that the energy of the thermal fluctuations is a small fraction of the vacuum energy, and we also make sure that modes with wavelengths close to the lattice spacing are suppressed.

We first determine the value of the cutoff frequency $\tilde{\Omega}$ by imposing a classical state, which means that all modes satisfy $\tilde{\omega}_n << \tilde{\Omega}$. This would be automatically satisfied if $\tilde{\Omega} > \tilde{\omega}_{\max}$, where $\tilde{\omega}_{\max} \sim 1/\Delta\tilde{x}$ is the maximum angular frequency allowed by the lattice spacing. Therefore, we might choose $\tilde{\Omega} = 10/\Delta\tilde{x}$, for instance. However, it would be preferable to have very short wavelength modes suppressed, as they are not well resolved by the lattice spacing and may be incorrectly evolved. Modes with wavelength $10\Delta\tilde{x}$ and shorter will be suppressed for $\tilde{\Omega}$ approximately given by

$$\tilde{\Omega} = \frac{1}{2\Delta\tilde{x}}\,. \tag{B.14}$$

We now turn to the specification of the temperature, Θ. On the one hand, for the initial vacuum in potential (2.42), the vacuum energy is

$$E_{\text{vacuum}} = LV(0) = \frac{\tilde{L}}{4}\sqrt{\lambda}\eta^3 \tag{B.15}$$

On the other hand, the thermal energy in the classical limit (no modes suppressed) can be estimated by invoking the equipartition theorem. Each quadratic degree of freedom in the discrete Hamiltonian contributes with $T/2$ to the average energy. In this case, if N denotes the number of lattice points, we have $2N$ degrees of freedom (ξ and π_ξ at each lattice point). The average kinetic energy and the average gradient+potential energy are both NT. Therefore, the thermal energy is

$$E_{\text{thermal}} \sim NT = \frac{\tilde{L}\sqrt{\lambda}\eta^3\Theta}{\Delta\tilde{x}}\,. \tag{B.16}$$

Finally, imposing that the thermal energy be $p\%$ of the vacuum energy, we get

$$\Theta \sim \frac{p}{400}\Delta\tilde{x}\,. \tag{B.17}$$

If a significant number of modes turned out to be suppressed by the choice of parameters, the thermal energy would be smaller than the value given in (B.16). As the temperature is lowered, $\tilde{\Omega}$ decreases and more and more high frequency modes become suppressed. Clearly, this implies that cooler configurations are smoother. We exemplify this effect in figures B.2 and B.3.

One can inmediately conclude from this brief analysis that the number density of kinks formed in a phase transition will depend crucially on the temperature of the initial state. Indeed, the spatial extent of the region over which the field oscillates coherently grows as the temperature decreases. In the limit of very low temperature, only long-wavelength modes survive and the formation of a small number of kinks is favoured (see figure B.4).

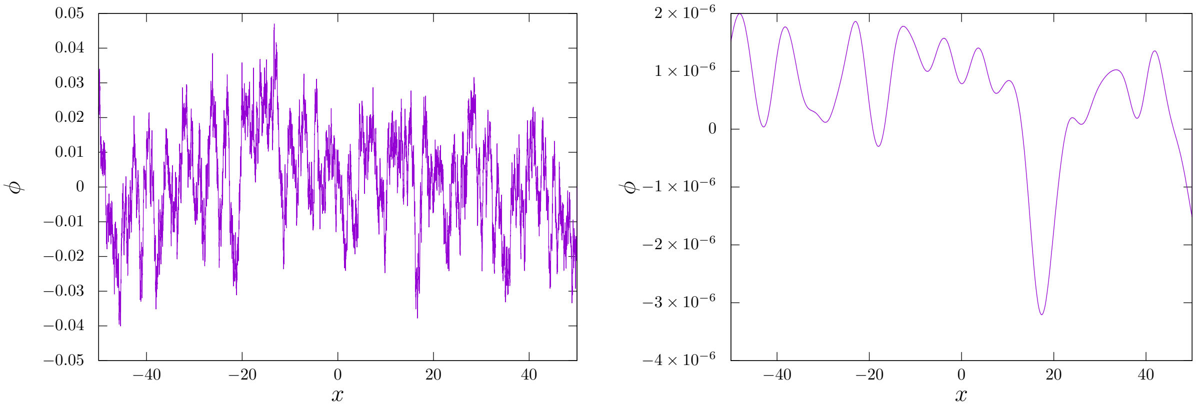

Figure B.2: Thermal state for the field for high temperature (left panel) and low temperature (right panel). The variables in this graph are dimensionless.

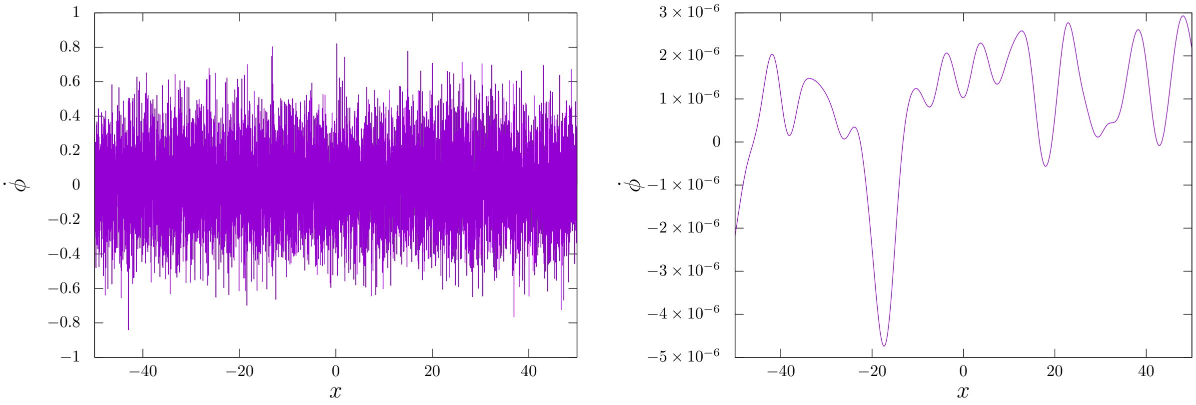

Figure B.3: Thermal state for the field velocity for high temperature (left panel) and low temperature (right panel). The variables in this graph are dimensionless.

B.1.2 Amplitude of the bound state as a function of temperature

Here we present an analytical estimate of the amplitude of the shape mode as a function of temperature when the $1 + 1$ dimensional kink is placed in a thermal bath.

Suppose we add the thermal fluctuations (B.12) and (B.13) directly on the kink configuration. Each mode contributes differently to the excitation of the bound state, depending on its amplitude and its frequency: the perturbations are the sum of cosines and sines with the allowed frequencies, but note that only the sines will contribute to the excitation of the bound state, because its amplitude is the projection of the perturbation over the shape mode, which is antisymmetric. Thus, the contribution of the cosines is identically zero.

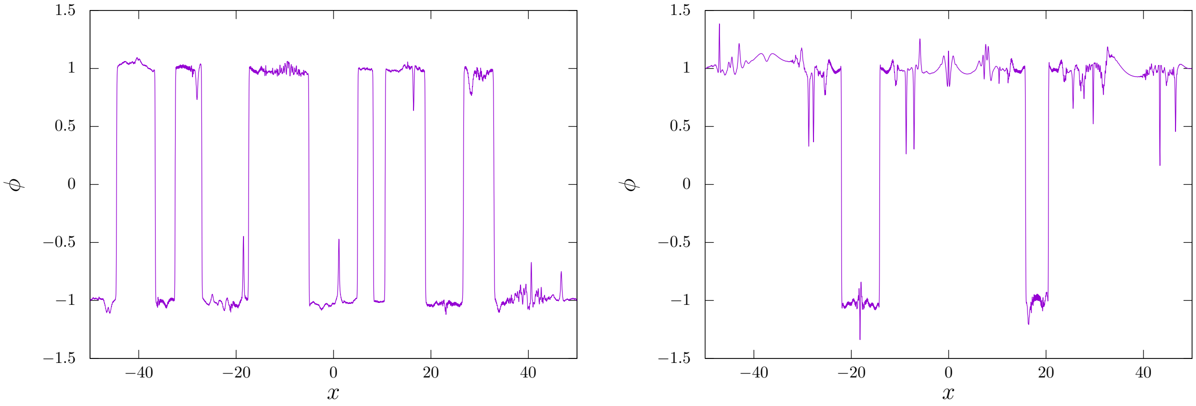

Figure B.4: Network of kinks resulting from a phase transition for a high-temperature initial state (left panel) and a low-temperature one (right panel). The variables in this graph are dimensionless.

First of all, let us perturb the kink configuration with a single mode with amplitude B and wave number $\tilde{k}$:

$$\tilde{\phi}\left(\tilde{t}=0,\tilde{x}\right) = \tanh\left(\frac{\tilde{x}}{\sqrt{2}}\right) + B\sin\left(\tilde{k}\tilde{x}\right) . \tag{B.18}$$

Making use of (2.25), the amplitude of the shape mode due to this perturbation can be found to be

$$A = 2\pi B\sqrt{\frac{3\sqrt{2}}{4}}\,\tilde{k}\ \mathrm{sech}\left(\frac{\pi\tilde{k}}{\sqrt{2}}\right) = 2\pi B\sqrt{\frac{3\sqrt{2}}{4}}\,g(\tilde{k})\,. \tag{B.19}$$

The function $g(\tilde{k})$ is plotted in figure B.5.

There is a specific wave number $\tilde{k}_* \approx 0.54$ for which the excitation is maximal. As illustrated in figure B.6, the wavelength of this mode is very similar to the length scale of the kink. Modes with much shorter or much longer wavelengths will not be able to excite the shape mode.

Let us now turn to the thermal perturbation (B.12). In this case, the initial amplitude of the shape mode can be easily shown to be

$$A\left(\tilde{t}=0\right) = -\pi\sqrt{\frac{6\sqrt{2}}{\tilde{L}}}\sum_{n=-N/2+1}^{N/2} B_n\,\frac{\tilde{k}_n}{\sqrt{\tilde{\omega}_n}}\ \mathrm{sech}\left(\frac{\pi\tilde{k}_n}{\sqrt{2}}\right) , \tag{B.20}$$

and the dependence on $\tilde{k}_n$ is very similar to the one plotted in figure B.5.

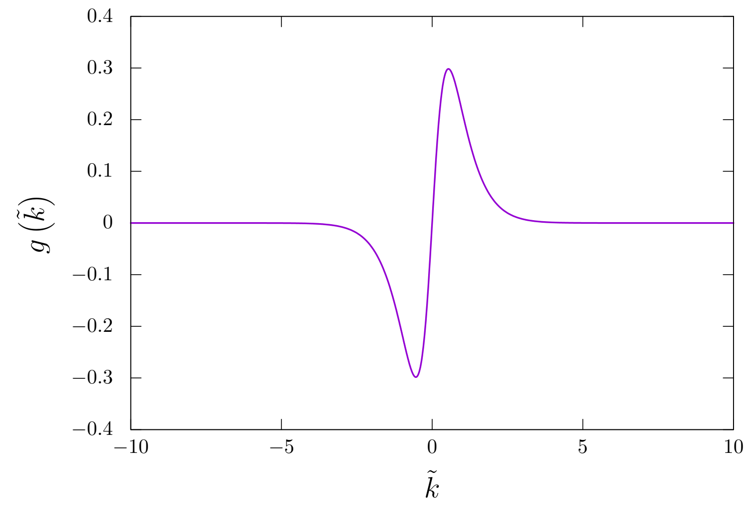

Figure B.5: Dependence of the amplitude of the shape mode on the wave number of the perturbation.

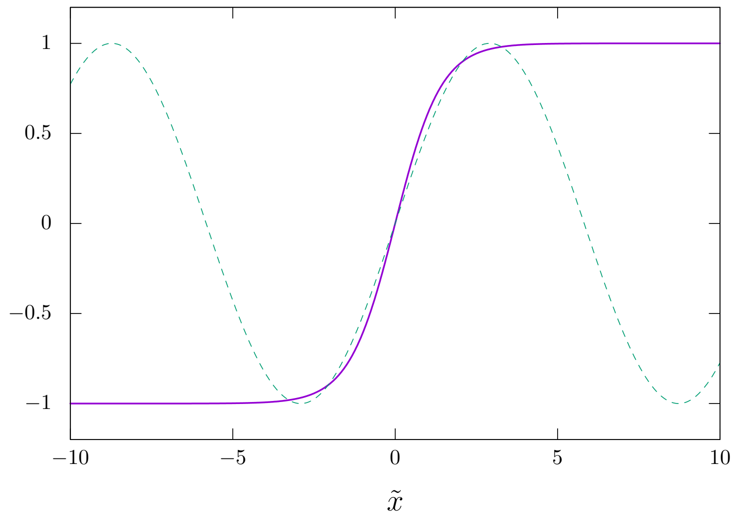

Figure B.6: Comparison of the length scales of the kink (solid purple curve) and the mode which produces the maximum excitation of the bound state (dashed green line).

If the thermal fluctuations are small, the amplitude of the shape mode is expected to oscillate harmonically with frequency $\tilde{\omega}_s = \sqrt{3/2}$. Let us write the amplitude of the shape mode at an arbitrary time as

$$A\left(\tilde{t}\right) = \hat{A}\,\sin\left(\tilde{\omega}_s\,\tilde{t} + \delta\right), \tag{B.21}$$

where $\hat{A}$ is the amplitude of the oscillations and δ is a random phase due to the fluctuations in the field velocity. Our goal is to find the average value of $\hat{A}$. This quantity will characterize the amount of excitation of the bound state when the kink is placed in a thermal bath at temperature Θ.

Evaluation of expression (B.21) at $\tilde{t} = 0$ yields

$$A\left(\tilde{t} = 0\right) \equiv u = \hat{A}\, \sin\delta\,. \tag{B.22}$$

We will also need to consider the time derivative of $A\left(\tilde{t}\right)$: $\dot{A}\left(\tilde{t}\right) = \hat{A}\,\tilde{\omega}_s \cos\left(\tilde{\omega}_s\,\tilde{t} + \delta\right)$. At $\tilde{t} = 0$ we have

$$\frac{\dot{A}\left(\tilde{t} = 0\right)}{\tilde{\omega}_s} \equiv v = \hat{A}\, \cos\delta\,. \tag{B.23}$$

The analytic expression for $\dot{A}\left(\tilde{t} = 0\right)$ can be found by projecting the initial field velocity $\tilde{\pi}_\xi\left(\tilde{x}, \tilde{t} = 0\right)$ onto the shape mode. The result is

$$\dot{A}\left(\tilde{t} = 0\right) = \pi\sqrt{\frac{6\sqrt{2}}{\tilde{L}}}\sum_{n=-N/2+1}^{N/2} A_n\;\tilde{k}_n\sqrt{\tilde{\omega}_n}\;\mathrm{sech}\left(\frac{\pi\tilde{k}_n}{\sqrt{2}}\right)\,. \tag{B.24}$$

The probability densities of the random variables u and v can be calculated as the densities of A_n and B_n are known. Recall from the previous subsection that A_n and B_n are Gaussian independent variables with zero mean and variance $\sigma_n^2 = \langle|\tilde{\alpha}_n|^2\rangle/2$ given by (B.9). Once we find the densities of u and v, we will be able to compute the joint probability density of $\hat{A}$ and δ using the change of variables (B.22),(B.23). From it we will calculate the marginal probability density of $\hat{A}$ to finally get $\langle\hat{A}\rangle$.

Let us start with the variable u, given by (B.20). Taking into account that the contribution of the $n = 0$ mode is zero ($\tilde{k}_0 = 0$) and that $k_n = -k_{-n}$, u can be rewritten as

$$\begin{aligned} u = -\pi\sqrt{\frac{6\sqrt{2}}{\tilde{L}}}\,\frac{\tilde{k}_{N/2}}{\sqrt{\tilde{\omega}_{N/2}}}\;\mathrm{sech}\left(\frac{\pi\tilde{k}_{N/2}}{\sqrt{2}}\right)B_{N/2} - \pi\sqrt{\frac{6\sqrt{2}}{\tilde{L}}}\sum_{j=1}^{N/2-1}\frac{\tilde{k}_j}{\sqrt{\tilde{\omega}_j}}\;\mathrm{sech}\left(\frac{\pi\tilde{k}_j}{\sqrt{2}}\right)\left(B_j - B_{-j}\right) \equiv \\ \equiv \gamma_{N/2}\,B_{N/2} + \sum_{j=1}^{N/2-1}\gamma_j\,C_j\;, \end{aligned} \tag{B.25}$$

where $C_j \equiv B_j - B_{-j}$ and

$$\gamma_j \equiv -\pi \sqrt{\frac{6\sqrt{2}}{\tilde{L}}\,\frac{\tilde{k}_j}{\sqrt{\tilde{\omega}_j}}}\ \mathrm{sech}\left(\frac{\pi \tilde{k}_j}{\sqrt{2}}\right) . \tag{B.26}$$

We further simplify notation by defining the variable $D_j \equiv \gamma_j\, C_j$. Then, u reads

$$u = \gamma_{N/2}\, B_{N/2} + \sum_{j=1}^{N/2-1} D_j\,. \tag{B.27}$$

Now consider the following theorem: *let P and Q be two independent random variables with probability density functions $f_P\,(p)$ and $f_Q\,(q)$. Then, the sum $R = P + Q$ is a random variable with probability density function*

$$f_R\,(r) = \int_{-\infty}^{\infty} f_P\,(r-q)\, f_Q\,(q)\; dq\ . \tag{B.28}$$

Applying this theorem to the variables C_j, we get

$$f_{\mathcal{C}_j}\,(C_j) = \frac{1}{2\sqrt{\pi}\,\sigma_j}\ \exp\left(-\frac{C_j^2}{4\sigma_j^2}\right)\ , \tag{B.29}$$

where $\sigma_j = \sqrt{\langle|\tilde{\alpha}_j|^2\rangle/2}$.

Therefore, the D_j variables have probability density function

$$f_{\mathcal{D}_j}\,(D_j) = f_{\mathcal{C}_j}\,(C_j\,(D_j)) \left|\frac{dC_j}{dD_j}\right| = \frac{1}{2\sqrt{\pi}\,\gamma_j\,\sigma_j}\ \exp\left(-\frac{D_j^2}{4\,\gamma_j^2\sigma_j^2}\right)\ , \tag{B.30}$$

Consider the partial sum $E_1 \equiv D_1 + D_2$ in equation (B.27). The convolution of the probability densities yields

$$f_{\mathcal{E}_1}\,(E_1) = \frac{1}{2\sqrt{\pi}\,\sqrt{\gamma_1^2\sigma_1^2 + \gamma_2^2\sigma_2^2}}\ \exp\left[-\frac{E_1^2}{4\,(\gamma_1^2\sigma_1^2 + \gamma_2^2\sigma_2^2)}\right]\ . \tag{B.31}$$

For $E_2 \equiv E_1 + D_3$ we get

$$f_{\mathcal{E}_2}\,(E_2) = \frac{1}{2\sqrt{\pi}\,\sqrt{\gamma_1^2\sigma_1^2 + \gamma_2^2\sigma_2^2 + \gamma_3^2\sigma_3^2}}\ \exp\left[-\frac{E_2^2}{4\,(\gamma_1^2\sigma_1^2 + \gamma_2^2\sigma_2^2 + \gamma_3^2\sigma_3^2)}\right]\ . \tag{B.32}$$

Now we can see that at the end of the iterative process we will be left with

$$u = \gamma_{N/2}\, B_{N/2} + E_{N/2-2}\,, \tag{B.33}$$

where the random variable $E_{N/2-2}$ has probability density function

$$f_{\mathcal{E}_{N/2-2}}\left(E_{N/2-2}\right) = \frac{1}{\sqrt{2\pi z^2}} \exp\left(-\frac{E_{N/2-2}^2}{2z^2}\right)\,, \tag{B.34}$$

with $z^2 = 2\sum_{j=1}^{N/2-1} \gamma_j^2 \sigma_j^2$.

Finally, the probability density function of u is obtained by convoluting the densities of the two terms in (B.33):

$$f_U\left(u\right) = \frac{1}{\sqrt{2\pi s_u^2}} \exp\left(-\frac{u^2}{2s_u^2}\right)\,. \tag{B.35}$$

Thus, the amplitude of the shape mode at $\tilde{t} = 0$ is a Gaussian random variable with zero mean and variance s_u^2 given by

$$s_u^2 = 2\sum_{j=1}^{N/2} \gamma_j^2 \sigma_j^2\,. \tag{B.36}$$

The calculation of the probability density function of v is analogous. The result is

$$f_V\left(v\right) = \frac{1}{\sqrt{2\pi s_v^2}} \exp\left(-\frac{v^2}{2s_v^2}\right)\,, \tag{B.37}$$

where the variance s_v^2 is given by

$$s_v^2 = 2\sum_{j=1}^{N/2} \tilde{\gamma}_j^2 \sigma_j^2\,, \tag{B.38}$$

with $\tilde{\gamma}_j \equiv -\frac{\tilde{\omega}_j}{\tilde{\omega}_s}\,\gamma_j$ (no sum over repeated indices).

Since u and v are independent, their joint probabilty density function is the product of their corresponding densities:

$$f_{U,V}\left(u,v\right) = f_U\left(u\right) f_V\left(v\right) = \frac{1}{2\pi s_u s_v}\, \exp\left(-\frac{u^2}{2s_u^2} - \frac{v^2}{2s_v^2}\right)\,. \tag{B.39}$$

Equations (B.22) and (B.23) give u and v in terms of $\hat{A}$ and δ. This can be thought of as a change of variables, so the joint probability density function of $\hat{A}$ and δ is given by

$$f_{A,\Delta}\left(\hat{A},\delta\right)=f_{U,V}\left(u\left(\hat{A},\delta\right),v\left(\hat{A},\delta\right)\right)|J|\,, \tag{B.40}$$

where J is the Jacobian of the transformation:

$$|J|=\begin{vmatrix}\frac{\partial u}{\partial\hat{A}} & \frac{\partial u}{\partial\delta}\\ \\ \frac{\partial v}{\partial\hat{A}} & \frac{\partial v}{\partial\delta}\end{vmatrix}=\begin{vmatrix}\sin\delta & \hat{A}\cos\delta\\ \\ \cos\delta & -\hat{A}\sin\delta\end{vmatrix}=\hat{A}\,. \tag{B.41}$$

Then, the joint probability density function of $\hat{A}$ and δ is

$$f_{A,\Delta}(\hat{A},\delta)=\frac{\hat{A}}{2\pi s_u s_v}\exp\left[-\frac{\hat{A}^2}{2}\left(\frac{\sin^2\delta}{s_u^2}+\frac{\cos^2\delta}{s_v^2}\right)\right]\,. \tag{B.42}$$

Now we can find the marginal probability density function of $\hat{A}$ by integrating out the phase δ:

$$f_A(\hat{A})=\int_0^{2\pi}f_{A,\Delta}(\hat{A},\delta)d\delta=\frac{\hat{A}}{s_u s_v}\exp\left[-\frac{\hat{A}^2\left(s_u^2+s_v^2\right)}{4s_u^2 s_v^2}\right]I_0\left[\frac{\hat{A}^2\left(s_v^2-s_u^2\right)}{4s_u^2 s_v^2}\right]\,, \tag{B.43}$$

where I_0 denotes the modified Bessel function of the first kind. This probability density function is plotted in figure B.7.

One can also find the marginal probability density function of δ by integrating out $\hat{A}$:

$$f_\Delta\left(\delta\right)=\int_0^{\infty}f_{A,\Delta}(\hat{A},\delta)d\hat{A}=\frac{s_u s_v}{2\pi\left(s_v^2\sin^2\delta+s_u^2\cos^2\delta\right)}\,. \tag{B.44}$$

We can calculate the expectation value and the variance of $\hat{A}$ using (B.43). We are mainly interested in the expectation value:

$$\langle\hat{A}\rangle=\int_0^{\infty}\hat{A}\,f_A(\hat{A})d\hat{A}=\sqrt{\frac{2}{\pi}}\,s_v\,E\left(\sqrt{1-\frac{s_u^2}{s_v^2}}\right)\,, \tag{B.45}$$

where E denotes the so-called complete elliptic integral of the second kind. This result leads to a particular geometrical interpretation of $\langle\hat{A}\rangle$: its numerical value is the perimeter of an ellipse with semi-minor axis $s_u/\sqrt{8\pi}$ and semi-major axis $s_v/\sqrt{8\pi}$.

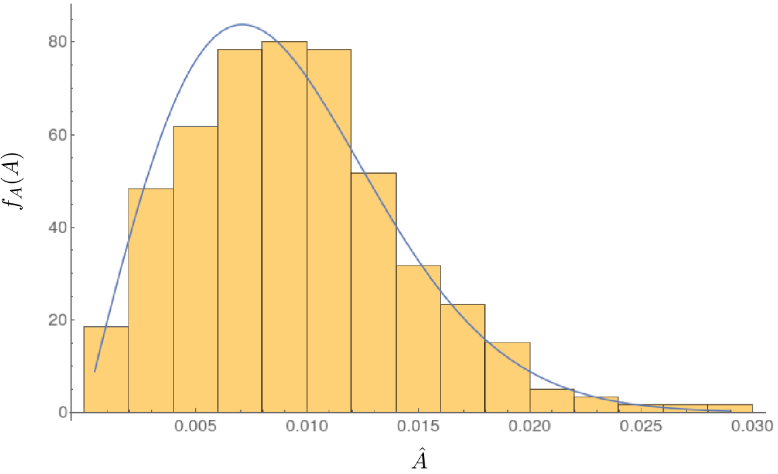

Figure B.7: Histogram of the probability density for the values of the amplitude of the bound state $\hat{A}$ at a temperature $\Theta = 10^{-4}$ from 300 simulations. The solid line represents the estimate of this distribution as given in equation (B.43).

Recall that all the temperature dependence is encoded in s_u and s_v, and that they are the standard deviations of the initial amplitude and the initial normalized amplitude velocity (normalized with respect to the shape mode angular frequency $\tilde{\omega}_s$). In the classical limit ($\Theta \gg \tilde{\omega}_{N/2}/\eta^2$), both s_u and s_v are proportional to $\sqrt{\Theta}$, so $\langle \hat{A} \rangle \propto \sqrt{\Theta}$.

B.1.3 Metropolis algorithm

In the main part of the text, we make use of a thermal state for a free massive scalar field as the initial conditions for some of our simulations. We do this by initializing the power spectrum of the field and its momentum in such a way that their occupation numbers satisfy the Bose-Einstein distribution.

Here, we use an alternative way to arrive at this state that is based on the classic Metropolis algorithm [112]. This procedure is more flexible since it does not assume that we are in a free field vacuum. In fact, we will also use it to consider thermal fluctuations around the background kink solution, which may seem to be a more accurate method than the one used in the main text.

Let us briefly review the main steps to achieve this thermal state. The initial field profile for the algorithm is chosen to be a constant value at one of the vacua[1] and we set the initial field velocity to zero. The algorithm then consists of the following steps:

1. We generate a new configuration which differs from the present one by changing the value of the field and its velocity at one lattice point[2].

2. We then calculate the difference in energy between the new state and the old one: $\Delta\tilde{E} = \tilde{E}_{new} - \tilde{E}_{old}$. Now there are two possibilities:

   (a) The energy has decreased or remained the same: $\Delta\tilde{E} \leq 0$. In this case, we accept the change.

   (b) The energy has increased: $\Delta\tilde{E} > 0$. In this case, we accept the change with probability

   $$p = e^{-\frac{\Delta\tilde{E}}{\Theta}} \ , \tag{B.46}$$

   with Θ the temperature at which we are simulating. This can be done as follows. We choose a random number r between zero and one, $0 \leq r < 1$. If this number is less than the acceptance probability, $r < p$, then we accept the change. Otherwise, we leave the value of the field and the field velocity unchanged.

After that, we just have to follow the same steps over and over again until the field reaches thermal equilibrium. We will consider that the field is in a state of thermal equilibrium when the following two conditions are satisfied:

1. The total energy of the perturbations has saturated to $N\Theta$, where N is the number of lattice points, and it is equally stored in kinetic energy and gradient+potential energy, in agreement with equipartition (see figure B.8).

2. The Fourier spectrum of both the field and the field velocity perturbations are well approximated by the classical limit of the theoretical thermal spectrum given in equation (B.7).

We show in figure (B.9) the comparison of the different spectra obtained using the Metropolis algorithm and the classical limit of the theoretical spectrum (B.7) at the same temperature. The coefficients $\tilde{\xi}_n$ are the Fourier coefficients of the thermal perturbation field, and they are related to the $\tilde{\alpha}_n$ parameters by

$$\tilde{\xi}_n = \frac{1}{\sqrt{2\tilde{\omega}_n}} \left(\tilde{\alpha}_n + \tilde{\alpha}^*_{-n}\right) \ . \tag{B.47}$$

---

[1] For the thermal state around the kink solution we start with the kink solution instead.

[2] Since field and field velocity are independent variables, they must be varied independently.

The $\tilde{\pi}_n$ are the analogous coefficients for the field velocity:

$$\tilde{\pi}_n = i\sqrt{\frac{\tilde{\omega}_n}{2}}\left(-\tilde{\alpha}_n + \tilde{\alpha}^*_{-n}\right) \ . \tag{B.48}$$

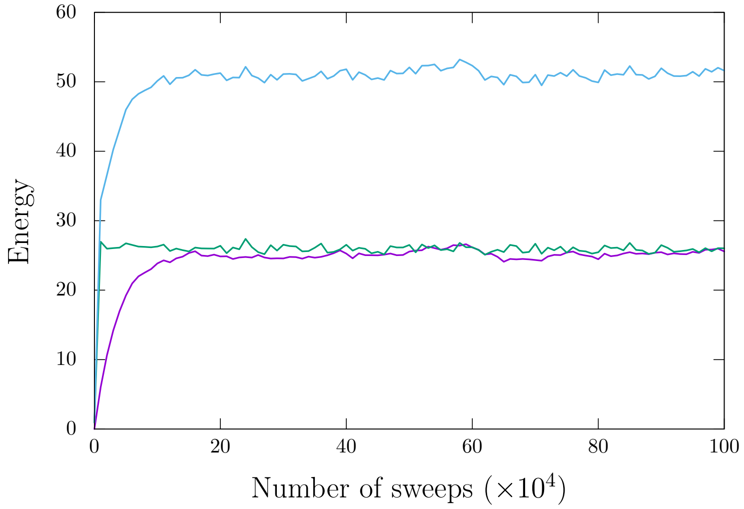

Figure B.8: Energy throughout the Metropolis algorithm with $\Theta = 0.01$, taking the kink solution as initial state. The kinetic energy (in purple) tends to $N\Theta/2$, while the gradient+potential energy (in green) saturates to $\tilde{M}_k + N\Theta/2$. The total energy (in blue) tends to $\tilde{M}_k + N\Theta$.

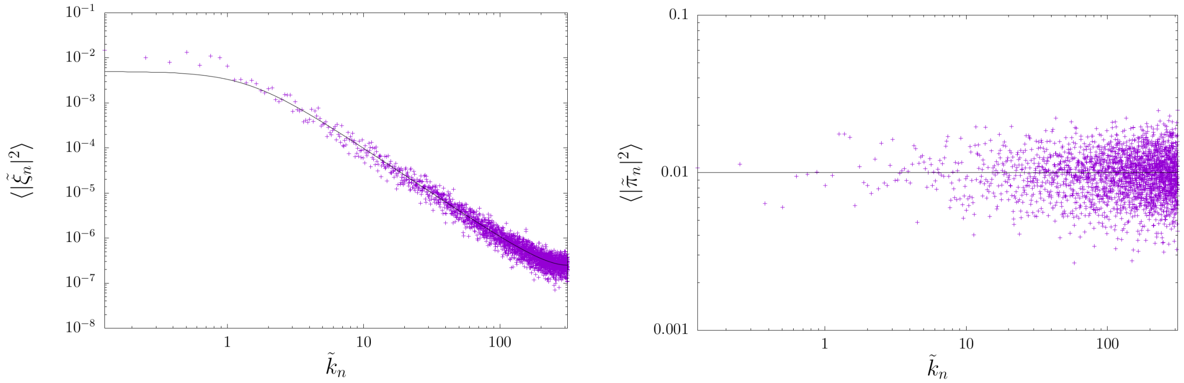

Figure B.9: Fourier spectrum of the thermal fluctuations $\tilde{\xi}$ (left) and $\tilde{\pi}_\xi$ (right) at temperature $\Theta = 0.01$ (average of 10 Metropolis realizations). The black curve corresponds to the classical limit of the theoretical spectrum (B.7) at this temperature.

We have also used the Metropolis algorithm to generate the spectrum of excitations of a kink in thermal equilibrium with a background. The simulations performed with these initial conditions yield statistically indistinguishable results from the classical limit of the spectrum (B.7). However, the Metropolis algorithm is much more costly in terms of computation time. This is why, at the end, we use the method described in section B.1.1 to generate a large set of realizations.

B.2 Real field in $2+1$ dimensions

In chapter 3, we showed that the parametric instability we found can take place for domain walls formed in a phase transition. The preparation of the thermal state in the vacuum is completely analogous to the $1+1$ dimensional case discussed above. The final result for the dimensionless thermal fluctuations $\tilde{\xi}$ and $\tilde{\pi}_\xi$ is

$$\tilde{\xi}\left(\tilde{t}=0,\tilde{x}_i,\tilde{y}_j\right) = \sum_{m=-N_y/2+1}^{N_y/2} \sum_{n=-N_x/2+1}^{N_x/2} \sqrt{\frac{\langle|\tilde{\alpha}_{mn}|^2\rangle}{\tilde{L}_x\tilde{L}_y\tilde{\omega}_{mn}}} r_{mn} \cos\left(\tilde{k}_x^{(m)}\tilde{x}_i + \tilde{k}_y^{(n)}\tilde{y}_j + \gamma_{mn}\right) \ , \tag{B.49}$$

$$\tilde{\pi}_\xi\left(\tilde{t}=0,\tilde{x}_i,\tilde{y}_j\right) = \sum_{m=-N_y/2+1}^{N_y/2} \sum_{n=-N_x/2+1}^{N_x/2} \sqrt{\frac{\tilde{\omega}_{mn}\langle|\tilde{\alpha}_{mn}|^2\rangle}{\tilde{L}_x\tilde{L}_y}} r_{mn} \cos\left(\tilde{k}_x^{(m)}\tilde{x}_i + \tilde{k}_y^{(n)}\tilde{y}_j - \gamma_{mn}\right) \ . \tag{B.50}$$

Note that the angular frequency, the Bose-Einstein variance and the random numbers r and γ are now 2×2 matrices due to the presence of a new spatial dimension.

Assuming that the lattice spacing is the same in both the x and y directions, the angular frequencies and wave numbers read

$$\tilde{\omega}_{mn} = \sqrt{\left[\frac{2\sin\left(\frac{\tilde{k}_x^{(n)}\Delta\tilde{x}}{2}\right)}{\Delta\tilde{x}}\right]^2 + \left[\frac{2\sin\left(\frac{\tilde{k}_y^{(m)}\Delta\tilde{x}}{2}\right)}{\Delta\tilde{x}}\right]^2 + 2} \tag{B.51}$$

and

$$\tilde{k}_x^{(n)} = \frac{2\pi n}{\tilde{L}_x} \quad , \quad \tilde{k}_y^{(m)} = \frac{2\pi m}{\tilde{L}_y} \, . \tag{B.52}$$

On the other hand, $\langle|\tilde{\alpha}_{mn}|^2\rangle$ is given by (B.7) with

$$\Theta = \frac{T}{\eta^2} \tag{B.53}$$

and

$$\tilde{\Omega} = \frac{\eta}{\sqrt{\lambda}}\Theta\,. \tag{B.54}$$

The thermal state is fully specified by determining the values of the cutoff frequency $\tilde{\Omega}$ and the temperature Θ. As in the previous section, we can choose $\tilde{\Omega}$ in such a way that modes with wavelengths shorter than $10\Delta x$ are suppressed, in which case it will be given by (B.14). To determine the value of Θ, we impose that the thermal energy be $p\%$ of the vacuum energy. This condition yields

$$\Theta \sim \frac{p}{400}\left(\Delta\tilde{x}\right)^2\,. \tag{B.55}$$

Such a thermal state is illustrated in figure B.10.

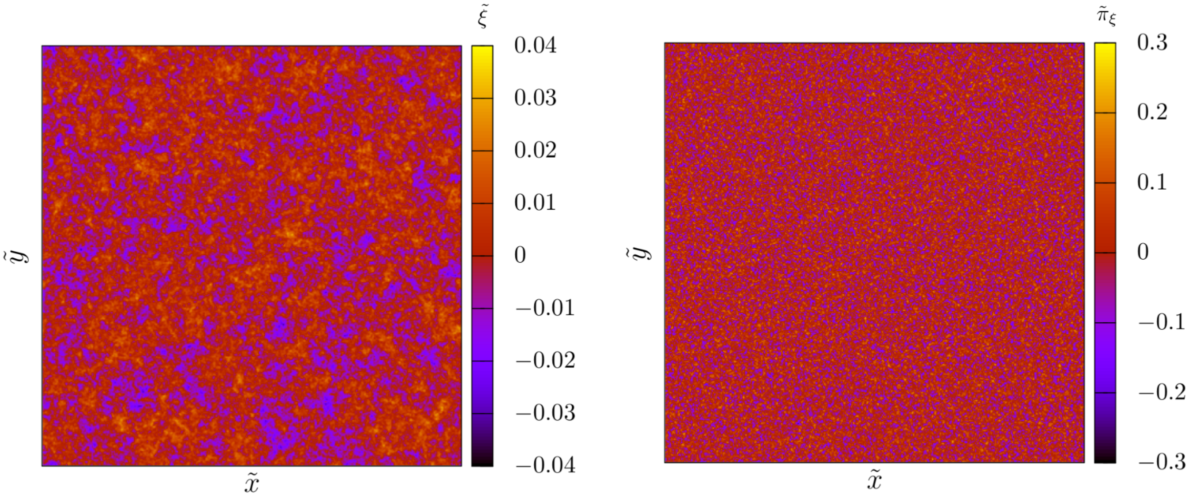

Figure B.10: Two-dimensional thermal state in the vacuum. Left panel: $\tilde{\xi}\left(\tilde{t}=0,\tilde{x}_i,\tilde{y}_j\right)$. Right panel: $\tilde{\pi}_\xi\left(\tilde{t}=0,\tilde{x}_i,\tilde{y}_j\right)$.

If instead we are interested in placing the domain wall string in a thermal bath, we force the thermal energy to be bounded from above by $p\%$ of the mass of the soliton. In this case, one gets

$$\Theta \sim \frac{\sqrt{2}p}{150}\frac{\left(\Delta\tilde{x}\right)^2}{\tilde{L}_x}\,. \tag{B.56}$$

B.3 Complex field in $2+1$ dimensions

As we will see in the following, the implementation of the thermal state is slightly different for the case of the phase transition and the soliton in a thermal bath when the scalar field is complex.

B.3.1 Thermal fluctuations for the phase transition

We need to generate a thermal state for the massive fields ϕ_1 and ϕ_2 in the vacuum of the $t < 0$ potential (4.34). Recall that the mass of these fields is $m_r = \sqrt{\lambda}\eta$. Let $\xi_{1,2}$ and $\pi_{1,2}$ be the corresponding thermal fluctuations of the field and the velocity. The implementation of this state is completely analogous to the $2+1$ dimensional case described in the previous section. The perturbation fields are given by (B.49) and (B.50), but the dimensionless mass equal to 2 on the right-hand side of (B.51) is now 1. Note also that we have to employ those expressions twice, as we now have two fields.

The dimensionless temperature and cutoff frequency are also given by (B.53) and (B.54). Once again, the latter is specified via (B.14). However, in order for the thermal energy in the classical limit to be $p\%$ of the initial vacuum energy, in this case we need

$$\Theta \sim \frac{p}{800} \left(\Delta \tilde{x}\right)^2 . \tag{B.57}$$

Note that a subtle difference with respect to the previous cases is that the number of quadratic degrees of freedom in the discrete Hamiltonian is now $4N$, where N is the number of lattice points. This is the reason for the extra factor of 2 with respect to (B.55).

One should also keep in mind that, since our choice of $\tilde{\Omega}$ implies that there are some modes suppressed, the energy of the thermal state with (B.57) will actually be smaller than $p\%$ of the initial vacuum energy.

B.3.2 Vortex in a thermal bath

Now we are interested in generating the thermal fluctuations directly on the vacua of the $t > 0$ potential in (4.34). In terms of the fields ϕ_1 and ϕ_2, the Lagrangian density reads

$$\mathcal{L} = \frac{1}{2}\partial_\mu \phi_1 \partial^\mu \phi_1 + \frac{1}{2}\partial_\mu \phi_2 \partial^\mu \phi_2 - \frac{\lambda}{4}\left(\frac{\phi_1^2 + \phi_2^2}{2} - \eta^2\right)^2 . \tag{B.58}$$

Let us consider fluctuations of the field ϕ_1 (again, we will denote the fluctuations by ξ_1) about the vacuum $\phi_2/\sqrt{2} = C$, $\phi_1/\sqrt{2} = \sqrt{\eta^2 - C^2}$:

$$\mathcal{L} \approx \frac{1}{2}\partial_\mu \xi_1 \partial^\mu \xi_1 - \frac{\lambda}{2}\left(\eta^2 - C^2\right)\xi_1^2 . \tag{B.59}$$

It is then clear than the squared mass of the field would be $m^2 = \lambda \left(\eta^2 - C^2\right)$. Note that the mass depends on the particular vacuum at which the oscillations take place, so (B.51) cannot be directly employed to construct the matrix of angular frequencies.

Consider instead the radial and angular fields φ and α in (4.3). In terms of these two fields, the Lagrangian reads

$$\mathcal{L} = \frac{1}{2}\partial_\mu \varphi \partial^\mu \varphi + \frac{\varphi^2}{2\eta^2}\partial_\mu \alpha \partial^\mu \alpha - \frac{\lambda}{4}\left(\frac{\varphi^2}{2} - \eta^2\right)^2 . \tag{B.60}$$

Considering fluctuations about any vacuum, that is, $\varphi = \sqrt{2}\eta + \xi$ and $\alpha = \eta\theta + \chi$ (where θ is the polar coordinate),

$$\mathcal{L} \approx \frac{1}{2}\partial_\mu \xi \partial^\mu \xi + \frac{1}{2}\partial_\mu \chi \partial^\mu \chi - \frac{\lambda}{2}\eta^2 \xi^2 , \tag{B.61}$$

so $m_r^2 = \lambda\eta^2$ and $m_\chi = 0$. Now we can find the thermal fluctuations ξ and χ following the procedure described in the previous subsection. The only difference now is that one of the fields is massless, so the dimensionless mass appearing in the matrix of angular frequencies has to be set to 0. These fluctuations are added to the static solution $\phi = \eta f\left(r\right) e^{i\theta}$, so the initial conditions for the dimensionless fields $\tilde{\phi}_1$ and $\tilde{\phi}_2$ are

$$\tilde{\phi}_1 = \sqrt{2}\left(f + \tilde{\xi}\right)\cos\left(\theta + \tilde{\chi}\right) , \tag{B.62}$$

$$\frac{\partial \tilde{\phi}_1}{\partial \tilde{t}} = \sqrt{2}\tilde{\pi}_\xi \cos\left(\theta + \tilde{\chi}\right) - \sqrt{2}\left(f + \tilde{\xi}\right)\tilde{\pi}_\chi \sin\left(\theta + \tilde{\chi}\right) , \tag{B.63}$$

$$\tilde{\phi}_2 = \sqrt{2}\left(f + \tilde{\xi}\right)\sin\left(\theta + \tilde{\chi}\right) , \tag{B.64}$$

$$\frac{\partial \tilde{\phi}_2}{\partial \tilde{t}} = \sqrt{2}\tilde{\pi}_\xi \sin\left(\theta + \tilde{\chi}\right) + \sqrt{2}\left(f + \tilde{\xi}\right)\tilde{\pi}_\chi \cos\left(\theta + \tilde{\chi}\right) . \tag{B.65}$$

The parameter $\tilde{\Omega}$ is again determined by the condition (B.14). However, the dimensionless temperature Θ is now chosen in such a way that the energy of the thermal fluctuations is a small fraction of the energy of the vortex solution. Using (4.11) and taking into account that $E_{\text{thermal}} \sim 2NT$, this thermal energy is $p\%$ of the energy of the vortex if

$$\Theta \sim \frac{p}{200}\frac{\left(\Delta\tilde{x}\right)^2}{\tilde{L}_x \tilde{L}_y}\left[4.9 + 2\pi \ln\left(\frac{\tilde{L}}{2.15}\right)\right] . \tag{B.66}$$

B.4 Complex field in $3+1$ dimensions

Here we will only explain how to generate the thermal fluctuations about the vacua of the Mexican-hat potential, in order to add them directly to the $3+1$ dimensional global string solution $\phi = \eta f\left(r\right) e^{i\theta}$. This was done in chapter 5 with the intention of triggering the resonant amplification of the zero mode.

The construction of the thermal state is completely analogous to the one described in the previous subsection. Let ξ and χ respectively denote the thermal fluctuations of the radial and angular parts of the field, and let π_ξ and π_χ be their corresponding velocities. The initial conditions for the string in a thermal bath are exactly given by equations (B.62) to (B.65). The radial perturbations have mass $m_r = \sqrt{\lambda}\eta$ and are given by

$$\tilde{\xi}\left(\tilde{t}=0, \tilde{x}_i, \tilde{y}_j, \tilde{z}_k\right) = \sum_l \sum_m \sum_n \sqrt{\frac{\langle|\tilde{\alpha}_{lmn}|^2\rangle}{\tilde{L}_x \tilde{L}_y \tilde{L}_z \tilde{\omega}_{lmn}}} r_{lmn} \cos\left(\tilde{k}_x^{(l)}\tilde{x}_i + \tilde{k}_y^{(m)}\tilde{y}_j + \tilde{k}_z^{(n)}\tilde{z}_k + \gamma_{lmn}\right) , \tag{B.67}$$

$$\tilde{\pi}_\xi\left(\tilde{t}=0, \tilde{x}_i, \tilde{y}_j, \tilde{z}_k\right) = \sum_l \sum_m \sum_n \sqrt{\frac{\tilde{\omega}_{lmn}\langle|\tilde{\alpha}_{lmn}|^2\rangle}{\tilde{L}_x \tilde{L}_y \tilde{L}_z}} r_{lmn} \cos\left(\tilde{k}_x^{(l)}\tilde{x}_i + \tilde{k}_y^{(m)}\tilde{y}_j + \tilde{k}_z^{(n)}\tilde{z}_k - \gamma_{lmn}\right) , \tag{B.68}$$

where the indices l, n, m run from $-N_{x,y,z}/2+1$ to $N_{x,y,z}/2$. The frequencies read

$$\tilde{\omega}_{lmn} = \sqrt{\left[\frac{2\sin\left(\frac{\tilde{k}_x^{(l)}\Delta\tilde{x}}{2}\right)}{\Delta\tilde{x}}\right]^2 + \left[\frac{2\sin\left(\frac{\tilde{k}_y^{(m)}\Delta\tilde{x}}{2}\right)}{\Delta\tilde{x}}\right]^2 + \left[\frac{2\sin\left(\frac{\tilde{k}_z^{(n)}\Delta\tilde{x}}{2}\right)}{\Delta\tilde{x}}\right]^2 + 1} \, , \tag{B.69}$$

where we have assumed that the lattice spacing is the same in all directions, and

$$\tilde{k}_x^{(l)} = \frac{2\pi l}{\tilde{L}_x} \quad , \quad \tilde{k}_y^{(m)} = \frac{2\pi m}{\tilde{L}_y} \quad , \quad \tilde{k}_z^{(n)} = \frac{2\pi n}{\tilde{L}_z} \, . \tag{B.70}$$

The variance $\langle|\tilde{\alpha}_{lmn}|^2\rangle$ is given by (B.7) with

$$\Theta = \frac{\sqrt{\lambda}}{\eta} T \tag{B.71}$$

and

$$\tilde{\Omega} = \frac{\Theta}{\lambda} \, . \tag{B.72}$$

The fluctuations for the angular part are generated in the same way, except for the fact that the 1 on the right-hand side of (B.69) is substituted by a 0.

Once again, the thermal state is specified by fixing $\tilde{\Omega}$ and Θ. On the one hand, in order for modes of wavelength smaller than $10\Delta x$ to be suppressed, we have to choose $\tilde{\Omega}$ given by (B.14). On the other hand, in order for E_{thermal} to be $p\%$ of the energy of the string solution, we need

$$\Theta \sim \frac{p}{200}\frac{(\Delta\tilde{x})^3}{\tilde{L}_x\tilde{L}_y}\left[4.9 + 2\pi\ln\left(\frac{\tilde{L}}{2.15}\right)\right] . \tag{B.73}$$

This follows from the same arguments we used to derive (B.66).

Appendix C

Decay rate of the bound states

In this appendix, we give analytical estimates for the decay rate of the bound states of the kink (chapter 2), the domain wall strings (chapter 3) and the global vortices (chapter 4).

C.1 $1+1$ dimensional kinks

As seen in chapter 2, at the linear level, the bound state (2.9) should oscillate with frequency $\omega_1 = \sqrt{3/2}$ and should not decay, since its frequency is smaller than the frequencies of the propagating modes outside the kink. However, since the bound state couples non-linearly to the propagating modes, its energy is radiated away. As a consequence, the oscillating amplitude of the shape mode slowly decreases with time. The particular time dependence of the amplitude can be estimated analytically. Let us describe this estimate following the calculation given in [107].

We consider a parametrization of the field given by

$$\phi(t,x) = \phi_k(x) + A(t)\bar{f}_1(x) + f_r(t,x)\ , \tag{C.1}$$

where the $f_r(t,x)$ term is related to the propagating modes (2.10), which are orthogonal to $\bar{f}_1$:

$$\int_{-\infty}^{\infty} \mathrm{d}x \bar{f}_1(x) f_r(t,x) = 0\,. \tag{C.2}$$

Plugging the decomposition (C.1) into the equation of motion (1.4), one can see that, at the lowest order in A, the frequency of the oscillation is ω_1, as we mentioned before. At the next order, at $\mathcal{O}(A^2)$, the equation becomes

$$\left(\ddot{A}+\frac{3}{2}A\right)\bar{f}_1+\ddot{f}_r-f_r^{''}+\left(3\phi_k^2-1\right)f_r=-3\phi_k\bar{f}_1^2A^2. \tag{C.3}$$

The term on the right-hand side constitutes a source term for f_r. We can now multiply this equation by the shape mode function $\bar{f}_1(x)$ and integrate over all space, employing the orthogonality of eigenstates. This operation yields[1]

$$\ddot{A}+\frac{3}{2}A=-3\alpha A^2, \tag{C.4}$$

where

$$\alpha=\int_{-\infty}^{\infty}dx\,\phi_k\left(x\right)\,\bar{f}_1^3\left(x\right)=\frac{3\sqrt{3}\,\pi}{32\times 2^{3/4}}\ . \tag{C.5}$$

Substituting equation (C.4) in (C.3), one gets

$$\ddot{f}_r-f_r^{''}+(3\phi_k^2-1)f_r=3\left(\alpha\bar{f}_1-\phi_k\bar{f}_1^2\right)A^2\ . \tag{C.6}$$

The amplitude can be expressed as (see equation (2.23))

$$A(t)=\hat{A}(t)\cos\left(\sqrt{\frac{3}{2}}\,t\right), \tag{C.7}$$

where $\hat{A}(t)$ carries the information of the decay of the amplitude, and at linear order, is a constant. The amplitude at $t=0$ is $A(0)=\hat{A}(0)$. The fact that $A(t)$ oscillates with frequency $\sqrt{3/2}$ implies that the source term on the right-hand side of equation (C.6) has frequency $2\sqrt{3/2}$:

$$A^2(t)=\frac{\hat{A}^2\left(t\right)}{2}\left[\cos\left(2\sqrt{\frac{3}{2}}\,t\right)+1\right]\ . \tag{C.8}$$

If one substitutes this in equation (C.6), the right-hand side will be the sum of a time-independent term and a time-dependent term, the latter being proportional to $\cos\left(2\sqrt{3/2}t\right)$. Since the equation is linear in f_r, the response of f_r to the time-independent term will be itself time-independent, thus carrying no energy. In this regard, only the time-dependent source is important. With these considerations, and setting $f_r\left(t,x\right)=\Re\left[f\left(x\right)\exp\left(i\omega t\right)\right]$,

---

[1] Note that, according to the equation of linear perturbations (2.6), the term $-f_r^{''}+(3\phi_k^2-1)f_r$ is proportional to f_r, and therefore, it is orthogonal to the shape mode.

the equation that we need to solve is

$$-f'' + (3\phi_k^2 - 1 - \omega^2)f = \frac{3}{2}\left(\alpha\bar{f}_1 - \phi_k\bar{f}_1^2\right)\hat{A}^2\exp\left[i\left(2\sqrt{\frac{3}{2}} - \omega\right)t\right] \, . \tag{C.9}$$

The left-hand side does not depend on time, so this equation only has solutions for $\omega = 2\sqrt{3/2}$. This is the reason why the frequency of the radiation is twice the frequency of the shape mode.

The solutions of the homogeneous equation are known:

$$f_q(x) = \left[3\phi_k^2(x) - 1 - q^2 - 3iq\phi_k(x)\right]\exp\left(\frac{iqx}{\sqrt{2}}\right) \, , \tag{C.10}$$

$$f_{-q}(x) = \left[3\phi_k^2(x) - 1 - q^2 + 3iq\phi_k(x)\right]\exp\left(-\frac{iqx}{\sqrt{2}}\right) \, , \tag{C.11}$$

where $q = \sqrt{2\omega^2 - 4} = \sqrt{8}$. With these solutions, we can construct the Green's function suitable for outgoing radiation:

$$G(x,y) = \begin{cases} -\frac{1}{W}f_{-q}(y)\,f_q(x) \, , & x < y \\ \\ -\frac{1}{W}f_q(y)\,f_{-q}(x) \, , & x > y \\ \end{cases} \tag{C.12}$$

where W is the Wronskian:

$$W = f_q(x)\,f'_{-q}(x) - f'_q(x)\,f_{-q}(x) = -\sqrt{2}\,iq\left(q^2+1\right)\left(q^2+4\right) . \tag{C.13}$$

The second equality follows from using the asymptotic ($x \to \infty$) form of the solutions (C.10) and (C.11). Now, the solution of the inhomogeneous equation (C.9) can be found by convoluting the source with the Green's function:

$$\begin{aligned} f(x) = &-\frac{1}{W}f_{-q}(x)\int_{-\infty}^{x} dy\, f_q(y)\,\frac{3}{2}\left[\alpha\bar{f}_1(y) - \phi_k(y)\,\bar{f}_1^2(y)\right]\hat{A}^2 - \\ &-\frac{1}{W}f_q(x)\int_{x}^{\infty} dy\, f_{-q}(y)\,\frac{3}{2}\left[\alpha\bar{f}_1(y) - \phi_k(y)\,\bar{f}_1^2(y)\right]\hat{A}^2 \, . \end{aligned} \tag{C.14}$$

In the $x \to \infty$ limit, we get

$$f_r\left(t,x\right) = \Re\left[-\frac{3\hat{A}^2}{2\sqrt{2}\,iq\left(2-q^2-3iq\right)}\exp\left[i\left(\omega t-\frac{qx}{\sqrt{2}}\right)\right]\int_{-\infty}^{\infty}dy\,f_q\left(y\right)\phi_k\left(y\right)\bar{f}_1^2\left(y\right)\right]. \tag{C.15}$$

In order to calculate the integral on the right-hand side, we use the result

$$\begin{aligned} I\left(q\right) = \int_{-\infty}^{\infty} dy\ \tanh\left(y\right)\sinh^2\left(y\right)\mathrm{sech}^4\left(y\right)\left[3\tanh^2\left(y\right)-1-q^2-3iq\tanh\left(y\right)\right]\exp\left(iqy\right) = \\ = \frac{i\pi q^2}{48\sinh\left(\frac{\pi q}{2}\right)}\left(q^2+4\right)\left(q^2-2\right). \end{aligned} \tag{C.16}$$

With a little more manipulation, and using $\omega = 2\sqrt{3/2}$ and $q = \sqrt{8}$, the following result for the radiation field in the $x \to \infty$ is obtained:

$$f_r\left(t,x\right) = \frac{3\sqrt{3}\,\pi\hat{A}^2}{8\sinh\left(\pi\sqrt{2}\right)}\cos\left[2\sqrt{\frac{3}{2}}\,t-2x-\arctan\left(\sqrt{2}\right)\right]. \tag{C.17}$$

Now we can find the energy flux by using the T_{0x} component of the energy-momentum tensor in equation (2.26). Including a factor of 2 to account for the radiation toward $x \to -\infty$ and averaging over a period, we get the radiated power

$$\frac{dE}{dt} = -0.0112909\hat{A}^4\,. \tag{C.18}$$

Finally, the backreaction on the amplitude of the shape mode can be estimated on the grounds of energy conservation. Combining (2.27) and (C.18), we get the following differential equation for $\hat{A}\left(t\right)$:

$$\frac{3}{4}\frac{d\hat{A}^2}{dt} = -0.0112909\,\hat{A}^4\,, \tag{C.19}$$

which yields

$$\hat{A}(t) = \frac{1}{\sqrt{\frac{1}{\hat{A}^2(0)}+0.0150546\,t}}\,. \tag{C.20}$$

This is the final result for the long-term evolution of the envelope amplitude of the bound state in Minkowski space.

C.2 $2+1$ dimensional domain walls

In this section, we calculate the decay rate of the amplitude of zero mode and shape mode excitations on the domain wall string studied in chapter 3.

C.2.1 Radiation from zero mode excitations

We first calculate the power radiated by domain wall strings in a standing wave configuration. Let us consider the ansatz

$$\phi(t,x,y) = \phi_k \left[\frac{x-\psi_0(t,y)}{\sqrt{1+{\psi_0'}^2 - \dot{\psi_0}^2}} \right] + R(t,x,y)\,, \tag{C.21}$$

where $R(t,x,y)$ denotes collectivelly the radiation modes and the transverse displacement $\psi_0(t,y)$ is given by

$$\psi_0(t,y) = \hat{D}(t)\cos(\omega_0 t)\cos(\omega_0 y)\ . \tag{C.22}$$

If we substitute (C.21) into the field equation (A.11) we obtain, at second order in the amplitude $\hat{D}(t)$, the following equation for the radiation modes:

$$\frac{\partial^2 R}{\partial t^2} - \frac{\partial^2 R}{\partial x^2} - \frac{\partial^2 R}{\partial y^2} + \left(3\phi_k^2 - 1\right)R = -\frac{1}{\sqrt{2}}\hat{D}^2\omega_0^4 x \,\mathrm{sech}^2\left(\frac{x}{\sqrt{2}}\right)\left[\cos(2\omega_0 t) + \cos(2\omega_0 y)\right]\ . \tag{C.23}$$

In this expression, we have kept only linear terms in $R(t,x,y)$, since the radiation has a quadratic source in $\hat{D}(t)$. The response of $R(t,x,y)$ to the time-independent term in the right-hand side of (C.23) will be itself time-independent and it will carry no energy. We may therefore consider the time-dependent part as source term for radiation and apply the Green's function method to obtain the following asymptotic expression for $R(t,x,y)$:

$$R = \frac{\hat{D}^2\pi\omega_0^4 q \mathrm{csch}\left(\frac{\pi q}{2}\right)}{2\sqrt{q^4+5q^2+4}}\cos\left[\omega t - \frac{qx}{\sqrt{2}} - \arctan\left(\frac{3q}{q^2-2}\right)\right]\,, \tag{C.24}$$

where

$$\omega = 2\omega_0, \qquad q = \sqrt{2\omega^2 - 4}\,. \tag{C.25}$$

The procedure is completely analogous to the one explained in the previous section.

Now, the averaged radiated power per unit length at infinity in the x-direction can be obtained from the energy-momentum tensor:

$$\frac{\langle \dot{E} \rangle}{L_y} = \langle T_{0x} \rangle = -\frac{\hat{D}^4 \pi^2 \omega_0^9 q^3 \text{csch}^2\left(\frac{\pi q}{2}\right)}{4\sqrt{2}\left(q^4+5q^2+4\right)} \,. \tag{C.26}$$

where L_y denotes the length of the straight domain wall string.

On the other hand, the total energy at quadratic order in $\hat{D}$ for a field configuration of the form (C.21) is the following:

$$E(t) = M_{DW} + \frac{\sqrt{2}}{6}\omega_0^2 L_y \hat{D}^2(t) + \mathcal{O}(\hat{D}^3(t)) \,, \tag{C.27}$$

where $M_{DW} = \sqrt{8/9}L_y$ is the mass of the static domain wall solution. If we assume that all the energy radiated to infinity comes from the zero mode, we obtain the following relation:

$$\frac{dE(t)}{dt} = \langle \dot{E} \rangle \,, \tag{C.28}$$

and therefore,

$$\frac{\sqrt{2}}{3}\omega_0^2 \frac{d}{dt}\hat{D}^2(t) = -\frac{\pi^2 \omega_0^9 q^3 \text{csch}^2\left(\frac{\pi q}{2}\right)}{4\sqrt{2}\left(q^4+5q^2+4\right)}\hat{D}^4(t) \equiv -\alpha(\omega_0)\hat{D}^4(t) \,, \tag{C.29}$$

which can be integrated to give

$$\hat{D}(t) = \frac{1}{\sqrt{\frac{1}{\hat{D}^2(0)} + \frac{3\alpha(\omega_0)}{\sqrt{2}\omega_0^2}t}} \,. \tag{C.30}$$

C.2.2 Radiation from shape mode excitations

Here we follow a similar procedure to that of the previous sections to obtain the radiation emitted by the internal excitations of the domain wall string. Let us consider the following ansatz:

$$\phi(t,x,y) = \phi_K(x) + \hat{A}\cos(\omega_1 t)\,\bar{f}_1(x)\cos(k_1 y) + R(t,x,y) \,, \tag{C.31}$$

where $R(t,x,y)$ corresponds to the radiation modes, $\bar{f}_1(x)$ is the shape mode profile and k_1 is the wave number of the perturbation in the longitudinal direction y. The angular frequency is given by $\omega_1 = \sqrt{3/2 + k_1^2}$. To second order in $\hat{A}$, we obtain the following equation for the radiation:

$$\frac{\partial^2 R}{\partial t^2}-\frac{\partial^2 R}{\partial x^2}-\frac{\partial^2 R}{\partial y^2}+\left(3\phi_k^2-1\right)R=-\frac{3}{4}\phi_k\hat{A}^2\bar{f}_1^2\cos(2\omega_1 t)\cos(2k_1 y)-\frac{3}{4}\phi_k\hat{A}^2\bar{f}_1^2\cos(2\omega_1 t) \tag{C.32}$$

where, following the reasoning of the previous sections, we have omitted time-dependent terms on the right-hand side of the equation. As it stands, the right-hand side suggests the following form of the radiation field:

$$R(t,x,y)=\Re\left[R_1(x)e^{2i\omega_1 t}+R_2(x)\cos(2k_1 y)e^{2i\omega_1 t}\right]\,. \tag{C.33}$$

Now, (C.32) is satisfied for the ansatz (C.33) if the following equations are satisfied simultaneously:

$$-R_1''+\left[3\phi_k^2-1-(2\omega_1)^2\right]R_1 = -\frac{3}{4}\phi_k\hat{A}^2\bar{f}_1^2\,, \tag{C.34}$$

$$-R_2''+\left(3\phi_k^2-7\right)R_2 = -\frac{3}{4}\phi_k\hat{A}^2\bar{f}_1^2\,. \tag{C.35}$$

Once again, the radiation at infinity can be obtained by means of the Green's function method. The result is

$$\begin{aligned}R(t,x,y)=&\frac{3}{16}\sqrt{3}\pi\hat{A}^2\mathrm{csch}\left(\sqrt{2}\pi\right)\cos\left[\sqrt{6}t-2x-\arctan\left(\sqrt{2}\right)\right]\cos(2k_1 y)+\\&+\frac{3\pi\hat{A}^2 q\left(q^2-2\right)\left(q^2+4\right)\mathrm{csch}\left(\frac{\pi q}{2}\right)\cos\left[\omega t-\frac{qx}{\sqrt{2}}+\arctan\left(\frac{3q}{2-q^2}\right)\right]}{128\sqrt{2}\sqrt{q^4+5q^2+4}}\,,\end{aligned} \tag{C.36}$$

where $q=\sqrt{2\omega^2-4}$ and $\omega=2\omega_1$. The averaged radiated power per unit length at infinity in the x-direction can be obtained again from the energy-momentum tensor. Using (C.28), one gets

$$\frac{1}{2}\left(\frac{3}{2}+k_1^2\right)\frac{d}{dt}\hat{A}^2(t)=\beta\left(k_1\right)\hat{A}^4(t)\,, \tag{C.37}$$

with

$$\beta\left(k_1\right)\approx 0.0014+\frac{9\pi^2 q^3\left(q^2-2\right)^2\left(q^2+4\right)^3\mathrm{csch}^2\left(\frac{\pi q}{2}\right)}{65536\sqrt{2}\left(q^4+5q^2+4\right)}\,. \tag{C.38}$$

Finally, integration of (C.37) yields

$$\hat{A}(t)=\frac{1}{\sqrt{\frac{1}{\hat{A}^2(0)}+\frac{4\beta(k_1)}{3}t}}\,. \tag{C.39}$$

C.3 $2+1$ dimensional global vortices

Consider the field configuration (4.24) for the first mode, $s^{(1)}(r)$. Substituting this expression into the equations of motion (4.5), we obtain, at $\mathcal{O}(A_1^2)$,

$$\ddot{\eta}_1 - \eta_1'' - \frac{\eta_1'}{r} + \frac{\eta_1}{r^2} + \frac{1}{2}\left(3f^2 - 1\right)\eta_1 + s^{(1)}\left(\ddot{A}_1 + \omega_1^2 A_1\right) + \frac{3}{2}A_1^2\left(s^{(1)}\right)^2 f = 0\,, \tag{C.40}$$

$$\ddot{\eta}_2 - \eta_2'' - \frac{\eta_2'}{r} + \frac{\eta_2}{r^2} + \frac{1}{2}\left(f^2 - 1\right)\eta_2 = 0\,, \tag{C.41}$$

where we have used (4.7) and (4.13). The equation for $\eta_2(t,r)$ is not sourced by the excitation of the first localized mode, so it corresponds to the usual equation for the scattering modes modified by the presence of the vortex. Since $s^{(1)}(r)$ is orthogonal to $\eta_1(t,r)$, in the sense that the integral of the product of these two functions is zero over the plane, we can multiply equation (C.40) by $s^{(1)}(r)$ to obtain the approximate expression

$$\ddot{A}_1 + \omega_1^2 A_1 + \frac{3\alpha}{2}A_1^2 = 0, \tag{C.42}$$

where

$$\alpha = \int_0^\infty dr\, r\left[s^{(1)}(r)\right]^3 f(r). \tag{C.43}$$

Using this expression for $A_1(t)$ in (C.40), we finally obtain

$$\ddot{\eta}_1 - \eta_1'' - \frac{\eta_1'}{r} + \frac{\eta_1}{r^2} + \frac{1}{2}\left(3f^2 - 1\right)\eta_1 = \frac{3}{2}A_1^2\left[\alpha s^{(1)} - \left(s^{(1)}\right)^2 f\right]. \tag{C.44}$$

Let us now assume that $\eta_1(t,r)$ is of the form

$$\eta_1(t,r) = \Re\left[g(r)e^{-i\omega t}\right]\,, \tag{C.45}$$

and let us take the amplitude of the perturbation to be

$$A_1(t) = \hat{A}_1(t)\cos\left(\omega_1 t\right)\,, \tag{C.46}$$

where $\hat{A}_1(t)$ captures the slow decay of the perturbation due to the radiation. Using the first order solution ($\hat{A}_1 = \text{constant}$) in equation (C.44), one concludes that the frequency of the radiation should be constrained to be $\omega = 2\omega_1$. Substituting (C.45) in (C.44), and using $\omega = 2\omega_1$, we get

$$-g'' - \frac{g'}{r} + \frac{g}{r^2} + \frac{1}{2}\left(3f^2 - 1\right)g - \omega^2 g = \frac{3}{4}\hat{A}_1^2\left[\alpha s^{(1)} - \left(s^{(1)}\right)^2 f\right]. \tag{C.47}$$

Here, as in the case of the kink, we have dismissed the time-independent part of the source term coming from the square of (C.46). We will now solve this equation using the Green's function method. Let $z_1(r)$ and $z_2(r)$ be exact solutions to the homogeneous version of equation (C.47). Then, an exact solution to the inhomogeneous equation is obtained by convoluting the source term on the right-hand side, which we denote as $F(r)$, with the Green's function:

$$g_{\text{sol}}(r) = -z_2(r)\int_0^r \frac{F(r')z_1(r')}{W(r')}dr' - z_1(r)\int_r^\infty \frac{F(r')z_2(r')}{W(r')}dr' \ , \tag{C.48}$$

where $W(r)$ is the Wronskian associated with $z_1(r)$ and $z_2(r)$: $W(r) = z_1(r)\,z_2'(r) - z_1'(r)\,z_2(r)$. Here we have added the subscript "sol" (which stands for "solution") to differenciate this complex function from $g(r)$, which is real[2]. Since equation (C.47) is linear, both the real and imaginary parts of $g_{\text{sol}}(r)$ are solutions.

Since we are only interested in the radiation in this $r \to \infty$ limit, the solution we seek is

$$g(r) \approx \Re\left[-z_2(r\to\infty)\int_0^\infty \frac{F(r')z_1(r')}{W(r')}dr'\right] \ . \tag{C.49}$$

On the one hand, the function $z_1(r)$ can be found by solving the homogeneous version of equation (C.47) with the initial conditions

$$z_1(0) = J_1\left(r\sqrt{1/2+\omega^2}\right)\Big|_{r=0} \ , \quad z_1'(0) = \partial_r J_1\left(r\sqrt{1/2+\omega^2}\right)\Big|_{r=0} \ , \tag{C.50}$$

since the Bessel function of the first kind $J_1\left(r\sqrt{1/2+\omega^2}\right)$ is the solution of equation (C.47) in the limit $r \to 0$. The Bessel function of the second kind $Y_1\left(r\sqrt{1/2+\omega^2}\right)$ is also a solution, but it is not the appropriate one as it is non-zero at the origin (indeed, it diverges).

On the other hand, $z_2(r)$ is determined by solving the homogeneous equation with the asymptotic conditions

$$z_2(r\to\infty) = H_1^{(2)}\left(r\sqrt{\omega^2-1}\right)\Big|_{r\to\infty} \ , \quad z_2'(r\to\infty) = \partial_r H_1^{(2)}\left(r\sqrt{\omega^2-1}\right)\Big|_{r\to\infty} \ , \tag{C.51}$$

where the Hankel function of the second kind $H_1^{(2)}\left(r\sqrt{\omega^2-1}\right) = J_1\left(r\sqrt{\omega^2-1}\right) - iY_1\left(r\sqrt{\omega^2-1}\right)$ is associated to outgoing cylindrical waves.

---

[2] Indeed, equation (C.47) is obtained if one assumes that $g(r)$ is real.

Once $z_1(r)$ and $z_2(r)$ are determined, the Wronskian can be explicitly computed:

$$W(r) = -\frac{0.63 + i\,0.18}{r}. \tag{C.52}$$

With all this information, expression (C.49) yields the following result for the asymptotic form of the radiation field $\eta_1(t,r)$:

$$\eta_1(t,r) = \sqrt{\frac{2I_1 I_1^*}{\pi\sqrt{4\omega_1^2 - 1}}}\frac{\hat{A}_1^2}{\sqrt{r}}\sin\left(2\omega_1 t - r\sqrt{4\omega_1^2 - 1} - \zeta\right), \tag{C.53}$$

where I_1 is the integral appearing in (C.49) and ζ is an irrelevant phase.

The energy flux in the radial direction can now be computed by plugging the result (C.53) in the $0r$ component of the energy-momentum tensor (4.8). Averaging over an oscillation of the bound state, one gets

$$\langle T_{0r}\rangle = -\frac{4\omega_1 I_1 I_1^*}{\pi r}\hat{A}^4\,. \tag{C.54}$$

Therefore, the power radiated to infinity is

$$\dot{E} = \int_0^{2\pi}\langle T_{0r}\rangle\, r\, d\theta = -8\omega_1 I_1 I_1^* \hat{A}^4\,. \tag{C.55}$$

Finally, combining this result with the time derivative of (4.28), we get

$$\frac{d\hat{A}_1^2}{dt} = -\frac{4I_1 I_1^*}{\pi\omega_1}\hat{A}_1^4 \equiv -\Omega_1\hat{A}_1^4\,, \tag{C.56}$$

which yields

$$\hat{A}_1^{-2}(t) = \hat{A}_1^{-2}(0) + \Omega_1 t \tag{C.57}$$

with $\Omega_1 = 0.00218$.

The procedure is completely analogous for the second mode. The result is

$$\hat{A}_2^{-2}(t) = \hat{A}_2^{-2}(0) + \Omega_2 t \tag{C.58}$$

with $\Omega_2 = 2.77 \times 10^{-7}$.

Appendix D

Scalar field ansatz for Nambu-Goto dynamics

In this appendix, we discuss some remarkable features of the ansatz (3.13) used in many of the simulations of chapter 3:

$$\phi(t,x,y) = \phi_k\left(\frac{x-\psi_0(t,y)}{\sqrt{1+\psi_0'^2-\dot{\psi_0}^2}}\right) , \tag{D.1}$$

where ϕ_k is the static domain wall string solution,

$$\phi_k(x) = \tanh\left(\frac{x}{2}\right) . \tag{D.2}$$

Here and henceforth, we use dimensionless variables.

An interesting feature of ansatz (D.1) is that it encompasses several exact solutions to the equation of motion, given in (3.2). We list some of them here:

1. Displaced domain wall.
   A domain wall centered at $x = x_0$ is, obviously, a solution to the equation of motion:

   $$\phi_d\left(x\right) = \phi_k\left(x - x_0\right) . \tag{D.3}$$

   This configuration can be obtained by choosing $\psi_0(t,y) = x_0$ in (D.1).

2. Boosted domain wall.
   In an inertial reference frame moving at speed v, the previous solution transforms into

$$\phi_b\left(t,x\right)=\phi_k\left[\frac{x-(x_0+vt)}{\sqrt{1-v^2}}\right]\ . \tag{D.4}$$

   Needless to say, this is also a solution to the equation of motion. This solution can be obtained by choosing $\psi_0(t,y)=x_0+vt$ in (D.1).

3. Inclined domain wall.
   One can also think of a domain wall which is not aligned with the y axis, but tilted with an angle θ with respect to it. This solution can be easily shown to be

$$\phi_\theta\left(t,x,y\right)=\phi_k\left[(x-x_0)\cos\theta-y\sin\theta\right]=\phi_k\left[\frac{x-(x_0+y\tan\theta)}{\sqrt{1+\tan^2\theta}}\right]\ . \tag{D.5}$$

   Therefore, this can be obtained with $\psi_0(t,y)=x_0+y\tan\theta$.

4. Vachaspati-Vachaspati solution.
   As mentioned in the main text, the field configuration

$$\phi(t,x,y)=\phi_k\left[x-\psi_0(y\pm t)\right] \tag{D.6}$$

   is also an exact solution to the equation of motion. One can inmediately check that this is of the form (D.1) by noticing that ${\psi'_0}^2=\dot\psi_0^2$.

All these examples strongly suggest the ansatz (D.1) could be a good description for a generic motion of the string. If one substitutes this configuration into the action, given in equation (3.47), one finds

$$S=-\mu\int dtdy\sqrt{1+{\psi'_0}^2-\dot\psi_0^2}\left[1-\frac{\pi^2-6}{12}\frac{\left(\psi'_0\dot\psi'_0-\dot\psi_0\ddot\psi_0\right)^2-\left(\psi'_0\psi''_0-\dot\psi_0\dot\psi'_0\right)^2}{\left(1+{\psi'_0}^2-{\dot\psi_0}^2\right)^2}\right]\ , \tag{D.7}$$

where $\mu=2\sqrt{2}/3$ is the dimensionless energy per unit length of the domain wall string. The first term is exactly the Nambu-Goto action in the static gauge (see equation (3.25)). Therefore, if the field configuration is well approximated by (D.1), the domain wall should behave as a Nambu-Goto string as long as the second term in (D.7), containing second derivatives of ψ_0, is irrelevant.

Finally, let us note that using this ansatz for the kink solution in $1+1$ dimensions yields the action for a point-like relativistic particle with the mass of the kink. This observation could be interesting in models that try to describe the motion of the kink with the use of the collective coordinate language.

Appendix E

Nambu-Goto reconstruction algorithms

In this appendix, we explain in detail how to reconstruct the Nambu-Goto trajectories of the local string loops of chapter 6 and the domain wall strings discussed in chapter 4.

E.1 Nambu-Goto reconstruction of field theory loops

The strarting point for the Nambu-Goto reconstruction is the data coming from the lattice field theory simulation. We need two files containing the spatial coordinates of the loop at $t = 0$ and $t = \Delta t$:

- Loop A: list of N vectors $\vec{X}_n^0$, with $n = 0, 1, 2, ..., N-1$, corresponding to the positions of every point of the loop at $t = 0$.
- Loop B: list of M vectors $\vec{\mathcal{X}}_m^0$, with $m = 0, 1, 2, ..., M-1$, corresponding to the positions of every point on the loop at $t = \Delta t$.

The Nambu-Goto reconstruction algorithm consists of the following steps:

1. Smoothing:
   As a consequence of the discretization, the data coming from the field theory simulation may present artificial structure at scales of the order of the lattice spacing, so our first task is to smooth out loops A and B. This can be done with a Gaussian window function with some width w given by a few lattice spacings[1]. For loop A, we replace

---

[1] Since the string thickness is somewhat larger than the lattice spacing, one should not expect to know the position of the center of the string with a precision much larger than this width w.

each $\vec{X}_n^0$ with a new vector $\vec{X}_n$ given by the weighted sum

$$\vec{X}_n = \frac{\sum_{i=0}^{N-1} \vec{X}_i^{\,0} c_i}{\sum_{i=0}^{N-1} c_i} \,, \tag{E.1}$$

where

$$c_i = \begin{cases} e^{-\frac{|\vec{X}_i^{\,0} - \vec{X}_n^{\,0}|^2}{2w^2}} & \text{if } |\vec{X}_i^{\,0} - \vec{X}_n^{\,0}| < 5w \,, \\ 0 & \text{otherwise.} \end{cases} \tag{E.2}$$

The replacements for the M vectors $\vec{\mathcal{X}}_m^0$ defining loop B are analogous.

The result of such a smoothing is illustrated in figure E.1. From now on, we will refer to loop A and loop B after smoothing as loop 1 and loop 2, respectively.

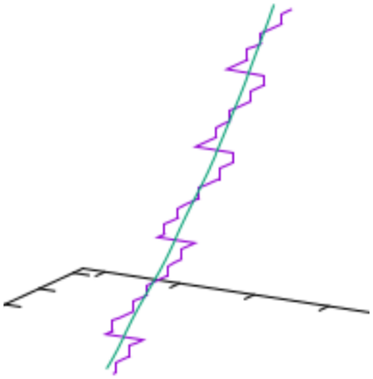

Figure E.1: A string segment before (purple) and after (green) smoothing.

2. Tangent vectors:
   The next step is to find the N vectors $\vec{X}_n^{\,t}$ which are tangent to loop 1 at each point n. For $n = 0$ to $n = N-1$, we compute

$$\vec{X}_n^{\,t} = \vec{X}_{n+1} - \vec{X}_n \,, \tag{E.3}$$

   where $\vec{X}_N = \vec{X}_0$. We will also need the unit tangent vectors:

$$\hat{\vec{X}}_n^{\,t} = \frac{\vec{X}_{n+1} - \vec{X}_n}{|\vec{X}_{n+1} - \vec{X}_n|} \,. \tag{E.4}$$

3. Nambu-Goto velocity and Lorentz factor:
   Now we find the velocities of each point of loop 1. For each point $\vec{X}_n$ on this loop, we

assume that its velocity is perpendicular to the tangent vector at that point, $\vec{X}_n^{\,t}$. This assumption relies on the Nambu-Goto approximation via equation (1.23). Therefore, in time Δt, this point has moved to another point which is the intersection of loop 2 with the plane perpendicular to $\vec{X}_n^{\,t}$. Let us call this plane Π_n. Note that, since we are dealing with closed strings, there will necessarily be more than one intersection point. Obviously, we will have to look for the one which is the closest to $\vec{X}_n$.

For point $\vec{X}_n$ of loop 1, let $\vec{\mathcal{X}}_q$ and $\vec{\mathcal{X}}_{q+1}$ be the two points of loop 2 which are closer to Π_n and are not more than a few lattice spacings away from $\vec{X}_n$. We will call this distance d. The point we are looking for, $\vec{\mathcal{X}}_n^*$, is the intersection of Π_n with the line that contains both $\vec{\mathcal{X}}_q$ and $\vec{\mathcal{X}}_{q+1}$.

Therefore, we first need to find $\vec{\mathcal{X}}_q$ and $\vec{\mathcal{X}}_{q+1}$. We can do this by calculating the distances D_m from each point $\vec{\mathcal{X}}_m$ of loop 2 satisfying $|\vec{X}_n - \vec{\mathcal{X}}_m| < d$ to Π_n. This distance is simply given by the scalar product

$$D_m = (\vec{X}_n - \vec{\mathcal{X}}_m) \cdot \hat{\vec{X}}_n^{\,t} \, . \tag{E.5}$$

Then, we can identify $\vec{\mathcal{X}}_q$ and $\vec{\mathcal{X}}_{q+1}$ as the two points with the smallest values of (E.5). However, one has to make sure that the two points found this way lie at opposite sides of Π_n.

Now we can find the intersection point $\vec{\mathcal{X}}_n^*$. First, let us set the notation for this computation. On the one hand, we will put a tilde on the components of the vectors correponding to points of loop 2: $\vec{\mathcal{X}}_n^* = (\tilde{x}_n^*, \tilde{y}_n^*, \tilde{z}_n^*)$, $\vec{\mathcal{X}}_m = (\tilde{x}_m, \tilde{y}_m, \tilde{z}_m)$. On the other hand, components without tilde will refer to points of loop 1: $\vec{X}_n = (x_n, y_n, z_n)$. Finally, the components of the tangent vector will be $\vec{X}_n^{\,t} = (x_n^t, y_n^t, z_n^t)$.

Since the intersection point $\vec{\mathcal{X}}_n^*$ is contained in the line that joins $\vec{\mathcal{X}}_q$ and $\vec{\mathcal{X}}_{q+1}$, it has to satisfy

$$\vec{\mathcal{X}}_n^* = \vec{\mathcal{X}}_q + s\left(\vec{\mathcal{X}}_{q+1} - \vec{\mathcal{X}}_q\right) \tag{E.6}$$

for some specific s. Written in components, this condition reads

$$\begin{cases} \tilde{x}_n^* = \tilde{x}_q + s\left(\tilde{x}_{q+1} - \tilde{x}_q\right) \, , \\ \tilde{y}_n^* = \tilde{y}_q + s\left(\tilde{y}_{q+1} - \tilde{y}_q\right) \, , \\ \tilde{z}_n^* = \tilde{z}_q + s\left(\tilde{z}_{q+1} - \tilde{z}_q\right) \, . \end{cases} \tag{E.7}$$

Furthermore, $\vec{\mathcal{X}}_n^*$ is contained in Π_n, so

$$x_n^t \tilde{x}_n^* + y_n^t \tilde{y}_n^* + z_n^t \tilde{z}_n^* = C\,, \tag{E.8}$$

where $C = x_n^t x_n + y_n^t y_n + z_n^t z_n$.

One can find s by substituting (E.7) in (E.8), and once this is done, $\tilde{x}_n^*$, $\tilde{y}_n^*$ and $\tilde{z}_n^*$ are fully determined by (E.7).

Now we can finally compute the Nambu-Goto velocity as

$$\dot{\vec{X}}_n = \frac{\vec{\mathcal{X}}_n^* - \vec{X}_n}{\Delta t}\,, \tag{E.9}$$

and the Lorentz factor as

$$\Gamma_n = \frac{1}{\sqrt{1 - |\dot{\vec{X}}_n|^2}}\,. \tag{E.10}$$

4. Redefinition of the tangent vectors:
   Now, we simply redefine the tangent vectors according to the Nambu-Goto transverse gauge:

   $$\vec{X}_n' = \frac{\vec{X}_{n+1} - \vec{X}_n}{\Delta\sigma_n} = \frac{\hat{\vec{X}}_n^{\,t}}{\Gamma_n}\,. \tag{E.11}$$

   Here, we have used equation (1.27), from which it follows inmediately that

   $$\Delta\sigma_n = \Gamma_n |\vec{X}_n^{\,t}|\,. \tag{E.12}$$

5. Left and right movers:
   With the Nambu-Goto velocities (E.9) and the redefined tangent vectors (E.11), we can find

   $$\vec{a}\,'(\sigma_n) = \vec{X}_n' - \dot{\vec{X}}_n\,, \tag{E.13}$$

   $$\vec{b}\,'(\sigma_n) = \vec{X}_n' + \dot{\vec{X}}_n\,, \tag{E.14}$$

in agreement with (1.31) and (1.32). As we know the amount of sigma parameter $\Delta\sigma_n$ in each string segment, we can write

$$\begin{aligned}
&\vec{a}\,(\sigma_1) = \vec{a}\,(0) + \Delta\sigma_0\vec{a}\,'\,(0)\ ,\\
&\vec{a}\,(\sigma_2) = \vec{a}\,(\sigma_1) + \Delta\sigma_1\vec{a}\,'\,(\sigma_1) = \vec{a}\,(0) + \Delta\sigma_0\vec{a}\,'\,(0) + \Delta\sigma_1\vec{a}\,'\,(\sigma_1)\ ,\\
&\vec{a}\,(\sigma_3) = \vec{a}\,(\sigma_2) + \Delta\sigma_2\vec{a}\,'\,(\sigma_2) = \vec{a}\,(0) + \Delta\sigma_0\vec{a}\,'\,(0) + \Delta\sigma_1\vec{a}\,'\,(\sigma_1) + \Delta\sigma_2\vec{a}\,'\,(\sigma_2)\ ,\\
&\qquad .\\
&\qquad .\\
&\qquad .\\
&\vec{a}\,(\sigma_{N-1}) = \vec{a}\,(\sigma_{N-2}) + \Delta\sigma_{N-2}\vec{a}\,'\,(\sigma_{N-2}) = \vec{a}\,(0) + \sum_{i=0}^{N-2}\Delta\sigma_i\vec{a}\,'\,(\sigma_i)\ ,
\end{aligned} \tag{E.15}$$

and analogous equations for $\vec{b}\,(\sigma_n)$. Therefore, all the vectors $\vec{a}\,(\sigma_n)$ and $\vec{b}\,(\sigma_n)$ can be found once $\vec{a}\,(0)$ and $\vec{b}\,(0)$ are specified. The position vector of point $n = 0$ at $t = 0$ is given by

$$\vec{X}_0 = \frac{1}{2}\left[\vec{a}\,(0) + \vec{b}\,(0)\right]\ , \tag{E.16}$$

so we may choose any pair of vectors $\vec{a}\,(0)$, $\vec{b}\,(0)$ that satisfy this relation. For instance, we can set $\vec{a}\,(0) = \vec{b}\,(0) = \vec{X}_0$.

We can also compute $\vec{a}\,(\sigma_N = L)$ and $\vec{b}\,(\sigma_N = L)$, where L is the invariant length of the loop, as

$$\vec{a}\,(L) = \vec{a}\,(\sigma_{N-1}) + \Delta\sigma_{N-1}\vec{a}\,'\,(\sigma_{N-1}) = \vec{a}\,(0) + \sum_{i=0}^{N-1}\Delta\sigma_i\vec{a}\,'\,(\sigma_i)\ , \tag{E.17}$$

where we have used the last equation in (E.16). Now we have the functions $\vec{a}\,(\sigma_n)$ and $\vec{b}\,(\sigma_n)$ for $\sigma_n \in [0, L]$.

Note that $\vec{a}\,(L)$ is not necessarily equal to $\vec{a}\,(0)$. The condition $\vec{X}_N = \vec{X}_0$ implies that

$$\sum_{i=0}^{N-1}\Delta\sigma_i\vec{X}_i' = \sum_{i=0}^{N-1}\vec{X}_i^{\,t} = \vec{0}\,. \tag{E.18}$$

Therefore, plugging (E.13) in equation (E.17) yields

$$\vec{a}\,(L) = \vec{a}\,(0) - \vec{\Delta}\,, \tag{E.19}$$

where we have defined

$$\vec{\Delta} = \sum_{i=0}^{N-1} \Delta\sigma_i \dot{\vec{X}}_i \,. \tag{E.20}$$

Since $\vec{\Delta} \neq \vec{0}$ in general, $\vec{a}\,(L) \neq \vec{a}\,(0)$. Similar arguments apply for $\vec{b}$. In this case, one finds

$$\vec{b}\,(L) = \vec{b}\,(0) + \vec{\Delta}\,. \tag{E.21}$$

6. Nambu-Goto trajectory:
The position vectors at any time t are given by (1.29):

$$\vec{X}_n\,(t) = \frac{1}{2}\left[\vec{a}\,(\sigma_n - t) + \vec{b}\,(\sigma_n + t)\right] \,. \tag{E.22}$$

The terms on the right-hand side are known as long as the arguments $\sigma_n - t$ and $\sigma_n + t$ are in the interval $[0, L]$, but what if this is not the case? For instance, for the point $n = 0$, it is clear that $\sigma_n - t$ will be out of that interval even at the very first time step. In the following, we explain in detail how to find the left and right movers at any time.

Firstly, note that equations (E.19) and (E.21) can be extended to

$$\vec{a}\,(\sigma_n - t) = \vec{a}\,(\sigma_n - t + L) + \vec{\Delta} \tag{E.23}$$

and

$$\vec{b}\,(\sigma_n + t) = \vec{b}\,(\sigma_n + t - L) + \vec{\Delta}\,. \tag{E.24}$$

Consider again point $n = 0$ at time $t = \Delta t$. On the one hand, we already know $\vec{b}\,(0 + \Delta t)$ as $0 + \Delta t \in [0, L]$. On the other hand, (E.23) tells us that $\vec{a}\,(0 - \Delta t) = \vec{a}\,(0 - \Delta t + L) + \vec{\Delta}$, and this is known because $0 - \Delta t + L \in [0, L]$.

Note, however, that the direct application of (E.23) and (E.24) is useless if $\sigma_n - t + L$ or $\sigma_n + t - L$ are not in the interval $[0, L]$. For example, if we consider once again point $n = 0$, at time $t = L + \Delta t$, we will have $0 - t + L = -\Delta t \notin [0, L]$, so $\vec{a}\,(0 - t + L)$ is still unknown. The obvious solution to this issue is the reiterated application of (E.23): $\vec{a}\,(0 - L - \Delta t) = \vec{a}\,(-\Delta t) + \vec{\Delta} = \vec{a}\,(-\Delta t + L) + 2\vec{\Delta}$. Similar observations can be easily made for $\vec{b}\,(\sigma_n + t)$.

All these considerations lead us to (E.23) and (E.24) rewritten in the more convenient form

$$\vec{a}\,(\sigma_n - t) = \vec{a}\,(\sigma_n - t + pL) + p\vec{\Delta}\,, \tag{E.25}$$

$$\vec{b}\,(\sigma_n + t) = \vec{b}\,(\sigma_n + t - qL) + q\vec{\Delta}\,, \tag{E.26}$$

where p and q are the unique natural numbers for which $\sigma_n - t + pL \in [0, L]$ and $\sigma_n + t - qL \in [0, L]$.

Putting it in words, in order to find $\vec{a}\,(\sigma_n - t)$ and $\vec{b}\,(\sigma_n + t)$, we just have to return the arguments to the interval $[0, L]$, and then add a correction term proportional to $\vec{\Delta}$ (which is given by (E.20), and it is $\vec{0}$ in the center of mass frame).

Finally, let us point out that, in general, the right-hand sides of (E.25) and (E.26) will not correspond to one of the $N + 1$ values we have for $\vec{a}$ and $\vec{b}$. Imagine that at some time t_* we are evaluating $\vec{a}\,(\sigma_4 - t_*)$ and that $\sigma_4 - t_* + pL \in (\sigma_{18}, \sigma_{19})$, for instance. In order to find the first term on the right hand side of (E.25), that is, $\vec{a}\,(\sigma_4 - t_* + pL)$, we simply interpolate linearly: $\vec{a}\,(\sigma_4 - t_* + pL) \approx \vec{a}\,(\sigma_{18}) + (\sigma_{19} - \sigma_{18})\,\vec{a}\,'\,(\sigma_{18})$.

E.2 Nambu-Goto reconstruction of field theory domain wall strings

Now we are interested in reconstructing the Nambu-Goto trajectory of a string with periodic boundary conditions in its longitudinal direction, which we choose to be the y direction, with finite extent l. In this case, the end points of the string (at $y = \pm l/2$) are identified with each other, that is, the value of the scalar field is forced to be the same at these two points. Any perturbation exiting at $y = l/2$ will automatically reenter the box at $y = -l/2$, and vice versa.

The algorithm we have described above is only valid for loops. In particular, a key point in the derivation of equations (E.25) and (E.26), needed in the last step of the Nambu-Goto reconstruction, was the condition $\vec{X}\,(\sigma_n \pm L, t) = \vec{X}\,(\sigma_n, t)$. It is clear that some modification has to be made for the new problem at hand. Consider, for instance, point $n = 0$ at $y = -l/2$, with $\sigma = 0$, and point $n = N$ at $y = l/2$, with $\sigma = L$. The position of the latter is $\vec{X}\,(L, t) = \vec{X}\,(0, t) + l\vec{j}$, where $\vec{j}$ is the unit vector in the y direction. If we impose the conditions $\vec{X}\,(\sigma_n \pm L, t) = \vec{X}\,(\sigma_n, t) \pm l\vec{j}$, the arguments used in the previous subsection yield

$$\vec{a}\,(\sigma_n - t) = \vec{a}\,(\sigma_n - t + pL) + p\vec{\Delta} - pl\vec{j}\,, \tag{E.27}$$

$$\vec{b}\left(\sigma_n + t\right) = \vec{b}\left(\sigma_n + t - qL\right) + q\vec{\Delta} + ql\vec{j}\,. \tag{E.28}$$

As before, p and q are the natural numbers for which $\sigma_n - t + pL \in [0, L]$ and $\sigma_n + t - qL \in [0, L]$. However, given the conditions we have just imposed, nothing prevents the end points of the string from moving; they are only constrained to be a distance l away from each other. This means that the points with $\sigma = 0$ and $\sigma = L$ might not always be located at $y = \pm l/2$. Indeed, if some wiggle reaches the y boundaries, the tangent vector at the end points of the string will not be parallel to the y axis, implying that the velocity of these points will have a nonzero component in this direction (recall that the velocity of each point on a Nambu-Goto string is perpendicular to the tangent vector at that point). If the y coordinate of some point becomes bigger than $l/2$ or smaller than $-l/2$, we simply subtract or add l so that the perturbation reappears at the other end of the string. Therefore, the coordinates of point n at time t are given by

$$x\left(\sigma_n, t\right) = \frac{1}{2}\left[a_x\left(\sigma_n - t\right) + b_x\left(\sigma_n + t\right)\right], \tag{E.29}$$

$$y\left(\sigma_n, t\right) = \begin{cases} \frac{1}{2}\left[a_y\left(\sigma_n - t\right) + b_y\left(\sigma_n + t\right)\right] + l & \text{if } \dfrac{1}{2}\left[a_y\left(\sigma_n - t\right) + b_y\left(\sigma_n + t\right)\right] < -l/2\,, \\ \frac{1}{2}\left[a_y\left(\sigma_n - t\right) + b_y\left(\sigma_n + t\right)\right] & \text{if } -l/2 \leq \dfrac{1}{2}\left[a_y\left(\sigma_n - t\right) + b_y\left(\sigma_n + t\right)\right] \leq l/2\,, \\ \frac{1}{2}\left[a_y\left(\sigma_n - t\right) + b_y\left(\sigma_n + t\right)\right] - l & \text{if } \dfrac{1}{2}\left[a_y\left(\sigma_n - t\right) + b_y\left(\sigma_n + t\right)\right] > l/2\,, \end{cases} \tag{E.30}$$

where $a_{x,y}$ and $b_{x,y}$ are the x, y components of the left and right movers, as given in equations (E.27) and (E.28).

References

[1] R. Rajaraman. *Solitons and Instantons. An introduction to solitons and instantons in Quantum Field Theory,*. North-Holland Publishing Company, 1982.

[2] N. D. Mermin. The topological theory of defects in ordered media. *Rev. Mod. Phys.*, 51:591–648, Jul 1979.

[3] Alfred Actor. Classical solutions of SU(2) yang—mills theories. *Rev. Mod. Phys.*, 51:461–525, Jul 1979.

[4] Sidney Coleman. *Aspects of Symmetry: Selected Erice Lectures.* Cambridge University Press, 1985.

[5] J Preskill. Magnetic monopoles. *Annual Review of Nuclear and Particle Science*, 34(1):461–530, 1984.

[6] T.W.B. Kibble. Topology of Cosmic Domains and Strings. *J. Phys. A*, 9:1387–1398, 1976.

[7] Eibun Senaha. Symmetry restoration and breaking at finite temperature: An introductory review. *Symmetry*, 12(5), 2020.

[8] Ya. B. Zeldovich, I. Yu. Kobzarev, and L. B. Okun. Cosmological Consequences of the Spontaneous Breakdown of Discrete Symmetry. *Zh. Eksp. Teor. Fiz.*, 67:3–11, 1974. [Sov. Phys. JETP40,1(1974)].

[9] GINZBURG V. L. Some remarks on phase transitions of the second kind and the microscopic theory of ferroelectric materials. *Soviet Phys. Solid State*, 2:1824–1834, 1961.

[10] W. H. Zurek. Cosmic strings in laboratory superfluids and the topological remnants of other phase transitions. *Acta Phys. Polon. B*, 24:1301–1311, 1993.

[11] W. H. Zurek. Cosmological experiments in condensed matter systems. *Phys. Rept.*, 276:177–221, 1996.

[12] Pablo Laguna and Wojciech Hubert Zurek. Density of kinks after a quench: When symmetry breaks, how big are the pieces? *Phys. Rev. Lett.*, 78:2519–2522, 1997.

[13] John Preskill. Cosmological Production of Superheavy Magnetic Monopoles. *Phys. Rev. Lett.*, 43:1365, 1979.

[14] Ya. B. Zeldovich. Cosmological fluctuations produced near a singularity. *Monthly Notices of the Royal Astronomical Society*, 192(4):663–667, 10 1980.

[15] Alexander Vilenkin. Cosmological density fluctuations produced by vacuum strings. *Phys. Rev. Lett.*, 46:1169–1172, Apr 1981.

[16] Alexander Vilenkin. Cosmic strings. *Phys. Rev. D*, 24:2082–2089, Oct 1981.

[17] Alexander Vilenkin and Qaisar Shafi. Density fluctuations from strings and galaxy formation. *Phys. Rev. Lett.*, 51:1716–1719, Oct 1983.

[18] P. de Bernardis et al. A Flat universe from high resolution maps of the cosmic microwave background radiation. *Nature*, 404:955–959, 2000.

[19] S. Hanany et al. MAXIMA-1: A Measurement of the cosmic microwave background anisotropy on angular scales of 10 arcminutes to 5 degrees. *Astrophys. J. Lett.*, 545:L5, 2000.

[20] Levon Pogosian, S. H. Henry Tye, Ira Wasserman, and Mark Wyman. Cosmic Strings as the Source of Small-Scale Microwave Background Anisotropy. *JCAP*, 02:013, 2009.

[21] Neil Bevis, Mark Hindmarsh, Martin Kunz, and Jon Urrestilla. Fitting CMB data with cosmic strings and inflation. *Phys. Rev. Lett.*, 100:021301, 2008.

[22] C. L. Bennett et al. First year Wilkinson Microwave Anisotropy Probe (WMAP) observations: Preliminary maps and basic results. *Astrophys. J. Suppl.*, 148:1–27, 2003.

[23] Qaisar Shafi and Alexander Vilenkin. Inflation with SU(5). *Phys. Rev. Lett.*, 52:691–694, 1984.

[24] Qaisar Shafi and Alexander Vilenkin. Spontaneously broken global symmetries and cosmology. *Phys. Rev. D*, 29:1870–1871, Apr 1984.

[25] Junichi Yokoyama. Natural Way Out of the Conflict Between Cosmic Strings and Inflation. *Phys. Lett. B*, 212:273–276, 1988.

[26] Jun'ichi Yokoyama. Inflation can save cosmic strings. *Phys. Rev. Lett.*, 63:712–715, Aug 1989.

[27] Ethan T. Vishniac, Keith A. Olive, and David Seckel. Cosmic Strings and Inflation. *Nucl. Phys. B*, 289:717–734, 1987.

[28] Andrei D. Linde and David H. Lyth. Axionic domain wall production during inflation. *Phys. Lett. B*, 246:353–358, 1990.

[29] Hardy M. Hodges and Joel R. Primack. Strings, texture, and inflation. *Phys. Rev. D*, 43:3155–3172, May 1991.

[30] Rama Basu, Alan H. Guth, and Alexander Vilenkin. Quantum creation of topological defects during inflation. *Phys. Rev. D*, 44:340–351, Jul 1991.

[31] G. S. F. Guedes, P. P. Avelino, and L. Sousa. Signature of inflation in the stochastic gravitational wave background generated by cosmic string networks. *Phys. Rev. D*, 98(12):123505, 2018.

[32] Yanou Cui, Marek Lewicki, and David E. Morrissey. Gravitational wave bursts as harbingers of cosmic strings diluted by inflation. *Phys. Rev. Lett.*, 125:211302, Nov 2020.

[33] R. D. Peccei and Helen R. Quinn. CP conservation in the presence of pseudoparticles. *Phys. Rev. Lett.*, 38:1440–1443, Jun 1977.

[34] Peter W. Higgs. Broken symmetries, massless particles and gauge fields. *Phys. Lett.*, 12:132–133, 1964.

[35] Holger Bech Nielsen and P. Olesen. Vortex Line Models for Dual Strings. *Nucl. Phys. B*, 61:45–61, 1973.

[36] Yoichiro Nambu. Lectures at the copenhagen symposium. *Symmetries and Quark Models, ed. R. Chand (Gordon and Breach, 1970)*, 269, 1970.

[37] Tetsuo Gotō. Relativistic Quantum Mechanics of One-Dimensional Mechanical Continuum and Subsidiary Condition of Dual Resonance Model. *Progress of Theoretical Physics*, 46(5):1560–1569, 11 1971.

[38] A. Vilenkin and E.P. S. Shellard. *Cosmic Strings and Other Topological Defects.* Cambridge University Press, 7 2000.

[39] Michael Kalb and Pierre Ramond. Classical direct interstring action. *Phys. Rev. D*, 9:2273–2284, 1974.

[40] T. W. B. Kibble and Neil Turok. Selfintersection of Cosmic Strings. *Phys. Lett. B*, 116:141–143, 1982.

[41] Pijushpani Bhattacharjee and Gunter Sigl. Origin and propagation of extremely high-energy cosmic rays. *Phys. Rept.*, 327:109–247, 2000.

[42] Ken D. Olum and J. J. Blanco-Pillado. Field theory simulation of abelian-higgs cosmic string cusps. *Phys. Rev. D*, 60:023503, May 1999.

[43] Andrew J. Long, Jeffrey M. Hyde, and Tanmay Vachaspati. Cosmic Strings in Hidden Sectors: 1. Radiation of Standard Model Particles. *JCAP*, 09:030, 2014.

[44] Pierre Auclair, Danièle A. Steer, and Tanmay Vachaspati. Particle emission and gravitational radiation from cosmic strings: observational constraints. *Phys. Rev. D*, 101(8):083511, 2020.

[45] Tammay Vachaspati and Alexander Vilenkin. Formation and evolution of cosmic strings. *Phys. Rev. D*, 30:2036–2045, Nov 1984.

[46] T.W.B. Kibble and Neil Turok. Self-intersection of cosmic strings. *Physics Letters B*, 116(2):141–143, 1982.

[47] Neil Turok. Grand unified strings and galaxy formation. *Nuclear Physics B*, 242(2):520–541, 1984.

[48] T.W.B. Kibble. Evolution of a system of cosmic strings. *Nuclear Physics B*, 252:227–244, 1985.

[49] A. Albrecht and N. Turok. Evolution of cosmic strings. *Phys. Rev. Lett.*, 54:1868–1871, Apr 1985.

[50] Edward W. Kolb and Michael S. Turner. *The Early Universe*, volume 69. 1990.

[51] Graham Vincent, Nuno D. Antunes, and Mark Hindmarsh. Numerical simulations of string networks in the abelian-higgs model. *Phys. Rev. Lett.*, 80:2277–2280, Mar 1998.

[52] Masahide Yamaguchi, M. Kawasaki, and Jun'ichi Yokoyama. Evolution of axionic strings and spectrum of axions radiated from them. *Phys. Rev. Lett.*, 82:4578–4581, 1999.

[53] Masahide Yamaguchi and Jun'ichi Yokoyama. Quantitative evolution of global strings from the Lagrangian view point. *Phys. Rev. D*, 67:103514, 2003.

[54] William H. Press, Barbara S. Ryden, and David N. Spergel. Dynamical Evolution of Domain Walls in an Expanding Universe. *Astrophys. J.*, 347:590–604, 1989.

[55] J. C. R. E. Oliveira, C. J. A. P. Martins, and P. P. Avelino. The Cosmological evolution of domain wall networks. *Phys. Rev. D*, 71:083509, 2005.

[56] A. M. M. Leite and C. J. A. P. Martins. Scaling Properties of Domain Wall Networks. *Phys. Rev. D*, 84:103523, 2011.

[57] E.P.S. Shellard. Cosmic string interactions. *Nuclear Physics B*, 283:624–656, 1987.

[58] Marco Gorghetto, Edward Hardy, and Giovanni Villadoro. Axions from Strings: the Attractive Solution. *JHEP*, 07:151, 2018.

[59] Masahiro Kawasaki, Toyokazu Sekiguchi, Masahide Yamaguchi, and Jun'ichi Yokoyama. Long-term dynamics of cosmological axion strings. *PTEP*, 2018(9):091E01, 2018.

[60] Alejandro Vaquero, Javier Redondo, and Julia Stadler. Early seeds of axion miniclusters. 2018. [JCAP1904,012(2019)].

[61] C. J. A. P. Martins. Scaling properties of cosmological axion strings. *Phys. Lett. B*, 788:147–151, 2019.

[62] Mark Hindmarsh, Joanes Lizarraga, Asier Lopez-Eiguren, and Jon Urrestilla. Scaling Density of Axion Strings. *Phys. Rev. Lett.*, 124(2):021301, 2020.

[63] Mark Hindmarsh, Joanes Lizarraga, Asier Lopez-Eiguren, and Jon Urrestilla. Approach to scaling in axion string networks. *Phys. Rev. D*, 103(10):103534, 2021.

[64] Marco Gorghetto, Edward Hardy, and Giovanni Villadoro. More Axions from Strings. *SciPost Phys.*, 10:050, 2021.

[65] David P. Bennett and François R. Bouchet. Evidence for a scaling solution in cosmic-string evolution. *Phys. Rev. Lett.*, 60:257–260, Jan 1988.

[66] David P. Bennett and François R. Bouchet. Cosmic-string evolution. *Phys. Rev. Lett.*, 63:2776–2779, Dec 1989.

[67] Andreas Albrecht and Neil Turok. Evolution of cosmic string networks. *Phys. Rev. D*, 40:973–1001, Aug 1989.

[68] B. Allen and E. P. S. Shellard. Cosmic-string evolution: A numerical simulation. *Phys. Rev. Lett.*, 64:119–122, Jan 1990.

[69] Maria Sakellariadou and Alexander Vilenkin. Cosmic-string evolution in flat spacetime. *Phys. Rev. D*, 42:349–353, Jul 1990.

[70] Daren Austin, E. J. Copeland, and T. W. B. Kibble. Evolution of cosmic string configurations. *Phys. Rev. D*, 48:5594–5627, Dec 1993.

[71] Graham R. Vincent, Mark Hindmarsh, and Mairi Sakellariadou. Scaling and small-scale structure in cosmic string networks. *Phys. Rev. D*, 56:637–646, Jul 1997.

[72] J. N. Moore and E. P. S. Shellard. On the evolution of Abelian Higgs string networks. 8 1998.

[73] Ken D. Olum and J. J. Blanco-Pillado. Radiation from cosmic string standing waves. *Phys. Rev. Lett.*, 84:4288–4291, May 2000.

[74] Vitaly Vanchurin, Ken Olum, and Alexander Vilenkin. Cosmic string scaling in flat space. *Phys. Rev. D*, 72:063514, 2005.

[75] Ken D. Olum and Vitaly Vanchurin. Cosmic string loops in the expanding Universe. *Phys. Rev. D*, 75:063521, 2007.

[76] Jose J. Blanco-Pillado, Ken D. Olum, and Benjamin Shlaer. Large parallel cosmic string simulations: New results on loop production. *Phys. Rev. D*, 83:083514, 2011.

[77] Mark Hindmarsh, Stephanie Stuckey, and Neil Bevis. Abelian higgs cosmic strings: Small-scale structure and loops. *Phys. Rev. D*, 79:123504, Jun 2009.

[78] Pierre Auclair et al. Probing the gravitational wave background from cosmic strings with LISA. *JCAP*, 04:034, 2020.

[79] B. P. Abbott et al. Constraints on cosmic strings using data from the first Advanced LIGO observing run. *Phys. Rev. D*, 97(10):102002, 2018.

[80] Paul D. Lasky et al. Gravitational-wave cosmology across 29 decades in frequency. *Phys. Rev. X*, 6(1):011035, 2016.

[81] Jose J. Blanco-Pillado, Ken D. Olum, and Xavier Siemens. New limits on cosmic strings from gravitational wave observation. *Phys. Lett. B*, 778:392–396, 2018.

[82] Daiju Matsunami, Levon Pogosian, Ayush Saurabh, and Tanmay Vachaspati. Decay of Cosmic String Loops Due to Particle Radiation. *Phys. Rev. Lett.*, 122(20):201301, 2019.

[83] Mark Hindmarsh, Joanes Lizarraga, Ander Urio, and Jon Urrestilla. Loop decay in Abelian-Higgs string networks. *Phys. Rev. D*, 104(4):043519, 2021.

[84] Ayush Saurabh, Tanmay Vachaspati, and Levon Pogosian. Decay of Cosmic Global String Loops. *Phys. Rev. D*, 101(8):083522, 2020.

[85] Ken D. Olum and Jose J. Blanco-Pillado. Field theory simulation of Abelian Higgs cosmic string cusps. *Phys. Rev. D*, 60:023503, 1999.

[86] Ken D. Olum and Jose J. Blanco-Pillado. Radiation from cosmic string standing waves. *Phys. Rev. Lett.*, 84:4288–4291, 2000.

[87] Mark Hindmarsh, Joanes Lizarraga, Jon Urrestilla, David Daverio, and Martin Kunz. Scaling from gauge and scalar radiation in Abelian Higgs string networks. *Phys. Rev. D*, 96(2):023525, 2017.

[88] A. R. Bishop, J. A. Krumhansl, and S. E. Trullinger. Solitons in condensed matter: A paradigm. *Physica D Nonlinear Phenomena*, 1(1):1–44, April 1980.

[89] T.H.R. Skyrme. A Nonlinear field theory. *Proc. Roy. Soc. Lond. A*, A260:127–138, 1961.

[90] J. Polchinski. *String theory*. Cambridge Monographs on Mathematical Physics. Cambridge University Press, 12 2007.

[91] Gerard 't Hooft. Magnetic Monopoles in Unified Gauge Theories. *Nucl. Phys. B*, 79:276–284, 1974.

[92] Alexander M. Polyakov. Particle Spectrum in the Quantum Field Theory. *JETP Lett.*, 20:194–195, 1974.

[93] Alexander Evgenyevich Kudryavtsev. About Soliton Similar Solutions for Higgs Scalar Field. *Pisma Zh. Eksp. Teor. Fiz.*, 22:178–181, 1975.

[94] I.L. Bogolyubsky and V.G. Makhankov. On the Pulsed Soliton Lifetime in Two Classical Relativistic Theory Models. *JETP Lett.*, 24:12, 1976.

[95] I.L. Bogolyubsky and V.G. Makhankov. Lifetime of Pulsating Solitons in Some Classical Models. *Pisma Zh. Eksp. Teor. Fiz.*, 24:15–18, 1976.

[96] Marcelo Gleiser. Pseudostable bubbles. *Phys. Rev. D*, 49:2978–2981, 1994.

[97] Tanmay Vachaspati. *Kinks and domain walls: An introduction to classical and quantum solitons.* Cambridge University Press, 4 2010.

[98] Roger F. Dashen, Brosl Hasslacher, and Andre Neveu. The Particle Spectrum in Model Field Theories from Semiclassical Functional Integral Techniques. *Phys. Rev.*, D11:3424, 1975.

[99] M. J. Ablowitz, M. D. Kruskal, and J. F. Ladik. Solitary wave collisions. *SIAM J. Appl. Math.*, 36:428, 1978.

[100] David K. Campbell, Jonathan F. Schonfeld, and Charles A. Wingate. Resonance Structure in Kink - Antikink Interactions in ϕ^4 Theory. *Physica D*, 9:1, 1983.

[101] P. Anninos, S. Oliveira, and R.A. Matzner. Fractal structure in the scalar lambda (phi**2-1)**2 theory. *Phys. Rev. D*, 44:1147–1160, 1991.

[102] H. Segur and M. D. Kruskal. Nonexistence of Small Amplitude Breather Solutions in ϕ^4 Theory. *Phys. Rev. Lett.*, 58:747–750, 1987.

[103] Philip M. Morse and Herman Feshbach. *Methods of theoretical physics,.* McGraw-Hill Book Co., New York, 1953.

[104] M. J. Rice. Physical dynamics of solitons. *Phys. Rev. B*, 28(6):3587–3589, September 1983.

[105] Tomasz Romanczukiewicz and Yakov Shnir. Some Recent Developments on Kink Collisions and Related Topics. 9 2018.

[106] Bjorn Engquist and Andrew Majda. Absorbing Boundary Conditions for Numerical Simulation of Waves. *Mathematics of Computation*, 31(139):629–651, 1977.

[107] N.S. Manton and H. Merabet. Phi**4 kinks: Gradient flow and dynamics. *Nonlinearity*, 10:3, 1997.

[108] B. S. Getmanov. Soliton Bound States in the phi**4 in Two-Dimensions Field Theory. *Pisma Zh. Eksp. Teor. Fiz.*, 24:323–327, 1976.

[109] Rama Basu and Alexander Vilenkin. Evolution of topological defects during inflation. *Phys. Rev. D*, 50:7150–7153, 1994.

[110] E. Farhi, N. Graham, Alan H. Guth, N. Iqbal, R.R. Rosales, and N. Stamatopoulos. Emergence of Oscillons in an Expanding Background. *Phys. Rev. D*, 77:085019, 2008.

[111] I.I. Tkachev. Phase transitions at preheating. *Phys. Lett. B*, 376:35–40, 1996.

[112] Nicholas Metropolis, Arianna W. Rosenbluth, Marshall N. Rosenbluth, Augusta H. Teller, and Edward Teller. Equation of state calculations by fast computing machines. *The Journal of Chemical Physics*, 21(6):1087–1092, 1953.

[113] Dmitri Yu. Grigoriev and V.A. Rubakov. Soliton Pair Creation at Finite Temperatures. Numerical Study in (1+1)-dimensions. *Nucl. Phys. B*, 299:67–78, 1988.

[114] Mark G. Alford, Hume Feldman, and Marcelo Gleiser. Thermal nucleation of kink - anti-kink pairs. *Phys. Rev. Lett.*, 68:1645–1648, 1992.

[115] Vachaspati and T. Vachaspati. Traveling Waves on Domain Walls and Cosmic Strings. *Phys. Lett. B*, 238:41–44, 1990.

[116] Edward Witten. Superconducting Strings. *Nucl. Phys. B*, 249:557–592, 1985.

[117] R. L. Davis and E. P. S. Shellard. COSMIC VORTONS. *Nucl. Phys. B*, 323:209–224, 1989.

[118] Lord Rayleigh. Xvii. on the maintenance of vibrations by forces of double frequency, and on the propagation of waves through a medium endowed with a periodic structure. *The London, Edinburgh, and Dublin Philosophical Magazine and Journal of Science*, 24(147):145–159, 1887.

[119] Ivana Kovacic, Richard Rand, and Si Mohamed Sah. Mathieu's Equation and Its Generalizations: Overview of Stability Charts and Their Features. *Applied Mechanics Reviews*, 70(2), 02 2018.

[120] E. Mettler. Stability and vibration problems of mechanical systems under harmonic excitation. In G. Herrmann, editor, *Dynamic Stability of Structures*, pages 169–188. Pergamon, 1967.

[121] Kei-ichi Maeda and Neil Turok. Finite Width Corrections to the Nambu Action for the Nielsen-Olesen String. *Phys. Lett. B*, 202:376–380, 1988.

[122] Ruth Gregory, David Haws, and David Garfinkle. The Dynamics of Domain Walls and Strings. *Phys. Rev. D*, 42:343–348, 1990.

[123] Ruth Gregory. Effective actions for bosonic topological defects. *Phys. Rev. D*, 43:520–525, 1991.

[124] Malcolm R. Anderson, Filipe Bonjour, Ruth Gregory, and John Stewart. Effective action and motion of a cosmic string. *Phys. Rev. D*, 56:8014–8028, 1997.

[125] A. Vilenkin and A. E. Everett. Cosmic Strings and Domain Walls in Models with Goldstone and PseudoGoldstone Bosons. *Phys. Rev. Lett.*, 48:1867–1870, 1982.

[126] John Preskill, Mark B. Wise, and Frank Wilczek. Cosmology of the Invisible Axion. *Phys. Lett. B*, 120:127–132, 1983.

[127] L. F. Abbott and P. Sikivie. A Cosmological Bound on the Invisible Axion. *Phys. Lett. B*, 120:133–136, 1983.

[128] Michael Dine and Willy Fischler. The Not So Harmless Axion. *Phys. Lett. B*, 120:137–141, 1983.

[129] Leesa Fleury and Guy D. Moore. Axion dark matter: strings and their cores. *JCAP*, 1601:004, 2016.

[130] Leesa M. Fleury and Guy D. Moore. Axion String Dynamics I: 2+1D. *JCAP*, 1605:005, 2016.

[131] Vincent B. Klaer and Guy D. Moore. How to simulate global cosmic strings with large string tension. *JCAP*, 1710:043, 2017.

[132] P. Sikivie. Of Axions, Domain Walls and the Early Universe. *Phys. Rev. Lett.*, 48:1156–1159, 1982.

[133] C. Hagmann and P. Sikivie. Computer simulations of the motion and decay of global strings. *Nucl. Phys.*, B363:247–280, 1991.

[134] C. Hagmann, Sanghyeon Chang, and P. Sikivie. Axion radiation from strings. *Phys. Rev.*, D63:125018, 2001.

[135] Alexander Vilenkin and Tanmay Vachaspati. Radiation of Goldstone Bosons From Cosmic Strings. *Phys. Rev.*, D35:1138, 1987.

[136] D. Garfinkle and T. Vachaspati. FIELDS DUE TO KINKY, CUSPLESS, COSMIC LOOPS. *Phys. Rev. D*, 37:257–262, 1988.

[137] Atish Dabholkar and Jean M. Quashnock. Pinning Down the Axion. *Nucl. Phys. B*, 333:815–832, 1990.

[138] Amelia Drew and E. P. S. Shellard. Radiation from Global Topological Strings using Adaptive Mesh Refinement: Methodology and Massless Modes. 10 2019.

[139] Amelia Drew and E. P. S. Shellard. Radiation from Global Topological Strings using Adaptive Mesh Refinement: Massive Modes. 11 2022.

[140] R. A. Battye and E. P. S. Shellard. Global string radiation. *Nucl. Phys.*, B423:260–304, 1994.

[141] R. A. Battye and E. P. S. Shellard. Radiative back reaction on global strings. *Phys. Rev.*, D53:1811–1826, 1996.

[142] R. A. Battye and E. P. S. Shellard. Spectrum of radiation from axion strings. *Nucl. Phys. Proc. Suppl.*, 72:88–93, 1999.

[143] R. L. Davis and E. P. S. Shellard. Antisymmetric Tensors and Spontaneous Symmetry Breaking. *Phys. Lett. B*, 214:219–222, 1988.

[144] Michael Goodband and Mark Hindmarsh. Bound states and instabilities of vortices. *Phys. Rev.*, D52:4621–4632, 1995.

[145] L. D. Landau and L. M. Lifshitz. *Quantum Mechanics Non-Relativistic Theory, Third Edition: Volume 3*. Butterworth-Heinemann, jan 1981.

[146] Philip M. Morse and Herman Feshbach. *Methods of Theoretical Physics,*. McGraw-Hill Book Company, 1953.

[147] Tomasz Romanczukiewicz. Creation of kink and antikink pairs forced by radiation. *J. Phys.*, A39:3479, 2006.

[148] Peter Forgacs, Arpad Lukacs, and Tomasz Romanczukiewicz. Negative radiation pressure exerted on kinks. *Phys. Rev.*, D77:125012, 2008.

[149] Tomasz Romanczukiewicz. Interaction between kink and radiation in phi**4 model. *Acta Phys. Polon.*, B35:523–540, 2004.

[150] Péter Forgács, Árpád Lukács, and Tomasz Romańczukiewicz. Plane waves as tractor beams. *Phys. Rev. D*, 88(12):125007, 2013.

[151] Tomasz Romanczukiewicz. Negative radiation pressure in case of two interacting fields. *Acta Phys. Polon. B*, 39:3449–3462, 2008.

[152] Matthew W. Hecht and Thomas A. DeGrand. RADIATION PATTERNS FROM VORTEX - ANTIVORTEX ANNIHILATION. *Phys. Rev. D*, 42:519–528, 1990.

[153] Jose J. Blanco-Pillado, Delia Schwartz-Perlov, and Alexander Vilenkin. Quantum Tunneling in Flux Compactifications. *JCAP*, 0912:006, 2009.

[154] Masahide Yamaguchi, Jun'ichi Yokoyama, and M. Kawasaki. Numerical analysis of formation and evolution of global strings in (2+1)-dimensions. *Prog. Theor. Phys.*, 100:535–545, 1998.

[155] Neil Bevis, Mark Hindmarsh, Martin Kunz, and Jon Urrestilla. CMB power spectrum contribution from cosmic strings using field-evolution simulations of the Abelian Higgs model. *Phys. Rev. D*, 75:065015, 2007.

[156] Marcelo Gleiser and Joel Thorarinson. A Phase transition in U(1) configuration space: Oscillons as remnants of vortex-antivortex annihilation. *Phys. Rev. D*, 76:041701, 2007.

[157] Steven Weinberg. A new light boson? *Phys. Rev. Lett.*, 40:223–226, Jan 1978.

[158] F. Wilczek. Problem of strong p and t invariance in the presence of instantons. *Phys. Rev. Lett.*, 40:279–282, Jan 1978.

[159] John Preskill, Mark B. Wise, and Frank Wilczek. Cosmology of the invisible axion. *Physics Letters B*, 120(1):127–132, 1983.

[160] L.F. Abbott and P. Sikivie. A cosmological bound on the invisible axion. *Physics Letters B*, 120(1):133–136, 1983.

[161] Michael Dine and Willy Fischler. The not-so-harmless axion. *Physics Letters B*, 120(1):137–141, 1983.

[162] Masahiro Kawasaki, Ken'ichi Saikawa, and Toyokazu Sekiguchi. Axion dark matter from topological defects. *Phys. Rev. D*, 91(6):065014, 2015.

[163] Mark Hindmarsh, Joanes Lizarraga, Asier Lopez-Eiguren, and Jon Urrestilla. Comment on "More Axions from Strings". 9 2021.

[164] Malte Buschmann, Joshua W. Foster, Anson Hook, Adam Peterson, Don E. Willcox, Weiqun Zhang, and Benjamin R. Safdi. Dark matter from axion strings with adaptive mesh refinement. *Nature Commun.*, 13(1):1049, 2022.

[165] H.B. Nielsen and P. Olesen. Vortex-line models for dual strings. *Nuclear Physics B*, 61:45–61, 1973.

[166] Y. Nambu. *Lectures at the Copenhagen Summer Symposium*, 1970.

[167] Tetsuo Goto. Relativistic quantum mechanics of one-dimensional mechanical continuum and subsidiary condition of dual resonance model. *Prog. Theor. Phys.*, 46:1560–1569, 1971.

[168] Graham Vincent, Nuno D. Antunes, and Mark Hindmarsh. Numerical simulations of string networks in the Abelian Higgs model. *Phys. Rev. Lett.*, 80:2277–2280, 1998.

[169] J. N. Moore, E. P. S. Shellard, and C. J. A. P. Martins. On the evolution of Abelian-Higgs string networks. *Phys. Rev. D*, 65:023503, 2002.

[170] Mark Hindmarsh, Stephanie Stuckey, and Neil Bevis. Abelian Higgs Cosmic Strings: Small Scale Structure and Loops. *Phys. Rev. D*, 79:123504, 2009.

[171] Thomas Helfer, Josu C. Aurrekoetxea, and Eugene A. Lim. Cosmic String Loop Collapse in Full General Relativity. *Phys. Rev. D*, 99(10):104028, 2019.

[172] J. R. C. C. C. Correia and C. J. A. P. Martins. Abelian–Higgs cosmic string evolution with multiple GPUs. *Astron. Comput.*, 34:100438, 2021.

[173] J. R. C. C. C. Correia and C. J. A. P. Martins. High resolution calibration of the cosmic strings velocity dependent one-scale model. *Phys. Rev. D*, 104(6):063511, 2021.

[174] Andreas Albrecht and N. Turok. Evolution of Cosmic Strings. *Phys. Rev. Lett.*, 54:1868–1871, 1985.

[175] David P. Bennett and Francois R. Bouchet. Cosmic string evolution. *Phys. Rev. Lett.*, 63:2776, 1989.

[176] Bruce Allen and E. P. S. Shellard. Cosmic string evolution: a numerical simulation. *Phys. Rev. Lett.*, 64:119–122, 1990.

[177] Vitaly Vanchurin, Ken D. Olum, and Alexander Vilenkin. Scaling of cosmic string loops. *Phys. Rev. D*, 74:063527, 2006.

[178] C. J. A. P. Martins and E. P. S. Shellard. Fractal properties and small-scale structure of cosmic string networks. *Phys. Rev. D*, 73:043515, 2006.

[179] Christophe Ringeval, Mairi Sakellariadou, and Francois Bouchet. Cosmological evolution of cosmic string loops. *JCAP*, 02:023, 2007.

[180] Jose J. Blanco-Pillado, Ken D. Olum, and Benjamin Shlaer. The number of cosmic string loops. *Phys. Rev. D*, 89(2):023512, 2014.

[181] D. Forster. Dynamics of Relativistic Vortex Lines and their Relation to Dual Theory. *Nucl. Phys. B*, 81:84–92, 1974.

[182] Richard A. Matzner. Interaction of U(1) cosmic strings: Numerical intercommutation. *Comput. Phys.*, 2(5):51–64, 1988.

[183] Jose J. Blanco-Pillado and Ken D. Olum. Stochastic gravitational wave background from smoothed cosmic string loops. *Phys. Rev. D*, 96(10):104046, 2017.

[184] Gerrit Mur. Absorbing Boundary Conditions for the Finite-Difference Approximation of the Time-Domain Electromagnetic-Field Equations. *IEEE Transactions on Electromagnetic Compatibility*, EMC-23(4):377–382, 1981.